7-11-2019

Utility Analysis for Optimizing Compact Adaptive Spectral Imaging Systems for Subpixel Target Detection Applications

Sanghui Han
sxh8907@rit.edu

Utility Analysis for Optimizing Compact Adaptive Spectral Imaging Systems for Subpixel Target Detection Applications

by

Sanghui Han

B.S. University of Colorado at Colorado Springs, 2007

M.S. Rochester Institute of Technology, 2015

A dissertation submitted in partial fulfillment of the
requirements for the degree of Doctor of Philosophy
in the Chester F. Carlson Center for Imaging Science
College of Science
Rochester Institute of Technology

July 11, 2019

Signature of the Author _____

Accepted by _____
Coordinator, Ph.D. Degree Program Date

CHESTER F. CARLSON CENTER FOR IMAGING SCIENCE
COLLEGE OF SCIENCE
ROCHESTER INSTITUTE OF TECHNOLOGY
ROCHESTER, NEW YORK

CERTIFICATE OF APPROVAL

Ph.D. DEGREE DISSERTATION

The Ph.D. Degree Dissertation of Sanghui Han
has been examined and approved by the
dissertation committee as satisfactory for the
dissertation required for the
Ph.D. degree in Imaging Science

Dr. John P. Kerekes,

Dissertation Advisor

Dr. David Ross, External Chair

Dr. David Messinger

Dr. Emmett Ientilucci

Date

For my son Jerry,

I hope one day you will be able to go further than I ever could.

Love,

Mom

Utility Analysis for Optimizing Compact Adaptive Spectral Imaging Systems for Subpixel Target Detection Applications

by

Sanghui Han

Submitted to the
Chester F. Carlson Center for Imaging Science
in partial fulfillment of the requirements
for the Doctor of Philosophy Degree
at the Rochester Institute of Technology

Abstract

Since the development of spectral imaging systems where we transitioned from panchromatic, single band images to multiple bands, we have pursued a way to evaluate the quality of spectral images. As spectral imaging capabilities improved and the bands collected wavelengths outside of the visible spectrum they could be used to gain information about the earth such as material identification that would have been a challenge with panchromatic images. We now have imaging systems capable of collecting images with hundreds of contiguous bands across the reflective portion of the electromagnetic spectrum that allows us to extract information at subpixel levels. Prediction and assessment methods for panchromatic image quality, while well-established are continuing to be improved. For spectral images however, methods for analyzing quality and what this entails have yet to form a solid framework.

In this research, we built on previous work to develop a process to optimize the design of spectral imaging systems. We used methods for predicting quality of spectral images and extended the existing framework for analyzing efficacy of miniature systems. We comprehensively analyzed utility of spectral images and efficacy of compact systems for a set of application scenarios designed to test the relationships of system parameters, figures of merit, and mission requirements in the trade space

for spectral images collected by a compact imaging system from design to operation. We focused on subpixel target detection to analyze spectral image quality of compact spaceborne systems with adaptive band selection capabilities.

In order to adequately account for the operational aspect of exploiting adaptive band collection capabilities, we developed a method for band selection. Dimension reduction is a step often employed in processing spectral images, not only to improve computation time but to avoid errors associated with high dimensionality. An adaptive system with a tunable filter can select which bands to collect for each target so the dimension reduction happens at the collection stage instead of the processing stage. We developed the band selection method to optimize detection probability using only the target reflectance signature. This method was conceived to be simple enough to be calculated by a small on-board CPU, to be able to drive collection decisions, and reduce data processing requirements. We predicted the utility of the selected bands using this method, then validated the results using real images, and cross-validated them using simulated image associated with perfect truth data. In this way, we simultaneously validated the band selection method we developed and the combined use of the simulation and prediction tools used as part of the analytic process to optimize system design.

We selected a small set of mission scenarios and demonstrated the use of this process to provide example recommendations for efficacy and utility based on the mission. The key parameters we analyzed to drive the design recommendations were target abundance, noise, number of bands, and scene complexity. We found critical points in the system design trade space, and coupled with operational requirements, formed a set of mission feasibility and system design recommendations. The selected scenarios demonstrated the relationship between the imaging system design and operational requirements based on the mission. We found key points in the spectral imaging trade space that indicated relationships within the spectral image utility trade space that can be used to further solidify the frameworks for compact spectral imaging systems.

List of Tables

List of Figures

Contents

"We live in a world bathed in light. We see with light, plants draw energy from light, and light is at the core of technologies from computing to surgical techniques. Light influences our lives today in new ways that we could never have imagined just a few decades ago. As we move into the next century, light will play an even more significant role, enabling a revolution in world fiberoptic communications, new modalities in the practice of medicine, a more effective national defense, exploration of the frontiers of science, and much more."

- National Research Council, *Harnessing Light*, 1998

1 Introduction

The development of imaging systems and our methods of recording light have had a profound effect on image collection and exploitation capabilities. In less than a century, we moved from taking panchromatic aerial photographs [1] to high spatial resolution images that can be acquired at any time during almost any weather conditions [2]. In this research, our focus was on the design of passive imaging systems capable of collecting spectral images in the reflective portion of the electro-magnetic spectrum. We built on previous frameworks for analyzing spectral image quality [3] and the efficacy of miniature satellite systems for wide area search missions [4] to develop a process for optimizing imaging system designs with application performance as the objective function. We used existing tools to form a process for traversing the trade space for spectral imaging system to find the relationships between components of spectral imaging systems that affect performance. We took advantage of the computing power available today that was not possible a decade ago to analyze thousands of images with billions of pixels. The context in which we developed our objectives was for compact spectral imaging systems with wide area search missions for subpixel targets.

1.1 Motivation

Traditional spectral imaging systems often attempt to simultaneously increase spectral resolution and spatial resolution. Hyperspectral imaging systems currently in use have powerful detectors, that collect images with hundreds of contiguous bands across the reflective portion of the electromagnetic spectrum where every pixel in the image contains information about the materials present. Target detection using Hyperspectral Images (HSI) does not always require spatial resolution that allows an analyst to visually identify an object of interest, and two objects that may look the same (green camouflage vs green vegetation), can be differentiated using spectral signatures outside of the visible spectrum.

When it comes to analyzing HSI to extract the information required, there are challenges to processing the data. When HSI is collected, the hundreds of bands in each image means a single spatial sample is hundreds of more bits than a panchromatic image. This amount of data needs to be go through several data handling steps, each of which can be costly. Usually, every band collected does not contribute to utility and justify these costs. For example, when looking for an object with a specific spectral signature, only the bands containing the detectable signatures are of use. With this in mind, a method for reducing the number of bands that are transmitted or stored during collection can be beneficial. Given the amount of data inherent in HSI combined with the use of automation for extracting information, their utility is often limited by the processing, exploitation, and dissemination capabilities. A spectral imaging system that has adaptive band selection capabilities can allow us to bypass the costs of handling all the data that is collected while meeting the information requirements.

Designing and building such a system required comprehensive analysis of the efficacy of the mission, performance analysis of the the design, and the operational feasibility. There were some missions - targets and locations - where a compact spectral imaging system was not the appropriate tool, and to determine this, we needed a process that could define and test the limits. The statistical component of uncertainty for subpixel target detection missions using compact systems first required a decision for the efficacy of a mission. Not only of whether a target was detectable using spectral images, but if the uncertainty inherent in the given mission was acceptable. However, this could only be answered if the mission was defined. A system designed with an unknown mission, may not be able to meet its performance goals once it was operational and

given specific targets and locations. We determined that the decision point for designing a compact spectral imaging system was between the efficacy of the mission, the trade space between spectral image figures of merit, and the operational feasibility of processing the collected images.

We predicted then assessed the system design for a small set of missions as the methodology for analyzing the utility trade space for spectral imaging systems. Our goal was to provide design recommendations for an imaging system that was cost effective, robust, with adequate performance within the operational constraints. We developed an approach to facilitate decisions for building and operating compact spectral imaging systems with adaptive band selection capabilities for wide area search missions.

1.2 Imaging System Context

In this section we elaborate on the imaging system context for which we develop our process and detail the parameters. Reference to compact systems refer to low earth orbit systems weighing less than 10 kilograms [5]. One unit of measure (1U) for these compact systems is 10cm on each side. The systems we considered in our design analysis are 3-6U in size. We envisioned this process to be used for systems that resemble a CubeSat, which is self-contained with its own communication, power and navigation system within the spacecraft. A single compact imaging system would be part of a constellation for wide area search missions, capable of high temporal frequency, with daily revisit times or less.

The adaptive band selection capability refers to a tunable filter that can modify its spectral resolution by changing its tuning time. If high spectral resolution is required, the tuning time is decreased, and visa versa. The system is capable of selecting the wavelengths of the bands and collecting the desired number of bands. While theoretically it can collect the number of bands with the spectral resolution matching the traditional HSI systems, we only considered the range of bands that we determined to be operationally feasible for compact systems. What we did not consider was the calibration errors associated with the time it takes for the tunable filter to select the wavelength. We assumed negligible error due to tuning time, which may or may not affect the final recommendation. We leave the error analysis for these system effects for future studies.

The process was developed to determine the mission efficacy,

optimal system design implementation, and the operational feasibility of subpixel target detection using images collected using these systems. What this process does not do, is analyze individual components in the design such as optical diameter, telescope design, detector sensitivity, and many other components in building a spectral imaging system. We assume that it is a modular CubeSat that already has most of the system components built, but with a few elements of the system design such as the focal length, height of the orbit, and some noise reduction or signal boosting capabilities that can be modified.

1.3 Semantics

When describing and explaining image quality, many terms are used interchangeably. In our references, the subtleties between the definitions and use of these terms were explained in detail [6] [3]. We reiterate these definitions and terms in this dissertation for clarification of their use throughout this document. We defined image *quality* in two components - 1) *fidelity* which is the accuracy of information that is contained in a scene and 2) *utility* which is the ability to extract the information needed from the image. Both of these terms are tied to specific portions of the imaging chain but are not mutually exclusive.

Fidelity is defined as how accurately an image captures the real world. It is the component of quality that answers to the reliability of the information contained in an image and is usually tied to the sensor figures of merit and collection capabilities of the imaging chain. Fidelity can be further divided into spatial, spectral, and radiometric components. Spatial fidelity speaks to how well an image projects the 3-D object shapes in the real world into the 2-D image space. With digital imaging, it also represents how accurately the continuous signal from the real world can be replicated by the image sampling. Spectral fidelity answers to how well an imaging system captures a material's reflective properties. It represents how precisely the continuous reflective spectrum of the materials in the real world are spectrally sampled. Radiometric fidelity spans both the spatial and spectral aspects of fidelity and represents the pixel by pixel accuracy in which the signal that reaches the sensor is captured. It can be degraded by the atmosphere, noise, or poor calibration.

Utility is how easily an image can deliver the information we need from it or how useful an image is. It answers to the required steps or processes to extract the information we want from an image, and is usually

tied to the exploitation activities in the imaging chain. We present two broad separations in the exploitation methods. One method of exploitation is by a human observer who can identify objects and activities from an image. The other method is information extraction using automated processing. Many exploitation activities in the past used automated processing for HSI and a human observer for panchromatic images. More recently however, image exploitation is done using automated processing and machine learning algorithms for all types of images.

We focused on the *utility* of spectral images, with the assumption that information was extracted using automation and machine learning algorithms. Therefore computational efficiency, reducing processing cost while maintaining the ability to extract the required information, was a key consideration in our approach. Image quality for the purposes of this dissertation refers to both our ability to extract the needed information as well as how accurately it captures the real world scene that was being imaged. These two measures of image quality are defined as image utility and image fidelity. For panchromatic images, we mostly refer to quality, as this definition encompasses both fidelity and utility and for these types of images, one directly affects the other. What a human observer is able to ascertain from an image is the standard for defining image quality, and so a high level of image fidelity is responsible for improved information extraction leading to a high level of utility. Furthermore, spatial fidelity of a scene is usually the primary concern in panchromatic images, and so spatial fidelity leads directly to utility. We do not expand definitions of utility for panchromatic images that use machine learning for image exploitation, although in the future, this shift will need to be addressed when analyzing image quality even for panchromatic images.

For spectral images, the relationship between fidelity and utility for spectral images do not necessarily go hand in hand. Unlike panchromatic images where the ability of a human observer to extract information is the main criterion for quality, automated processing is the primary method for image exploitation. Furthermore, spectral fidelity is an additional component that contributes to the quality of spectral images, and changes the relationship between fidelity, utility, and quality. While high spatial and spectral fidelity both contribute to utility, the relationship is not direct nor linear. For example, an image with only a few bands with a low spatial resolution can detect some targets with a high level of accuracy. This is a case where low fidelity measures can still result in high utility. Furthermore, since there is a wider range of uses for spectral images, utility depends on application. In Chapter 3 we explicitly and quantitatively define utility for subpixel target detection applications, but

in this section, we define utility of spectral images as the performance an image exploitation algorithm achieves.

We also define *assessment* and *prediction* when related to spectral image utility analysis for subpixel target detection. Both are necessary steps in analyzing image quality within the system design process. *Assessment* is applying a target detection algorithm directly to a large set of images in order to generate detection statistics. *Prediction* on the other hand, is a model that when given certain figures of merit or imaging system parameters, can produce the most likely detection results without the images. There are many methods for predicting image quality, but we focus on the analytic method which is explained in the subsequent chapters. We parameterized target abundance, number of bands, noise, and scene complexity to predict utility. Following prediction, we used simulation to account for the operational aspects of exploiting images collected by a compact spectral imaging system with adaptive band selection capabilities. We assessed the simulated images with associated truth data. We used both the prediction and assessment results to determine our recommendations.

Scene complexity is a term we also define in this section to clarify its use in the subsequent chapters of this dissertation. It was used in two ways, first in Chapter 3 in order to stay consistent with the reference that first used this as a figure of merit [7]. Then in Section 3.2 where we described how this value is calculated and used in some of the prediction methods for spectral image utility. In the subsequent chapters however, for the purpose of this research, we refer to scene complexity in a more general sense to describe the overall intrinsic properties of a location where homogeneity, spectral variations of the materials present, and other physical phenomena that can contribute to *complexity*. We separated the two measures of scene complexity as *background complexity* which is a metric we developed in this research, and *scene volume* which is a metric developed by previous research for spectral image analysis [8]. The calculations, descriptions, as well as motivations for their use is described in detail in Chapter 6.

1.4 Previous System Design Processes

Previous methods for optimizing system design also used simulation and modeling of spectral imaging systems [9] and some of them encompassed the entire remote sensing process [10]. These methods also conducted

trade studies using both analytic and simulation models to configure complex data selection parameters [11]. Other methods for studying system designs from a mission and operation perspective exist for satellite systems where the optimal designs of small satellites were outlined in detail for a list of mission objectives [12]. The state of the art processes that facilitate decision making on design of remote sensing satellites used an approach called multidisciplinary design optimization [13] and multi-parameters joint optimization [14].

Other works also attempted to account for several elements of the image chain to include dimension reduction methods to determine detection performance. One of them started by characterizing the background and its effect on target detection performance [15]. Others compared target detection algorithms and their performance after images went through the pre-processing steps of atmospheric compensation and dimension reduction [16] [17]. However, all of these projects used a single HSI of the same scene and targets. Therefore the effects of detection performance due to the target and the location was not determined.

There were several gaps in the previous work and current state of the art that we wished to close in this research. The first was that all these methods assumed a fixed band imaging system, and so if the band selection and dimension reduction step were accounted for, it assumed post collection processing. Also, while these methods were appropriate for many aspects of designing a spectral imaging system, they did not comprehensively account for the operational aspect of exploiting a spectral image to include band selection or the input mission scenarios before the design. The assumptions of the methods were either that the system existed and the utility prediction was for the purpose of selecting the appropriate spectral image, or that the final mission scenario was unknown. For subpixel target detection, the target and background combination had significant effects on the final detection performance. What we addressed in this research by selecting a few input scenarios for analysis, was the operational aspects of image collection and the effects of the mission scenario in the final utility.

The process we proposed analyzed selected mission scenarios, and assumed that the bands were selected for collection depending on target. Our assumption was that small, inexpensive spectral imaging systems were not required to detect all possible targets, but only a few, leveraging the constellation of satellites, each with a separate mission set. We also accounted for the operation and anticipated the decisions that a collection manager would make in order to meet the mission requirements. As a

result, we not only developed a band selection method that could be used to determine which bands to collect, but also a metric that tied the design to the operation in determining the number of bands. We developed metrics that quantified the effects of a target and its location on mission feasibility and utility.

1.5 Objectives

The primary objective of this research was to develop a practical process for determining the efficacy of missions and analyzing utility of spectral images collected by compact systems. A key task in forming this process was to develop a dynamic band selection algorithm that could be implemented in a compact spectral imaging system with adaptive band selection capabilities. The insertion of this capability to the process was to account for the operational requirements in wide area search missions where transmission bandwidth or data storage requirements can be limited. We built on previous work that defined figures of merit for spectral images and used existing tools in a novel manner for analyzing spectral image utility to examine a few mission scenarios and how they occupy the trade space. By doing so, developed a decision process to facilitate the design of compact imaging systems and determine the feasibility of selected missions.

Figure 1.1 shows an overview of the steps in the process to study the trade space of spectral imaging systems. We examined the feasibility of a mission by predicting the detection performance for a target against the background composition to find critical points in the trade space for the mission. We then designed a scene similar to the location in which we wished to confirm or deny the presence of a target, and generated simulated images that encompassed the critical design elements found in the prediction process. Then we assessed the simulated images using target detection algorithms to justify the determination of whether a mission was operationally feasible, and a set of recommended spectral imagining system design parameters to achieve the desired performance.

The process was developed within the framework for analyzing efficacy of missions for compact satellite imaging systems that was previously focused on panchromatic images and the figures of merit that govern them. We also built on the framework for analyzing spectral image utility that was previously focused on spectral imaging systems with fixed bands. We selected four criteria that affected detection performance, tied to the mission, imaging system design, and the exploitation of spectral

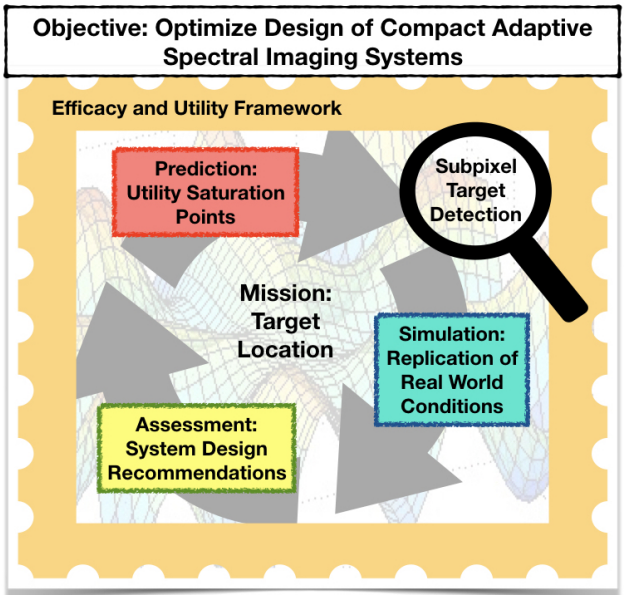

Figure 1.1: Overall objective and process to analyze efficacy, and predict and assess utility for selected subpixel target detection mission scenarios.

images for wide area search. The four criteria were target fill fraction or target abundance (two terms that are used interchangeably in this dissertation), number of bands, scene complexity, and signal to noise ratio. The analytic model that was used to predict utility parameterized these four components to find points in the trade space where improving the imaging system design metric had limited effect on utility. The prediction also produced information about the feasibility of a mission and imaging system parameters that would allow detection of the target above a desired performance criterion. The goal of the simulation process was to design a scene and use a method for placing targets that replicated the operations framing the wide area search mission. The assessment of the simulated images validated the predictions or highlighted possible challenges that may exist in real operations that would affect utility that was not captured in the prediction process.

Table 1.1 shows the sequence of the optimization process and the trade space parameters analyzed in each step to form recommendations for a system design. In each step there was an output for a mission set with a target and location related to the system. For example, if our mission was to confirm or deny the presence of an orange airplane in the Rochester, NY in the month of June, the prediction for this mission determined whether this mission was feasible. If it was feasible, the critical points in the trade

space for target abundance, number of bands, noise, and background complexity were used to find a set of recommendations for a system design. The prediction determined a set of possible spatial resolutions, acceptable noise, and the number of bands required. In the simulation and scene design step, the target geometry along with the real world scene resembling the Rochester airport and the operational conditions were replicated to generate synthetic images.

Table 1.1: Sequence of the Optimization Process

Process	**Mission**	**System**
1) Prediction	Feasibility Determination or Saturation Points	Spatial Resolution, Noise, Number of Bands
2) Simulation and Scene Design	Target Geometry, Location and Operations Replication	Optics, Platform Height, Detector, Collection Conditions
3) Assessment	Operational Effects and Performance Ceilings	Detectability, System Recommendations

The simulation was designed with imaging system parameters for optics, platform height, and detector characteristics such as the pixel pitch and detector response functions of the bands, and collection conditions such as illumination, smear or look angle, that generated the optimal spatial resolution and bands found by the prediction. The assessment step included the post-processing of the simulated images and replicated the predicted acceptable noise and selected bands to assess the images using target detection algorithms. The assessment as it related to the mission determined the effects of the operational process, computational requirements for processing the amount of data required affected by the number of bands and the temporal frequency for accomplishing the mission and performance ceilings due to a combination of these factors. For the system, it determined the detectability of the target based on its target abundance distribution and scene complexity produced by the simulated system parameters, which led to a set of recommendations for a system design.

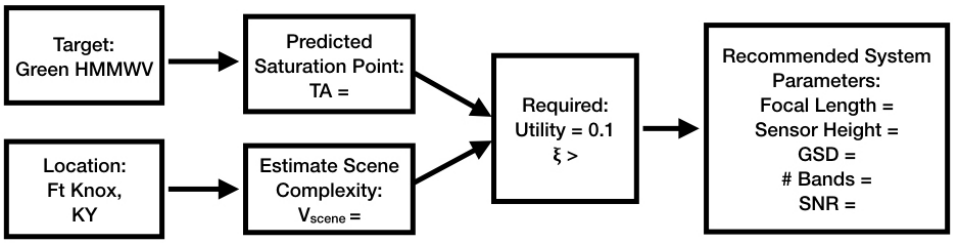

Figure 1.2: Example mission that use process to determine points in trade space that lead to a set of system parameter recommendations.

1.6 Example Mission

In this section we present an example mission and the flow of this process to reach a recommendation for a set of parameters. We present this to illustrate the determination of the optimal design that also accounts for operational limitations. We reiterate the context, and the process that was considered to make design decisions.

Mission Scenario: Collect weekly images from June to July to detect presence of green vehicles in training areas of Ft Knox, KY. The presence of a target is easily verifiable by other sources of intelligence collection. Data processing capabilities for weekly images are a maximum of 15 bands.

Figure 1.2 shows the target and location and the information that needs to be determined to provide a feasibility recommendation of whether this mission scenario is appropriate to employ compact imaging systems. If the mission is feasible, the optimal system parameters are determined. The key parameters in the imaging system that we provide a recommendation for, were the spatial resolution determined by the focal length and sensor height, number of bands needed to accomplish the mission, and the acceptable noise level. The subsequent chapters of this dissertation detail the experiments and analysis that was done to not only provide recommendations for this mission but also others.

1.7 Overview

We present a methodology for comprehensively analyzing the spectral image utility trade space for the purpose of optimizing the design of a

compact imaging system. We begin be describing panchromatic image figures of merit used to predict quality in Chapter 2 on which we build the descriptions of the spectral image quality metrics in Chapter 3. We differentiate multi-spectral images from hyper-spectral images, discuss some spectral image figures of merit, quantitatively define utility, and present existing utility prediction methods including the analytic method used in this project. Then in Chapter 4 we describe the simulation tool used to generate spectral images and the techniques used to ensure key real world image characteristics were captured in the simulation model or in the post-processing step. In Chapter 5 we describe dimension reduction and band selection methods. We also describe the development of a novel band selection method that was employed as part of the process in order to account for the operation of an adaptive spectral imaging system, and the validation process.

In Chapter 6, we describe the approach used to comprehensively analyze the different components of the spectral image utility trade space. The parameters used in the prediction, and the methods used to design the scenes, the post-processing steps, and the target detection algorithms used in the assessment are described. The overall approach divides the tests into two parts - the simple scene and the complex scene. Chapter 7 describes the operational context and the details for the two parts of the testing. Then Chapter 8 presents the results of the tested scenes and Chapter 9 provides the conclusions and contributions of this research.

"The dwarf sees farther than the giant, when he has the giant's shoulder to mount on."

- Samuel Taylor Coleridge, *The Friend*, 1828

2

Panchromatic Image Quality

Image quality for panchromatic images have been analyzed for many decades and there is a solid framework for predicting quality with well-defined figures of merit. The General Image Quality Equation (GIQE) is the widely accepted method for predicting panchromatic image quality using various figures of merit [18]. In this chapter we present the prediction method and the three figures of merit used to predict panchromatic image quality.

2.1 National Image Interpretability Rating Scale

The most widely used measure of quality for panchromatic images is the National Image Interpretability Rating Scale (NIIRS). This is a numbered rating between 0 and 9 that is given by a trained image analyst to an image based on the amount of information that can be extracted. It is a subjective measure of utility that increases when a human observer is able to extract more information about the real world scene. The GIQE is a quality prediction model that was modified several times over the last decade. The three figures of merit used in the current version, GIQE version 5 (GIQE 5) [19], are the Ground Sampled Distance (GSD), Signal-to-Noise Ratio (SNR), and Relative Edge Response (RER). The

predicted NIIRS value (P_{NIIRS}) is calculated using the coefficients in Table 2.1 (Eq. 2.1).

$$P_{NIIRS} = A_0 + A_1 \cdot Log_{10}(GSD) \quad [in] \quad + \quad A_2 \cdot [1 - e^{\frac{A_3}{SNR}}] \cdot Log_{10}(RER) + \quad A_4 \cdot Log_{10}(RER)^4 + \frac{A_5}{SNR} \tag{2.1}$$

We used these three parameters as the starting point for exploring panchromatic image quality.

Table 2.1: GIQE 5 equation coefficients

A_0	A_1	A_2	A_3	A_4	A_5
9.57	-3.32	3.32	-1.9	-2	-1.8

2.2 Ground Sampled Distance

In remote sensing, the GSD is a measure of the distance between the projection of two pixels onto the ground. It is dictated by the Effective Focal Length (EFL), detector pixel pitch, and collection geometry of the imaging system. For an image that is collected by a sensor that is directly above the scene, Eq. 2.2

$$GSD = \frac{p}{F} \cdot H_{\perp} \quad [m] \tag{2.2}$$

shows the parameters that contribute to the GSD in both the x and y directions. Table 2.2 shows the parameters that are used to calculate GSD.

Table 2.2: Parameter definitions for GSD calculation

Parameter	**Symbol**
Detector Pixel Pitch	p $[\mu m]$
Height	H $[m]$
Effective Focal Length	F $[mm]$
Line of Sight Tilt Angle	α
Imaging System Elevation Angle	β
Angle between x and y	θ

For collection geometry where the sensor is not directly above the scene, the GSD in each direction is calculated separately according to Eq. 2.3

$$GSD_x = \left(\frac{p}{F} \cdot H_r\right) \cdot \left(cos^2(\alpha) + \left[\frac{sin(\alpha)}{cos(\beta)}\right]^2\right)^{1/2} \quad [m] \tag{2.3}$$

and Eq. 2.4.

$$GSD_y = \left(\frac{p}{F} \cdot H_r\right) \cdot \left(sin^2(\alpha) + \left[\frac{cos(\alpha)}{sin(\beta)}\right]^2\right)^{1/2} \quad [m] \tag{2.4}$$

In this case, the parameter used in the GIQE is the geometrical mean of the GSD in both directions (Eq. 2.5),

$$GSD_{GM} = \sqrt{GSD_x \cdot GSD_y} \quad [m] \tag{2.5}$$

or in the case where the along-scan and cross-scan are not orthogonal, the angle between the scanning directions is accounted for by using the angle θ (Eq. 2.6).

$$GSD_{GM} = \sqrt{GSD_x \cdot GSD_y \cdot sin(\theta)} \quad [m] \tag{2.6}$$

Figure 2.1 shows a diagram of what the GSD parameters represent within the imaging system. Figure 2.1a shows the GSD calculation parameters for nadir collection where the angle between the GSD in the x and y directions are perpendicular (Eq. 2.2). Figure 2.1b shows the calculation parameters for a collection angle that is tilted and so the line of sight is at an angle α to the ground and the elevation of the imaging system is at an angle of β. The image shows straight lines that represent the ground, which is a sufficient approximation for small GSDs, but there is also a curvature of the earth that may have effects on larger GSDs. The final GSD for this figure is calculated by using the geometric mean (Eq. 2.6).

In this research we used meters as the units to calculate the GSD since the input variables were in metric unit. However, the units of the GSD value used to calculate the predicted NIIRS value (Eq. 2.1), are in inches. Therefore, the GSD value was converted to inches prior to calculating the P_{NIIRS} value.

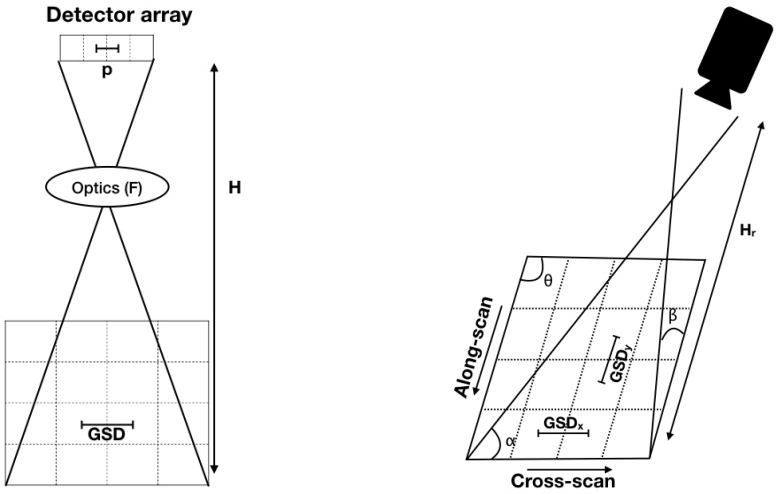

(a) Diagram illustrating GSD for nadir collection.

(b) Diagram illustrating GSD for angled collection.

Figure 2.1: Diagrams representing GSD for different collection geometry.

2.3 Signal-to-Noise Ratio

The SNR is an image quality metric that is often used on its own to indicate the level of detector sensitivity. A high quality detector has high SNR, and differentiates small changes in signal. As the name implies, it is the ratio between the signal and the noise. While the base concept is simple, there can be many different values for the same detector, depending on how signal and noise are defined and calculated.

For remote sensing systems, one object on the earth is differentiated from another when the change in reflectance at a set wavelength or bandwidth registers a signal that is greater than the noise. It is why the noise equivalent change in reflectance ($NE\Delta\rho$) is often used to determine image utility. For target detection, the difference in reflectance between the target and background determines signal, since a target that does not have a sufficiently higher reflectance than the noise can not be detected (Eq. 2.7).

$$S_{\Delta\rho} = S_{\rho_{high}} - S_{\rho_{low}} \tag{2.7}$$

The definition of signal we used is one that was provided by the GIQE manual for image-based SNR calculations. It used the difference in the sensor reaching radiance (L) from a high and low reflectance value and

converted it into signal electrons (S_e) [20]. The selection of the high and low reflectance affected the signal value, and for our simulation validation, explained in chapter 4, we used 7% and 15%. Table 2.3 shows the parameters that were used to calculate the SNR.

Table 2.3: Parameter definitions for SNR calculation

Parameter	**Symbol**
Dark Noise	σ_d $[e-]$
Quantization Noise	σ_q $[e-]$
Quantum Efficiency	QE
Optical Transmission	τ
Aperture Diameter	D $[mm]$
Integration Time	t_{int} $[\mu s]$
Detector Area	A $[m^2]$
Radiance	L $[W/m^2 sr]$
Focal Length	F $[m]$

The noise is typically calculated from the standard deviation of the high reflectance signal value, which is the shot noise. The F# (Eq. 2.8),

$$F\# = \frac{F}{D} \tag{2.8}$$

is used to calculate the G# (Eq. 2.9),

$$G\# = \frac{1 + 4F\#^2}{\tau\pi} \tag{2.9}$$

which along with the radiance and integration time, is used to calculate the number of photons incident onto a detector area (Eq. 2.10).

$$S_\Phi = \frac{t_{int} \cdot A \cdot L}{G\#} \cdot \frac{\lambda}{hc} \quad [photons] \tag{2.10}$$

We assumed that the signal had a Poisson distribution, and so the variance was equal to the mean of the signal level. The average shot noise was then assumed to be equal to the standard deviation of the signal, which in terms of electrons was calculated by scaling the photon signal by the quantum efficiency of the detector (Eq 2.11).

$$S_e = S_\Phi \cdot QE \quad [e-] \tag{2.11}$$

We defined noise as a combination of fixed noise and shot noise, and the total noise was the the combination of all the components (Eq. 2.12).

$$N = \sqrt{S_e + \sigma_d^2 + \sigma_q^2} \quad [e-] \tag{2.12}$$

While there were many different sources of fixed noise, we focused on two fixed noise values that was separated into dark noise (σ_d) and quantization noise (σ_q). This allowed us to calculate SNR directly from the difference in radiance values of a high and low reflector in the image (Eq. 2.13).

$$SNR = \frac{S_e}{N} \tag{2.13}$$

2.4 Relative Edge Response

The RER is a measure of how sharply an edge is represented in an image and how much blur there is. It is a metric that is dependent on the Modulation Transfer Function (MTF). The GIQE definition of the MTF is a combination of the imaging system components that include the optics, detector, clocking (that causes scan smear), and other imaging system components that can cause blurriness. We focused on the diffraction resolution and detector resolution [6] as sources of the blur from the diffraction from widening of a point source of light, and smear due to movement of the imaging system. Figure 2.2 illustrates the edge response where 2.2a shows an image of a perfect edge with no blur and its plot showing the transition between the high reflectance area and the low reflectance area and 2.2b shows the same for a blurry edge.

The normalized edge response that was used in our GIQE calculation was the MTF that was integrated through an imaging system's spatial frequencies. In Eq. 2.14

$$ER_x(\zeta) = 0.5 + \frac{1}{\pi}\int_0^{u_c} \frac{MTF_x(u)}{u} sin(2\pi u\zeta)du \tag{2.14}$$

ζ is the response relative to the center of a pixel and u is the spatial frequency that produces the MTF in either the x or y direction. The MTF values are integrated along each frequency where u_c is the optics cutoff

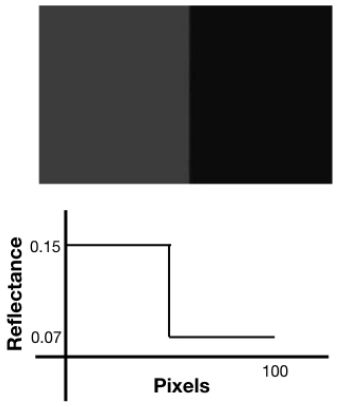

(a) Image of perfect edge with no blur and plot of its edge response.

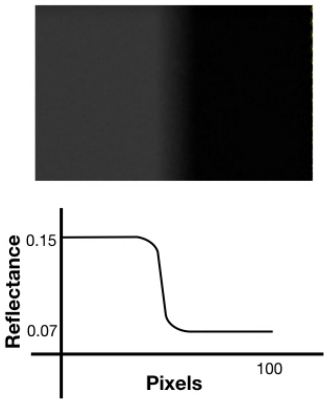

(b) Image of edge with some blur and plot of its edge response.

Figure 2.2: Illustration of edge response function showing difference in transition between a perfect edge with no blur and edge with blur incorporated.

frequency normalized to its sample spacing. The RER was calculated by taking the slope between the edge response at half a pixel to the left of the edge and half a pixel to the right of the edge.

Figure 2.3 shows a diagram of the values that are used in Eq. 2.15

$$RER_x = ER_x(+0.5) - ER_x(-0.5) \tag{2.15}$$

to calculate the RER. An edge such as the ones shown in Figure 2.2 was an RER in the x direction. A platform moving in a direction other than what is perpendicular to an edge would produce smear differently for edges in the x and y direction. The geometric mean of the RER in both the x and y directions (Eq. 2.16)

$$RER_{GM} = \sqrt{RER_x \cdot RER_y} \tag{2.16}$$

was the parameter used to calculate the GIQE along with the GSD and SNR.

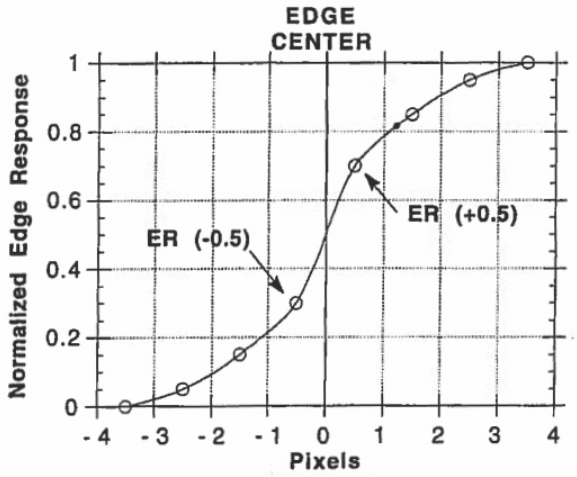

Figure 2.3: Diagram of relative edge response [18].

2.5 Summary

Three panchromatic figures of merit that are used in the GIQE were described in this chapter. We first analyzed the image quality metrics that were determined by a human observer as a starting point for contrast to spectral image utility metrics. While spectral images derived its utility from automated processing, the metrics presented in this chapter still permeated all aspects of spectral image utility. The image quality described by spatial resolution, edge response, and noise were still components within the spectral image quality trade space. Their relationship in spectral images became more complicated and challenging to express as an equation as was done with the GIQE.

"In that direction," the Cat said, waving its right paw round, "lives a Hatter: and in that direction," waving the other paw, "lives a March Hare. Visit either you like: they're both mad."
"But I don't want to go among mad people," Alice remarked.
"Oh, you can't help that," said the Cat: "we're all mad here. I'm mad. You're mad."
"How do you know I'm mad?" said Alice.
"You must be," said the Cat, "or you wouldn't have come here."

- Lewis Carroll, *Alice in Wonderland*, 1865

3 Spectral Image Utility

Traditional quality measurements of panchromatic images were derived from human observers and their ability to extract information about the scene. Fidelity and how accurately an image was able to depict what was in a scene was the primary driver for utility. The measures we used to determine utility for panchromatic images were relevant also for spectral images. However, the addition of another dimension of quality - spectral resolution - complicated the intuitive relationships between the figures of merit that were described in Section 2 as well as those that were specific to spectral images.

With spectral images, the reflectance properties of a material could identify an object within a scene even at sub-pixel levels [21]. The shape of an object and what was perceived by a human observer was less relevant in identifying it. Quality for spectral images was dependent on automation and its algorithms to extract information [22]. Fidelity was no longer the primary driver for utility in spectral images, and the accuracy in which an image captured the shapes of objects played minor roles in determining quality. The application and the capabilities of automation and the suitability of algorithms determined the ability to extract information.

The applications of spectral images were more diverse than

panchromatic images and so the relationship between the existing figures of merit and their contribution to utility was challenging to express in a single equation. In this chapter we focus on the figures of merit that contribute to performance for subpixel target detection applications. We refer to utility in this document to be synonymous to application performance, which for subpixel target detection algorithms, was detection probability.

3.1 Utility Assessment Metric

For target detection, there were several metrics to quantify utility. The primary method for quantifying detection performance was the Receiver Operating Characteristic (ROC) curve that compared the True Positive Rate (TPR) to the False Positive Rate (FPR). The Area Under the Curve (AUC) was a commonly used metric that was calculated from the ROC curve. The maximum AUC was 1.0 which indicated that all the true positive were detected with no false positives. The TPR at a Specified False Positive Rate (SFPR) or Constant False Alarm Rate (CFPR) was also a commonly used utility metric when the number of false alarms were of primary concern. Each utility metric had its advantages and disadvantages. The AUC did not contain full information about the false alarm rates, and the TPR at a SFPR or CFPR did not contain information of the detection performance outside of these values.

In order to address the need to account for false positives as well as performance behavior at more than one SFPR or CFPR value, we used a utility metric defined in [3]. This metric was ideal for the purpose of subpixel target detection as it combined the AUC and TPR at a SFPR or CFPR. It was the AUC below an FPR divided by the Perfect Detection Area (PDA) (Eq. 3.1).

$$Util(FPR, AUC) = \frac{\int_0^{FPR} AUC}{\int_0^{FPR} PDA} \tag{3.1}$$

Figure 3.1 shows a diagram representing the components of the utility metric where the blue area represents the the utility value for the selected FPR. Figure 3.2 shows two example ROC curves with the same AUC and TPR at a single FPR value but with different utility values. Figure 3.2a shows a ROC curve with a utility value lower than the ROC curve shown in Figure 3.2b. These figures demonstrated a case where neither the AUC or FPR was able to capture the required information. What this metric

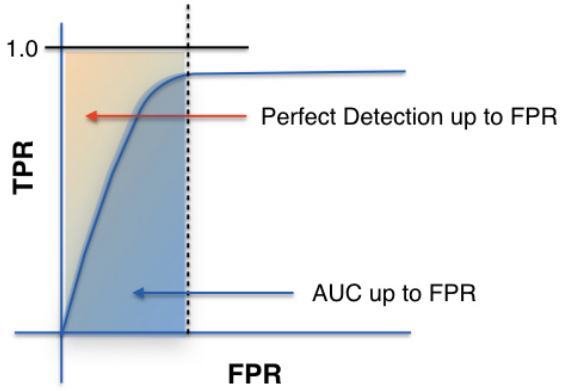

Figure 3.1: Graphical representation of utility metric.

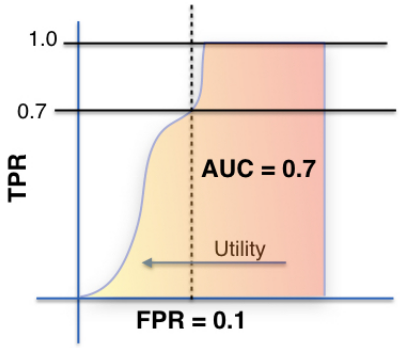

(a) Example of low utility at same FPR and AUC values as Figure 3.2b.

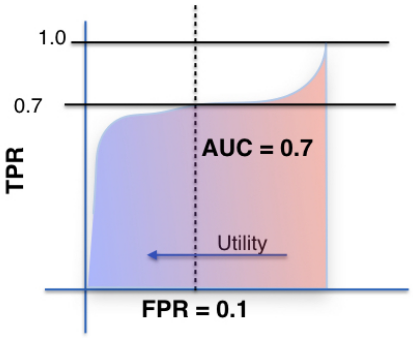

(b) Example of high utility at same FPR and AUC values as Figure 3.2a.

Figure 3.2: Examples of the high at low utility metrics for same FPR and AUC.

also allowed us to do was to analyze target detection performance without having to repeat our process for multiple FPR values. A low utility result indicated limited performance below the selected FPR, and a high utility result indicated otherwise.

3.2 Spatial Resolution vs. Scene Complexity

For panchromatic images, a smaller GSD was usually desirable and led to higher quality. In the GIQE, the GSD contributed to the NIIRS prediction

in the term $-3.32 * Log_{10}(GSD)$. However, increasing GSD also came at the cost of losing context in a single image, because the imaging system's field of view narrowed. Furthermore, increase in GSD only increased image quality if the RER did not change due to the optical Point Spread Function (PSF) that increased when GSD decreased while the optical diameter remained constant. The Q# which was a metric that related the detector resolution to the optical resolution described this phenomena [6]. The trade within the panchromatic image quality space between GSD and RER described by the Q# is explaned in detail in Chapter 4. Ultimately for panchromatic images, a smaller GSD meant more detail was seen of the objects in a scene that allowed for better identification by a human observer or for machine learning algorithms that were trained to identify an object based on specific features.

This may be true for spectral images in certain applications such as fine-grained object identification. For instance, an RGB image with a smaller GSD can provide more information about an object's features such as the type of vehicle. The utility of an image with low spectral resolution such as an RGB image can have a relationship to GSD that was similar to panchromatic images. The contribution of spectral information in the RGB image to utility was to allow finer separability between objects based on the additional information. For example, vehicles that could only be identified by type (sedan, van ect.) in panchromatic images can be identified by its color as well (white sedan, blue van). Spectral contribution to utility in such an application, was coupled with spatial resolution.

For subpixel target detection, contribution of the spectral information had a different relationship to spatial resolution. A smaller GSD increased the target fill fraction, so a target that is $2m^2$ in size that was imaged using a system with a 4m GSD produced spectral images with up to 12% pixel fill fraction of a target. If the GSD was increased by 2, the maximum target fill fraction decreased by 4. Increase in fill fraction often improved detection performance for subpixel target detection, which increased utility. However, the effects of increasing the target fill fraction or Target Abundance or Target Fill Fraction (TA) were limited, and reached a point where an increase in abundance did not significantly increase detection probability.

For spectral images, decreasing the GSD increased the variation in the background depending on the inherent complexity of the scene. This variation was mentioned in [7] as a scene complexity value (σ_{scene}), which was the average standard deviation of each band (σ_i) across the image for N bands (Eq. 3.2).

$$\sigma_{scene} = \frac{\sum_{i=1}^{n} \sigma_i}{N} \tag{3.2}$$

In spectral images, σ_{scene} changed due to the scene complexity and the GSD. A closer look at the materials on earth meant a greater variation from pixel to pixel, whereas a large GSD averaged the materials that composed the scene to decrease the pixel to pixel variation. The units for σ_{scene} depended on the units of the image and it could be in digital counts, radiance, or reflectance.

Assuming a linear mixture model, a mountainous scene that consisted of rocks, vegetation and soil, had background spectra that was a mixture of these materials in each pixel. A scene with a small GSD that separated the presence of these materials resulted in higher scene variation. A large GSD on the other hand, produced the average spectrum from these materials, making the scene more uniform, and thus produced a low σ_{scene}. The same scene of the mountains and the various materials in it had higher scene variation with higher spatial resolution, than at a lower spatial resolution. This could have effects on detection results for algorithms that depend on the background covariance to estimate the presence probability of a target. Figure 3.3 shows two images as examples of scenes with different complexity values. Figure 3.3a is a scene that inherently has a high σ_{scene} value and increasing spatial resolution would decrease detection probability of a target even if the TA was improved. On the other hand, for a scene such as the one shown in Figure 3.3b, the σ_{scene} value will not change significantly with the spatial resolution. Thus the spatial resolution could increase or decrease utility depending on the spectral separability of the target as well as the the type of scene it was in. Each target and background combination had different effects on utility and it relationship to the spatial resolution.

The σ_{scene} value was used to measure scene complexity, and because it was related to the background value used in many target detection algorithms, it was able to capture some of the effects it had on detection performance. What it did not fully account for was large areas with clustered changes in the scene such as an urban scene with buildings and roads, but with an immediate surrounding that was open and uniform. It also did not account for the reflectance of the materials that were present. Even if there was lower variation from pixel to pixel, highly reflective materials that surround a target, would make it difficult to detect. Therefore this was not a measure used in this project to quantify scene complexity. It is provided in this chapter to illustrate the intuitive trade between GSD and utility for subpixel target detection, and to

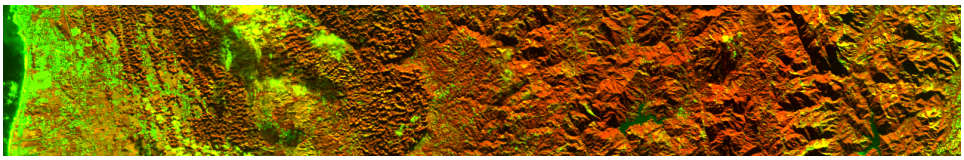

(a) Hyperion image of the Coast of Japan shown with bands 2, 5, and 10 - B(365.76nm), G(396.29nm), and R(447.17nm), average GSD = 30m. Example of scene with high degree of complexity. $\sigma_{scene} = 0.60$.

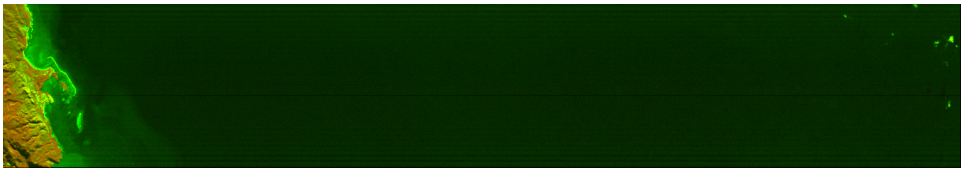

(b) Hyperion image of the Coast of Japan shown with bands 2, 5, and 10 - B(365.76nm), G(396.29nm), and R(447.17nm), average GSD = 30m. Example of scene with low complexity. $\sigma_{scene} = 0.15$.

Figure 3.3: Image examples with high and low σ_{scene}.

reference previous work we built on. A more comprehensive analysis of the metrics used for scene complexity is presented in Chapter 7.

3.3 Spectral Separability

The Spectral Similarity Value (SSV) is a comparison measurement that was described in [23] for different material classes. It accounted for the Euclidean distance (Eq. 3.3),

$$d_e = \sqrt{\frac{1}{N}\sum_{i=1}^{N}(x_i - y_i)^2} \tag{3.3}$$

and the correlation coefficient (Eq. 3.4),

$$r^2 = \left(\frac{\frac{1}{N-1}\sum_{i=1}^{N}(x_i - \mu_x)(y_i - \mu_y)}{\sigma_x \sigma_y} \right)^2 \tag{3.4}$$

$$\hat{r}^2 = 1 - r^2 \tag{3.5}$$

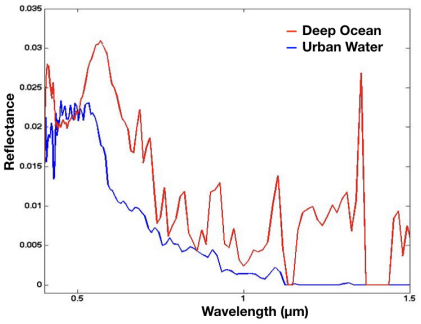

(a) Materials with similar spectral signatures. SSV = 0.244

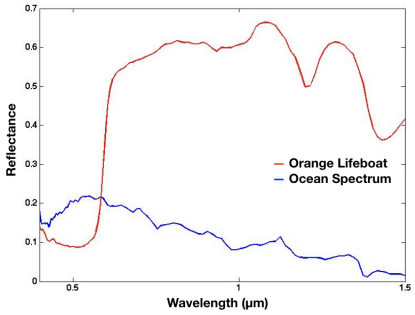

(b) Materials with distinct spectral signatures. SSV = 1.054

Figure 3.4: Examples of low SSV (spectrally similar) and high SSV (spectrally distinct). Max SSV ≈ 1.4

to produce a metric that measured how different one material spectrum was from another (Eq. 3.6).

$$SSV = \sqrt{d_e^2 + \hat{r}^2} \tag{3.6}$$

The spectrum of material X, its mean (μ_x) and standard deviation (σ_x) were compared to the material Y, across the number of bands (N) to produce a value. This metric produced a large value when X and Y were more distinct from each other. Figure 3.4 shows examples of two materials that have similar spectral reflectance signatures (low SSV), and two materials that are more distinct (high SSV). The maximum SSV was the square root of 2 (≈ 1.4).

Another method for calculating the spectral separability of the target and background used the Mahalanobis distance between them (Eq. 3.7). The SSV can be applied to any two materials whether it is a target or background or neither, and was often used for classification applications. A metric that was designed primarily for target detection applications was the Signal to Clutter Ratio (SCR).

$$SCR = \sqrt{(\mu_t - \mu_b)^T \Sigma_b^{-1} (\mu_t - \mu_b)} \tag{3.7}$$

This value was described in [24] and used as a metric in one of the spectral utility prediction methods that is described in Section 3.7. The difference in the mean of the target (μ_t) and background (μ_b) were multiplied to the

inverse covariance (Σ_b^{-1}) of the background, then multiplied to the transpose of the difference in means. What this metric took into account was the mean spectral difference of a target and background, as well as the scene variation that affected detectability. For subpixel target detection both the spectral separability of a target from its background as well as the complexity of the scene affected detection performance. The values for μ_b and Σ_b^{-1} were calculated from the image, and so it was appropriate for processing HSI, post collection or predicting utility. A modification of this metric was used to quantify background complexity in this research, which is described in Chapter 6.

While these figures of merit may not have a direct connection to the imaging system, for subpixel target detection they were useful in predicting and assessing utility. As discussed in Section 3.2, utility for subpixel target detection was dependent on the target and the scene. Dark materials with low reflectance values for most of the spectrum such as black rubber, were difficult to detect at subpixel levels, regardless of the background, since their contribution to the sensor reaching radiance was limited. Bright targets on the other hand, with high reflectance for large portions of the reflective spectrum contributed proportionally to the the final radiance, and if placed in a darker background, was the primary contributor to the final radiance. Furthermore, even bright targets, if surrounded by materials that were spectrally similar, became difficult to detect.

3.4 Spectral Fidelity

There were many ways spectral fidelity is measured and calculated. While we focused on utility as the primary component of spectral image quality. The fidelity measures can be separated into three categories - spectral resolution, spectral relative edge response, and spectral calibration accuracy. These three measures have complex spatial-spectral relationships and result from many physical phenomena intrinsic to spectral imaging systems. An initial attempt at replicating the image quality prediction model for panchromatic images for spectral images detailed these three spectral fidelity measures along with other metrics as figures of merit for a predictive model [25].

Depending of the spectral detector design and purpose, these three categories of spectral fidelity have different effects on the final image quality. The individual effects on image utility were not explored in this

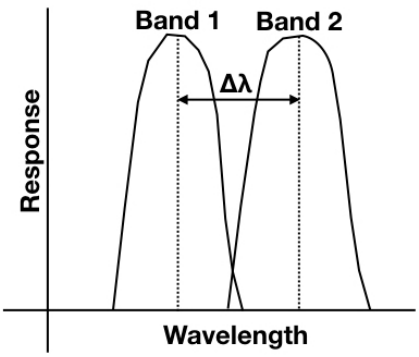

(a) Diagram of $\Delta\lambda$ as measured from center wavelengths of two bands. Measure used for systems with filters.

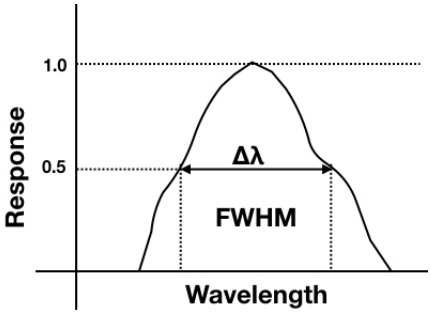

(b) Diagram of $\Delta\lambda$ as defined by the FWHM. Measure used by systems with light dispersion mechanisms such as prisms.

Figure 3.5: Diagram representing measures of spectral resolution ($\Delta\lambda$).

research, but they are presented in this chapter as they are intrinsic to the system design. We describe these categories of spectral fidelity that were intertwined and affected real systems, but they were not wholly accounted for in our prediction model or simulation. Furthermore, for compact imaging systems with adaptive band selection capabilities, the traditional methods for measuring them require further inspection in the future.

3.4.1 Spectral Sampling Interval

The spectral sampling interval ($\Delta\lambda$) is the width of the distance between the center wavelengths of each band. The spectral signature of a material in the real world and how it interacts with light at each wavelength is continuous. When imaging the spectral signature, $\Delta\lambda$ can be a measure of how fine the data sampling is. It can also be measured in terms of the Full-Width Half-Max (FWHM) of each band when there is no overlap as is the case with spectrometers that use a light dispersion method to record the spectral information. Figure 3.5 diagrams two ways in which $\Delta\lambda$ can be measured. For a spectral response function, we can define $\Delta\lambda$ in terms of FWHM or in terms of the difference in the peak radiometric response between two bands. For a tunable filter, $\Delta\lambda$ can be arbitrary, but reference to this measure of fidelity for this dissertation is with respect to sampling intervals as shown in Figure 3.5a.

High spectral sampling is a measure of quality for spectral

imaging systems as it increases our ability to characterize spectral signatures. However, high spectral sampling often increases noise and decreases spatial resolution. It also increases dimensionality which introduces errors and increases data processing costs. For target detection, spectral sampling has different effects on utility depending on the target, background and the algorithm used. If an algorithm depends on the slope of the spectra to determine detection statistics, then sufficiently high $\Delta\lambda$ can improve utility. However, for a highly reflective target, only a few bands can be sufficient for detection, and so increasing $\Delta\lambda$ is unnecessary. For a system with a tunable filter, this measure is only relevant when it is related to its ability to resolve a narrow spectral feature.

3.4.2 Spectral Relative Edge Response

The Spectral Relative Edge Response (SRER) is similar to the RER defined for panchromatic images, but is applied to the spectral response function. It is the measure of how well a narrow spectral feature can be resolved by the imaging system. For subpixel target detection, this metric plays a limited role. However, if the target is highly reflective only at a narrow bandwidth, then the SRER and the imaging system's ability to resolve this spectral feature, contributes to utility. This measure of fidelity for an imaging system with a tunable filter that can collect images at arbitrary wavelengths is intertwined with $\Delta\lambda$. Since center bands can be selected arbitrarily, the system's capability of collecting two bands that can resolve a narrow spectral feature determines its SRER. A detector that is not capable of producing sufficient spectral resolution can not produce a high SRER. The SRER is also affected by calibration where degradation of SRER can be caused by spectral calibration error, which is another measure of spectral fidelity.

3.4.3 Spectral Calibration Accuracy

The spectral calibration accuracy is how close to the actual center wavelength the determined or declared center wavelength is in a band's FWHM. When this is related to the spatial component, error in calibration accuracy can be from distortions in mapping of the spectrum to a spatial position. Figure 3.6 illustrates the spatial-spectral mapping distortion that can cause the spectral radiance at some wavelengths for materials in one pixel to contribute to the spectral radiance of another pixel. Calibration can correct for distortions that are well-behaved functions, but there is

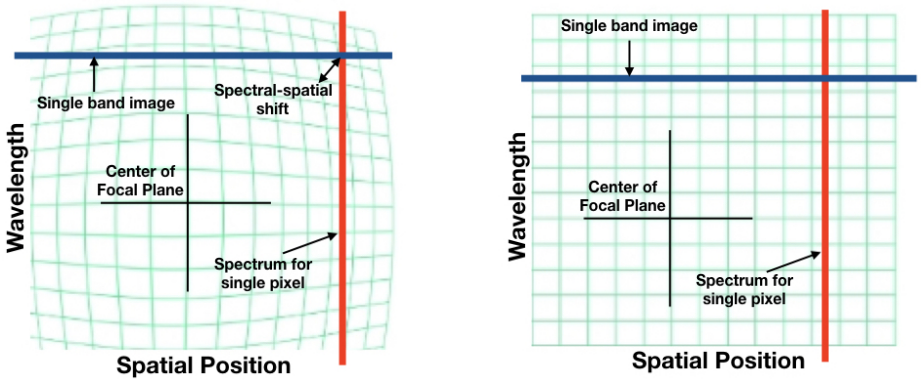

(a) Distorted mapping of spectrum for spatial position.

(b) Undistorted mapping of spectrum for spatial position.

Figure 3.6: Diagram showing spatial-spectral mapping in a dispersive imaging spectrometer. [26]

error when an imaging system's artifacts are not.

For subpixel target detection calibration accuracy can be important when it affects the wavelengths where a target is detectable. It is critical for imaging systems with tunable filters that is only collecting a few bands for a target that is only distinguishable from the background at the selected wavelengths. Error in calibration can mean the difference between collecting a band that is spectrally distinguishable from the background or not.

3.4.4 Spectral Fidelity Summary

These spectral fidelity measures are intimately related to each other in producing the final spectral image and determining its utility. Their effects can be compounded when the image is processed with machine learning algorithms that are trained with data that may be sensitive to differences in spectral fidelity. The individual contributions of each measure of utility and their effects on machine learning is beyond the scope of this project. Perhaps it is a research direction that can be taken in the future. What we did address in this dissertation was how the spectral fidelity measures would effect utility for an imaging system with tunable filters capable of selecting bands at arbitrary spectral sampling intervals. The calibration errors and band registration errors associated with the filter tuning or

collection methods are beyond the scope of this project, but are contributors to spectral fidelity and utility that may need to be addressed in the future.

3.5 Optimal Number of Bands

Given infinite time and computational resources, having high spectral resolution for the entire reflectance spectrum may help detection results, but for most operations using compact systems, we assumed both were limited. In many situations where spectral images were used for subpixel target detection, data transmission bandwidth, and turnaround time from when the data was collected to when it was needed were key constraints. Reducing the number of bands prior to collection was ideal, and even post-collection, it was an important step. However, fewer bands in many cases also led to limited detection performance.

There was a point in the spectral utility trade space where increasing the number of bands did not improve performance. In fact, increased dimensionality often had negative effects on performance. If we found the number of bands less than the full spectral collection capability of a hyperspectral imaging system that either optimized or equaled the performance compared to using all the available bands, then we asserted that these bands had higher utility values. If we assigned an acceptable error margin to the peak performance statistic that reduced the number of bands even further, the optimal number of bands were then tied to the operational requirements and could be quantified using an acceptable error value (ϵ). We defined this as the optimal number of bands and it was compared to the number of bands that achieved the highest possible detection performance.

We first defined the maximum number of bands that a system was capable of collecting (B_{max}) based on the wavelength range and $\Delta\lambda$. For example, a system with a wavelength range in the Visible Near Infrared (VNIR) spectrum (400-900nm) and a $\Delta\lambda$ of 10nm, had a maximum number of bands of 50 ($B_{max} = 50$).

We also defined a vector that was of length N such that $N < B_{max}$ that we selected as the subset of bands that achieved utility equal to B_{max} (Eq. 3.8).

$$Util(B_N) = Util(B_{max}) \tag{3.8}$$

Each of these bands were at wavelengths $i = 1, 2, ...N$ (λ_i) within the wavelength range of the imaging system. Then the number of bands that achieved a utility higher than the acceptable error value of the maximum achievable utility, was defined as a subset of the B_N. For an acceptable error value, we define $B(N, \epsilon)$ as the set of bands that achieved the fractional utility higher than $Util(B_N)$ (Eq. 3.9).

$$Util(B(N, \epsilon)) = Util(B_N) \cdot (1 - \epsilon) \tag{3.9}$$

This was the utility achieved within an acceptable error value, such that if $\epsilon = 0.2$, we could think of it as the 80% solution. The expectation was that there were several sets of bands that achieved utility higher than $Util(B_N) \cdot \epsilon$ depending on the band selection method used. The optimal number of bands then was the smallest set that could meet this requirement for the selected error value (Eq. 3.10).

$$B_{opt}(\epsilon) = min(B(N, \epsilon)) \tag{3.10}$$

Analyzing all the existing band selection methods for every mission scenario was not a tractable problem. Therefore we use the band selection method we developed to determine the band ranks for each target to analyze the number of bands and its relationship to utility.

Figure 3.7 shows an example curve calculating the utility value for a range of bands from 2 to 30 for a subpixel target detection scenario. The bands were selected using the method we developed that is described in detail in Section 5. The utility was calculated for an orange lifeboat target in open water using the spectral matched filter at FPR = 0.001. Using the full HSI, or the maximum utility for this scenario was 0.85 and the 99% solution or B_N was 17 bands. The optimal number of bands for the 90% solution was 7 bands. What these results illustrated was that the utility vs number of bands curve for a feasible range of bands appropriate for a compact system could be generated during the design phase, and the $B_{opt}(N, \epsilon)$ values could be determined during operations based on requirements.

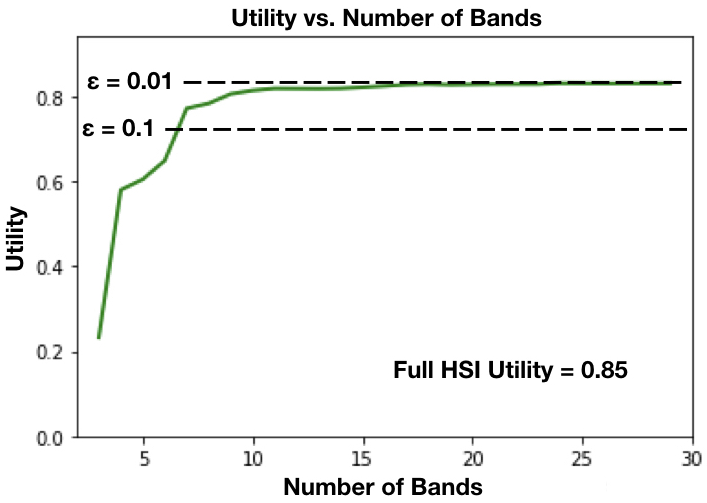

Figure 3.7: Example curves of $Util(B_i)$ for a range of 2-30 bands. For this mission scenario, N = 17, and $B_N = B(N, 0.01) = 17$. The $B_{opt}(N, 0.1) = 7$ or the 90% solution is 7 bands.

3.6 Noise Equivalent Spectral Radiance

Radiometric sensitivity is a figure of merit applicable for any imaging system. The SNR for spectral images is similar to the panchromatic SNR in that it is a statistical measure of variation in a signal. However in spectral images, the SNR needs to be applied to each band and comes with a trade-off between the spectral resolution. Higher spectral resolution means higher distribution of the total radiance to each band which lowers the SNR. There is an inverse relationship with spectral resolution in the case of dispersive spectrometers, where the narrow widths of the detector required for small $\Delta\lambda$ also degrades radiometric sensitivity. In this section we build on the SNR description for spectral images to be similar to that described in Section 4.4.3 and present a commonly used metric that accounts for noise that is described in [26].

The Noise Equivalent Spectral Radiance (NESR) is ratio between the spectral radiance ($L_s(\lambda_k)$) and the SNR of band k ($SNR(\lambda_K)$) (Eq. 3.11).

$$NESR(\lambda_k) = \frac{L_s(\lambda_k)}{SNR(\lambda_k)} \tag{3.11}$$

We consider two representations of the NESR - when shot noise is the

dominant contributor to noise (Eq. 3.12)

$$NESR(\lambda_k) = \sqrt{\frac{L_s(\lambda_k) \cdot hc \cdot G\#_k}{A \cdot QE \cdot \lambda_k \cdot t_{int} \cdot \Delta\lambda}} \tag{3.12}$$

and when the fixed-noise component (σ_{fixed}) is the dominant contributor to the total noise (Eq. 3.13).

$$NESR(\lambda_k) = \sqrt{\frac{\sigma_{fixed}^2 \cdot G\#_k \cdot hc}{A \cdot t_{int} \cdot \lambda_k \cdot \Delta\lambda}} \tag{3.13}$$

In this equation, we use σ_{fixed} as a general term that encompasses all possible fixed noise sources such as the dark noise (σ_d) and quantization noise (σ_q), or others such as detector noise or sensor noise. It is used as the summation of all fixed-noise sources.

The two different representations of NESR are presented here to provide the background for the method we used to parameterize noise. The transmission terms are simplified, which for spectral imaging systems can include spectrometer transmission, cold filter transmission, warm optics transmission and the quantum efficiency at each wavelength to be folded into the optical throughput term ($G\#_k$) for band k. In reality, each of these terms and their relevance depends on the mechanisms that disperse the light or collect each band. While they have effects in the final utility assessment, exploring each of these effects and phenomena are outside the scope of this project and perhaps a worthwhile future endeavor. Radiometric sensitivity is a utility metric that can be applied in the same way as the panchromatic measures of utility for each band, and the composite values and increasing NESR also increases spectral image utility.

For a tunable filter, the signal decreases as the FWHM of the spectral response function centered at a wavelength narrows. However, widening the filter width can also widen the SRER. As described in Section 3.4, this effect on utility for subpixel target detection will depend on the spectral signature of the target. A system with high noise contributions overall will degrade performance. However, if there is varying amounts of fixed noise at each band, while it may not have any effect on some targets, it may degrade detection performance for other targets.

3.7 Spectral Image Utility Prediction

There have been multiple efforts to analyze spectral image utility and many have attempted to produce prediction methods similar to the GIQE. The main motivation for prediction started as a way to establish a relationship between collection parameters and how they affect our ability to extract information from the spectral data [7]. We now rely on several methods for prediction to facilitate design of spectral imaging systems, provide a strategy for collection tasking, and develop archive indexing schemes [27]. In this section we outline several approaches for spectral image utility prediction.

3.7.1 Regression Approach

Regression models are empirically derived equations that relate imaging system parameters to utility measures. These regression models attempt to replicate the GIQE. They are equations formed by analyzing many spectral images to form a relationship between the selected utility measures and known imaging system parameters. We present two different regression models that combine traditional utility measures that are also used for panchromatic images and metrics that are specific for spectral iamges.

Spectral Quality Rating Scale

The Spectral Quality Rating Scale (SQRS) is rooted in the GIQE in that it uses similar figures of merit but the relationships are modified for spectral images. It is tested for subpixel target detection in the reflective wavelengths of the electro-magnetic spectrum [28]. It is based on the notional concept of defining quality as a surface within a space defined by the Ground Resolved Distance (GRD) in centimeters, noise, and spectral resolution. It tests a single background material and three different target materials. It relates GRD, SNR, and the number of bands (N) into a GIQE-like equation (Eq. 3.14).

$$SQRS = 9.65 - 3.22log_{10}(GRD) + 0.44log_{10}(SNR) + 0.8log_{10}(N) \quad (3.14)$$

Figure 3.8 shows an image from [28] that illustrates the envisioned relationship between the three selected spectral image quality measures that can be derived from the regression model.

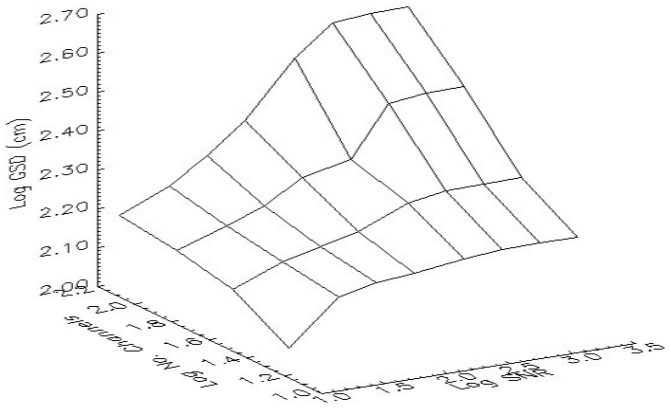

Figure 3.8: Image from [28] demonstrating spectral image quality as a surface within the space created by three measures of image quality.

While this approach was able to make a complex problem more tractable, it is limited to the single background case for the targets that were tested. It is also able to contract into the panchromatic case when $N = 1$ to replicate the GIQE, and accounts for an arbitrary selection of bands that may not be directly related to the spectral resolution. It does not account for the spectral separability between the target and background that would change the detection results, or the scene complexity. It also does not fold in the utility metrics of target detection such as FPR or AUC as part of the model.

This method was later updated to include the separability of the target and background along with the detection threshold values [24]. In the updated equation, the SNR is replaced by the SCR described in Section 3.3 for a target and background combination (3.7). The number of bands is no longer used, but instead replaced with a T value which is defined as the threshold on the algorithm test statistic that produces a desired P_{FA}. The revised SQRS (Eq. 3.15),

$$SQRS_{new} = 10.6 - 1.6log_{10}(T) - 3.3log_{10}(GSD) + 1.6log_{10}(SCR) \quad (3.15)$$

accounts for utility and target separability, which were limitations of the previous SQRS, and so it is useful for analyzing sensor designs for a specific target and background combinations.

Spectral Quality Equation

The Spectral Quality Equation (SQE) was developed for subpixel target detection of images in the VNIR spectrum, and related GSD $[in]$, spectral resolution ($\Delta\lambda$), detector performance (SNR), and scene complexity (σ_{scene}) [29] using an equation. It compared several TPRs (P_d) at SFPRs (P_{fa}) for these four measures of quality. Its purpose was to establish a relationship between collection parameters and utility of spectral images. It was not intended to mimic the GIQE but rooted in the assumption that spectral images will not be processed by a human observer but a machine. It upgraded the SQRS to include detection performance measures as part of the model.

The SQE was developed using desert and forest scenes collected using the Hyperspectral Digital Imagery Collection Experiment (HYDICE) data. The four figures of merit are combined to produce a P_d value (Eq. 3.16).

$$P_d = A_0 + A_1 log_{10}\left(\frac{1}{GSD^2}\right) + A_2 log_{10}\left(\frac{1}{\Delta\lambda}\right) + A_3 log_{10}(SNR) + A_4 log_{10}\left(\frac{1}{\sigma_{scene}}\right) \tag{3.16}$$

The Hyperspectral Digital Imagery Collection Experiment (HYDICE) data are analyzed to find regression coefficients for each of the figures of merit. Table 3.1 shows the coefficients that were found for two P_{fa} values.

Table 3.1: SQE equation coefficients found for the two P_{fa} values calculated in the regression analysis.

P_{fa}	A_0	A_1	A_2	A_3	A_4
0.001	6.09867	0.404654	0.203598	0.101418	2.3445
0.005	6.9537	0.405193	0.184891	0.133405	2.74164

The value of the model lies in the ability to both assess and predict the utility of spectral images as long as the four figures of merit are known or held as constants. It can assess the detection statistics for the imaging system parameters, or if a certain true positive rate is desired, the figures of merit combinations can be calculated to produce it. However, it does not fully address the trade-off between these figures of merit such as σ_{scene} and GSD or SNR and $\Delta\lambda$.

Overall, the regression methods are useful for the imaging

systems that were analyzed with the assumption that each of the figures of merit used were independent of each other. They apply to the spectral imaging systems that collected the images that were used to calculate the regression. For spectral imaging systems with adaptive band selection capabilities or compact systems, the regression may not be able to accurately predict utility.

3.7.2 Spectral-Spatial Confidence

An approach that combines the spectral figures of merit along with the spatial components is the General Spectral Utility Metric (GSUM) [30]. The purpose of this approach was to generalize spectral utility for more than one purpose under the assumption that the use of both spatial and spectral information will result in greater utility. It also assumed that spatial and spectral quality metrics are separable, and defined a metric to combine this information to predicts utility both as a machine extracted values and from visual inspection by a human observer.

The *confidence* term is the figure of merit that determines the level of confidence one can have in a spectral image of performing a given task. This method parameterized the GSD and the number of bands to determine the total *confidence* (C_{total}) that is calculated by combining the spatial confidence value ($C_{spatial}$) and the spectral confidence value ($C_{spectral}$) along with weighting functions (W_1 and W_2). The weighting functions allowed the method to account for different scenarios, requirements and the measures of utility between the spectral and spatial components of an image (Eq. 3.17).

$$C_{total} = 1 - (1 - W - 1 \cdot C_{spatial}) \cdot (1 - W_2 \cdot C_{spectral}) \tag{3.17}$$

This method is valid as a high level diagrammatic approach to predicting utility for all purposes of spectral images. It is most useful for spectral images with high spatial resolution and low spectral resolution such as RGB images where both spatial and spectral characteristics affect utility. Figure 3.9 shows the flow diagram from [30] for the GSUM method that assess the spectral and spatial components separately, then combines them to calculate to final confidence value.

Unfortunately, none of the values can be quantitatively expressed in terms of image quality parameters. Therefore, while useful as a starting

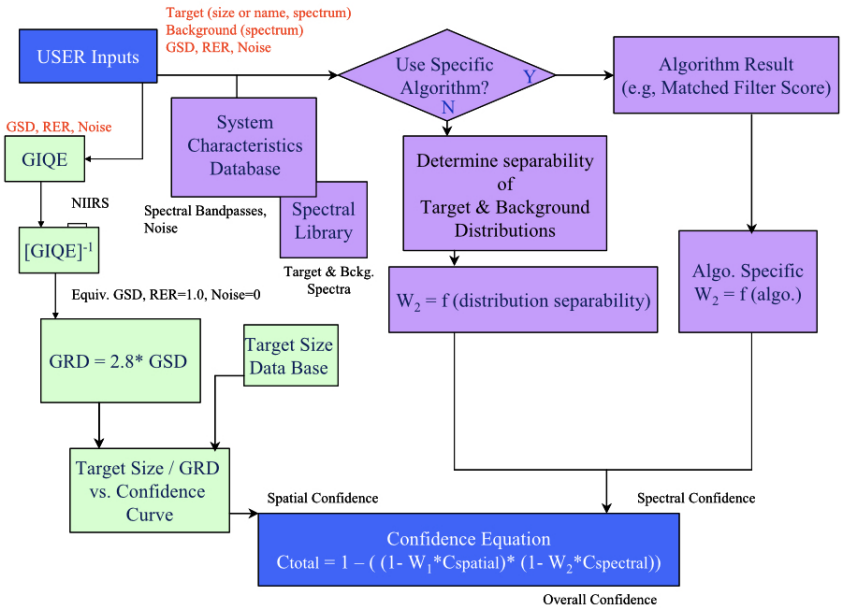

Figure 3.9: Diagram from [30] for utility prediction using spatial-spectral confidence of the GSUM.

point for developing a framework for spectral utility prediction, it has limited use in designing compact spectral imaging systems with adaptive band selection capabilities. Furthermore, the assumption that spatial and spectral figures of merit are separable and independent is limited in scope especially for cases where this method would be most useful such as RGB images which often find improved utility after pan-sharpening.

3.7.3 Forecasting and Analysis of Spectro-radiometric System Performance

A comprehensive method for predicting the spectral image utility trade space for the purpose of subpixel target detection is the Forecasting and Analysis of Spectro-radiometric System Performance (FASSP) method [31]. It is an analytic method that propagates the system parameters through the imaging chain, to generate ROC curves for targets and backgrounds at various abundances. The input parameters of the model include atmospheric conditions, TAs, and target and background spectra. The

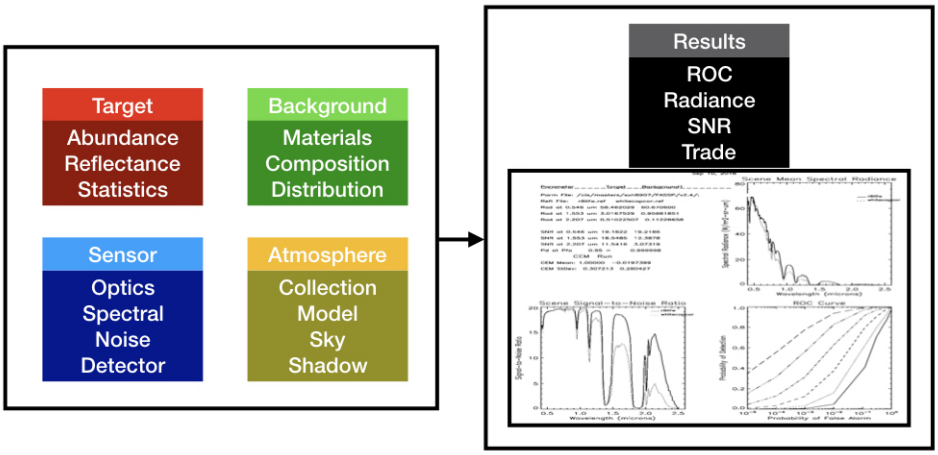

Figure 3.10: Diagram for the FASSP model showing input and output.

output of the model include the average radiance of target and background, SNR averages at each wavelength, and the ROC curve for the TA values. Figure 3.10 shows a diagram of the possible input one can provide in a FASSP run and the output. It primarily uses Moderate Resolution Transmission (MODTRAN) to analyze the single pixel radiometry, and the results are statistical calculations based on the input [32].

The FASSP model can be used as a top-level analytic solution to deciding various parameters in the design of a spectral imaging system for a specific task. It is able to capture information from reflectance data, sensor characteristics, and push them through a processing algorithm that produces results that can easily be used for trade studies [33]. It is an efficient and tractable way to predict imaging system performance for a specific target and various background characteristics. It can account for several noise sources such as detector gain or spectral calibration error, and even band selection.

For a well defined scene, imaging system, and collection parameters, it is an efficient method for analyzing an imaging system trade space and predicting utility. When combined with a 3-D simulation model, it can provide complementary analytic capabilities that can validate and assess the images generated from a system designed based on the predictions. The trade space analysis can be enhanced with studies for other imaging system characteristics and conditions such as shadow effects or oblique collection angle [34]. Figure 3.11 shows an example output from a FASSP model run for a range of TA percentages. It shows the TPR at

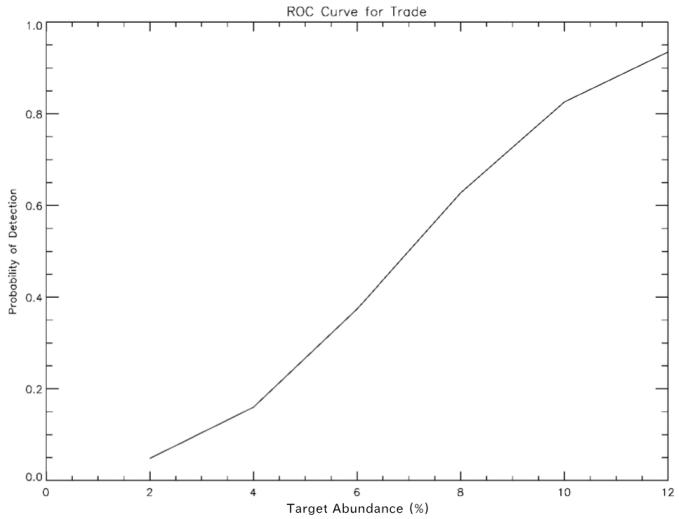

Figure 3.11: Example of trade analysis output for various target abundance percentages using FASSP model. The trade curve is for probability of detection at 0.1 false alarm rate.

0.01 FPR for the TA range of 2-12%. This type of curve can be used to find saturation points in the trade space. We define saturation points as locations in the trade curve where increase in the metric analyzed has limited or no increase in utility. The main disadvantage of this method is that we can not compare the prediction with assessment. It also requires detailed knowledge of the sensor and the covariance statistics, material reflectance, and collection geometry, and it cumbersome to account for various phenomena in a complex scene.

3.7.4 Image-derived Spectral Image Utility Approach

The image-derived spectral image utility prediction method uses real images and synthetically implants targets to assess detection results using a target detection algorithm. The motivation for this approach was to develop a method that was less computationally intensive and allowed for comparison between assessment and prediction [27]. This method calculates the statistical parameters of a real image along with the target, linearly mixes these statistics, then applies a target detection algorithm to generate a predicted ROC curve. It does not need detailed information about an imaging system such as the SNR of the sensor, and atmospheric effects are inherent in the prediction data. It is computationally efficient as

targets do not need to be implanted into each pixel and the sensor reaching radiance does not need to be calculated. This utility prediction method answers a critical operational question:

Can this spectral imaging system find this target?

If we know the size and spectral reflectance signature of a target, this method can predict the likelihood of successfully detecting the target using an existing spectral imaging system. It can be used to quickly iterate through available systems to determine which is best suited to find the required target. The prediction is independent of scene complexity, sensor-derived characteristics, and atmospheric compensation error. The main sources of error are parameter estimation errors and non-linear scene interactions between target and background. Since a linear mixture model is used to produce the target present statistics, any deviations from this estimate produces error. What this method is not appropriate for is predicting utility of compact spectral imaging systems designs and conducting trade studies for individual system parameters.

3.7.5 Prediction Methods: Advantages and Disadvantages

Table 3.2 summarizes the information presented in this section for a few spectral image utility prediction methods. A brief description of the method and the applications they are most suited for is followed by their advantages and disadvantages. While there may be other prediction methods, we present these as the baseline for utility prediction in our research. Many of these are not directly applicable to designing compact imaging systems with adaptive band selection capabilities, but we built on their analysis and methodology along with some of the figures of merit they developed.

We used the methodology of analyzing spectral images for subpixel target detection presented in the spectral-spatial confidence approach and the figures of merit that were introduced in the regression approaches. We built on the framework developed in the image-derived utility analysis to develop the process of prediction and assessment. The FASSP model was used as the primary tool in the prediction process to analyze the feasibility of a mission then to find optimal design parameters for a compact spectral imaging system for subpixel target detection applications.

Table 3.2: Summary of Spectral Image Utility Prediction Approaches

Regression Approach: Empirically derived, appropriate for sensor design trade studies [25] [29] [28]	
Advantages	**Disadvantages**
Simple and tractable with strong correlation to real spectral images	Required information not always available; does not account for non-linear relationships between parameters
Spectral Vector Analysis: Analyze separability of material classes treating spectra as vectors, appropriate for classification [23]	
Advantages	**Disadvantages**
Does not require details of sensor design	Not effective for sub-pixel target detection using small number of bands, does not account for spatial information or scene complexity
Spectral-spatial Confidence: Combine spatial and spectral information as contributors to utility, useful for predicting utility for spectral image exploitation by human analyst [30]	
Advantages	**Disadvantages**
Combine existing utility prediction methods	Does not account for redundant spectral and spatial information or pan-sharpened spectral images
FASSP: Propagates given system parameters through remote-sensing process, used for study of imaging chain effects on target detection, appropriate for utility prediction of specific target and background combinations [31]	
Advantages	**Disadvantages**
Prediction of performance for robust range of target and background scenarios, and imaging system parameters	Can not compare prediction and assessment, does not model spatial scene characteristics and complexities
Image-derived Utility Analysis: Use statistical parameters of an image to predict utility, most appropriate for utility prediction of target detection for existing spectral imaging systems [27]	
Advantages	**Disadvantages**
Use real images, does not require details of system parameters; Allows comparison of prediction to assessment; Computationally efficient	Can not parameterize individual imaging chain phenomena; target implant artifacts

3.8 Summary

In this chapter we explored the figures of merit that were unique to spectral images and their relationship to utility. We explored some measures of spectral image quality such as the NESR that had effects on spectral images utility that were parallel to SNR in panchromatic images. Some measures were described such as the GSD that had an inverse relationship to scene complexity which complicated its relationship to utility. We also explored some other measures that were only relevant to spectral images such as the SSV, σ_{scene}, and $\Delta\lambda$. Each of these contributed to the design or the operation of the phase in various ways. For example, while $\Delta\lambda$ was directly tied to the sensor characteristics, SSV was dependent on the mission requirements. We presented these figures of merit to distinguish spectral image utility measures from the panchromatic metrics.

"There is an idea of a Patrick Bateman, some kind of abstraction, but there is no real me, only an entity, something illusory, and though I can hide my cold gaze and you can shake my hand and feel flesh gripping yours and maybe you can even sense our lifestyles are probably comparable: I simply am not there."

- Bret Easton Ellis, *American Psycho*, 1991

4

Simulation

Simulation is a capability that can provide labeled data, truth information, user control of system parameters, and produce a large amount of data with limited resources compared to collecting real images. These are all critical requirements for analyzing spectral image utility and optimizing designs of compact systems. In order to generate spectral images for assessment of spectral image utility, we used a synthetic image generation tool that uses physics-based modeling. In this chapter we explain the simulation tool and its sub-models that replicated the real world scene, operational conditions, and generated spectral images that were used in the assessment phase of our process.

4.1 Physics-based Simulation

The simulation tool we used modeled the physical processes in the collection of photons in remote sensing systems [35]. It incorporated the radiative transfer model to account for the propagation of light from its source to sensor, through the atmosphere, that was reflected or absorbed by surfaces and objects in a scene. The radiance field at the sensor (L_s) was calculated using radiometric equations such as Eq. 4.1.

Table 4.1: Variables in the sensor reaching radiance equation.

E_s	direct solar irradiance at surface
E_D	diffuse solar irradiance at surface are emitted
r_o	surface object reflectance
ϵ_0	surface object emissivity
$B(T_o)$	surface object blackbody radiance for temperature T_o
τ	atmospheric transmittance from surface to sensor
L_u	upwelling radiance (both solar and emitted)

$$L_s = \left[(E_s + E_D)\frac{r_0}{\pi} + \epsilon_0 B(T_0)\right]\tau + L_u \tag{4.1}$$

This equation was a simplified version that consolidated the components in the physics-based simulation [36] that were used in the calculation of $L_[s]$. Table 4.1 shows the components that were considered in our analysis. The calculations performed by the physics-based simulation was complex since the 3-D world had many components such as vertical relief, adjacent objects, clouds, and spatial heterogeneity in the scene, that affected the possible paths a photon can take. A simulation model when accounting for many of these phenomena can become computationally expensive [37].

A method for generating a realistic sensor reaching radiance is through ray tracing [38]. Many models use ray-tracing to calculate complex interactions of a photon that produce an image. The implementations are often complex, but the fundamental mechanism is to trace the path of photons from the source, the interactions with the possible surfaces and media, then through the sensor aperture. This is coupled with Monte Carlo calculations to account for randomness. This type of photon mapping, can provide the realism required to assess an imaging system's performance [39].

The simulations use sub-models to account for the 3-D photon interactions in a single pixel which are integrated into the simulation to produce the final image. The synthetic image, with appropriate simulation techniques with the correct parameters and appropriate sub-models, can adequately represent the a real image that may be collected of the physical scene. The benefits of using simulation is that the user is able to control key aspects of an imaging system that affect the final image, from the optical system to the scene itself. Improbable real world situations can be created to test the output of conceptual imaging systems at desired capability points. Changing key collection parameters for a range of

values, can allow us to analyze the trade space that would be challenging or unfeasible to do with real images.

4.2 Digital Imaging and Remote Sensing Image Generation

The primary tool we used to simulate our image collection scenario was the Digital Imaging and Remote Sensing Image Generation (DIRSIG) model [40]. It used path-tracing to generate images of a scene captured by a remote sensing system, and samples the photon interactions with the materials in a scene using a Monte Carlo model to capture the random nature of scattering photons. Several sub-models were used to simulate a remote sensing system's sensor characteristics, platform motion, collection geometry, and the atmospheric effects on image collection.

Figure 4.1 shows a diagram of the various sub-models that are used to produce a synthetic image. Using DIRSIG, we simulated images of a large area scene generated by a spectral imaging system [41], using a database of material spectra to calculate the radiometry of each band. The simulation model was used to design a scene that represented the location and target, along with the collection conditions that generated images similar to those collected in real operations.

4.3 Sub-Models for Single Pixel Radiance Calculation

Many simulation methods that generate images of a large area scene use single pixel models to calculate the final sensor reaching radiance. This models remote sensing systems as different components of the earth affect the final image produced in real imaging systems in their own way. The two single-pixel models we focused on for this dissertation was atmospheric modeling and surface reflectance modeling. In this section we describe the single pixel models that we used to simulate then replicate the scene in our analysis.

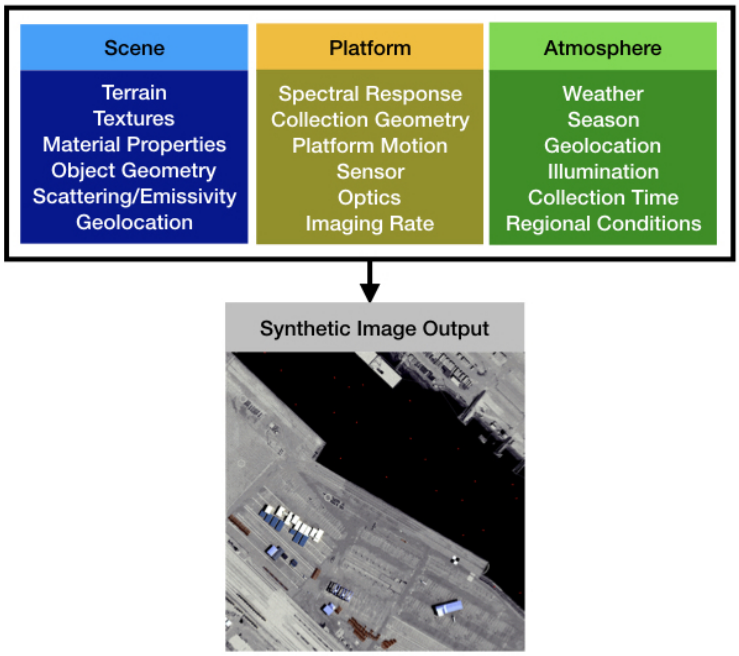

Figure 4.1: Diagram of some sub-model and parameters that are used to generate final image in DIRSIG.

4.3.1 Surface Reflectance and Emissivity of Materials

Various surfaces scatter light in different ways depending on the material and collection geometry. For example, shiny materials such as metals are highly specular, while other materials such as paper are not. A specular material can give off glints and produce changes in the sensor reaching radiance depending of the angle at which the image is collected with respect to the material's 3-D geometry and illumination angle. Therefore, the radiance signatures of some materials can change significantly depending on the collection conditions. The Bi-directional Reflectance Distribution Function (BRDF) describes the surface scattering of materials with angular dependence.

The Hapke BRDF model [42] [43] and Ross-Li model [44] [45] are examples of models that calculate the BRDF. In DIRSIG, both models can be used depending on the radiometry model that is selected as part of the simulation. The reflectance and emissivity files that are used as input also account for the BRDF characteristics that can provide realism and radiometric accuracy in the simulated images. Some materials can be

Figure 4.2: Example output from DIRSIG generated with high spatial resolution to show texture of materials within scene that was created using texture map (road and shore) and BRDF models (lifeboat and ship).

given reflectance or emissivity data that that can produce variations in a single material from pixel to pixel as it would in real spectral images.

The amount of variation can also be controlled using a texture map, which is an 8-bit image that maps the pixel values in the image to the material reflectance data. In this research, a combination of BRDF models along with texture maps were used to introduce variations in the final images to more closely model real world phenomena. Figure 4.2 shows a high spatial resolution image of a lifeboat and ship that were placed in the scene that was generated using DIRSIG. The surface characteristics of the lifeboat and ship as well as the texture of road and shore was generated using the available tools to provide realism.

4.3.2 Atmospheric Effects

An important effect on the the sensor reaching radiance in remote sensing systems for spectral images is the atmosphere. The materials on the ground of the scene that are imaged reflect or emit light, but first goes through the atmosphere before reaching the sensor. If the imaging system is directly above the material being imaged, the atmosphere has limited effects, but if the sensor is many kilometers above the material, each layer of the atmosphere up to where the sensor is, has a significant effect on the at sensor radiance for each wavelength.

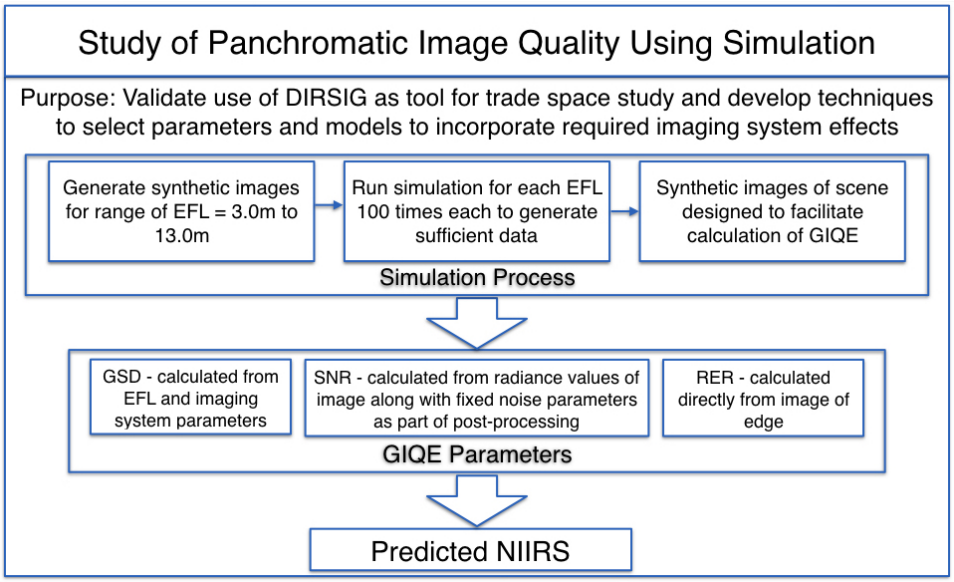

Figure 4.3: Workflow diagram for the panchromatic image quality study for the purpose of validating use of simulation.

MODTRAN is a model that can account for the effects of the atmosphere by calculating the line-of-sight transmittance and radiance at each layer of the atmosphere [46]. It has a spectral range of 0.2-100 $[\mu m]$ with a band-based resolution of 0.1 $[cm^{-1}]$. Newer versions of the model can also account for cloud cover[47]. It can be user defined by modifying the input files that are used in the DIRSIG simulation.

4.4 Simulation Validation

We validated the use of simulation for trade studies of spectral imaging systems by generating the panchromatic images that could be used to calculate the GIQE as described in Chapter 2. We developed techniques for generating images that reproduced key real world phenomena for a range of parameters, and tested them against the well-established figures of merit for panchromatic images [48]. Figure 4.3 shows the workflow of the process to develop the simulation techniques for panchromatic image utility prediction that we used to transition into the spectral images.

We first designed a scene and modified some of the sub-models in DIRSIG to facilitate the calculation of the GIQE parameters that are used

to predict the NIIRS. We used the images we generated to calculate the RER, SNR and GSD. The EFL was the variable parameters which with constant diameter, predicted the NIIRS by generating a range of GSD, RER, and SNR. We used the calculated parameters and the GIQE to produce a range of predicted NIIRS values.

4.4.1 Scene Design

The scene background we used was a railroad track in the desert which was a relatively flat, uniform area. We placed panels that were Lambertian with 7% and 15% reflectance. These panels were placed directly next to one another to create edges in both the x and y directions. This generated images of perfect edges that could be used to directly calculate the RER as described in [18]. The reflectance values were selected to replicate the calculation described in [20] for the SNR. The platform motion was also simulated to ensure smear was incorporated. The direction of movement was simulated so the edges were the same in both directions, thus simplifying calculation of the RER. The illumination and sensor position was selected to be directly above the scene. This allowed the GSD to be calculated using the sensor height, pixel pitch, and EFL.

4.4.2 Ground Sampled Distance Calculation

All imaging system parameters were kept constant except for the EFL. The GSD could be calculated without consideration for angular changes due to collection geometry because the scene was designed as such (Eq. 2.2). In this way, the GSD was solely a function of the changing EFL. Figure 4.4 shows a few examples of the images that were generated. Each image in Figure 4.4 are 500x500 pixels, but the EFL parameters used in the simulation changed the field of view and the extent of the area that was imaged.

4.4.3 Signal to Noise Ratio Calculation

The signal values were dependent on the system throughput and so while the image pixel values were assumed to be noiseless, the SNR was calculated using the image pixel values along with the changing system throughput values that depended on the EFL. To calculate the SNR we selected sections of the images generated that were of the reflectance

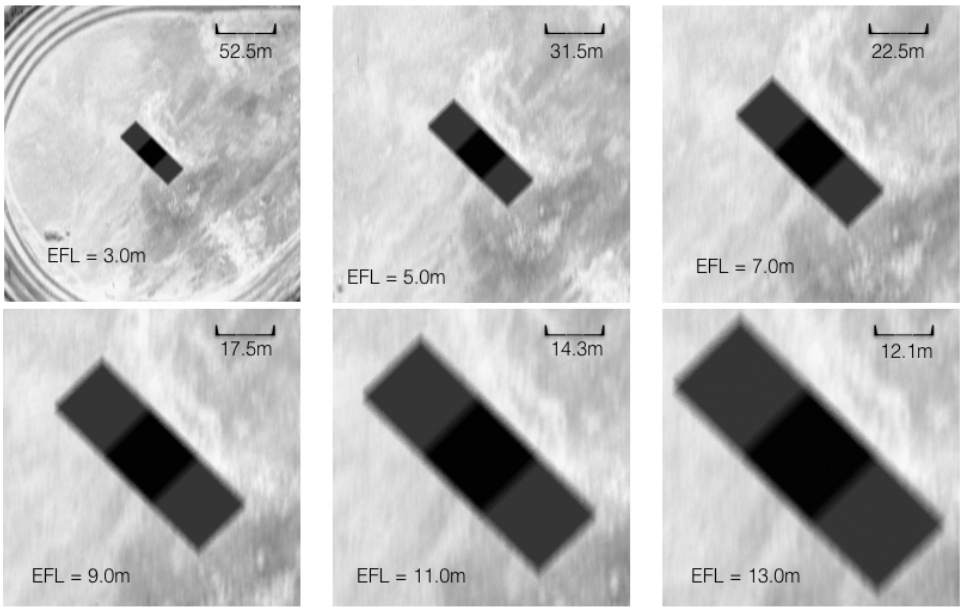

Figure 4.4: 500x500 pixel DIRSIG generated images at selected focal lengths.

panels placed in the scene. The 15% and 7% reflectance panels were used for the high and low reflectance values. Figure 4.5 shows the sub-image sections that were selected.

The electron signal was calculated using Eq. 2.11, using QE and t_{int} values shown in Table 4.2. The high reflectance signal ($\Phi_{\rho_{high}}$) and low reflectance signal ($\Phi_{\rho_{low}}$) was the average of the subimage pixel values. Then following the prescribed method for SNR calculation in our reference [20], the difference between the high and low reflectance values were used as the signal (Eq. 4.2),

$$\Phi_{\Delta\rho} = \Phi_{\rho_{high}} - \Phi_{\rho_{low}} \tag{4.2}$$

and the standard deviation of $\Phi_{\Delta\rho}$ was used as the shot noise where we assumed the signal had a Poisson distribution (Eq. 4.3).

$$\sigma_s = \sqrt{\Phi_{\Delta\rho}} \tag{4.3}$$

The total noise (σ_T) was assumed to be composed of the shot noise ($\sqrt{\Phi_e}$) and two fixed noise sources. The total noise (σ_T) was calculated using the three noise components that were summed in quadrature (Eq. 4.4).

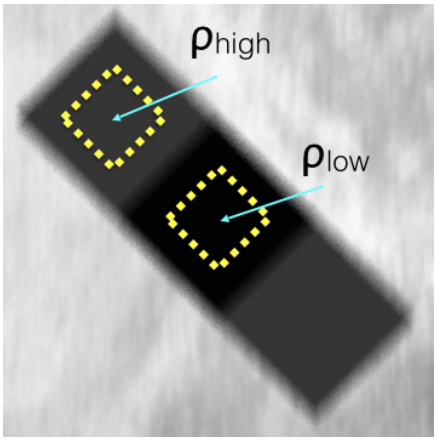

Figure 4.5: Scene showing subimage of low reflectance and high reflectance panels selected for SNR calculation in yellow boxes.

Table 4.2: Imaging system parameter values used to generate panchromatic images that were used to calculate SNR for simulation validation.

Parameter	**Symbol**	**Values Simulated**
Integration Time	t_{int}	600 μs
Quantum Efficiency	QE	0.76
Wavelength	λ	0.5 μm
Dark Noise	σ_d	10 electrons
Other Fixed Noise	σ_f	5 electrons

$$\sigma_T = \sqrt{\sigma_s^2 + \sigma_d^2 + \sigma_f^2} \tag{4.4}$$

Finally, the SNR was calculated as the ratio of the difference in electron signal of the high and low reflectance values and the total noise (Eq. 4.5).

$$SNR = \frac{\Phi_{\Delta\rho}}{\sigma_T} \tag{4.5}$$

We calculated the SNR in a way that replicated the GIQE definitions directly from the images. Table 4.2 shows the values of the parameters that were used in the simulation along with the assumed fixed noise values. This method produced SNR that was expected for a compact imaging system, and changed according to the system throughput that was dependent on the EFL.

4.4.4 Relative Edge Response Calculation

In Section 2.4 we described the RER and how it is calculated. To simulate varying degrees of sharpness of an edge in an image, we focused on two contributions to the edge response - Point Spread Function (PSF) and smear. We incorporated these real image phenomena by simulating platform motion and implementing an optical PSF that changed with the EFL.

The optical PSF for the panchromatic study was simulated in DIRSIG by using an 8-bit image of a diffraction pattern of a circular aperture. The image was given a scale that corresponded to the instantaneous field of view so the grayscale values of the image were used to produce an importance sampling of the ray-tracing mechanism. This method of sampling replicated a blur that would normally be observed in a real imaging system's optics due to its PSF where the scale dictated the extent of the blur. By changing the scale given to the PSF parameter within DIRSIG, we generated images that would be produced from imaging systems with different EFLs that had a constant aperture diameter. All the other system parameters such as detector pitch, diameter of the primary optical lens, and center wavelength of the bandwidth, were kept constant, but the EFL changed and the PSF changed accordingly. The diameter of the airy disc that produced the blur was calculated using the Rayleigh criterion (Eq. 4.6).

$$d_{rayleigh} = 2.44\lambda\frac{EFL}{D} \tag{4.6}$$

We then calculated a scale factor by using the Q# defined in [6] (Eq. 4.7)

$$Q\# = \frac{\lambda_{center} \cdot EFL}{p \cdot D} \tag{4.7}$$

The the edge response in the image that was generated by the scale input in DIRSIG was examined to ensure it corresponded to the Q# for the EFL that was simulated. Since this relationship between the EFL and Q# was linear, we examined one of these relationships and scaled the others by their Q#. At the EFL value where $Q\# = 1$, the EFL = 4.25m for the selected imaging system parameters shown in Table 4.3. Therefore for the images simulated at this EFL, we expected an edge response that was consistent with a system that had a Q# of 1. We calculated the scale factor that would produce an edge response that was consistent with an airy disc diameter produced by an imaging system with this Q#, and

Table 4.3: Imaging system parameter values used to generate panchromatic images that were used to calculate RER.

Parameter	**Symbol**	**Values Simulated**
Aperture Diameter	D	45cm
Pixel Pitch	p	4.5 μm
Center wavelength	λ_{center}	0.5 μm
Effective Focal Length	EFL	3.0m - 13.0m

scaled the image of the diffraction pattern to produce and edge response that was consistent with this Q#. We generated images for a range of EFLs that had edge responses that would first be limited by the detector resolution when the Q# was small, then limited by the diffraction resolution when the Q# increased. Figure 4.7 shows and example of an edge that was used to calculate the RER of each simulation set.

Another contribution to the RER is smear produced from the movement of the imaging system platform. Depending on the spatial relationship between the edge to the direction of movement, smear is produced differently for each edge. For this reason, the GIQE calculates the RER in both the x and y direction and the RER used in the NIIRS prediction is the geometric mean of these two values. We simulated platform motion to be 45 degrees with respect to our simulated scene, and the panels were placed with their edges perpendicular to the direction of the platform motion. This allowed us to simply calculate the RER of one edge, which would be equivalent to the geometric mean of the RER in both direction. Figure 4.6 shows an edge response that was calculated using a subimage such as the one shown in Figure 4.7. The subimages were first tilted using nearest-neighbor interpolation to have the columns of the pixels to line up with the edge, then the columns of the pixel values of the tilted subimage was averaged to produce the edge response. The RER was then calculated by taking the slope of the edge response function.

The method of tilting the image first before calculating the edge response as opposed to projecting the image of a tilted edge to a step function was used because of the EFL range we simulated. For edge responses that only span one or two pixels, or even a partial pixel, projecting the values of a tilted edge onto a step function is required. However, for the range of EFLs we selected to simulate along with our other imaging system parameters, the edge response spanned more than

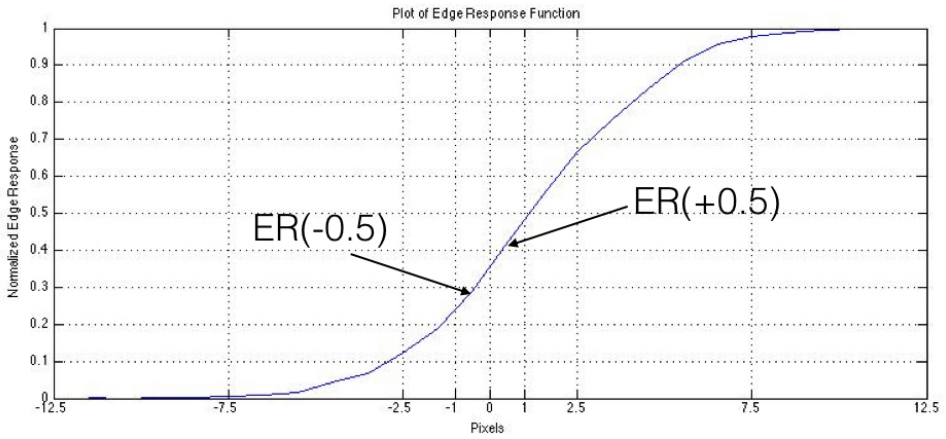

Figure 4.6: Example edge response calculated from subimage of edge.

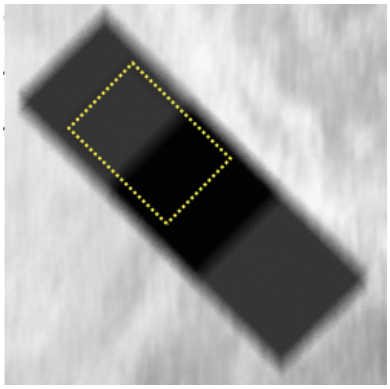

Figure 4.7: Example scene showing subimage selected for RER calculation.

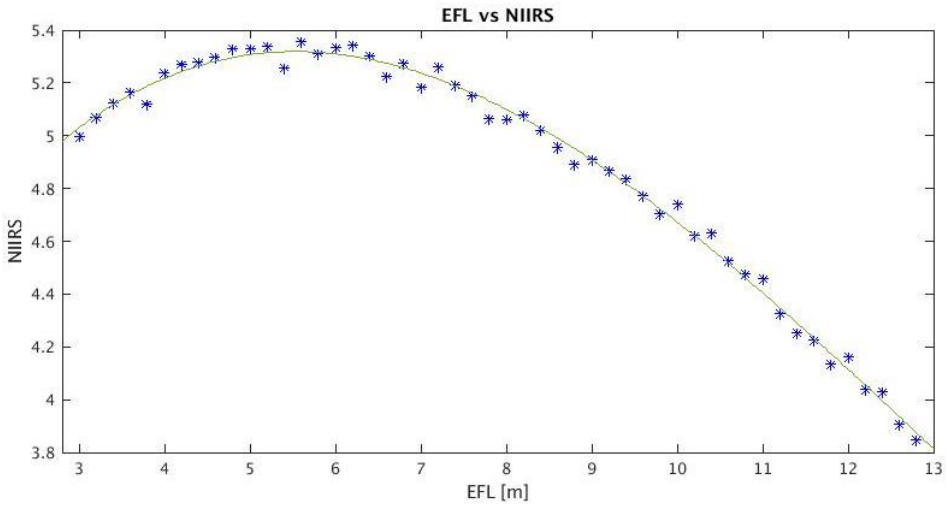

Figure 4.8: EFL vs NIIRS curve

two pixels. Therefore attempting to project the edge response that might span over 25 pixels onto a step function would have unnecessarily complicated the RER calculation. Overall, the relative edge response that was produced from the simulation was found to be sufficient replications of the edge responses in real imaging systems for the range of focal lengths we analyzed.

4.4.5 GIQE Calculation

The GSD, RER, and SNR values that were calculated for the range of EFLs that were simulated were used as input into the GIQE (Eq. 2.1) to predict the NIIRS values at each EFL. Figure 4.8 shows the predicted NIIRS value at each of the simulated EFL values. The simulation generated 100 images for each EFL value ranging from 3.0m to 12.8m at 0.2m increments. This produced a dataset that could be used to test any inconsistencies of DIRSIG 5, which was still at the beta release stage of development as opposed to its previous version, DIRSIG 4.

What we found was that the final calculation produced results that were consistent with expected results and our references. The peak EFL was found at 5.8m, the point where the Q# = 1.5, a peak quality point described by [6]. For most applications, this is where the detector resolution limit meets the optical resolution limit. The variations in the results were due to discretization of the sampling that was selected to

reduce computation time, and from the randomization seeds used for the Monte Carlo calculations that changed from one run to another. There was also a change in the spatial location of the edge with respect to the pixel location that changed as the GSD changed and affected the RER of the images differently for each EFL value. Despite the small variations, we found that after implementing the selected parameters and sub-models in DIRSIG, the images generated sufficient realism and replicated key components of a spectral imaging system that could be used for trade space analysis.

4.5 Summary

In this chapter, we validated the use of simulation for imaging system trade studies by demonstrating that we could adequately replicate the well-established panchromatic methods for predicting utility. These techniques and parameters that were developed for the panchromatic images were then translated to simulating spectral imaging systems to ensure the point spread function, collection geometry and motion, and sensor characteristics were correctly implemented within the simulation tool.

"And how many hours a day did you do lessons?" said Alice, in a hurry to change the subject.
"Ten hours the first day," said the Mock Turtle: "nine the next, and so on."
"What a curious plan!" exclaimed Alice.
"That's the reason they're called lessons," the Gryphon remarked: "because they lessen from day to day."

- Lewis Carroll, *Alice in Wonderland*, 1865

5 Band Selection

Increasing spectral resolution provides us the ability to identify materials and detect objects that are subpixel based on their spectral signatures. However, this also increases dimensionality which can often lead to computational complications. With automated processing being the primary method of material identification, classification or detection, there is a need to analyze the trade between increasing the numbers of bands that improve our ability to identify materials and increasing dimensionality that stresses computational resources and introduce error. Dimension reduction is an often employed step in spectral image processing as a way to find the "sweet spot" to having just enough bands that contribute to utility. In this chapter, we present the background for spectral image that form the trade space dimension of spectral bands, and the method we develop that is suited for compact imaging systems.

5.1 Definition: HSI vs MSI

In the previous chapters, we used the term spectral images to encompass both HSI and Multispectral Images (MSI), and used it to reference any image other than panchromatic, to include RGB images. While there may be wide variations in how MSI and HSI are differentiated and defined, the

two modalities are not necessarily separate. In this work, we differentiate them by their sampling capability of a material's spectral signature, which dictates their data extraction approaches. MSI can be viewed from an imaging aspect where selecting the correct bands is of primary importance. HSI on the other hand can be viewed from a signal processing perspective where separating the signal, or the correct spectral signature of a material, is the primary requirement.

From these viewpoints of MSI and HSI, MSI is simply a set of data that does not require dimensionality reduction as it is under-sampled data of a material's spectral signature. On the other hand, we can consider HSI as an over-sampled set of data that requires dimensionality reduction. Here we define the number of bands that make an image an MSI to be relative to what is required to extract information. For example, to calculate the Normalized Difference Vegetation Index (NDVI), only two bands are needed as long as they are the correct bands [49]. If the application is material classification of the earth's surface into four categories, then an image that has 7 bands can adequately accomplish this task with some level of error as long as they are the correct 7 bands. An imaging system with just the two bands or the 7 bands can be considered an MSI where more bands may improve the results, but with careful selection, they adequately extract the required information. Any more bands than what is required, can be seen as being over-sampled, and an HSI.

For subpixel target detection, 7 bands can be insufficient to determine the presence of a target, especially if they are not optimized for the target. In this case, a 7 band spectral image is under-sampled for the signal that needs to be extracted. It is why hyperspectral imaging systems that collect hundreds of contiguous bands are used for this task. Of these hundreds of bands however, far fewer bands are needed to detect a subpixel target, but the wavelength of the bands and the number of bands needed, change depending on the target. The signal is the target we wish to identify, and the noise is the background materials surrounding the target that contribute to the sensor reaching spectral radiance. An HSI is therefore over-sampled for any one target, but without adaptive collection capabilities it can not be avoided because what constitutes a signal can change from target to target.

In sections 5.2 and 5.3, we explain the representation of HSI data and different methods of dimension reduction, which are widely used in the post-processing steps for HSI exploitation. Band selection methods can be seen as a dimension reduction method approach that is optimized for a

specific target and scene, when it is used as a post-collection step and in 5.4 we present some of the existing methods. In Section 5.5 we present the motivation for developing a novel band selection method for a future spectral imaging system with adaptive band selection capabilities.

An imaging system with the flexibility for selecting which bands are collected from mission to mission can be both a multi-spectral or hyper-spectral imaging system. An adaptive system that can change the wavelengths and the number of bands has neither requirements to under-sample nor over-sample the signal and can adapt as needed. What we explore in Section 5.6 is a method suited for band selection prior to collection to meet the task at hand for an imaging system with adaptive band selection capabilities that can collect only what is needed based on the target. Thus for the purpose of this research, HSI and MSI are defined in terms of their requirements for subpixel target detection, where an HSI is an over-sampled data set, and an MSI is an under-sampled one.

5.2 Data Representation Methods

There are several data representation methods for spectral images that depend on their application. With the development of machine learning algorithms, and the increase in their use for exploiting high dimensional data, tensor-based representation of HSI has become common [50] [51] [52]. This can be used to automate data processing, but for subpixel target detection, there are two representations that form the underlying premise for this application. The tensor-based representation when used for automated subpixel target detection, assumes either or both the geometric or statistic representation of the spectral image. In this section we present the two representation methods that drive calculations for subpixel target detection algorithms.

5.2.1 Geometrical Representation

When using the geometrical representation of HSI, each spatial pixel can be seen as separate vectors of N dimensions where N is the number of bands. Between the vectors, we can calculate a distance component (Eq. 5.1),

$$d = |\mathbf{x}_1 - \mathbf{x}_2| = \sqrt{(\mathbf{x}_1 - \mathbf{x}_2)^T(\mathbf{x}_1 - \mathbf{x}_2)} \tag{5.1}$$

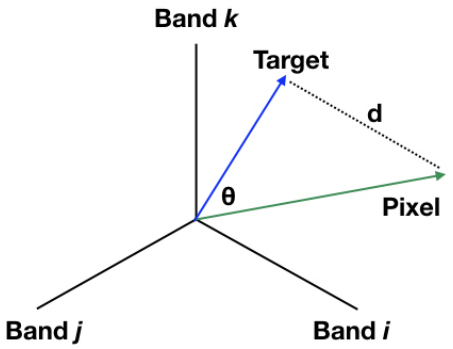

Figure 5.1: Geometrical representation of spectral data.

where $\mathbf{x}_i$ is the i^{th} pixel of an HSI, and d is the distance between two pixels. Their location within the N-dimensional space, can also have an angle (Eq. 5.2),

$$\theta = cos^{-1}\left(\frac{\mathbf{x}_1^T\mathbf{x}_2}{\sqrt{(\mathbf{x}_1^T\mathbf{x}_1)(\mathbf{x}_2^T\mathbf{x}_2)}}\right) \tag{5.2}$$

which along with the distance, can represent how spectrally similar two pixels are. When using the geometrical representation of the data, we assume the mixture of materials of the different spectra within a pixel are linearly additive. The amount of material present in a pixel using this representation, is the amount of contribution each material has to the distance and angle (Eq. 5.3),

$$\mathbf{x} = a \cdot \mathbf{p} + b \cdot \mathbf{q} \tag{5.3}$$

where a and b are the fractional amounts of materials $\mathbf{p}$ and $\mathbf{q}$ present. Figure 5.1 shows a diagram that illustrates the distance (d) and angle (θ) of a pixel and target spectra when represented geometrically. For example, if the spectrum of pixel $\mathbf{x}$ is composed of two materials whose pure spectra is $\mathbf{p}$ and $\mathbf{q}$, each contributing a fractional amount of a and b respectively, a linear mixture of the two pure material spectra will produce the pixel spectrum of $\mathbf{x}$. This is the underlying assumption for subpixel target detection algorithms. The distance or angle of a pixel to the pure target signature, gives the likelihood of whether the target material contributes to the spectrum or not.

5.2.2 Statistical Representation

Another data representation method for spectral images is to consider the pixels as random data points with a distribution function representing the variations and combinations of materials present. This type of representation can characterize the distribution of sensor noise, inherent variation in a single material spectrum, along with variations from the combination of the materials. It can capture the randomness produced by noise, scene complexity, and other inherent variations of spectral images. A pixel of a spectral image with N bands, can be represented statistically as a combination of signal ($\mathbf{s}$) and noise ($\mathbf{n}$) (Eq. 5.4).

$$\mathbf{x} = \mathbf{s} + \mathbf{n} \tag{5.4}$$

The probability density of the pixels (Eq. 5.5)

$$p(\mathbf{x}; \Sigma, \mu) = \frac{exp\left(-\frac{1}{2}[\mathbf{x} - \mu]^T \Sigma^{-1}[\mathbf{x} - \mu]\right)}{(2\pi)^{K/2}|\Sigma|^{1/2}} \tag{5.5}$$

can be represented with a mean (μ) which converges to the true signal value (Eq. 5.6),

$$\mu = \mathbf{s} \tag{5.6}$$

and an example of a covariance matrix (Σ) can be used to represent the noise. In this representation of Σ, the diagonal matrix contains the variance values of each band (σ^2) multiplied by the identity matrix ($\mathbf{I}$) (Eq. 5.7).

$$\Sigma = \sigma^2 \mathbf{I} \tag{5.7}$$

This method of representing spectral images along with the geometric method, allows us to analyze the statistical variations of the distances between a target spectrum and the pixel that is analyzed. We can assume that the target material we are looking for is the signal and the background surrounding the target as noise, and the probability of the target presence is represented by the distance or angle between the target and background spectra.

5.3 Dimension Reduction Methods

Subpixel target detection methods combine both the geometrical and statistical representation of spectral images to calculate detection probabilities. Therefore high dimensionality of data can not only complicate the computation, but produce undesirable effects that can skew the detection results. Therefore dimensionality reduction for HSI is a key aspect of subpixel target detection. The requirement to reduce complexity for optimal detection is balanced with retaining sufficient amount of signal. The three types of dimension reduction methods we present in this section have the primary purpose of finding the lower-dimensional sub-space that contain most of the signal information that will allow optimal target detection results.

5.3.1 Principal Component Analysis

The first type of approach for dimension reduction is the use of second order statistics of a spectral image to find the most significant dimensions. One of the most widely used methods of type is the Principal Component Analysis (PCA). There are many implementations of PCA to compress HSI to store and process the data specifically for subpixel target detection applications [53]. The underlying assumption of this algorithm is that HSI bands are highly correlated, and once the data is converted into linearly uncorrelated datasets, the information of interest is contained in the subspace of the HSI bands with the highest amount of variation. PCA uses linear fitting and Singular Value Decomposition (SVD) to project the higher dimensions into a lower dimension [54]. This projection depends on the global linearity of the data, and so whitening and noise-adjusting are common pre-processing steps for transforming HSI when using PCA for target detection.

For the purpose of target detection, both of these pre-processing steps are often used to to enhance the distance between target and background and boost the signal content separate from the noise. However, even with these steps, for subpixel target detection, PCA often falls short of preserving the bands that would optimize detection. This transform derives its results solely from second order statistics of the data, and it inherently assumes that the data has normal distribution. For scenes and low abundance targets, this assumption may not hold, and so the target signal is often lost.

To illustrate the effects of PCA, we present an experiment that was conducted to study applications of HSI including subpixel target detection [55]. The experiment and the data that was collected is explained in detail in Section 5.7.2, but we zoom in on the portion of the scene that was designed specifically for subpixel target detection to examine the latent data that contain the subpixel targets. Three sets of bands after transformation are selected and displayed as an RGB image to illustrate the effects of PCA and how the algorithm handles latent subpixel information.

Figure 5.2 shows the three bands with the highest variation. The PCA transformed bands were rank ordered by their eigenvalues, and the three images shown in 5.2a are the bands with the highest eigenvalues. We can see that these image are the most distinct from each other for the whole scene, and so is believed to contain the most information. However the RGB composite shown in Figure 5.2b and a subset of the scene that was used in the experiment for subpixel target detection shown in Figure 5.2c, loses the latent subpixel information.

Figure 5.3 shows images of the three bands that had the lowest eigenvalues after the PCA transform and thus the lowest variation. The three images in Figure 5.3a have almost no differences between them, and the RGB composite of these three images confirms it as shown in Figure 5.3b. The subset of the scene shown in Figure 5.3c shows limited values in these bands for subpixel target detection as expected.

Figure 5.4 shows the images of the bands with the 15th, 16th, and 17th highest eigenvalues after PCA transformation. While the individual bands in Figure 5.4a shows some, but limited differences between the images for the scene as a whole, the RGB composite shown in 5.4b indicates that these bands likely contain information of interest for subpixel detection.

The areas containing the subpixel targets in the subset scene shown in Figure 5.4c appeared to be uniform in Figures 5.2 and 5.3, but has variations using the 15th, 16th, and 17th bands. The figure shows intermittent dark pixels among the green grass area, and green pixels in the black asphalt area. Here we illustrate the dimension reduction mechanism of the PCA transform for HSI, and its potential for its use in subpixel target detection. As long as enough dimensions are preserved, it is a method that can be used, but the amount of latent subpixel information it preserves, even in the 15th-17th bands is limited. Furthermore, knowing how many dimensions to preserve using this method

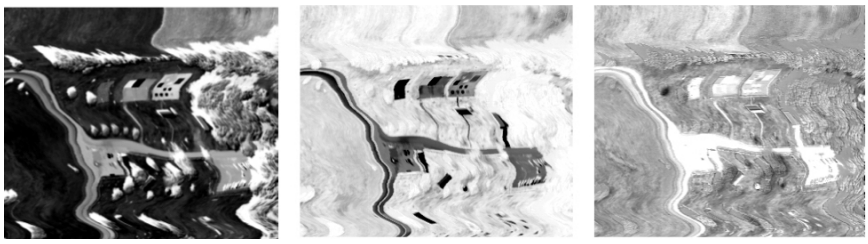

(a) Images of three bands with the highest eigenvalues after PCA transformation. Shows highest variation where distinct differences can be observed between the three images.

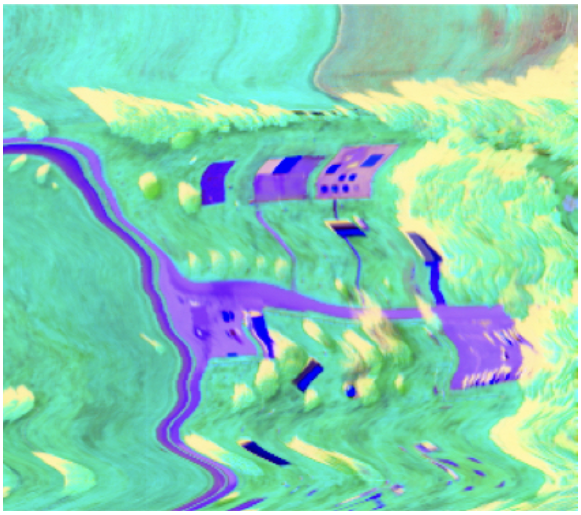

(b) RGB composite of the three bands with the highest eigenvalues and highest variation.

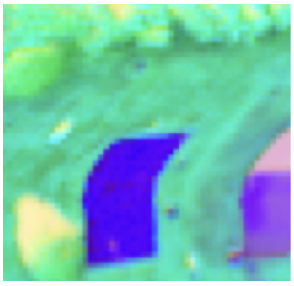

(c) Subset of scene used for sub-pixel target detection experiment.

Figure 5.2: Images of a 360 band HSI that was transformed using PCA with highest variation.

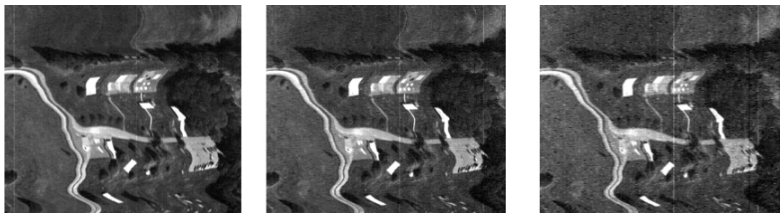

(a) Images of three bands with the lowest eigenvalues after PCA transformation. Shows lowest variation where almost no differences can be observed between the three images.

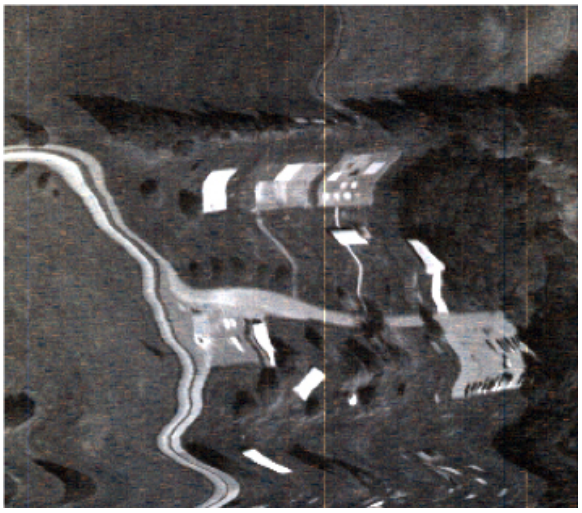

(b) RGB composite of the three bands with the lowest eigenvalues and lowest variation.

(c) Subset of scene used for subpixel target detection experiment.

Figure 5.3: Images of a 360 band HSI that was transformed using PCA with lowest variation.

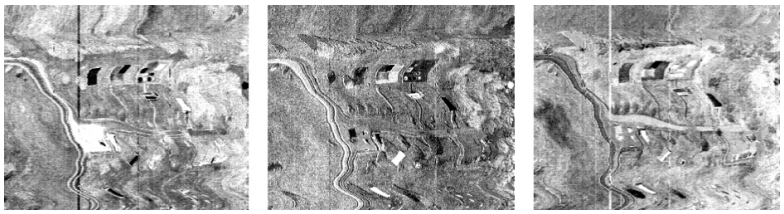

(a) Images of three bands with the 15th, 16th, and 17th highest eigenvalues after PCA transformation. Shows moderate variation between the bands where some differences can be observed between the three images.

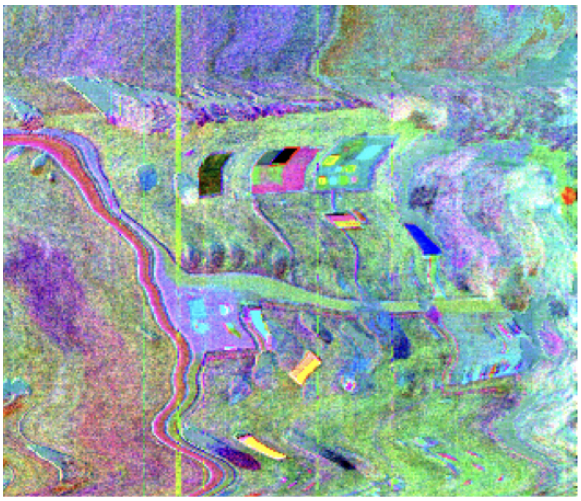

(b) RGB composite of the three bands with the 15th, 16th, and 17th highest eigenvalues.

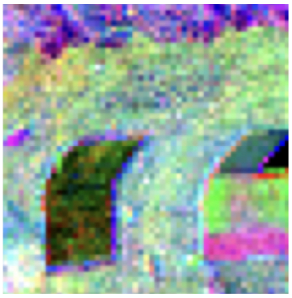

(c) Subset of scene used for subpixel target detection experiment showing some indication of subpixel targets.

Figure 5.4: Images of a 360 band HSI that was transformed using PCA with moderate variation.

can be a challenge. While this method is widely used for processing HSI, for subpixel target detection, dimension reduction methods that preserve latent information is more appropriate.

5.3.2 Non-negative Matrix Factorization

Non-negative Matrix Factorization (NMF) is an algorithm that is being used increasingly for target detection purposes as it can preserve more latent information compared to PCA. For spectral images, this method works well since all spectral data is non-negative, which means the

underlying assumption of the algorithm holds [56]. It has an advantage over PCA or even ICA because it approaches the data in parts and so reducing the dimensionality is a natural process of the algorithm. It does not need to assume the pixels are combinations of pure pixels like PCA does. A disadvantage of NMF is that it is sensitive to spectral variations of the material caused by collection geometry or atmospheric effects. Another challenge of using NMF is that it assumes the data is smooth, which is not always the case with HSI, especially if pre-processing is done to discard bad bands before dimension reduction. There are many variants of NMF that attempts to overcome challenges presented by the inherent characteristics of HSI depending on the use such as clustering bands to ensure smoothness [57].

NMF is a popular dimension reduction method for unmixing applications as it can better preserve latent information. However, it is becoming increasingly prevalent for subpixel target detection as well for the same reason. Both PCA and NMF are widely used dimension reduction methods that can be used without a prior knowledge of the target, and the background is calculated from the collected image, to identify anomalies. Their disadvantage is that they assume the normal statistical distribution of the HSI pixels, and become inaccurate with poor detection performance when these assumptions do not hold.

5.3.3 Independent Component Analysis

The two methods presented in Section 5.3.1 and 5.3.2 assumed each pixel was an independent random process with normal distribution. For cases where this assumption does not hold, and the bands are not independent processes, a dimension reduction method that takes a numerical approach can be used, such as the Independent Component Analysis (ICA) [58]. Unlike PCA which transforms the HSI using principal components, the ICA transform uses the inverse of the principal components matrix, making the transformed data statistically independent.

ICA makes each component independent, then selects the dimensions that have the highest variations in the distribution. Like NMF, it is capable of preserving latent information within the data and does not assume Gaussian distribution. As a results, it can be successful for many different target or background combinations. There are many variations of ICA that overcome specific challenges inherent in the method when applied to HSI to select the best dimensions depending on use [59]. We

examined the same HSI of the scene that was used to illustrate the effects of PCA for subpixel target detection in the previous section. We transformed this image using ICA and select a similar set of bands to analyze how the latent subpixel information was preserved.

Figure 5.5 show the bands and the RGB composite of the top three bands with the highest amount of variation. The bands were not rank ordered by its eigenvalues, but an iterative variation analysis was done after making the data statistically independent. The processing time as a result was much longer for the same image than it was to calculate the PCA transform. Figure 5.5a shows that each band is distinct from each other, indicating that they do contain the most information as was the case with the PCA bands with the highest eigenvalues. However, unlike PCA where the latent target information was averaged out in the in the bands with the highest eigenvalues, ICA was able to preserve some subpixel target signatures which can be seen in Figure 5.2c. The asphalt area in the image that appears mostly yellow has green speckles, indicating the presence of subpixel targets. However, the grass area shown in pink that contained the more difficult target did not preserve the latent target information in the top three bands.

Figure 5.6 shows the bands with the 10th, 12th, and 13th highest variations. They still have distinct differences as seen in Figure 5.6a. Since the bands are statistically independent, the information contained does not decrease linearly in the lower ranked bands as is the case with PCA transform. With these bands, the target that was more difficult to detect can now be seen in Figure 5.6c. The blue area representing the grass background has darker blue pixels speckled in the scene indicating the presence of subpixel targets. This illustrates that this method is able to preserve latent information better than PCA, although the challenge of knowing how many dimensions to preserve persists.

While these methods can be used for post-collection data processing when target and background information is not available, for subpixel target detection, they will likely have poor performance due to loss of latent information. Furthermore, the amount of processing required even for a single image can be operationally unfeasible, even with the advanced computational capabilities we have today. When applying machine learning applications to process the data, where many images are needed to train the algorithms, this type of computational cost can be prohibitive. Even though our CPUs are more capable today for computationally complex tasks, when processing a large number of images as can be required for wide area search or when using machine learning

(a) Images of three bands with the highest variations after ICA transformation. Shows largest difference between each band.

(b) RGB composite of the three bands with the highest variations.

(c) Subset scene used for target detection experiment. Unlike PCA, easy targets apparent.

Figure 5.5: Images of a 360 band HSI that was transformed using ICA using the bands with the highest variations.

algorithms, there is immense value in reducing the image processing requirements. The challenge with all of these methods is that while they can be used for subpixel target detection, not only do we need to process all the bands to make the transforms, but the decision of how many dimensions to preserve is also required. These two requirements pose limitations, especially if the data is automatically processed.

5.4 Band Selection Methods

The dimension reduction methods presented in Section 5.3, despite their limitations are prevalent, as they can be used for most applications of spectral images. However for subpixel target detection, we can take a more

(a) Images of three bands with the 10th, 12th, and 13th highest variations after ICA transformation. Shows moderate but distinct differences between the three images.

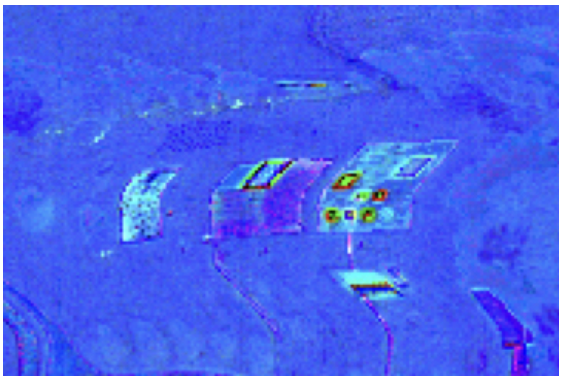

(b) RGB composite of the three bands with moderate variations.

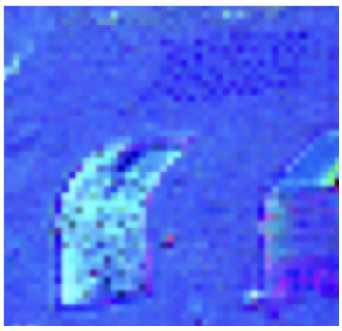

(c) Subset scene used for target detection experiment. Anomalies can be observed for easy and difficult targets.

Figure 5.6: Images of a 360 band HSI that was transformed using ICA with moderate correlation.

discriminate approach that is tailored to the target and scene. Band selection is such an approach that can reduce the dimensionality of the data without losing latent target information, potentially for a much smaller number of dimensions. While some of the methods find a value akin to B_opt in their selection, which is a metric we developed as part of this research and explained in Section 3.5, but the band selection method we developed had an explicitly developed to have a connection to operations.

There are a myriad of band selection methods, that can be used for different applications of HSI, and in this section we present three methods. One is used when the target and background are both known and selects bands after comparing them. It uses the inner product of the two spectra to calculate the distance between them, and is appropriate for subpixel target detection as long as the background can be characterized. This method was selected for comparison for its potential for use in a

compact imaging system because it could be used to select bands prior to collection if the background was known.

We selected two other methods for comparison because they were considered state of the art. We used the results of a study that compared 17 different band selection methods that were considered state of the art to narrow down the ones to use for comparison [60]. The two methods that were selected found at least 4 out of the 15 targets from the HYDICE [61] Forest Radiance I dataset [24], and their computation time was less than 0.5 seconds. One of these methods was based on divergence-based decorrelation, and the other was based on the Constrained Energy Minimzer (CEM) target detection algorithm.

5.4.1 Target and Background Comparison (TBC) Method

This method was selected for comparison because of it was simple enough to calculate using an small on-board CPU, and so held potential for use in a compact imaging system if background information was available. This method used an algorithm that maximizes the distance between the background and target spectral signatures. It rank ordered the bands by projecting the subspace spanned by the target to the background and finding the bands that are orthogonal to the subspace [62]. The band ranking was ordered for the best bands ($\mathbf{z}$) based on the spectra where target was most distinct from the background (Eq. 5.8).

$$\mathbf{z} = \mathbf{t} - (\mathbf{b}^T \cdot \mathbf{t}) \cdot \mathbf{b} \tag{5.8}$$

This method was designed to select bands using radiance data in the the thermal portion of the electro-magnetic spectrum and so it has potential for use with radiance data or digital counts for target detection. We used a simplified version of this method on the reflectance data to find the bands with the largest differences between the target and background to be able to compare with the other methods. The effectiveness and its advantage over other dimension reduction methods such as PCA or NMF was when the background is (1) known, (2) uniform, or (3) well characterized.

5.4.2 Information Divergence (ID) Method

A method that maximized information divergence, a concept based on information theory [63], prioritized bands using PCA-based transforms, then minimized correlation by calculating the cross-entropy [64]. The advantage of this method is that it was able to calculate a value akin to B_{opt} when error was minimized. The disadvantage of this method was that it was an iterative method, and so the computation time increased with the number of bands needed.

This method calculated the noise-adjusted PCA and prioritized the bands according to the largest eigenvalues, followed by a calculation of the divergence between each set of bands. The divergence $D(\mathbf{p}, \mathbf{q})$ was calculated using the log sums of the sets of bands $\mathbf{p}$ and $\mathbf{q}$ (Eq. 5.9)

$$D(\mathbf{p}, \mathbf{q}) = \sum_{i}^{l} p_i log \frac{p_i}{q_i} + \sum_{i}^{l} q_i log \frac{q_i}{p_i} \tag{5.9}$$

In this equation, $\mathbf{p}$ and $\mathbf{q}$ are arbitrary sets consisting of any number of bands less than the total. In this equation, the the total number of bands in each set was l. The set of bands were selected if the divergence was greater than a given threshold. In order to compare the detection performance of the bands selected using this method with the other three methods, we iterated though the bands to find the best N bands. This algorithm was implemented for a range of of 2-30 bands in the comparison. The computation time to select all N bands were measured. The $\mathbf{z}$-values were calculated using Eq. 5.10

$$\mathbf{z} = D(\mathbf{p}, q_i) \tag{5.10}$$

where $\mathbf{p}$ was the top 30 bands after the noise-adjusted PCA was calculated and q_i were the individual bands in the HSI at each wavelength for $i = 1...N$. Therefore the divergence was calculated for each band against the initial top 30 bands, and a $\mathbf{z}$ value was assigned accordingly.

5.4.3 Linearly Constrained Minimum Variance (LCMV) based Method

A method that was based on the CEM algorithm, constrained the correlation of each band to the correlation matrix of the HSI [65]. The

bands were rank ordered so that the ones with the least amount of correlation was the highest ranked. A band dependence factor was also calculated, and the highest ranked bands had both lowest correlation and dependence. Applying this method to every pixel in the image took between 18 seconds to 43 minutes to find 9 bands in our reference. A modified version of this algorithm was the LCMV, which reduced the computation time by constraining a spatial dimension as a single vector. Using the LCMV, the CEM algorithm was calculated for every row in the image instead of every pixel.

This method was implemented by calculating the CEM of the y-axis pixels as the constrained input vector $\mathbf{v}$ and the bands were ranked using Eq. 5.11

$$\mathbf{z} = \Sigma^{-1}\mathbf{B}(\mathbf{B}^T\Sigma^{-1}\mathbf{B})^{-1}\mathbf{1}_N \tag{5.11}$$

where

$$\mathbf{1}_N = \mathbf{B}^T\mathbf{w} \tag{5.12}$$

and

$$\mathbf{w} = \mathbf{t} \cdot \mathbf{v} \tag{5.13}$$

where the spectral reflectance signature of the target $\mathbf{t}$ was used as the weighting vector $\mathbf{w}$, to rank order the bands for the input vector $\mathbf{v}$. This value was compared to the entire image used to calculate the background $\mathbf{B}$, from which the inverse covariance matrix Σ^{-1} was also calculated.

5.5 Motivation for Novel Band Selection Method

The advantages that dimension reduction methods have over band selection methods, is that they require little information about the target or background. They select the best bands based on the most statistically important information, and so the calculations can be modified based on the application. However, they also require a decision for which dimensions are the most important, and often result in loss of information.

All the methods mentioned in sections 5.3 and 5.4 assumed systems that collected fixed bands, and operated on images that were

already collected, transmitted, stored, and disseminated for processing. Their primary purpose was to improve detection performance, and computation time was generally not a concern since the calculations were done post-collection. In essence, the existing band selection methods were optimized for exploiting HSI collected by imaging systems with fixed bands following collection. The purpose of these methods was to facilitate image exploitation and maximize detection performance, not as a design optimization tool where computation time was a component to consider.

What we wanted was a band selection method that was simple enough be implemented and computed using a small on-board CPU of a compact spaceborne system. The method we developed for this purpose selected the bands using only the target reflectance signature. It was a method that could be used to drive the collection decisions based on mission for compact spectral imaging systems with adaptive band selection capabilities. Its primary purpose was not simply to maximize detection probability, but to reduce data processing requirements for a given target. In the design phase, the detection performance for a range of bands can be computed to drive feasibility decisions for compact systems, and in the operational phase use this information to compute B_{opt} based on requirements. This method could be used without consideration of the background prior to collection.

5.6 Bands from Only the Target Spectrum (BOTS)

We developed a band selection method that could be used to make collection decisions for an adaptive system. The method only needed the target reflectance signature to calculate the best bands, and the analysis results in the design phase could be used to calculate B_{opt} in the operations. Its purpose was to minimize the number of bands that are collected and subsequently processed, depending on the operational requirements.

To achieve this, we calculated the band rankings as a function of the magnitude of the target reflectance signature and the slope (Eq. 5.14).

$$\mathbf{z} = f\left(a \cdot \frac{d\mathbf{t}}{d\lambda}, b \cdot \mathbf{t}\right); \qquad a + b = 1 \tag{5.14}$$

We wanted a function that was adjustable as needed depending on the

amount of a priori knowledge of the background or the type of target. For example, if we knew the background spectra was similar to the target (green vehicle in area with high amount of vegetation), then we can increase the slope of the target for this scenario to emphasize the spectral features of the target. Or if we have a target that is bright with limited spectral features, (white vehicle in urban area) then we can increase the magnitude of the target signature to emphasize the bands with the highest reflectance.

This method took advantage of the fact that targets are more detectable at wavelengths where its reflectance is higher, thus the use of the highest reflectance values, and by using the slope of the reflectance we found points where a target's spectral signature was likely to be distinguishable from others. It combined the two qualities of a material's reflectance signature that increased its detectability at subpixel levels without comparing it to a background.

We tested different combinations of the two values to find a function that related the magnitude and slope, such as multiplying the two values, subtracting them, or using the absolute values of the slope. We tested the functions for the orange target which had both high and low reflectance regions in the spectrum along with a distinct feature. The best results were obtained when the two values were added, without using the absolute values (Eq. 5.15).

$$\mathbf{z} = a \cdot \frac{d\mathbf{t}}{d\lambda} + b \cdot \mathbf{t} \tag{5.15}$$

While the magnitude of the reflectance was a number between 0 to 1, the slope could be positive or negative but bounded since the target reflectance was a sampling of a continuous curve. Given these properties of the slope and magnitude of a material's reflectance, the sum of the magnitude and slope were used to rank order the bands. This led to portions of a target's spectral signature where reflectance decreased, to be ranked lower than the wavelengths with no change. The following sections outline the testing and validation process of this band selection method.

5.7 Testing and Validation

Once the best function for combining the magnitude and slope of the target signature was found, we tested the utility of changing the

coefficients for different targets and scenes. We started with the orange lifeboat in open ocean, where we generated curves for utility vs number of bands using the DIRSIG images of the open ocean. The best results for this target and scene was when $a = 0.7$, where the spectral features were emphasized more than the magnitude of reflectance. We then tested the effects of changing the coefficients for the green and yellow targets using real data. We used FASSP to generate trade curves for various values of a and b. Then tested the range of values on the real data generating curves for utility vs number of bands. A value of $a = 0.2$ for the green wood target, and $a = 0.8$ for the yellow target produced the best results on the real data, and so these were the values that were used for comparison to the other band selection methods. The details of the results for analyzing the coefficients are in Appendix A.

For the other band selection methods, we selected the bands for the yellow and green targets using asphalt and grass backgrounds respectively [66]. We compared BOTS to a method that used the inner product comparison of two materials (TBC), and the two state of the art methods ID and LCMV. Figure 5.7 shows the normalized $\mathbf{z}$ values calculated from the the four band selection methods to rank the bands.

The HSI sensor we modeled using DIRSIG was the sensor that was used in the SHARE 2012 data collection. The wavelengths of the 360 bands of the real and simulated images were then interpolated to match the 210 bands of the HYDICE sensor used in the FASSP model. We used the bands that corresponded to the VNIR spectrum for analysis which corresponded to bands 4-97 of the HYDICE sensor. From this range of bands, the wavelength of the selected band that was closest to the wavelength of the 360 band sensor of the SHARE 2012 and DIRSIG data was used in the band selection analysis. The results using the 93 bands was used to compare the band selection results. Our reference to using *all* the bands refer to this set of 94 bands of the HYDICE sensor in the VNIR spectrum. The highest $\mathbf{z}$ values corresponded to the best bands and the top 30 bands from the four methods were selected for analysis. The utility results for the range of 2-30 bands were compared to the results for all the bands.

We started by predicting the utility of the bands selected for the four methods with FASSP for the range of 2-30 bands. The same bands were used to assess utility using real data to validate the BOTS method. We then used simulated images with associated perfect truth data to cross-validate these results. We built on previous work done to compare the SHARE 2012 data and DIRSIG data and modified the existing

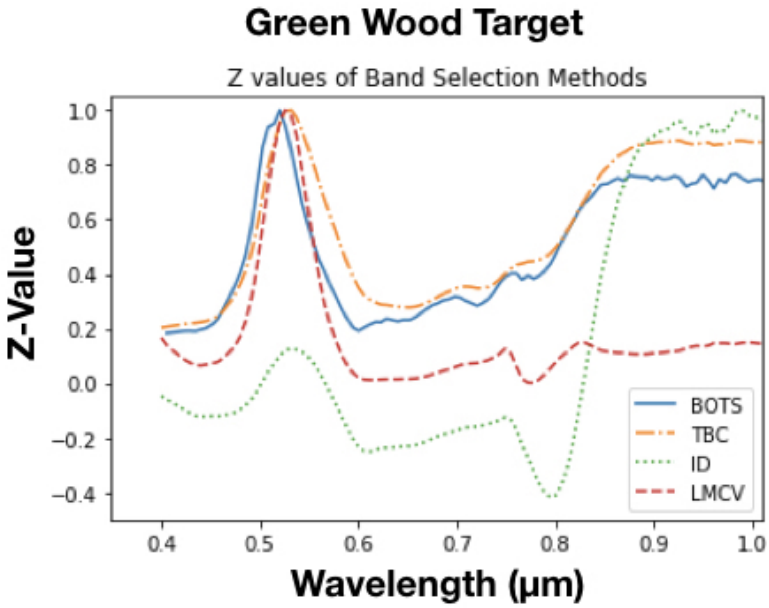

(a) Normalized **z** values for the green targets where the highest values are the best bands for target detection.

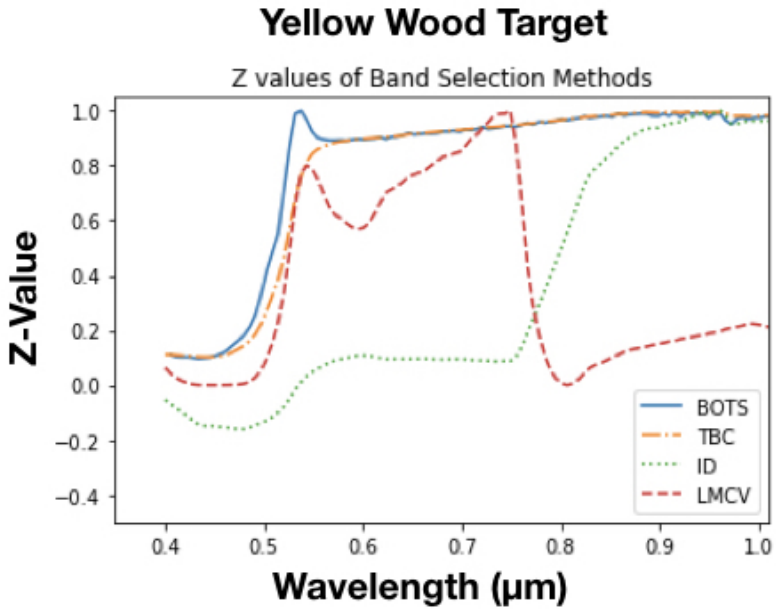

(b) Normalized **z** values for the yellow targets where the highest values are the best bands for target detection.

Figure 5.7: Normalized **z** values for the green and yellow wood targets.

simulation files with different techniques to fit our purpose [67] [68]. The process of validation with with real images, followed by a cross-validation using simulated images had the dual purpose of not only validating BOTS as a band selection method, but also validating the combined use of FASSP and DIRSIG for spectral utility trade space analysis. By comparing their results, we verified that the utility predictions were congruent to the assessments.

5.7.1 Testing with Utility Prediction Method (FASSP)

To predict utility using the FASSP modeling tool, we generated FASSP reflectance files from the field data collected as part of the SHARE 2012 experiment. Additional reflectance spectra of the asphalt where the yellow wood panels were placed, was also collected. The additional background spectra was collected in order to calculate the covariance matrix that is required for the FASSP reflectance files when they are used as background spectra. Figure 5.8 shows the mean reflectance curves of the target and background that were used to predict utility with FASSP. These reflectance data were also used to select the bands and in the material property files in the DIRSIG simulations to attribute the simulated scene materials with the same spectral reflectances.

Trade curves were then generated for the TAs at FPR = 0.01 and FPR = 0.001 to predict the utility values for the real and simulated images. ROC curves were calculated for a range of 2 - 30 bands at 6%, 10%, and 15% TAs. The final results of the real images were compared to the performance results of the three abundance values, and the predicted utility values for the 10% TA matched the assessment results. Since the expected TA for the real and simulated images given the size of the wood panels and pixel size was also 10%, this indicated congruence between the prediction and assessment.

The final utility metric using FASSP was calculated by summing the probability of detection values below FPR = 0.01 and FPR = 0.001 to compare the detection statistics from the real and simulated data. The FASSP model used the CEM target detection algorithm to generate detection statistics. This algorithm was similar to the SMF where it compares the orthogonal subspace of the target and background spectra. While ACE and SAM target detection algorithms were also used to assess utility of the real and simulated data, the results from the SMF algorithm was used for comparison.

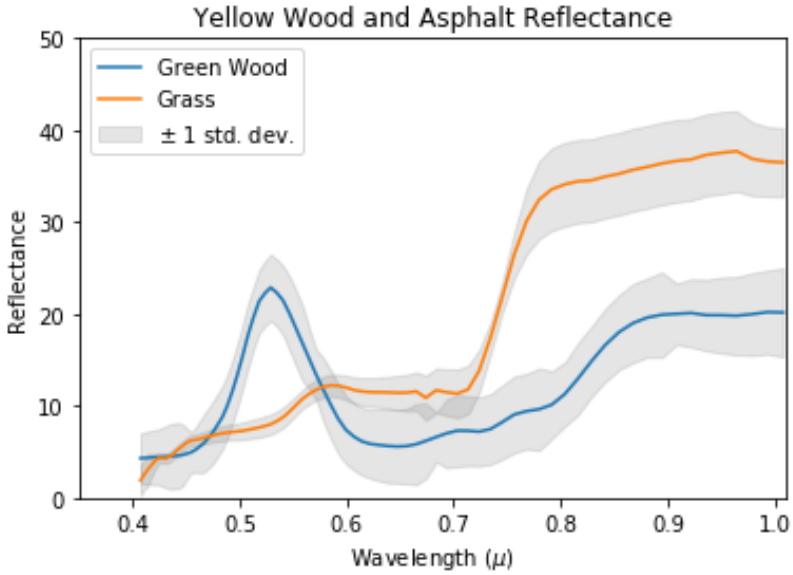

(a) Spectral reflectance signatures of green wood panel targets and grass background.

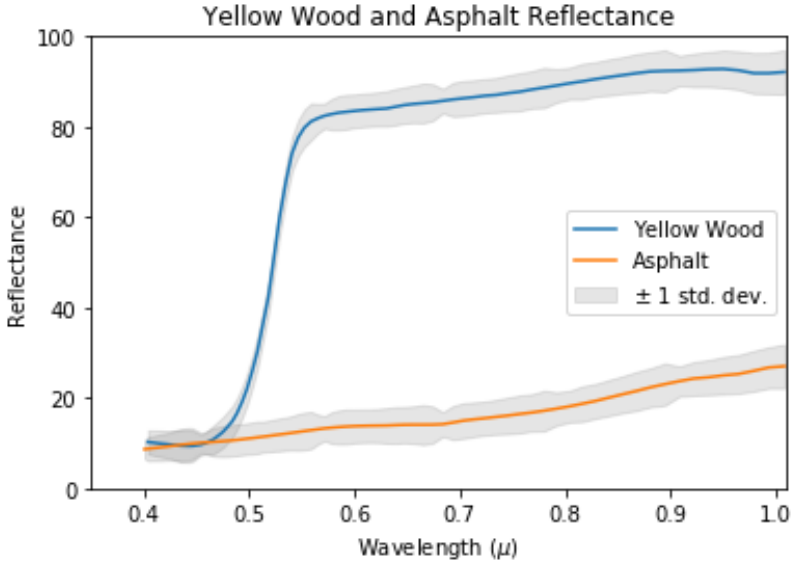

(b) Spectral reflectance signatures of yellow wood panel targets and asphalt background.

Figure 5.8: Target and background spectral reflectance curves used for the band selection method analysis.

5.7.2 Validation with Real Images (SHARE 2012)

The data we used to validate the FASSP results were from a data collection campaign that was conducted in 2012 in Rochester, NY [69]. The SpectTIR Hyperspectral Airborne Rochester Experiment 2012 (SHARE 2012) was a joint effort to collect data for various studies using HSI including subpixel target detection [55]. As part of the study, large black and white panels were placed in the scene that could be used for calibration and atmospheric compensation [70]. This allowed the radiance images to be converted to reflectance images with a high degree of accuracy. We used the reflectance images that were produced after atmospheric compensation using the empirical line method from the calibration panels. Higher spatial resolution imagery using an RGB sensor was collected concurrently for visualization as part of the experiment. The RGB sensor used to collect the high spatial resolution imagery was part of the Wildfire Airborne Sensor Program (WASP) imaging system suite.

The images for the SHARE 2012 experiment were acquired using the ProSpecTIR-VS sensor operated by SpecTIR, LLC. The sensor collected HSI that had 360 bands from 400 to 2450 nm wavelengths and had a focal length of 23.1mm. The airborne platform collected data at an average altitude of 936m, which produced an average GSD of 1.22m. The imaging system was a pushbroom sensor, and so we could approximate nadir collection geometry for all the images. We used four of the atmospherically compensated reflectance images collected during the day for the analysis.

The ground reflectance spectra of the two targets and two background materials were collected using a SpectraVista SVC-1024 field spectrometer. This was the same instrument that was used to collect the additional asphalt reflectance data as part of this project. These measurements were used to create the reflectance files in FASSP as well as the material data files in DIRSIG. The numerous measurements made using the spectrometer were not only used to generated the covariance data for the material reflectance files used in FASSP, but also implemented into the DIRSIG files to replicate the real world variations. They were also used to calculate the band ranking values for the band selection methods. The bands collected using the spectrometer were interpolated to match the bands of the sensors on the airborne platform prior use in the DIRSIG simulation. Then for band selection, the bands of the SpecTIR sensor were interpolated to match the HYDICE sensor. Once the bands were selected, the bands in the SpecTIR sensor with wavelengths that were closest to the

selected bands of the HYDICE sensor were used for the utility analysis.

The images we used were not georectified as this was an additional computational step that did not provide any analytic or procedural benefits for testing the band selection methods. Furthermore, in at least one experiment using the same data, georectification was found to cause changes in detection results [71]. The four selected reflectance images therefore had a separate truth file associated with each. We cropped the images to match the scene and image size of our simulated images where each was approximately 250 $\times$ 350 pixels, This gave us a total of 350,000 pixels to use for analysis.

The portion of the SHARE 2012 experiment that was designed for subpixel target detection used two targets - green and yellow wood panels that were 0.3m x 0.5m in size. The green panels were placed on a grass background, and the yellow panels were placed on an asphalt background. The targets were placed in semi-random positions at least 2m apart to ensure that each pixel had at most one target instance. This produced a target area of $0.155m^2$, and for an average GSD of 1.22m, the expected target fill fraction was approximately 10%. Figure 5.9 shows WASP images and ground photographs from [55] showing the target placement and the experiment designed for target detection analysis.

The truth data that was used to calculate the utility metrics were first estimated using a spectral angle mapping tool in ENVI [72] using the bands 4-97 (400.32nm - 849.3nm). These values were compared to independently derived truth data for one of the images, and a mask was used to reject any "positive" values found by the angle calculation tool outside of the target area. This method of estimating the truth data likely eliminated many of the pixels with very small target fill fractions as positives, but it was found to be a sufficient truth map for comparison since most of the pixels within the target area were likely positive.

5.7.3 Cross-validation using simulation and perfect truth data

To generate the synthetic spectral images, we used existing simulation files used from the comparative studies between the real and simulated images, and made some modifications. Table 5.1 shows the parameters used in the simulation along with the real image collection data. These parameters were selected to produce GSD that were similar to the real images and the same number of bands, bandwidth, and similar spectral resolution.

(a) Ground image showing placement of green wood panels.

(b) Ground image showing placement of yellow wood panels.

(c) High resolution WASP imagery of scene used for subpixel target detection.

Figure 5.9: Images from [55] for visualization of SHARE 2012 experiment setup to collect SpecTIR HSI.

Table 5.1: Comparison of simulation parameters to real image collection data.

Parameter	**DIRSIG**	**SpecTIR**
Sensor Altitude	1923m	936m (average)
Focal Length	23mm	23.1mm
GSD	0.99m	1.22m (average)
Sensor Type	Pushbroom	Pushbroom
Time of Collection	09/25/12 11:57	11:00-14:00
Spectral Bandpass	400.32 - 2452.81 nm	same
Bandwidth	6 nm Gaussian	3 - 9 nm
Pixel Pitch	11.96 μ m	30 μ m
Geo-location	42.9° N 77.76° W	42.54° N 77.46°W

The scene in the simulation was designed to be representative of the area in the real image, and not an exact replica. The materials of interest such as the targets and the background were represented using the field spectral measurements described in Section 5.7.2, but other materials in the scene were represented with existing spectral material files that may or may not have had the same reflectance as the materials that were present in the real image scene.

Since the real images we used were not georectified, the distortions due to variations in the roll, pitch and yaw of the airborne platform in these images led to variations in the truth data. The original simulation files that existed for this scene assumed georectified images, and so did not contain these variations. For our purposes, locational variation was added to simulate the platform movements that caused the distortions that would vary the truth maps. The modifications were made to the platform simulation file to mimic not only the locational and rotational noise of the platform movement, but also small gradual changes in the flight path. These gradual directional changes simulated slight adjustments that a pilot may have made mid collection to stay on the flight path.

Figure 5.10 shows the progression of developing the simulated images, starting with one of the real images shown in 5.10a. An image that was generated using the existing simulation files is shown in Figure 5.10b. Figure 5.10c shows a subset scene with added locational and rotational noise of the platform movement. Figure 5.10d shows an example of the final simulated image after the changes in the platform movement noise and flight path was added to resemble the real images.

We generated 12 different variations of the scene adding different platform movement effects. Each of the images were 250 $\times$ 350 pixels to produce a data size of 1,050,000 pixels. This generated a range of TAs and different true positive pixel locations within the scene. The distortions caused a change in the location of the target present pixels as well as the abundance values. We made an assessment of the truth data distributions by examining the images alongside the truth map they were associated with. Figure 5.11 shows an example DIRSIG image and truth map combination. Figure 5.11a shows a closeup of the scene location where the green and yellow wood panels were placed in the simulation. Figure 5.11b shows the associated truth map where the target locations and abundance follow the distortions of the scene. The green pixels in 5.11b correspond to the green wood panels and the blue pixels correspond to the yellow wood panels. Pixels with higher intensity are also pixels with higher TAs. The distribution of the TAs changed from image to image due to the

(a) A SHARE 2012 SpecTIR image of the scene used for the sub-pixel target detection experiment. Shown using three bands - R(650nm), G(550nm), and B(450nm).

(b) A simulated image of the Avon, NY scene generated with no motion noise as georectified image. Shown using three bands - R(650nm), G(550nm), and B(450nm).

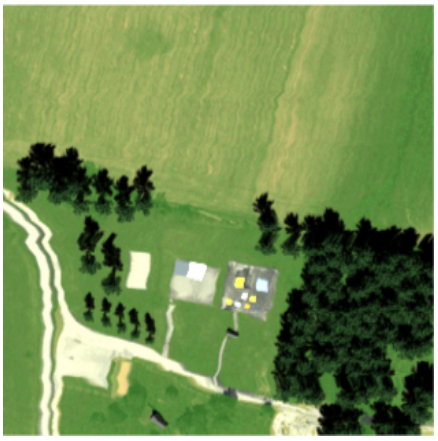

(c) A simulated image of the same scene generated using DIRSIG. Shown using three bands - R(650nm), G(550nm), and B(450nm).

(d) A simulated image of the same scene generated using DIRSIG. Shown using three bands - R(650nm), G(550nm), and B(450nm).

Figure 5.10: Images illustrating process for developing simulated image to produce variation in target abundance similar to real images.

(a) A closeup of the scene generated where targets were placed.

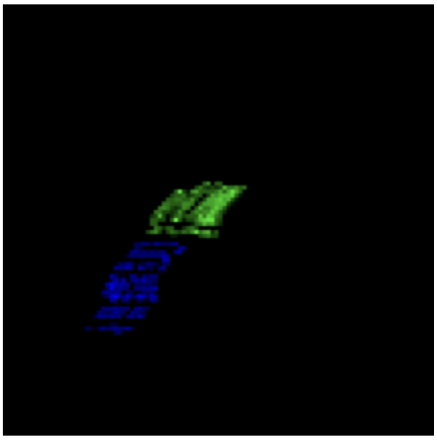

(b) Truth map generated alongside the simulated images.

Figure 5.11: Closeup of scene and truth map used for target detection analysis of DIRSIG generated data.

modifications made to the platform movement.

Shot noise was added to the radiance images, then converted to reflectance for target detection as a post-processing step for the simulated images. The noise was calculated by multiplying the radiance values of the noiseless synthetic image at each pixel and band ($f(i,j,k)_{sim}$) with a random number that had a Gaussian distribution, zero mean, and unit standard deviation ($g(i,j,k)$). This value was scaled by the SNR we wished to produce which was $SNR = 20$, to match the noise modeled in FASSP and described in Section 4.4.3. This step was necessary to ensure proper comparison could be made between the simulation and real image data that we expected to have noise sources not only from the published detector characteristics but also from other undefined sources.

5.7.4 Band Selection Results

The resulting utility values for the four band selection methods were comparable. Also, the trends for the FASSP results, simulation, and real data were congruent. The green targets that were placed in grass was a difficult detection case while the yellow targets placed in asphalt was an easier case. Figure 5.12 shows example ROC curves generated for the SHARE 2012 data using all the bands, as described in the previous

section, and 10 bands selected using BOTS. All the images available were combined, then the target present pixels and target absent pixels were split randomly into 8 folds to calculate statistical variations in detection performance.

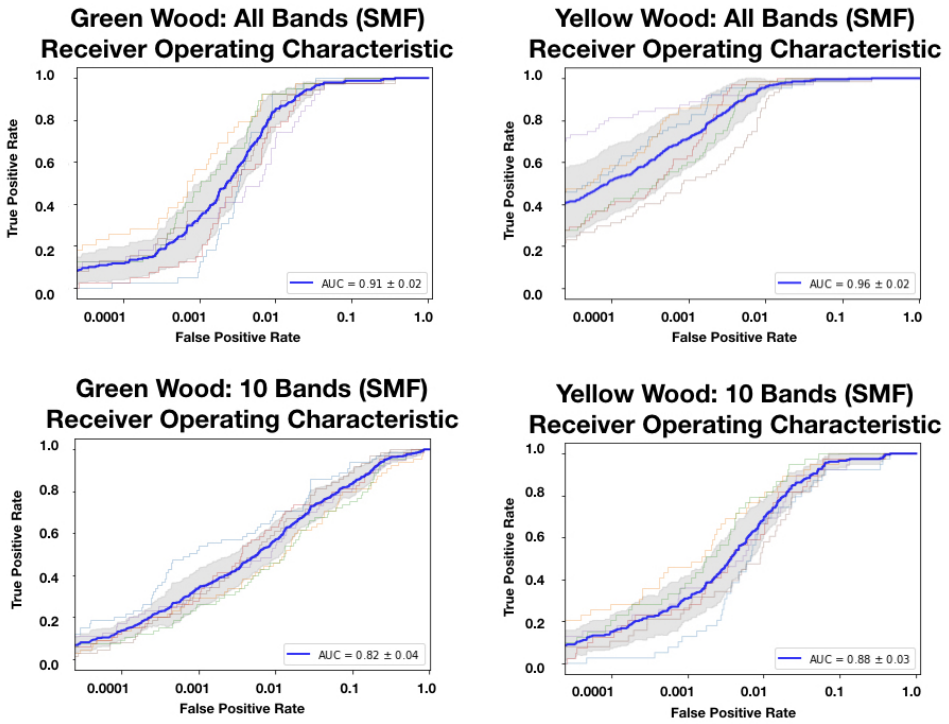

Figure 5.12: ROC curves of the SHARE 2012 data for the two targets shown for all bands and for 10 bands.

The split data was used to calculate the FPR, TPR, and AUC for each fold. The 8 folds generated 8 different ROC curves, which were then used to calculate a mean ROC curve with standard deviations. The figure shows the individual results for the two targets with the dark blue line showing the average ROC curve, and the gray area showing the standard deviation.

The ROC curves for the DIRSIG data had a similar shape but with a smaller standard deviations. The spectral similarity value that was calculated for the yellow target compared to the asphalt background was 0.5614. The spectral similarity value for the green targets compared to the grass background was 0.2144. This indicates that the grass and green wood panels have similar spectral reflectance signatures as opposed to the asphalt and yellow wood panels that are dissimilar. Furthermore, for most

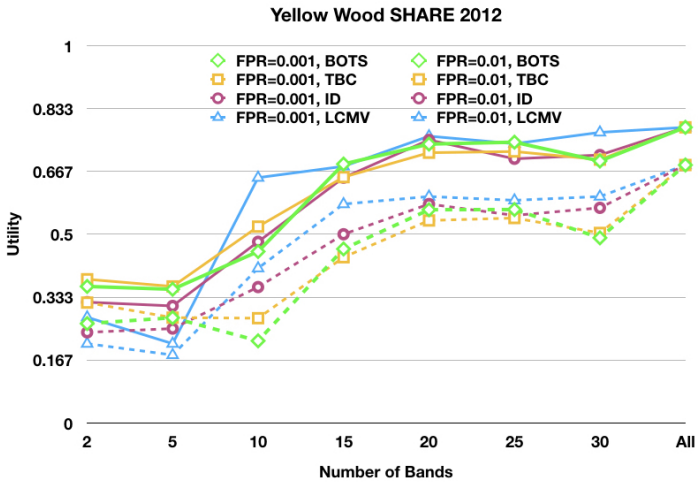

Figure 5.13: Utility values for yellow wood targets using SHARE 2012 data.

of the wavelengths, the green wood panel is darker than the grass, with a lower reflectance except at a few wavelengths as was seen in Figure 5.8a. The yellow target on the other hand had a higher reflectance value at almost every wavelength than its background as was seen in Figure 5.8b.

To compare the three methods used for utility assessment and prediction, we summed the TPR values at the same FPR values we used for the FASSP analysis. For the FASSP analysis a range of TPR values were calculated for FPR values of 1.0×10^{-1} to 1.0×10^{-5}. The utility values were then calculated for the ROC curves at 2, 5, 10, 15, 20, 25, and 30 bands for the yellow target. Then for the green target, the utility values were calculated for 5, 10, 15, 20, 25, and 30 bands. Figures 5.13 - 5.15 shows the utility values at each of the number of bands for the yellow wood target. Figures 5.16 - 5.18 shows the results for the green wood target.

The utility values of TBC and BOTS were were similar for the range of bands and two targets we examined. The utility values of ID and LCMV were higher in some instances, especially for higher number of bands, but neither stood out when comparing the results from all three data sources, and the trends for both targets were mostly in agreement. The results from the other target detection algorithms (SAM and ACE) that were used used for the DIRSIG and SHARE 2012 data did not have any significantly differing results or trends from the SMF and CEM methods.

The detection performance due to reduction in bands compared

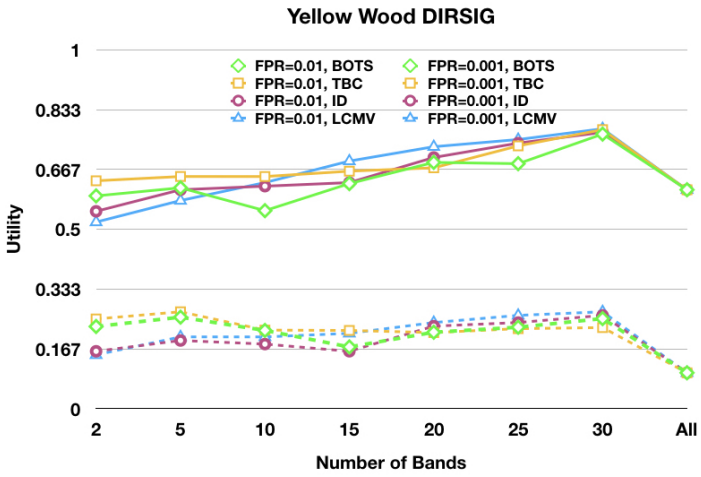

Figure 5.14: Utility values for yellow wood targets using DIRSIG data.

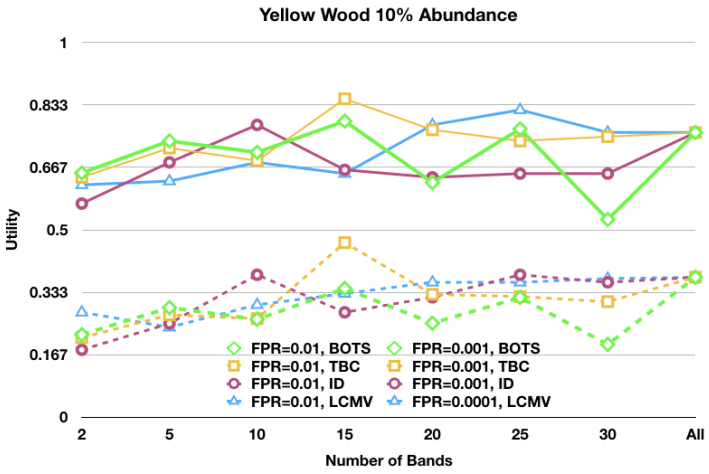

Figure 5.15: FASSP prediction of utility values for yellow wood target at 10% abundance.

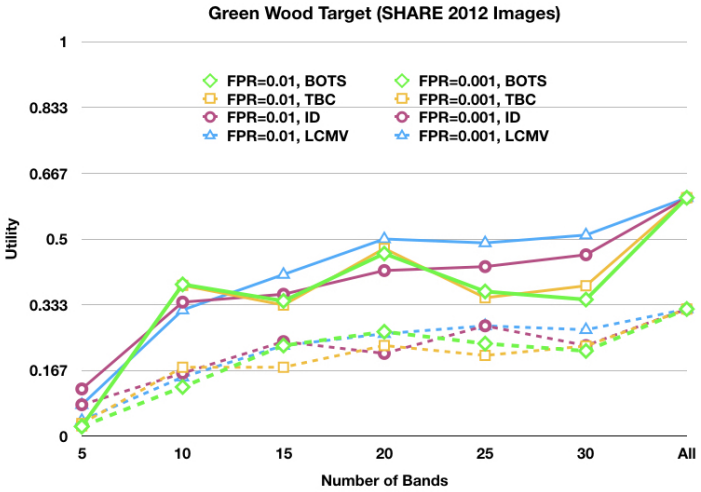

Figure 5.16: Utility values for green wood targets using SHARE 2012 data.

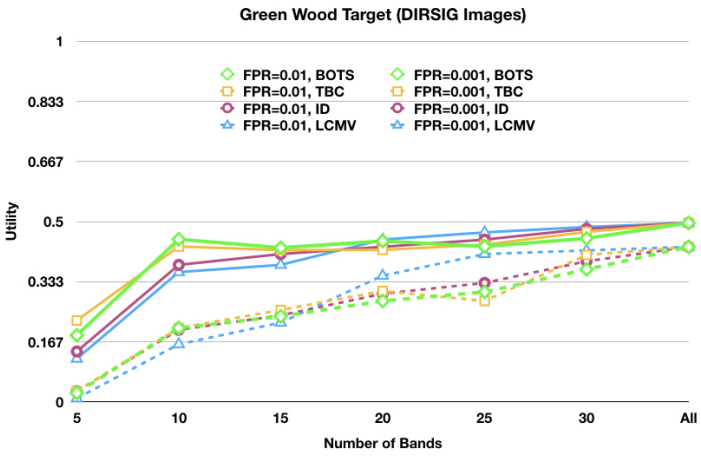

Figure 5.17: Utility values for green wood targets using DIRSIG data.

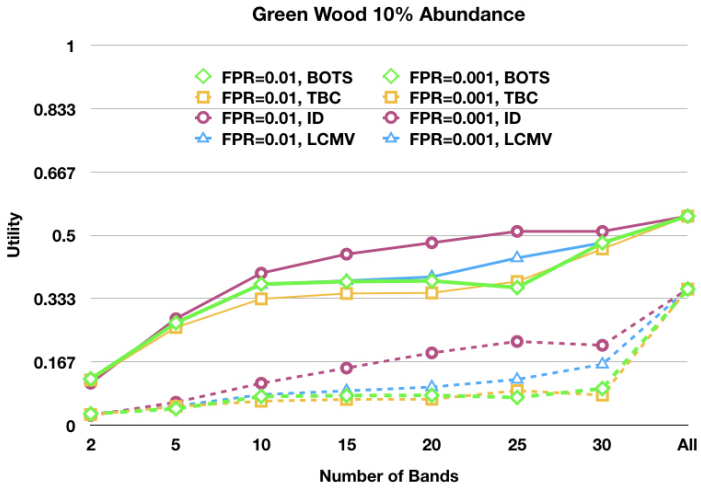

Figure 5.18: FASSP prediction of utility values for green wood target at 10% abundance.

to all the bands for the yellow target was not significant, and there was detection even when using 2 bands. For the green target, the difference in utility was significantly higher when using all the bands as opposed to the reduced number of bands. This indicated that reducing the number of bands in difficult detection scenarios had a more significant effect, regardless of the band selection method.

For the yellow target, there was some differences in trends for the predicted utility, simulated data, and real data. The prediction showed limited effects on utility for the yellow targets for reducing the number of bands even as low as 2 bands. The simulated data showed an improvement in utility for reducing the number of bands. For the real data however, while the utility value was similar up to 20 bands, but with less bands, utility decreased significantly. Unlike the FASSP or DIRSIG results, the utility value using all the bands remained the highest.

Differences in the results between the real data, analytic prediction, and the simulated images show that there are non-linear effects that was not accounted for in the models. Analyzing the cause of the differences between the models and real images is beyond the scope of this research, but perhaps a subject for future studies.

Table 5.2: Computation times in seconds for each band selection method for the number of bands.

Computation Time (s)				
Method	**2 Bands**	**10 Bands**	**20 Bands**	**30 Bands**
BOTS	9.143×10^{-5}	1.022×10^{-4}	9.988×10^{-5}	1.002×10^{-4}
TBC	2.113×10^{-2}	2.126×10^{-2}	2.081×10^{-2}	2.132×10^{-2}
ID	5.019×10^{-2}	0.2012	0.3488	0.5001
LCMV	0.8344	0.7749	0.8122	0.8779

5.7.5 Computation Time

The computation time of BOTS was significantly less than any of the other band selection methods. The primary advantage of this method was not only that it was simple and did not need background information, but also that the computation complexity was independent of image size or number of bands needed. The computation complexity of TBC was also independent of number of bands to select or image size, which signals its potential for implementation in a CubeSat as an alternative method if background information is known. The computation time for these two methods would change based on the spectral resolution of the input reflectance file, but since all the bands considered were ranked as part of the computation, there was no change in computation time whether we were selecting 5 or 30 bands. The primary advantage of TBC over BOTS was that it could use digital counts to select the best bands and so for some operations, the bands for an opportunistic target could be selected mid-mission.

The other two methods, although considered state of the art for detection performance using the data that these methods were tested on, was found to have complexity dependent on image size as was with LCMV or number of bands selected as was with ID. Both of these methods, while they had acceptable performance finding 9 bands for the HYDICE Forest Radiance I data, were found to have unacceptable computation time when the image size increased from 145 $\times$ 145 pixel to 250 $\times$ 350 pixels, or when 30 bands were selected instead of 9. Table 5.2 shows the computation time of each method for this dataset and the number of bands selected.

5.7.6 BOTS Validation Summary

In analyzing the predicted results using FASSP, simulated images, and real data, we found that their results were congruent, thus validating its use for band selection in future studies. The computation time to select bands using BOTS was found to be acceptable for use on a small on-board CPU of a miniature satellite system. While TBC showed potential for similar use in a compact system, it was still 200 times slower to compute than BOTS. The state of the art band selection methods were appropriate for image exploitation of HSI with fixed bands, following collection when there was no constraint on computational resources. However, given the congruence in results both when comparing the prediction, simulation, and real data as well as for performance, we found that BOTS was a method that could select bands for target detection without significant impact on performance that was computationally feasible for use in a compact spectral imaging system with adaptive band selection capabilities.

5.8 Summary

When using HSI for any application, dimension reduction was often employed, and for subpixel target detection, band selection was prevalent for this purpose. In the design of a compact system with adaptive band selection capabilities, we not only needed to consider performance but computation time as well. Existing methods however, required background information which may not be available prior to collection, and often had unacceptably complex calculations. All the methods for dimensions reduction so far were designed for post-collection processing for hyperspectral imaging systems with fixed bands. In developing this method, we met the requirements in the design of an adaptive spectral imaging system capable of adaptive band selection to save data handling costs. In this chapter we presented the validation of BOTS as a band selection method, that could be used for an adaptive and compact system with limited on-board computational capabilities.

The validation method for BOTS also had the purpose of validating the combined use of FASSP and DIRSIG images for analyzing spectral imaging system designs. In finding that the prediction and assessed results from the simulated images were congruent to results from real images, we can surmise that the parameters selected for the models and the simulation techniques adequately captured real world phenomena

that affect subpixel target detection.

"Don't forget - no one else sees the world the way you do, so no one else can tell the stories that you have to tell."

- Charles de Lint, *The Blue Girl*, 2004

6

Overall Project Approach

The goal of this project was to determine if the use of spectral images collected by a compact system was the appropriate tool for a given mission. In developing this process for practical use, the critical answer we answered was:

Is the use of a compact spectral imaging system for this target in this area of operation feasible, given our computational resources and other assets available to confirm or deny its presence?

We comprehensively analyzed spectral image utility in the design phase as well as the operational phase. We accounted for the design costs of improving a system figures of merit, but also the operational costs once deployed. We created a workflow to using FASSP to find the saturation points in the utility trade space for four system parameters - TA, B_{opt}, SNR, and Γ. B_{opt} and Γ are metrics we developed as part of this research. B_{opt} was described in Chapter 3 Section 3.5, and Γ is described in 6.5.2 as one of the scene complexity measures we use. We designed a scene with targets to replicate the operational context for a set of GSDs based on the TA saturation points and target size. We generated the spectral images based on the saturation points, selected bands, added noise, and generated ROC curves using three different target detection algorithms. We described the simulation validation process in Chapter 4 where we

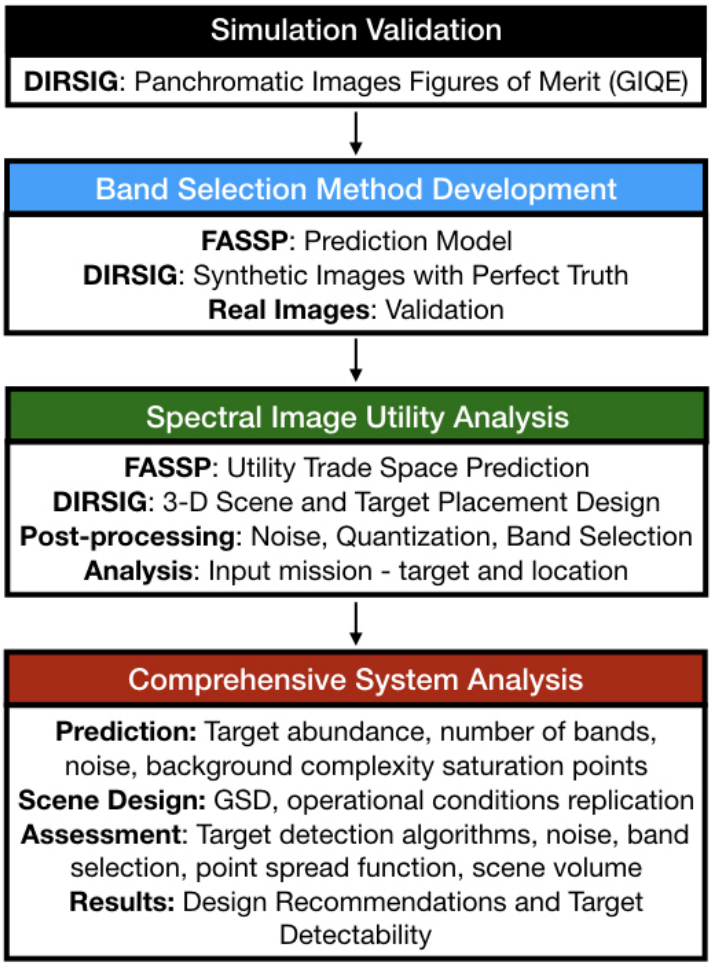

Figure 6.1: Diagram showing the progression of developing the methodology to comprehensively analyze spectral image utility.

developed the techniques and selected the simulation parameters that adequately captured real world phenomena. We used BOTS that was described in Chapter 5 to select the bands. In this chapter we describe the overall methodology for comprehensive system analysis to facilitate the design of compact spectral imaging systems with adaptive band selection capabilities. Figure 6.1 shows the progression in developing this process.

6.1 Analysis Methodology

The use of FASSP to predict spectral image utility was introduced in the band selection method validation. Simulating an entire scene composed of various materials and attributing each object with the material reflectance was found to be intractable to study a range of parameters that affected spectral image utility. With the simulation method, while it was possible to control each portion of a system design, their study as separate parameters that affect utility was cumbersome. An analytic model that used first and second order statistics of a target's spectral signature compared to the background, was a tractable and efficient way to analyze different components of the trade space separately as they related to utility. For example, studying the TA as related to utility required the design of a scene and the generation of thousands of images when using DIRSIG that took on the order of days to generate using high performance computing. Using FASSP, computing the trade curve of TA vs utility was a single analysis that took a few minutes using a personal computer.

While it was possible to provide the necessary input in the FASSP model to create a background with varying complexity that affected utility, replicating the interactions of different objects in a scene as they would in the real world using FASSP was cumbersome. While it was possible to model a uniform background in the real world such as the open ocean or a vast desert using FASSP, any other scene with man made objects such as an urban scene or even a scene with a rapid change between two backgrounds such as a coastal scene was a challenge to model using FASSP. Therefore the analytic model and the simulation tool were both used to comprehensively analyze the spectral image utility trade space.

We used FASSP to test various target detection scenarios for four key parameters that affected target detection, and DIRSIG to design a parallel scene for assessment. The analysis was divided into two separate studies. The first was a simple scene analysis using an open ocean scene with orange and black lifeboat targets. The purpose of this study was to compare the FASSP predictions to the DIRSIG image assessments. The open ocean was an ideal uniform background that could be characterized with a few spectra, and spectral images of the real world scene were not expected to have any significant differences. The expectation was that for this simple scene the differences between the FASSP predictions and assessment using DIRSIG images were going to be minimal. Any significant differences would indicate a need to modify the simulation techniques and modeling parameters.

Once the simple scene analysis and the results from both the prediction and assessment were congruent which indicated that the simulation techniques and modeling parameters were selected and adequately developed, we were able to analyze a complex scene. Two background compositions and analogous scene types were selected for the complex scene analysis. Using FASSP we composed a grass background and sand background. The four trade variables (TA, SNR, B_{opt}, and Γ) were tested for the sand and grass background compositions.

Using DIRSIG, we designed a complex heterogenous scene with geometry effects and pixel to pixel variations. The assessment allowed the study of the operational conditions encompassing subpixel target detection and its effect on utility. We wanted to study the relationship between system parameters such as GSD, PSF, or smear and how the operational conditions affected their impact on utility. Table 6.1 summarizes the parameters analyzed using FASSP and DIRSIG along with their analysis.

6.2 Prediction

We used FASSP to generate trade curves and find critical points or saturation points in the trade space for the selected targets and background. Saturation points in the trade space were points where increase/decrease in a tested metric no longer contributed to utility. The scenes for analysis were divided into two types - simple and complex. An open ocean scene was used as a simple scene example. This was the type of scene that could be modeled using a few material spectra and the variations that contribute to background complexity was going to be from the inherent variations of the materials as opposed to scene geometry or various objects within a scene. We describe this scene as homogeneous because the background composition does not change from pixel to pixel and it has limited 3-D geometry effects. In the prediction, four water spectra was used to compose the background of the open ocean scene. Two target materials were selected for testing the simple scene case - the orange life vest and black tire. Since the purpose of analyzing the open ocean scene was to compare the simulation and assessment results to the prediction, only the TA component was analyzed.

A saturation point was found for the orange target using the open ocean background spectra, and it was compared to the results found for sets of simulated spectral images with corresponding median target fill fractions. The black target in the simple scene was used to get a

Table 6.1: Summary of FASSP and DIRSIG experiments for different target detection scenarios to analyze spectral image utility.

FASSP	
Spectral Similarity Value (SSV)	Test two background composites and four targets to calculate their spectral separability.
Analysis: Utility trends for 8 different spectral similarity values	
Target Abundance/Pixel fill fraction (TA)	Generate trade curve for range of target abundances for each target and background combination to find saturation points.
Analysis: Find points for different target and background combinations where perfect detection is achieved.	
Number of bands (B_{opt})	Select bands using BOTS to find saturation points if any for a range of 2-30 bands.
Analysis: Find effects of reducing the number of bands on utility.	
Signal to Noise Ratio (SNR)	Generate ROC curves for various noise values
Analysis: Test effects of various SNR values on utility.	
Background Complexity (Γ)	Use various background compositions to generate range of background complexity values.
Analysis: Introduce novel metric to measure background complexity for uniform large area scenes and test its relationship to utility.	
DIRSIG	
Mean Target Abundance (TA_{mean})	Use various methods for placing targets in scene to generate distribution of abundances.
Analysis: Effects of real world situations on target abundance and its relationship to detectability.	
Scene Volume (V_{scene})	Separate complex scene into subset scenes with various scene complexity values.
Analysis: Effects of 3-D geometry and scene complexity on detectability.	
Detectability (ξ)	Combine mean target abundance values and scene volumes to analyze their combined effect on utility.
Analysis: Introduce novel metric that can tractably capture operational effects on real world target detection missions.	

comparison for targets that were likely to be categorized as one that was operationally unfeasible or suitable for use with compact spectral imaging systems. Therefore for the simple ocean scene, the TA metric was tested with the orange target that was likely to be categorized as a mission suitable for compact imaging systems and the black target that was expected to an unsuitable mission, to compare the predicted utility and assessed utility.

For the complex scene, two sets of background compositions were selected along with four targets for a total of 8 mission sets. Four types of grass background spectra were used to compose one of the sets in the complex scene analysis and four spectra of various sand and light soil materials were used to compose the other set. These were background spectra that were congruent to a suburban scene where the open areas and the bulk of the background materials were composed of grass, or a desert scene where the bulk of the background was composed of sand and light soil. Each of the four targets were tested against these background compositions to find saturation points.

To quantify background complexity for utility prediction, we first combined the mean spectral signature of the materials that composed the background (Eq. 6.1)

$$\mathbf{B} = \sum_{i=1}^{K} a_i \cdot \mathbf{b}_i \tag{6.1}$$

and the spectral variations of the material signatures by calculating the total inverse covariance (Eq. 6.2)

$$\Sigma_T = \sum_{i=1}^{K} a_i \cdot \Sigma_i \tag{6.2}$$

to get the background complexity value (Eq. 6.3).

$$\Gamma = \sqrt{|\mathbf{B}^T \cdot {\Sigma_T}^{-1} \cdot \mathbf{B}|} \tag{6.3}$$

Here the total number of materials that the background is composed of is K, and $\mathbf{b}_i$ is the spectral signature of one material's reflectance data and Σ_i its covariance. The spectral signature and covariance are scaled by the fractional amount (a_i) of that material presence in the background composition. The background complexity value (Γ) is used in the complex

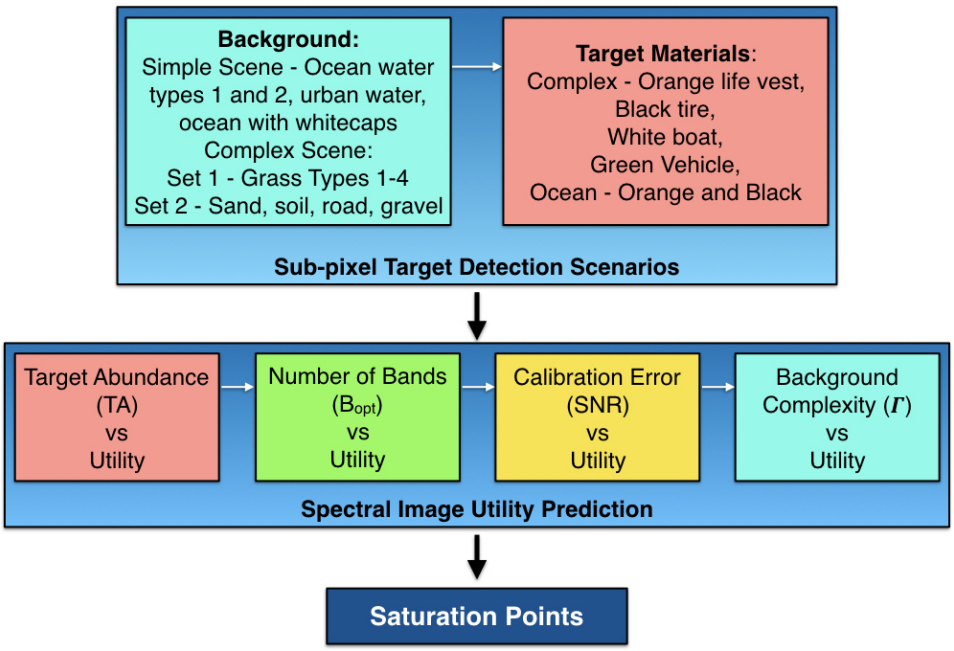

Figure 6.2: Prediction process.

scene analysis to parameterize the background effects on utility. Varying the background composition of materials and their fractions generated a limited range of Γ values. This value was used because the spectral signature of a material was considered in the quantity of Γ, and brighter materials increased complexity and darker materials contributed less to Γ. What this metric does not account for is the degree of heterogeneity in a scene that can be caused from macro changes in a scene content. Examples are urban scenes where the contents of the scene changes from man-made buildings, roads ect. to forest or sand or a coastal scene where it can change from the ocean to land along with man-made construction. This metric accounted for was intrinsic variation within a homogeneous scene.

Figure 6.2 diagrams the process for predicting utility. It outlines the target materials that were tested and the background materials that were combined to produce a comparable scenario to the simulations. In order to narrow the trade space to allow the analysis to be tractable, each metric was traversed through their saturation points. It shows the four components in the trade space and the order in which they were analyzed to find each of the saturation points.

The first metric analyzed was the TA. Using all the bands, the

lowest TA value that produced perfect detection was determined to be the saturation point. This value then was set as a fixed input in the analysis for the number of bands. For the 8 scenarios, a range of the number of bands from 2-30 were analyzed at the TA saturation points. If a scenario did not reach the TA saturation point, a 100% target fill fraction was used as the input value. The saturation point for the number of bands were then set as the input for the noise analysis and background complexity analysis. While the background complexity metric was not expected to reach a saturation point, it was the last metric that was analyzed at each of the saturation points to find a relationship between utility and Γ. Using the saturation points, a set of initial recommendations for a system design could be formed for range of acceptable error values along with a operational feasibility decision. These system design parameters were then used to simulate a spectral imaging system that could be used for assessment.

6.3 Spectral Image Simulation

The process for developing the simulation techniques to ensure the spatial characteristics of an image were adequately captured were explained in Chapter 4, and we used these techniques to generate the spectral images also. The panchromatic image simulation was extended to spectral image simulation by generating multiple bands with a narrow detector response function, which were then combined to produce the spectral image. Figure 6.3 shows the simulation and assessment process for analyzing the imaging system parameters and solidify the recommendations formed by the prediction process. In this section we describe the simulation techniques to design the scenes to replicate spectral images that would be collected in real operations.

6.3.1 Spectral Imaging System Parameters: Sensor Characteristics

In order to simulate an adaptive spectral imaging system that could collect any number of bands at variable spectral resolution and wavelengths, individual panchromatic image were generated where the detector response function was tabulated to be similar to that of the adaptive filter. The platform height was kept constant at 350km, but the focal length was changed as needed for each set of simulations to produce the desired GSDs.

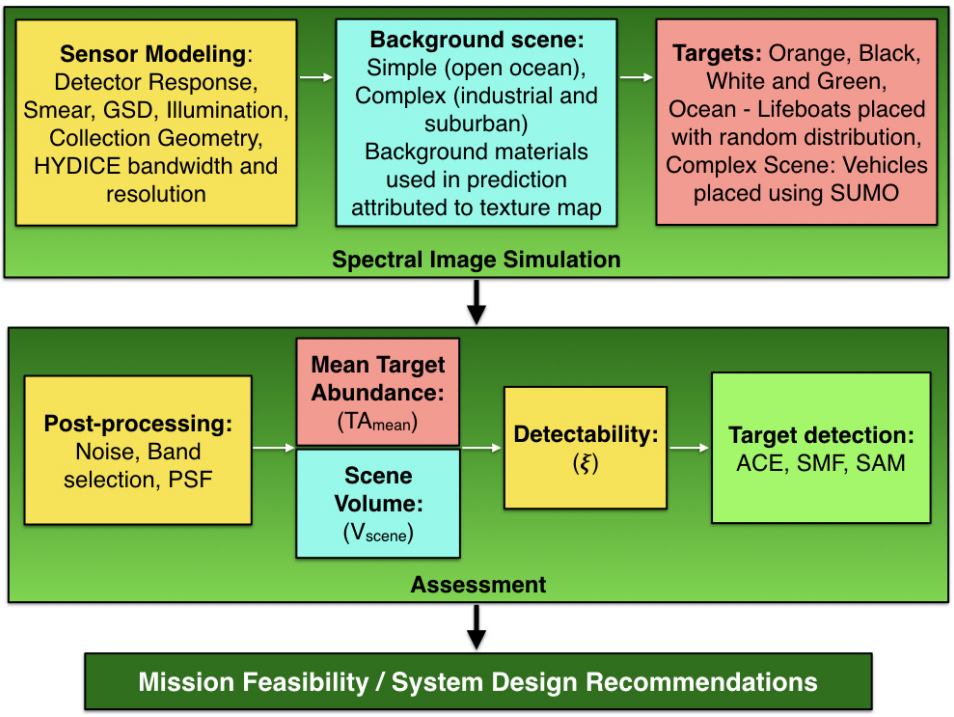

Figure 6.3: Simulation and assessment process.

We were able to generate a range of TAs that resulted from the GSD, target shape/size, and distribution due to the relative location of the target to the detector's pixel pitch. The simulation process encompassed a TA distribution that resulted from the target size, location, and GSD. A small GSD could increase TA, but so could a large target. With simulation, we generated spectral images that would be collected of targets with varying sizes by an imaging system with a fixed collection geometry relative to the platform. Table 6.2 shows the imaging system parameters that were modeled in the simulation.

Figure 6.4 shows two images that illustrate the scaling effects of the simulated sensor that produced subpixel target image for the open ocean scene. This figure shows the change in spatial resolution that produced the range of TAs. The image on the left represents a pixel in the image on the right. The two images generated the same scene, but the size of the image on the right was 500x500 pixels, modeling a sensor with 20 times the focal length as the image on the right producing a spatial resolution of 1m GSD. The image on the right was generated at a spatial resolution of 24m GSD and its size is 25x25 pixels that represent the same

Imaging System Parameters		Notes
Aperture Diameter	44.5mm	F/2.4 - F/7.1
Effective Focal Length	105-315mm	10-15m GSD
Spectral Bandwidth	400-1000nm	97 bands
Spectral Resolution	6.19nm	Narrow Response Function
Pixel Pitch	4.5 μm	Square detectors
Integration Time	0.6 ms	Smear from 45° orbital velocity
Sensor Altitude	650 km	
Look Angle	Nadir	
Solar Angle	Zenith	
Platform Velocity	7000 m/s	

Table 6.2: Parameters selected for the optical system simulation.

scene as the 500x500 pixel image on the left. Using the two images, the TA of the pixel shown can be estimated to be 10-12%. This type of comparison was used to design the simulation sets for the open ocean to generate a range of TAs using the simulation. This type of scaling was also used to select the GSD and target types in the commplex scene to ensure there was sufficient distribution of target fill fractions of the TA saturation points found each of the targets the simulation.

6.3.2 Scene Development: Target and Background

We used the four types of reflectance spectra used for the FASSP background compositions in the DIRSIG simulations as well. The four spectra of the background types - open ocean, desert, and suburban - were attributed to the scene's base image that was used as a texture map of the material reflectance files. Figure 6.5 shows an 8-bit image of the texture map that was used to create variations in the ocean spectra. Each of the 4 spectra was assigned to a pixel intensity level between 0-255. The intensity level of the pixels in the texture map would assign the corresponding mixtures of materials. For example, if the Ocean Type 1 spectrum was assigned the pixel intensity of 100, and Ocean with Whitecaps spectrum was assigned the pixel intensity level of 200, then a pixel in the texture map with a pixel intensity value of 175 would mix the output image spectra with 25% Ocean Type 1 and 75% Ocean with Whitecaps. The material map was given a spatial GSD scale to which its pixels would correspond to. If the material map was given a GSD of scale of 1m, then for a 30m image, 30 of the material map pixels would be mixed, producing

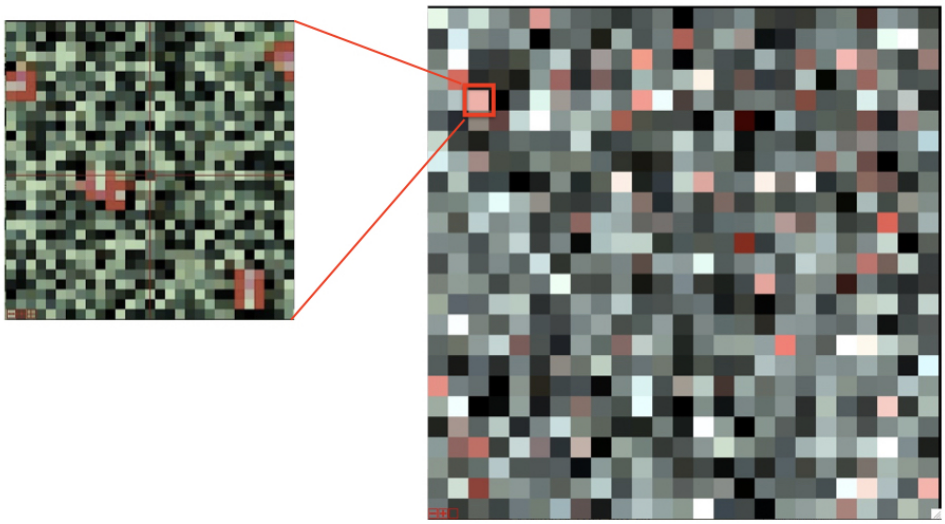

Figure 6.4: Scaling example to generate spectral images with subpixel targets. Image shown with three bands at R(650nm), G(550nm), and B(450nm). Image on left is a 1m GSD resolution image of the open ocean scene that is then generated at 24m (image on right).

a mixture that could potentially consist of all 4 spectra in one pixel with varying amounts. In this way we were able to produce a scene complexity that was comparable to a real image and corresponded to the prediction model background.

The ocean scene was an example of a simple scene with uniform background. For the complex scene analysis we used existing an simulation of Trona, CA. We generated imagery of an existing scene of Trona, CA that is routinely used for studies involving spectral images [73]. Figure 6.6

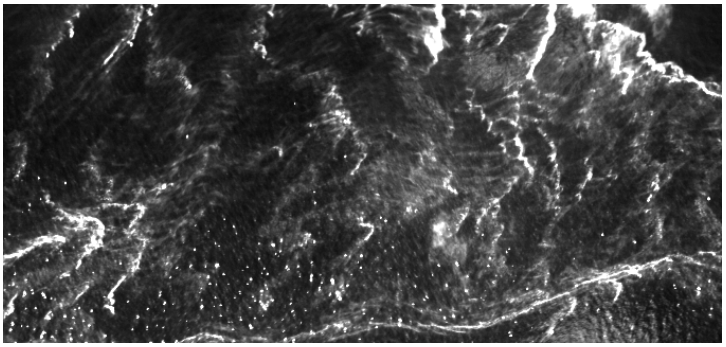

Figure 6.5: Texture map used to mix ocean spectra.

Figure 6.6: High spatial resolution image of Trona, CA as a desert scene.

shows a synthetic image of this scene generated as a desert/industrial area where the primary background materials it is composed of are sand, dirt roads, and gravel. The DIRSIG scene of Trona, CA was originally an industrial desert scene with the material map attributed with various sand and soil spectral reflectance curves. This attribution was modified to match the reflectance curves used in with the FASSP model to generate a background that was comparable.

This scene was then modified to resemble a suburban scene by attributing the background material map with the four grass spectra used in the FASSP model. The two types of scenes of the same area was used to place different types of vehicles, each attributed with the four target spectra. This scene contained 3-D geometry of various types of buildings, other vehicles, trees, and objects normally seen in a complex scene. All of these 3-D objects were attributed with spectral reflectances of the materials the objects were usually made of. The objects were large enough to create shadows that could affect subpixel target detection performance.

6.4 Assessment

The spectral images generated by DIRSIG are always noiseless with perfect edges. Smear from platform movement however was incorporated as shown in Table 6.2 and the edges were blurred accordingly. Post-processing was necessary to incorporate noise and additional effects due to the optical PSF. For the panchromatic images generated for the validation study, the PSF was incorporated into the simulation. However, for the spectral image analysis, each band was convolved with a model of the PSF. This allowed modification of the PSF implementation to study its effects on utility in future studies. Once the PSF was implemented, the bands were selected using BOTS for each target. Once the bands were selected, three target detection algorithms were used to generate ROC curves for each of the simulation sets. The assessment process involved ensuring proper incorporation of key real world effects that may affect utility and the use of three target detection algorithms on the simulated spectral images.

6.4.1 Post-processing

To ensure we sufficiently captured the key real world effects that affected detection performance, the images that were generated had to go through post-processing. The first step in preparing the data for assessment was to select the bands, not only because this was a critical component of the envisioned operational process, but as a dimension reduction step for computation. With the reduced amount of data, the computation time to add noise, apply a point spread function, and finally to assess utility was reduced. The same bands that were used for the prediction process were also used for the assessment process. The second part of the post-processing was to add noise. We added noise to the image to account for the shot noise. Detector noise was not captured in order to develop a process that could parameterize the SNR as it related to utility. However, future studies can fold in the entire noise calculation process that can determine the effects of any fixed noise on utility. Then final processing step was PSF implementation.

6.4.2 Noise

Noise was added to the radiance images, in the form of shot noise as a post-processing step of the simulated images. The amount of noise added

produced variance in each data point to simulate images with average SNRs of our selection. The noise was added by multiplying the simulated image value at each pixel and band ($f(i,j,k)_{sim}$) with a random number that had a Gaussian distribution (gi,j,k) of zero mean and unit standard deviation. This value was scaled by the SNR we wished to produce and our first selection was $SNR = 20$ (Eq. 6.4).

$$n(i,j,k) = g(i,j,k) \cdot f(i,j,k)_{sim}/SNR \tag{6.4}$$

Then we added the noise to the simulated image pixel value to produce the noisy image (Eq. 6.5).

$$f(i,j,k)_{noisy} = f(i,j,k)_{sim} + n(i,j,k) \tag{6.5}$$

The output units of the simulated data was in radiance ($\frac{W}{m^2 sr}$) in 32-bit floating point format. We wanted to convert this into what we expected from a small CubSsat.

To the radiance values, we first added a gain and bias. The gain slowly increased from the shortest wavelengths to the center wavelength (620nm), then decreased down to the highest wavelengths. This added more gain to the wavelengths between 550-700nm, and less to the lowest and highest wavelengths. There was some additional randomness added between the 5-10% gain that changed from pixel to pixel and band to band.

This selection of gain values while arbitrary, was a simple method to mimic quantization noise in real images. The bias added was a random number centered at 2.5% with up to 0.1% fluctuation. We essentially converted each band from radiance to digital counts by incorporating a gain and bias to the 32-bit floating point value, then converted it to an 8-bit integer. Figure 6.7 shows example curves of the gain and bias that was added to the simulated radiance data, then converted into digital counts. This was done to test and develop a process that could potentially allow calculating detection probabilities on board the CPU if the target reflectance signature was forward modeled, converted to radiance, then to digital counts. The entire process from start to finish may be outside the scope of this project, however the addition of quantization noise to the data gives us detection statistics that at least account for this phenomena in addition to the shot noise.

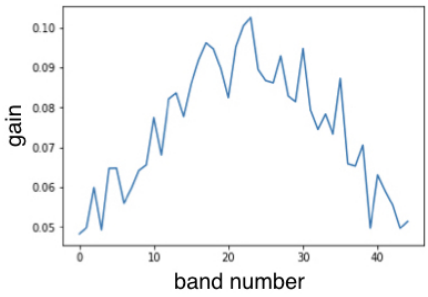

(a) Example curve of gain incorporated into to simulated radiance images.

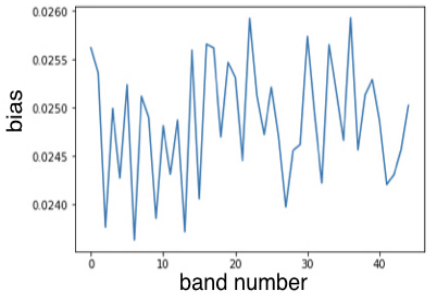

(b) Example curve of bias added to simulated radiance images.

Figure 6.7: Gain and bias added to convert simulated radiance images into digital counts.

6.4.3 Band Selection

Following the development and validation of BOTS, we used this method to reduce dimensionality and generate the data needed to find B_{opt} for each mission. For each target, we generated a trade curve at a specified FPR for utility vs number of bands. The curve of possible B_{opt} values were first predicted using FASSP then assessed using DIRSIG images. This allowed us to analyze the trade space for the number of bands for various mission scenarios. This also allowed us to find data points to reveal potential relationships between GSD, target size, background, target type, and the number of bands. For example, we found that the orange target placed in a dark background such as the open ocean, could not only be detected at low TAs, but could be detected using less than 5 bands.

The range for the number of bands we tested was from 2 to 30 bands. The number of bands beyond 30 was not analyzed because the operational feasibility for a compact system's processing architecture to collect and ingest this amount of data seemed unlikely. We determined that for the automated image exploitation architecture of the miniature satellite imaging systems, our recommendation for a target that needed more than 30 bands was unfeasible for compact imaging systems and better handled by larger existing, hyperspectral systems.

6.4.4 Point Spread Function

Once the bands were selected, and noise was added, we convolved the image with a point spread function. We applied a blurring kernel to the noisy image using a discrete Fourier transform that replicated the effects of an airy disc from a circular aperture [74] [75]. The airy disc radius was set to $0.5 \cdot \lambda/\lambda_c$ for the 15m GSD images, $1.0 \cdot \lambda/\lambda_c$ for the 10m GSD images, and $1.5 \cdot \lambda/\lambda_c$ for the 5m GSD images. Here λ is the center wavelength of each band, and λ_c is the selected wavelength representing the overall sensor spectral band range, which in order to coincide with our panchromatic study was set to 500 nm [48]. This in effect simulated the optical resolution effects that coincided with Q numbers of 0.5, 1.0 and 1.5 [6].

6.5 Spectral Utility Analysis

We selected two major components related to subpixel target detection that could be analyzed for their relationship to spectral utility using the simulated images - mean TA and scene complexity. In the simple scene analysis we compared the predicted utility for a range of TA values to sets of simulated images that had a range of median TAs. For the complex scene there were two scene types - desert and suburban - and they were both divided into subsets, each with different scene complexity. The vehicle targets that were placed in the scene also generated different TA distributions in these sets due to their size. In this section we describe how different TA distributions were generated, how scene complexity was quantified and how they were combined to produce a detectability metric.

6.5.1 Target Abundance

We examined a range of TAs for different types of targets for the open ocean scene and the complex scene. In the open ocean scene, the target size and GSD was kept constant in the analysis, so the range of TAs were generated by changing the number of targets in the scene. This produced a predictable increase in the TA values as the number of targets increased. This was to isolate the TA distribution in the simulation for comparison to the predicted utility values. Figure 6.8 shows the workflow of generating images for a range of TAs to examine utility saturation points in the simple scene analysis.

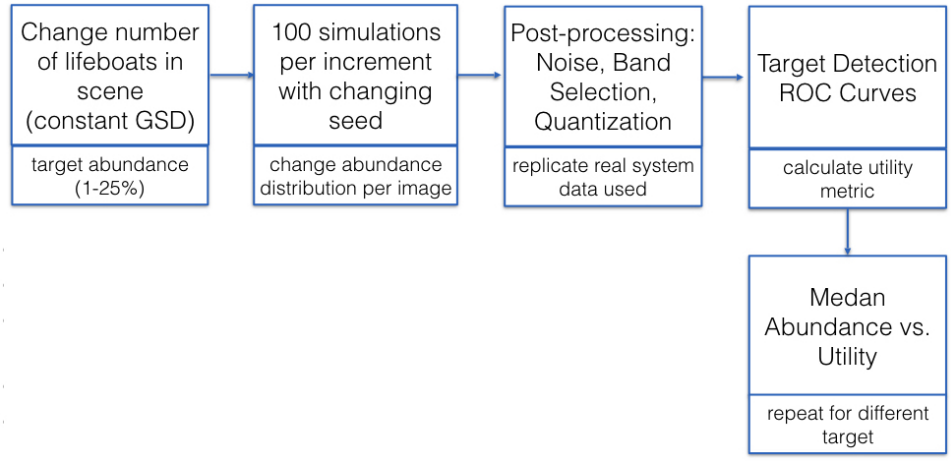

Figure 6.8: Process for generating images with varying target abundance within scene with orange lifeboat targets.

For the orange lifeboats in the open ocean scene, 15 simulation sets sets were generated, each with an increasing number of lifeboat. With each image being 25x25 pixels the first set had 1250 lifeboats in the scene - an average of 2 lifeboats per pixel. This produced a median abundance of 1% TA. For each subsequent set, 625 lifeboats were added to the scene. While the increase in the median abundance was not linear, overall the first 10 sets generated a TA distribution in the range of 1-8%. Using the 15 sets of orange lifeboats placed in the open ocean scene, we generated a trade curve for utility vs median TA.

For the complex scene, the TA was calculated for each set of images, but the values were a result of the simulation design. The distribution of TA was a combined result of the various target sizes, the spatial location of the target within the image, and GSD. The mean TA (TA_{mean}) values were used to analyze the complex scene and the distribution methodology of the targets generated a range of these values. However, the distribution was deliberately designed to reflect real world operations and so there was no direct correlation in the TA_{mean} to any simulation design parameters.

For the black lifeboats, because we needed a higher TA to study utility, we placed a higher number of lifeboats in the scene. Furthermore, in order to avoid contamination effects when computing the ROC curves using the three target detection algorithms, we also generated images without any lifeboats and combined these images with the target images.

The target absent images and target present images were combined at a ratio of 10:1 where a data set consisted of 10 negative images per positive image or a total of 625,000 negative pixels with 65,000 positive pixels. The goal was to generate a range of median TAs from 40-80%, and so 25,000 lifeboats were placed in the scene in the first set, and 6250 lifeboats were added to the scene in each subsequent set.

Using the simulated images to examine TA, we used the simple scene to compare the assessment results to the predicted utility. With the complex scene, we used simulation to replicate the operational aspect of subpixel target detection to generate images that would be collected in real operations.

6.5.2 Scene Complexity

We examined scene complexity using the simulated images by using the four background material spectra that was used in the prediction. The spectra used for the background composition of the FASSP experiments were used to attribute these material spectra into the texture maps of the simulated scenes. For the open ocean scene there were no other complications inherent in the the scene, and so this provided a congruent simulated scene to the background composition of the prediction model.

For the complex scene, the material maps were associated with the four background material spectra in a similar manner to the simple scene, but the entire scene was also divided into 9 subsets in order to vary the complexity contributions from other objects that were present in the scene. Figure 6.9 shows a subset scene with a higher complexity value due to a large number of other objects within the scene that contribute to the background. This is a scene that could not be adequately characterized using Γ. Figure 6.10 on the other hand, shows a subset scene with lower complexity with only a small number of objects and materials that contribute to the background. The background spectrum calculated from this scene for target detection, would not deviate significantly from the background complexity value (Γ) calculated using the four spectra that the base image texture map was associated with.

In order to quantify the measure of scene complexity for the simulated images, we used the scene volume that was calculated using endmembers. This was a geometric approach to quantifying scene complexity by representing spectral data as described in Section 5.2. In this case, the endmembers of the spectral image formed the vertices of the

Figure 6.9: High spatial resolution subset of DIRSIG rendering of Trona, CA as suburban scene shown as example of scene with high degree of complexity.

Figure 6.10: High spatial resolution subset of DIRSIG rendering of Trona, CA as suburban scene shown as example of scene with low degree of complexity.

space occupied by the data, and the volume of this space was calculated [8]. The volume of the convex set was enclosed by the endmembers present in a scene, which was calculated directly if this number is known. If the number of endmembers present was not known, the volume of the scene was calculated by finding the parallelotope using the Gram matrix of the image between pixel i and j (Eq. 6.6).

$$\mathbf{G}_{i,j} =< \mathbf{x}_i, \mathbf{x}_j > \tag{6.6}$$

The Gram matrix was the same size as the spatial dimensions of the image. The determinant of the Gram matrix was the square of the volume of the paralleotope for k endmembers (Eq. 6.7).

$$V_k = \sqrt{det(\mathbf{G})} \tag{6.7}$$

The volume was calculated for a range of endmembers from 3 to N, where N was the maximum number of endmembers to calculate determined by the user. After calculating the volume for several scenes using various values of N, the highest endmembers found was 12. We set N to 15 endmembers in order to encompass the highest number of endmembers found in all the subset scenes.

The maximum volume determined scene complexity for the input images (Eq. 6.8).

$$V_{scene} = max(V_k|_{k=1}^{N}) \tag{6.8}$$

A scene with a larger volume consisted of a higher number of materials and brighter materials and thus had higher complexity. What this method accounted for is not only the complexity due to the number of materials present but also the spectral signatures of the materials in a scene. Higher volume was consistent with brighter materials that have higher spectral reflectance values, while darker materials occupied less volume. Therefore, like the background complexity value (Γ), the scene volume (V_{scene}) was able to account for the brightness of the material's spectral signature which affects subpixel target detection. Furthermore, it was able to account for the heterogeneity of a scene. A homogeneous scene that is composed of a single material (even if it is bright) such as the vast desert, would have a low V_{scene} value. On the other hand, if a scene was heterogeneous such as a coastal scene, even if most of the materials present in the scene were dark, the scene would have a higher V_{scene} value.

6.5.3 Detectability

Another metric that was developed for this analysis is the detectability value (ξ) that combines the TA_{mean} value and the V_{scene}. A low TA_{mean} and high V_{scene} indicated a difficult detection scenario, and so these values are inversely related. We determine the detectability of a target for each simulation sets by relating these two values (Eq. 6.9).

$$\xi_{set} = \frac{T_{mean}}{V_{scene}} \tag{6.9}$$

The ξ values found for each set was normalized for comparison (Eq. 6.10).

$$\xi = \frac{\xi_{set}}{max(\xi_{set})} \tag{6.10}$$

A high ξ value indicated an easy detection scenario, and a low ξ value indicated a difficult detection scenario. In order to allow comparison, the ξ values calculated for each set were normalized. For the scene types and GSD, the calculated ξ were sorted and plotted against their assessed utility value. This value was used to ingest the effects of the target type, size, and location in the images generated by a system design to quantify detectability. It provided a range utility values that pointed to a combination of system design parameters for a given mission.

6.6 Target Detection

We implemented three different target detection algorithms for performance comparison - Spectral Angle Mapper (SAM), Spectral Matched Filter (SMF), and Adaptive Cosine Estimator (ACE). These algorithms were selected for their wide use, and because they formed the core of what many other target detection algorithms modified for their purpose. They were implemented to calculate the ROC curves for subpixel target detection [26]. SAM was selected as an example of a detection method that used the angle between a target and its background (Eq. 6.11).

$$\mathbf{r}_{SAM}(\mathbf{x}) = -cos^{-1}\left(\frac{\mathbf{s}^T\mathbf{x}}{\sqrt{(\mathbf{s}^T\mathbf{s})(\mathbf{x}^T\mathbf{x})}}\right) \tag{6.11}$$

This method used the spectral signature of a target ($\mathbf{s}$) compared directly to a pixel spectrum ($\mathbf{x}$) to determine the probability of a target's presence. ACE was selected because it was often accepted as the "state of the art" for subpixel target detection, especially for subpixel target detection. It also used the spectral angle between the target and background but incorporated the inverse covariance (Σ^{-1}) of the data to account for inherent variability of the pixels (Eq. 6.12).

$$\mathbf{r}_{ACE}(\mathbf{x}) = \frac{(\mathbf{s}^T\Sigma^{-1}\mathbf{x})^2}{(\mathbf{s}^T\Sigma^{-1}\mathbf{s})(\mathbf{x}^T\Sigma^{-1}\mathbf{x})} \tag{6.12}$$

SMF was selected for use because this was a method similar to the CEM. SMF subtracted the mean spectrum of the image from a pixel prior to comparing the target spectrum to the pixel, in order to determine the likelihood of a target's presence (Eq. 6.13).

$$\mathbf{r}_{SMF}(\mathbf{x}) = \frac{[\mathbf{s}^T\Sigma^{-1}(\mathbf{x}-\mu)]^2}{\mathbf{s}^T\Sigma^{-1}\mathbf{s}} \tag{6.13}$$

It assumed the target was an anomaly, and also incorporated the covariance to account for inherent variations in a scene. The CEM algorithm used in FASSP was similar to the SMF except that it did not subtract the mean spectrum of the image (Eq. 6.14),

$$\mathbf{r}_{CEM}(\mathbf{x}) = \frac{\mathbf{s}^T\Sigma^{-1}\mathbf{x}}{\mathbf{s}^T\Sigma^{-1}\mathbf{s}} \tag{6.14}$$

which made it appropriate for an analytic model that used first and second order statistics and did not have an image to calculate the mean spectrum from. The SMF and CEM were equivalent calculations adapted for the two types of data, to calculate the probability distributions of the target's presence.

The three algorithms were selected not only for their distinct detection mechanisms, but also as a control measure in the utility analysis. While the purpose of this project was not for algorithm comparison, using at least three different algorithms to assess utility shifted the dependence of the results on a single algorithm. Any anomalous result that were attributed mostly to a single algorithm and its method of calculation, could be reasonably discarded without further analysis. Algorithm selection depending on the target and background combination was another layer of complexity in assessing spectral image utility that in this

project we limited to only these three. However, future studies can expand on this dimension in the spectral image utility trade space.

6.7 Summary

Our overall approach to developing a process for optimizing a system design for various missions was to predict utility using FASSP, design a scene to simulate real world operational conditions, then assess utility from images generated to provide a mission feasibility recommendation or system design recommendations. We tested two different type of scenes - a simple scene of a open ocean and a complex scene of Trona, CA. The purpose of the simple scene was to compare and validate the congruence in results between the prediction and assessment. Then we tested a complex scene designed both as an industrial/desert scene and a suburban scene as an example use of this process for a potential real world scenario.

"Intuition is really a sudden immersion of the soul into the universal current of life."

- Paulo Coelho *The Alchemist*, 1988

7

Process Description

In this chapter, we present how the process described in Chapter 6 was used for a simple open ocean scene and a complex industrial/suburban scene. We first present the operational context in which we envision this process to be used and the motivation for selecting the target and background spectra. Then we describe the process for comparing the prediction and assessment steps. We then present the methodology of analyzing the trade space for the example mission scenarios in a complex real world scene to produce recommendations for the design of a spectral imaging system.

Figure 7.1 shows the steps for predicting then assessing utility, starting with the mission scenario as input. The prediction method parameterized four components of spectral image utility to find saturation points. Then the simulation was designed to generate spectral images from a system design based on the predictions, but also replicating the operational context of the mission. This allowed us to capture more real world considerations that would have been challenging using the analytic model. The we assessed the simulated images using three target detection algorithms after adding noise and selecting bands to generate a utility vs detectability (ξ) curve that was used to form the mission feasibility recommendation and to develop a set of system design recommendations.

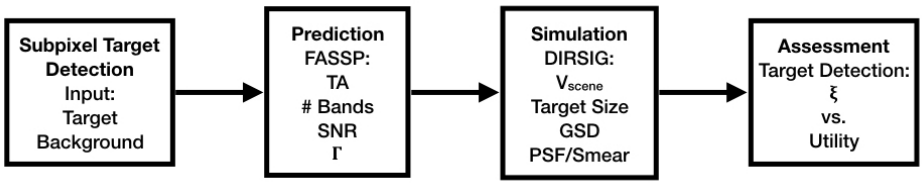

Figure 7.1: Diagram of approach to analyze spectral image utility starting with mission input.

7.1 Operational Context

When employing a compact spectral imaging system for subpixel target detection, the first question we asked was - *what is the target, and can we find it?* Given the limitations of compact systems, we needed to first decide if what we were looking for was an appropriate target [4]. In order to wholly analyze the utility trade space for the compact imaging systems, we considered not just the design decisions for optimizing an imaging system, but also the operations following the deployment of the system. Figure 7.2 shows where the utility analysis fits within the overall process from design to deployment of the systems. It shows the design phase starts with a desired set of mission scenarios that are analyzed using the prediction and assessment process that produce system design recommendations for feasible missions. Once the imaging system is deployed, is selected which bands to collect based on the tasking, which we assumed was processed using automation and machine learning algorithms. Once operational, the compact system could tip and cue other systems to confirm or deny the presence of a target.

7.2 Targets and Backgrounds

We selected four targets - black, white, orange, and green. The spectral reflectance data for these materials were obtained from ground measurements using a spectrometer. The black target measured the spectral reflectance of a black tire, and was an example of a difficult (if not impossible) target to find. It served as our floor or worst case target. The white target used measurements from a white boat, and it served as our ceiling, or best case target where its spectral reflectance for most of the VNIR spectrum was high. The green target used measurements from a

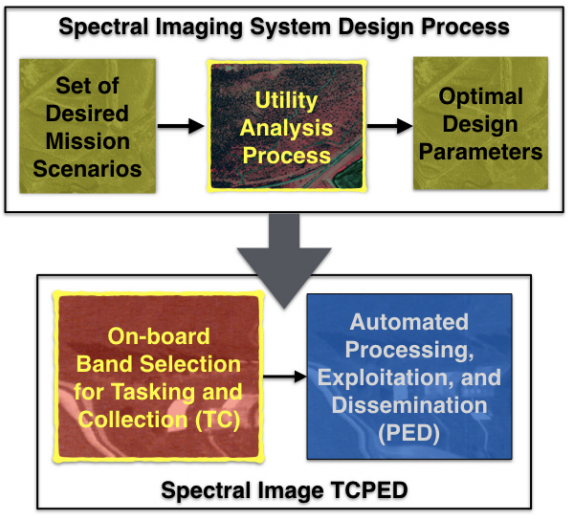

Figure 7.2: Envisioned use of optimization process within the imaging system design and operation.

green BMW, and was an example of a realistic, but difficult target to detect. The orange target used measurements from a orange life-vest, and was an example of an easy target. Figure 7.3 shows the mean spectral reflectance curves of the four materials along with the standard deviations of the spectra.

The initial background selected for the simple scene analysis was an open ocean scene which was used as an example of the ideal background to test target detectability. It was ideal because it was uniform, and could reasonably be modeled using a single material reflectance curve. It was also dark across the VNIR spectrum, and so any contribution to the sensor reaching radiance would be from the target. In order to introduce realistic variability, we used four different types of ocean spectra to produce a background composite. Figure 7.4 shows the four mean spectral reflectance curves along with their standard deviations to compose the open ocean background. These were the four spectral reflectance curves that were attributed to the material map as described in Section 6.3.2.

The targets that were tested with the ocean background was the orange life-vest and black tire materials. The orange target was the easy target example, and the black target was the difficult target example to test for unexpected behavior in the spectral utility trade space. This background and the two targets were used for the simple scene analysis to compare the prediction and assessment methods. The open ocean scene

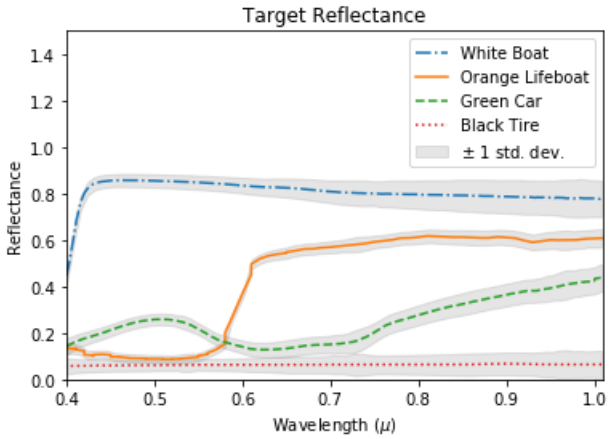

Figure 7.3: Target reflectance curves used for FASSP analysis and DIRSIG objects placed in scene. Also used to select bands.

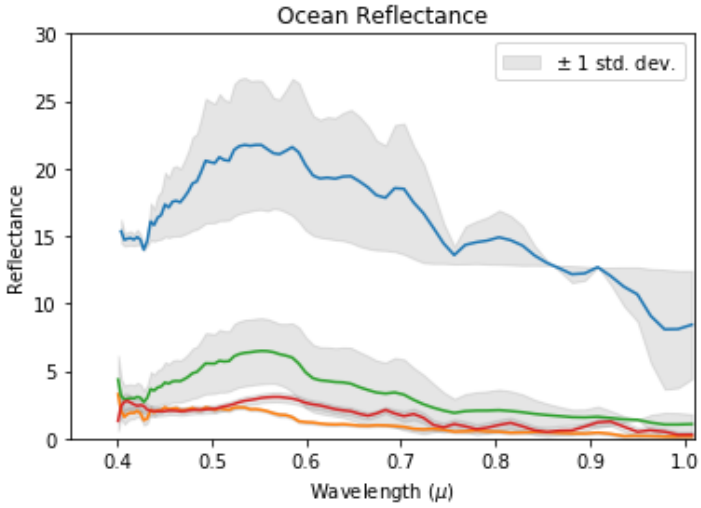

Figure 7.4: Background reflectance curves used to compose ocean background used for FASSP and DIRSIG scenes.

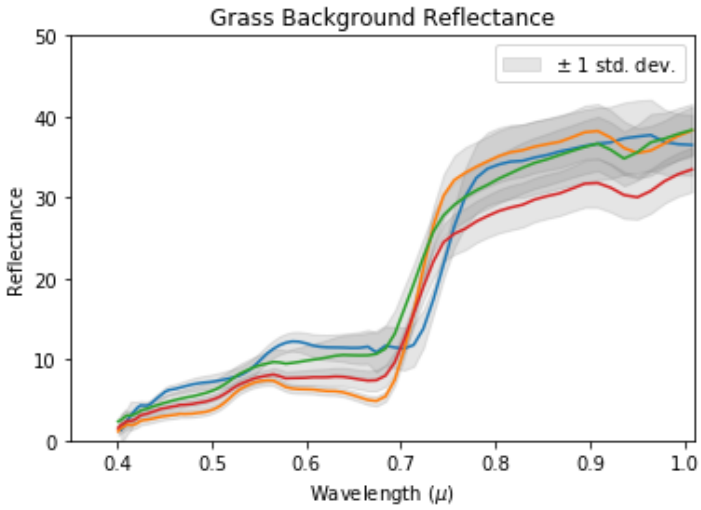

Figure 7.5: Background reflectance curves used to compose grass background used for FASSP and DIRSIG scenes.

was also an example of a real world scene that was homogeneous, and so could be characterized by the background complexity value Γ, described in Section 6.5.2 (Eq. 6.3).

The two background types selected for the complex scene analysis were sand and grass composites. They were selected for their prevalence in target detection missions, and because existing spectral reflectance files with sufficient variation data were available for use with both FASSP and DIRSIG. For the grass background, the measurements were taken from several areas, and the variations were attributed to their species or other environmental factors. Figure 7.5 shows the four curves that were used for the grass background composite in the prediction and also used in the simulation for the suburban scene. The four curves were attributed to the texture map as described in Section 6.3.2. For the sand background and the primary materials selected for the composite used in the prediction and the simulated desert/industrial scene were light brown soil, brown soil, gravel, and ocean sand. Figure 7.6 shows the four curves used to compose the sand background.

The two difficult and two easy targets were selected for their spectral contrast against two background materials we selected for the complex scene analysis. The orange and green targets were less spectrally distinct from the grass background, and the white and black target were less distinct from the sand background. Therefore we had both an easy

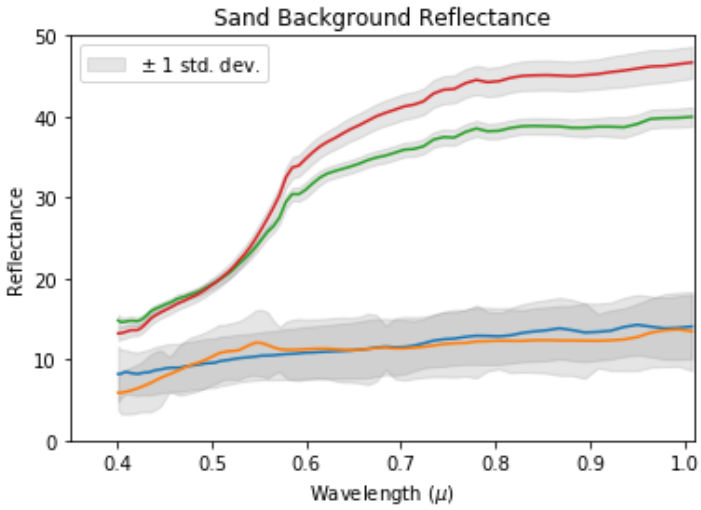

Figure 7.6: Background reflectance curves used to compose sand background used for FASSP and DIRSIG scenes.

and difficult target with relatively high and low spectral contrast to the two backgrounds. The SSV values were relative to the type of target, since the easy targets had higher SSV overall, since their reflectance magnitude was higher compared to the difficult targets.

7.3 Band Selection

We used the BOTS method to select the bands for each of the targets in our analysis [66]. In Chapter 5, the optimal coefficient for the green target, which was an example of a difficult target, was found to be $a = 0.2$. For the yellow target, which was an example of an easy target, the optimal coefficient was $a = 0.8$. Therefore, these were the coefficients that were used for the targets based on their detection difficulty. Figure 7.7 shows the normalized $\mathbf{z}$ values calculated. The bands that corresponded with the highest 30 $\mathbf{z}$ values for each target were used in the analysis. Details on the selection of coefficients and the list of best bands for all the target materials are in Appendix A.

For the prediction, the top 30 bands for each target was analyzed to generate the utility vs number of bands curve. This produced data that calculated B_{opt} values in the design phase for a range of utility values up to 30 bands. In the assessment phase that replicated the operational phase,

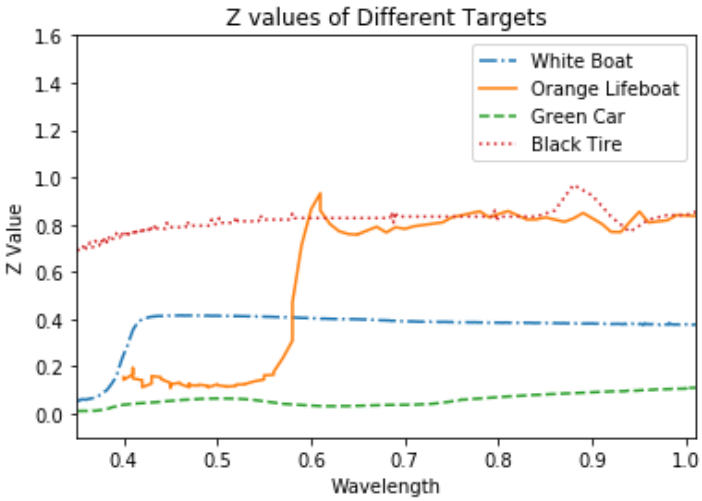

Figure 7.7: Normalized **z** values of band selection methods for the bands between 400-1000 nm. The highest **z** values are selected.

this data was used to select B_{opt} for the required utility that could provide a feasibility recommendation based on resource constraints. The details with potential decision points for required utility values are in Appendix B. Therefore B_{opt} was a metric that could be calculated in the design phase that would be used in the operational phase to drive feasibility decision driven by the utility requirements and computational resource constraints. For the assessment, any saturation points that were found in the number of bands were used, otherwise the maximum 30 bands were used. This reduced the computational requirements of our assessment.

7.4 Comparison: Simple Scene

The simple scene with the open ocean background was used for the comparison study because it was a scene in which the prediction and assessment were inherently congruent. The expectation was that there would not be any statistically significant differences between the utility of the prediction and the assessment due to real world characteristics of the scene. Any significant difference would indicate a need to modify the modeled parameters and simulation techniques. The comparison between the results from FASSP and DIRSIG served as a step to further validate the combined use of the two models for utility analysis along with the validation that resulted from the band selection method analysis described

Table 7.1: Table of parameters used for FASSP model and DIRSIG simulation.

Paramters	FASSP	DIRSIG
Target Abundance	0.1-20%	0-16%
Algorithm	CEM	SMF
Background	4 ocean spectra	4 ocean spectra
Band Range	$\approx$ 400-850nm	400-850nm
Number of Bands	45	45
Bandwidth	$\approx$ 10 nm	10 nm
SNR	$\leq$ 20	$\approx$ 20

in Chapter 5.

We started with the orange target, and using FASSP, the trade curve for various TA values was generated to find a saturation point. This result was compared to various sets of DIRSIG simulations that produced a range of TA_{mean} values. Table 7.1 shows the parameters used in both the FASSP and DIRSIG models for this comparison step. The SMF algorithm was used to generate ROC curves using the DIRSIG images that could be compared to the results from the CEM algorithm that was used in FASSP to calculate the detection statistics.

7.4.1 Prediction

The background was composed of different percentages of the four types of water spectra shown in Figure 7.4 to introduce variations similar to what would be observed in a real ocean scene. The sensor model we used as part of the prediction was for the HYDICE sensor which collects 210 bands in the range of 350-2500nm [61]. The DIRSIG simulation generated 45 bands at 10nm increments from 400-850nm. To match this, we used bands 4-94 which had approximate wavelengths between 400-850nm, and set the grouping function to 2 so these 90 bands were grouped into sets of 2, and analyzed as though they were 45 bands.

For the initial simple scene analysis, we used a single spectral reflectance curve to characterize the background. The Ocean Type 1 spectrum shown in Figure 7.4 was used for this purpose to test the best case scenario where background complexity was close to 0. Then the four types of ocean spectra were used to introduce some variations in the background complexity that would be analogous to the simulated images.

Table 7.2: Percentages of the four spectra used to compose background to introduce realistic complexity in ocean scene analysis.

Ocean Spectrum Type	**Percentage Composition**
Ocean with Whitecaps	10%
Ocean Type 1	60%
Ocean Type 2	20%
Urban Water	10%
Total	**100%**

Table 7.2 shows the background composition that was used to analyze the detection statistics to introduce realistic background complexity. This composition was used to introduce effects of whitecaps and spectral variations from other inherent real world complexities that affect detection performance.

7.4.2 Assessment

For the DIRSIG simulations, we generated a scene with a mixture of the four ocean spectra with orange lifeboats placed randomly within the scene. We used the simulation techniques described in [48] to produce spectral images where each band had a narrow spectral response function, and was generated separately each with its own PSF incorporated that was related to its center wavelength. The individual bands were combined to produce the final spectral image which consisted of 45 bands with 10nm spectral resolution with band wavelengths between 400-850nm.

Figure 7.8 shows a high spatial resolution image rendered at 0.3m GSD of the open ocean scene shown with bands R(580nm), G(550nm) and B(450nm). The large lifeboat placed in the corner produced a pure target pixel that was used in the target detection algorithms. Only one was generatd for each set to avoid contamination of the data. The images used to assess subpixel target detection performance were generated at 30m GSD to produce a range of target fill fractions. We generated 15 sets of simulations where an increasing number of lifeboats were placed in each set. Each set had 100 images that consisted of 625 pixels with a distribution of TAs that had increasing median values as the number of lifeboats placed in the scene increased.

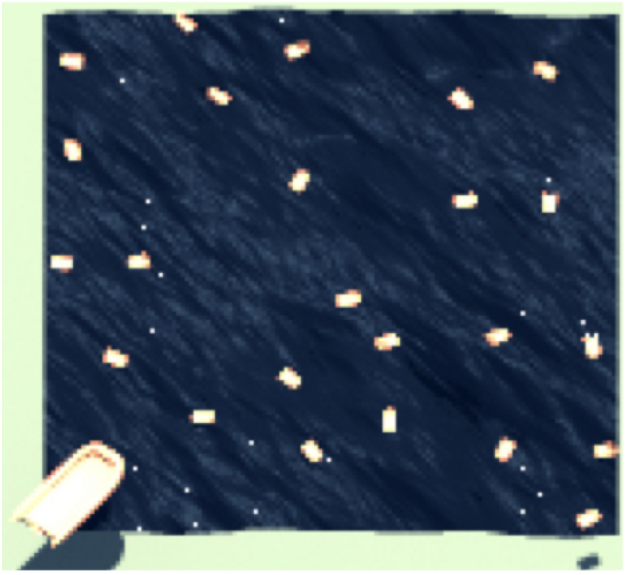

Figure 7.8: High spatial resolution image of open ocean scene rendered at 0.3m GSD using DIRSIG for visualization. Shown using bands R(580nm), G(550nm) and B(450nm).

This method of increasing the number of targets placed in the scene to increase TA was used to generate a relationship between TA and utility independent from GSD or target size. The GSD would have an effect on the PSF, and the target size would generate a distribution of TAs based on its relative spatial location to the pixel pitch. To mitigate these complications, the GSD and lifeboats sizes were kept constant. A single lifeboat was 2.0m x 1.5m which at $3.0m^2$ produced a TA of 0.5% per boat when rendered at 24m GSD. The median abundances were used to compare the assessed detection performance from the simulated images, to the range of TAs used to calculate the FASSP predictions.

7.5 Testing: Complex Scene

For the complex scene analysis, we use an existing DIRSIG scene of Trona, CA that was rendered both as the original desert/industrial scene and modified to be a suburban scene. The texture maps in the two variations of the Trona, CA scene were associated with the background spectra described in Section 7.2. Figure 7.9 shows the sets of target and background combinations that were analyzed for the prediction using

FASSP then the assessment using synthetic images of the two versions of Trona, CA. The background compositions we analyzed were the grass which was analogous to the suburban scene and sand which was analogous to the desert scene.

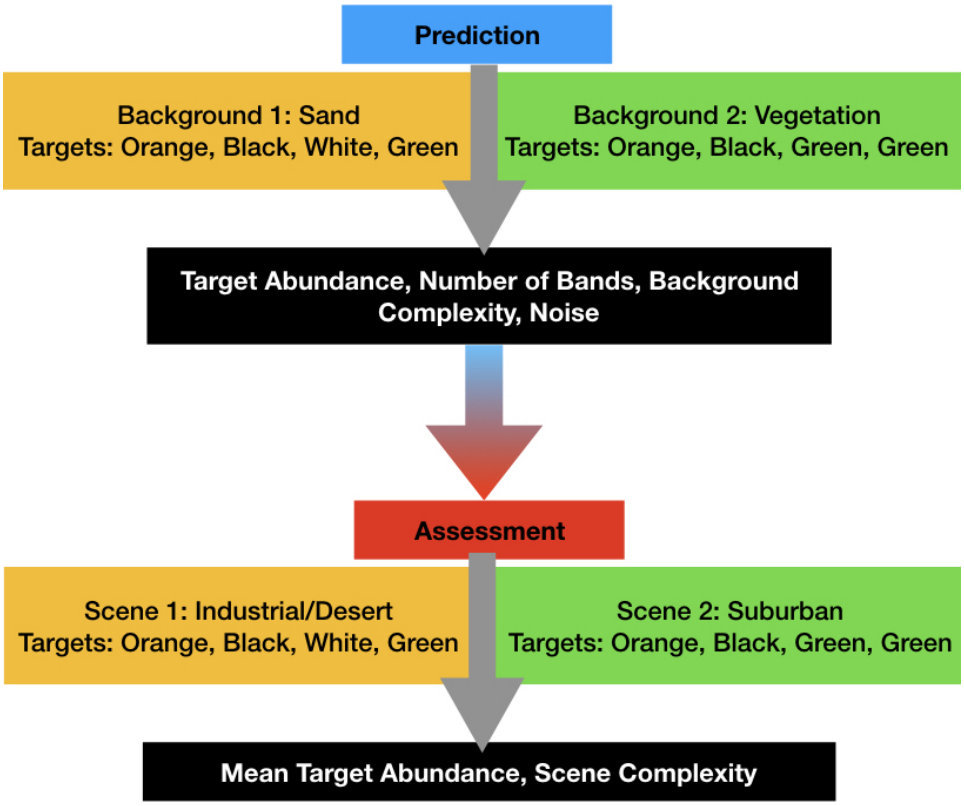

Figure 7.9: Target and background combinations tested for the prediction and assessment of utility.

The parameters we analyzed in the prediction process was TA, number of bands, noise, and background complexity. This was used to determine the GSDs for the simulation based on the size of the targets. Then the number of bands and noise predictions were used in the post-processing step to assess the predicted parameters. The background complexity analysis used to predict the mission feasibility recommendation that was verified by the assessment. The purpose of the complex scene analysis was to find changes between the prediction and assessment due to complexities introduced by real world operations. Using the simulation, we not only wanted to replicated images captured for moving targets, but also in a heterogeneous scene that could not characterized by a few spectra.

Table 7.3: Initial composition of the sand background.

Background Spectrum	**Percentage Composition**
Ocean Sand	10%
Dirt Road	60%
Light Dirt Road	20%
Gravel	10%
Total	**100%**

Table 7.4: Initial composition of the grass background.

Background Spectrum	**Percentage Composition**
Grass 1	10%
Grass 2	20%
Vegetation 1	40%
Shrubbery	30%
Total	**100%**

7.5.1 Prediction

Two backgrounds and four targets were used to predict utility for the complex scene. The input value for each subsequent parameter that was analyzed was the saturation points of the previous one. The initial set up for the prediction was with a noise parameter that produced a maximum SNR of 20, using *all* the bands in the VNIR spectrum, and background composites shown in Tables 7.3 and 7.4. The SNR maximum for each band was achieved by setting the relative calibration error value to 5%, and each band had varying SNR predictions based on the calculated radiance resulting from the target fill fraction and the background. The compositions of the two background types produced complexity values of $\Gamma = 0.17$ for the sand composite, and $\Gamma = 0.075$ for the grass composite. The set we reference as *all* the bands were those of the HYDICE sensor that were within the VNIR spectrum as described in Chapter 5. The first parameter that was analyzed was TA using this initial setup.

The saturation points for the TA was used as the input to analyze the number of bands. Each target and background combination was evaluated at its TA saturation point for the number of bands. The trade curves for each scenario was generated for the top 2, 5, 10, 15, 20, 25, and 30 bands that were selected for each target using BOTS. If an input scenario did not reach a saturation point, which we expected for the black target and possibly even the green target, we used the maximum TA

of 100% as the input value for analyzing the number of bands. We analyzed the effects of reducing the number of bands, and looked for possible saturation points reached with less than 30 bands. If a saturation point was found, this value was used to analyze the effects of noise. If a saturation point was not found with 30 bands, noise was analyzed using all the bands for the input scenarios. The noise effects were analyzed for a range of calibration errors that produced a maximum SNR of 5, 10, 20, 30, 40, and 50.

The background was analyzed at the critical points found for TA, number of bands, and noise. To do this, a range of background complexity values (Eq. 6.3) were generated by changing the composition of the four curves that were used for each background type. The percentages of each reflectance curve that were shown in tables 7.3 and 7.4, were changed to find different Γ values. This was done by setting the TA to 0, then taking the inverse of the signal to clutter ratio calculated by FASSP for each background composition. If the desired Γ value for this composition was found, then the TA and number of bands were set and tested for each input scenario at the critical points for the three parameters previously evaluated to produce a utility value.

The utility was analyzed for TA, number of bands, noise, and background complexity, to predict the points of interest in the trade space. The purpose of the prediction step was to determine the simulation parameter and form the initial mission feasibility recommendations. Each step in the prediction process was associated with some level of error. The TA saturation point changed depending on the initial background composition that was selected as well as the noise. The errors associated with the TA saturation point, then changed the trade curves for the number of bands. However, each subsequent step also served as feedback for each of the previous steps, thus making a traditional error propagation analysis challenging. Perhaps in the future, different initial values can be used for the prediction process to evaluate the error in the saturation points that lead to the final recommendations.

7.5.2 Assessment

To verify the predictions, the DIRSIG scene of Trona, CA was rendered both as a desert and suburban scene mostly composed of the four sand and grass spectral reflectance curves used for the FASSP analysis. This was an existing scene that was routinely used for studies with spectral images [73].

Table 7.5: Parameters selected for the optical system simulation.

Imaging System Parameters		Notes
Aperture Diameter	44.5mm	F/4.4 - F/13.1
Effective Focal Length	9.6 - 28.9mm	5-15m GSD
Spectral Bandwidth	400-1000nm	
Spectral Resolution	5nm	Filter Response Function
Pixel Pitch	4.5 μm	Square detectors
Integration Time	0.6 ms	Smear at (45°)
Sensor Altitude	350 km	
Look Angle	Nadir	
Illumination Angle	Solar Zenith	
Platform Velocity	7000 m/s	

Several vehicles of varying sizes were placed in the scene to produce the TA saturation points found for each mission scenario. These scenes were generated at three different spatial resolutions of 5m, 10m, and 15m GSD by changing the focal length. The simulations generated HSI, so all the bands that were needed for the targets were available.

Table 7.5 shows the simulation parameters that were used to generate the HSI. These deliberately replicated the panchromatic image simulation parameters described in Chapter 4 to ensure we captured key real world phenomena at least in the spatial domain [48]. The simulation techniques that were used for the panchromatic images were extended into the spectral domain by generating many bands using the same techniques, but with narrow spectral response functions centered at selected wavelengths. The HSI consisted of bandwidths that were similar to what would be collected by an adaptive spectral imaging system, but with center wavelengths that matched the HYDICE sensor.

The entirety of the existing scene was divided in to 9 subsets. Figure 7.10 shows an image of the existing scene rendered as a suburb, and the subsets it was divided into. The high spatial resolution image of the Trona, CA scene shown in 7.10 is 1m GSD, with a size of 4000x4000 pixels. At 5m GSD, to produce a single image that captured the entire scene or most of it would be 800x800 pixels. The computation time required to generate a single spectral image of this size was impractical. So the simulation was setup to generate a subset of the entire scene where a single image at 5m GSD was 300x300 pixels in size, covering a portion of the scene. Each subset scene was not only more computationally feasible to

generate, but had different scene complexities that were used as part of the analysis.

Figure 7.10: DIRSIG generated Trona, CA scene divided into 9 subset scenes.

Four types of vehicles were placed within the road network of the scene using Simulation of Urban Mobility (SUMO) [76] [77]. The SUMO model generated movement files with the locations of objects at different time increments similar to how vehicles would move in traffic. The sensor was modeled with a capture rate of 1Hz so there was one image per second of the scene with the location of the vehicles dictated by the movement files. Each image generated at a single time of capture that was different from an image at a different time, and when set to collect for 20 seconds, generated 20 different time correlated images [78] [79]. This allowed a single simulation run to generate 20 different images of a single subset scene with changing locations of the target. However, this setup did not incorporate platform movement as the mechanism for the changing images since this would require 20 images of different locations on earth, and we wished to keep the 9 subset scenes constant. What this replicated was 20

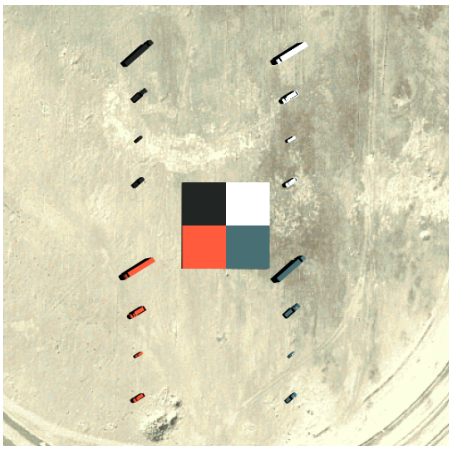

(a) High spatial resolution image of panels and vehicles attributed with each target material type.

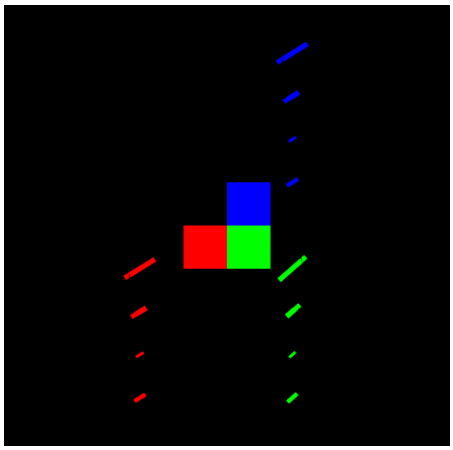

(b) Truth map of the image with array of vehicles for 3 out of the 4 targets generated with each image.

Figure 7.11: Panels and demonstration array of vehicles associated with each target material type.

different satellites taking an image with identical collection geometry of the same scene at 1 second intervals. It would be an impossible scenario to achieve in real life, but it was necessary to analyze the relationship between the imaging system parameters that produced the TA_{mean} distribution with a tractable scene complexity analysis.

Figures 7.11 shows a high spatial resolution image to demonstrate the material attribution and vehicle types that were used in the simulation. Figure 7.11a shows four calibration panels attributed with the four target materials, along with the four vehicle types attributed with them as well. Figure 7.11b shows the truth map of this image with the white material shown in blue, green material shown in green, and orange material shown in red.

The 18-wheeler was selected as a vehicle that was large enough to generate a full target pixel at 5m GSD. In a similar manner, the dump truck could produce up to a 85% target fill fraction, and the SUV and sedan up to 45%. The targets' ground location with respect to the detector's pixel pitch could spectrally split a target between several pixels. Therefore, the vehicles would not always produce the maximum TA, since the sensor was not "tracking" the vehicles. However, we expected this simulation technique to generate sufficient number pixels with these TA values to analyze detection performance of the green and black materials.

Table 7.6: Different vehicle types used in simulation, their dimensions and maximum target abundance possible when rendered at 5m GSD.

Vehicle Type	Size	Max TA (5m GSD)
Semi	4.5m x 20m	100%
Dump Truck	3.5m x 9.5m	100%
SUV	2.2m x 6.5m	85%
Sedan	1.7m X 4.5	45%

With this simulation setup, the different vehicle types could generate a range of TAs that changed due to spatial resolution and target size. This accounted for an operational component of subpixel target detection where target fill fraction was simultaneously characterized by semi-random components consisting of the ground location of the target relative to the sensor, spatial resolution, and target size. Table 7.6 summarizes the vehicle sizes and the maximum target fill fractions each type could potentially generate for images rendered at 5m GSD.

Figure 7.12 shows high spatial resolution images of a residential location in the Trona, CA scene to demonstrate vehicle placement using SUMO. Figure 7.12a shows the scene rendered as a desert scene, and Figure 7.12b shows the identical location rendered as a suburb. Figure 7.12b is displayed as a false color composite with the infrared wavelength displayed as red to emphasize the attribution of the composite grass spectral reflectance curves to the background. Using using SUMO to place the vehicles in the scene, where the movement files were selected at random, there was variation in the number of targets present in each image. There were 9 white and orange vehicles, and 15 green and black vehicles placed in the entire scene. For a subset scene, there was potential for none or several of a target to be present. However, on average, 1 white and orange vehicle and 1.7 green and black vehicles were expected per image. The additional green and black vehicles were added to increase the chance of obtaining higher target fill fractions since the TA saturation points for these materials were higher.

The spectral images of the two scene types were separated into 9 subsets, where the vehicles and movement file combinations were selected using a different random generator seed for each set. Each set generated 20 different time correlated images of the vehicles moving across a scene (or standing still) at various speeds. Table 7.7 shows a summary of the sets in the complex scene analysis. Once the images were generated, they were processed to add noise, apply a point spread function, and select bands as

(a) High spatial resolution subset scene rendered as desert/industrial scene.

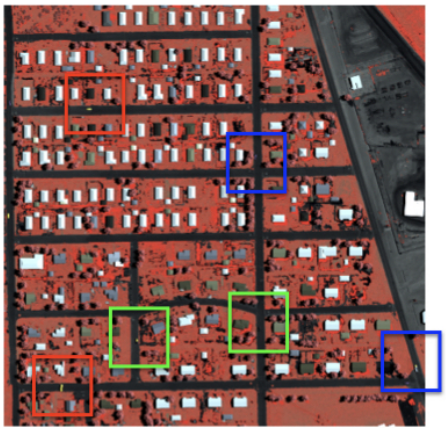

(b) High spatial resolution subset scene rendered as suburb shown in false color composite.

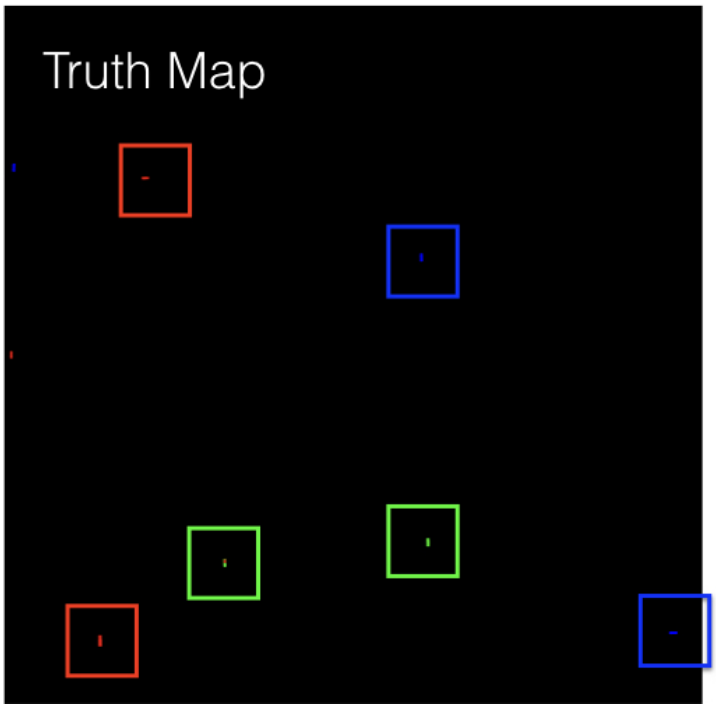

(c) Truth map of the high spatial resolution scenes showing three of the vehicle material types within scenes.

Figure 7.12: Subset scenes along with truth map to demonstrate vehicle placement using SUMO.

Table 7.7: Summary of Simulation Sets

	Number of Sets	Description
GSD	3	5m, 10m, 15m
Background	2	Desert and Suburban
Subset Scenes	9	1.5x1.5km areas
Total	54	6 Utility vs ξ Curves

described in Section 6.4. The post-processed images were then used with the three target detection algorithms described in 6.6 to generate ROC curves and compute utility. The TA_{mean} and V_{scene} values were computed for each set to produce a range of ξ values that were plotted against the utility values. Therefore each scene type and GSD produced a total of six renderings to generate six separate utility vs. ξ curves.

7.6 Summary

We divided the analysis for comprehensive system design into two scene types - simple and complex. The simple scene analysis using the open ocean scene was a validation step to ensure the prediction and assessment processes were congruent. This validation was a complementary step to the band selection method validation where we compared the prediction and assessment results to real image subpixel target detection. The complex scene analysis was the proof of concept for this type of system analysis where the assessment was not a validation step for the prediction but to expand the system analysis from the parameter requirements of the design to the operational feasibility determination. We formed a practical, cost-effective process to reach recommendations for the design and operation of compact spectral imaging systems with adaptive band selection capabilities.

"And once the storm is over, you won't remember how you made it through, how you managed to survive. You won't even be sure, whether the storm is really over. But one thing is certain. When you come out of the storm, you won't be the same person who walked in. That's what this storm's all about."

- Haruki Murakami

8 Results

In this chapter, we present the results with a set of recommendations for a mission scenario such as the one set in Ft Knox, KY using the process that was described in Section 1.6. Given the many dimensions of the trade space, these results serve as examples and a few data points that indicate relationships between the variables in the exploitation of spectral images. However, even with the small set of target and background combinations, we were able to make some observations about spectral image utility and the figures of merit. The first set of results were from analyzing the simple scene to compare the prediction to the assessment, followed by the complex scene analysis results. Then example recommendations are presented following the results of the simple and complex scenes.

8.1 Open Ocean Scene Analysis

The open ocean scene was used as the background for the orange and black targets to compare the predictions from the assessment results. The orange and black targets were used to generate trade curves using FASSP, and placed in the ocean scene as lifeboats to generate DIRSIG images. The predicted utility was compared to the assessment from the SMF target detection algorithm using the simulated images.

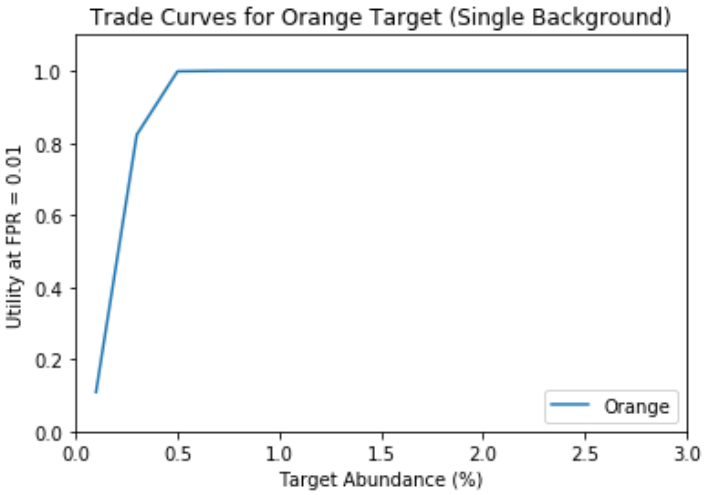

Figure 8.1: Utility trade curve for orange target using only the Ocean Type 1 reflectance file to characterize the background.

8.1.1 Orange Target

The first scenario that we analyzed was the orange lifeboats in the open ocean scene. We generated trade curves using FASSP, first for a uniform background to get the best case scenario. This was done by characterizing the background with a single material reflectance curve. Figure 8.1 shows the TA trade curve for the orange target using only the Ocean Type 1 reflectance. Utility was calculated for FPR = 0.01 and the figure shows the curve for the TA range of 0-3%. Perfect detection was achieved at 0.5% abundance.

The uniform background had the minimum Γ value possible, and demonstrated the best case scenario, but was highly unrealistic. In order to increase Γ, the background was characterized using four curves as described in Section 7.2. Figure 8.2 shows the trade curve when Γ was increased by using more materials to characterize the background. The utility was calculated for FPR = 0.01 and for a TA range of 0-25% with perfect detection achieved at 9%.

DIRSIG images were generated as described in Section 7.4.2 where the sets of simulations had a range of TA_{mean} values. The images went through the post-processing steps as described in 6.4, and the ROC curves for these sets were calculated and analyzed. A total of 15 sets were generated, but 6 sets that had the TA value that matched the FASSP TA

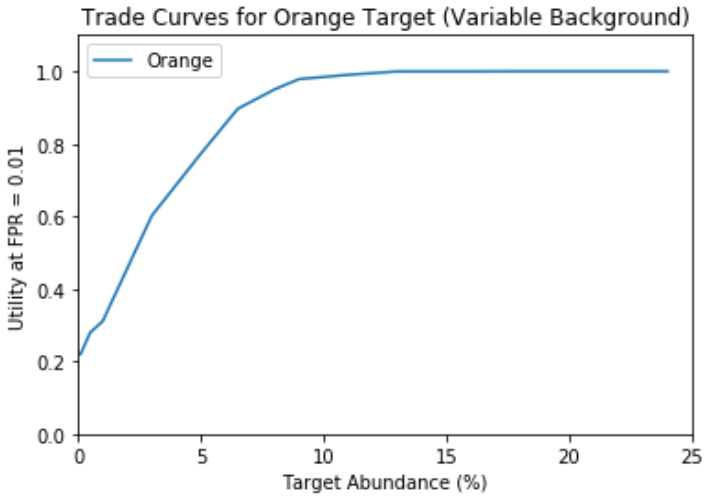

Figure 8.2: Utility trade curve for orange target using using a combination of four spectra to characterize the background.

values were selected. Figure 8.3 shows the ROC curves for the 6 sets selected. The peak TA was found with the set that had $TA_{mean} = 9.3\%$, and the sets with higher TA_{mean} values all had perfect detection. Separate ROC curves were generated by randomly splitting the positive and negative pixel in each set into 6 folds. The average ROC curve of the folds were used to calculate utility.

The ROC curves generated using the DIRSIG images show that at each comparable TA percentage, the detection results are congruent to the FASSP predictions. Figure 8.4 shows the trade curve from the assessment of the DIRSIG image sets. It shows a similar saturation point to the FASSP trade curve shown in Figure 8.2. With the DIRSIG images, perfect detection was never achieved, and there were slight differences between the target detection algorithms, unlike the FASSP results. However, we determined the results from both the prediction and assessment were congruent.

These results indicated the challenges posed in assessing utility compared to predicting it, but the comparison of the two methods highlighted the potential for their combined use. The analytic model was able to efficiently parameterize key elements of spectral image utility to find saturation points. Then by simulating an imaging system design based on the predictions, real world operational considerations was accounted for to validate or modify the predicted parameters to optimize system design.

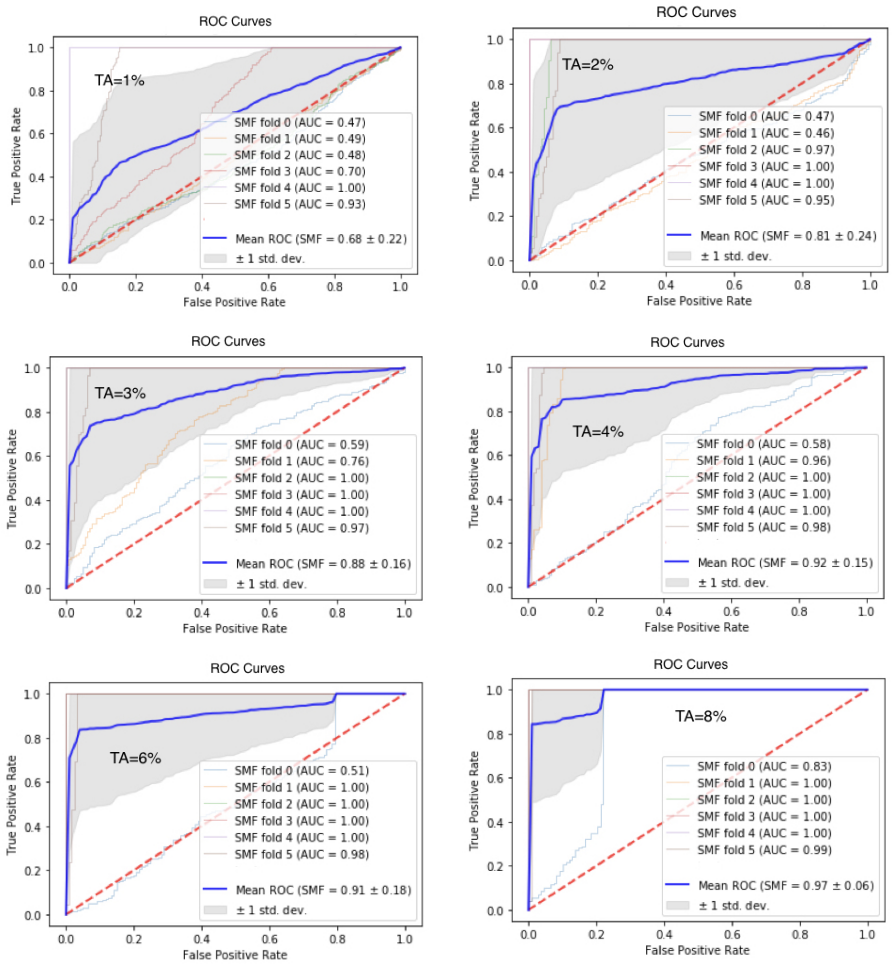

Figure 8.3: ROC curves for the orange target in open ocean scene from six sets with range of TA_{mean} values.

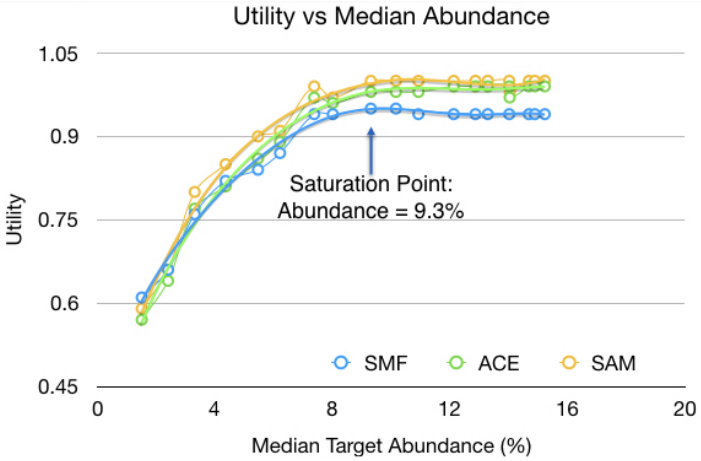

Figure 8.4: Trade curve for the orange target assessed using DIRSIG images for open ocean scene.

This comparison was replicated for the black target to test the limits of this process and analyze the trade space behavior for targets that should not be candidates for subpixel detection using compact spectral imaging systems.

8.1.2 Black Target

The black target was analyzed using the same process as the orange target using FASSP. Figure 8.5 shows the trade curve for the black target using one background spectrum. Utility for the black target was calculated at FPR = 0.01 for the range of 0-25% TA. Perfect detection was achieved at 18% TA.

Figure 8.6 shows the trade curve for the black target using the four ocean spectra with the same composition that was used for the orange target. The utility for a TA range of 0-95% was calculated at FPR = 0.01. Perfect detection was never achieved, and so no saturation point was observed. This indicated that even with full target pixels, the detection performance was likely to be poor.

Simulated images were generated with black lifeboats in a similar manner to the orange lifeboats, but with a higher number of lifeboats placed in the scene to increase the range of target fill fractions. Figure 8.7 shows a histogram of the target fill fractions of the first few sets that were generated with the black lifeboats. With the high number of lifeboats that were placed in the scene, there was a wider distribution of target fill

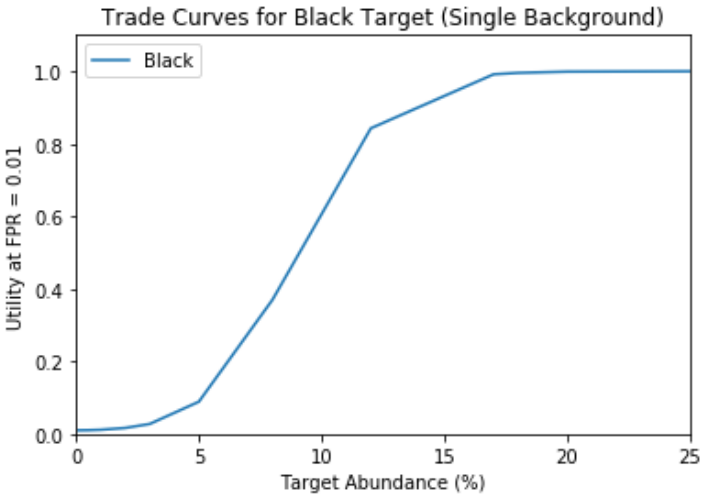

Figure 8.5: Trade curve for the black target using only Ocean Type 1 spectrum to characterize the background.

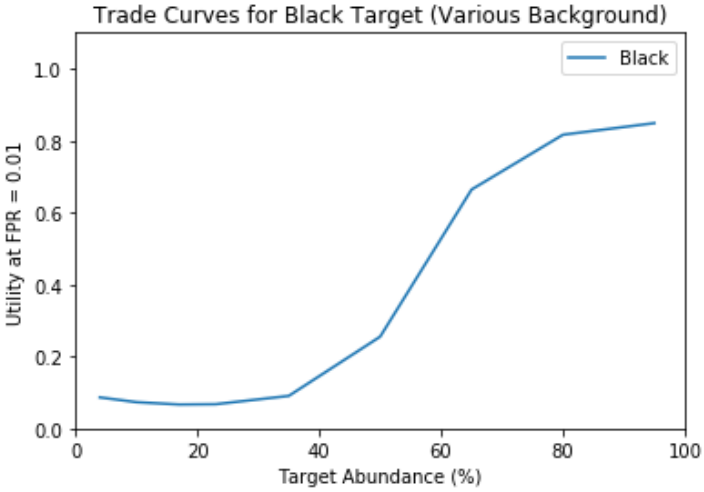

Figure 8.6: Trade curve for the black target using a combination of four ocean spectra to characterize the background.

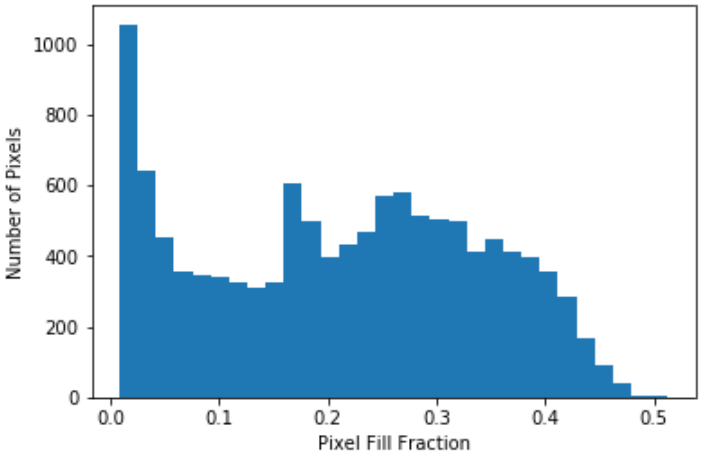

Figure 8.7: Histogram of the spectral images of the ocean for the sets with the lowest number of black lifeboats placed in the scene. Median TA for this set was 30%, with maximum TA of 50%.

fractions, without a gradual change in the means as we had with the orange lifeboat, making analysis challenging. When the number of lifeboats placed in the scene increased, the distribution widened, as opposed to a shifting mean.

The distribution of the set with the lowest number of black lifeboats placed in the scene produced a median TA of 30% with a maximum target fill fraction of 50%. Figure 8.8 shows the ROC curve that was generated for this set. It shows limited detection with an AUC value close to chance, and utility value close to 0. This was an expected result for this type of target for the TA values that were generated.

Figure 8.9 shows the histogram of the sets with the highest number of lifeboats placed in the scene. There were a higher number of pixel with TA values above 60% for this set, but the TA_{mean} value remained at 40%. As a result, a range of TA_{mean} values could not be produced for the black lifeboats as was done for the orange lifeboats. Therefore the data for the black lifeboats were divided into 20 folds to separate the data with high target fill fractions from those with the low fill fractions as much as possible. This generated many ROC curves from a single data set so ROC curves from folds with higher target fill fractions could be differentiated from sets with lower fill fractions.

Figure 8.10 shows the ROC curves generated from these sets of

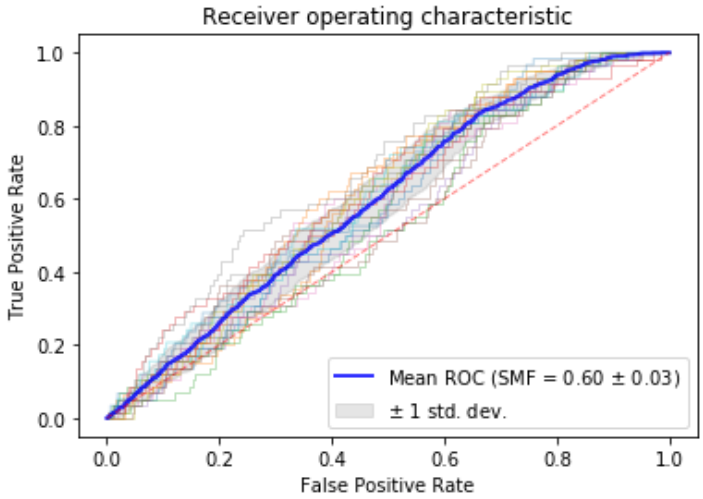

Figure 8.8: ROC curve generated for set of DIRSIG images with TA = 40% in open ocean scene. Limited detection with AUC = 0.6, consistent with FASSP results for targets with less than 40% TA.

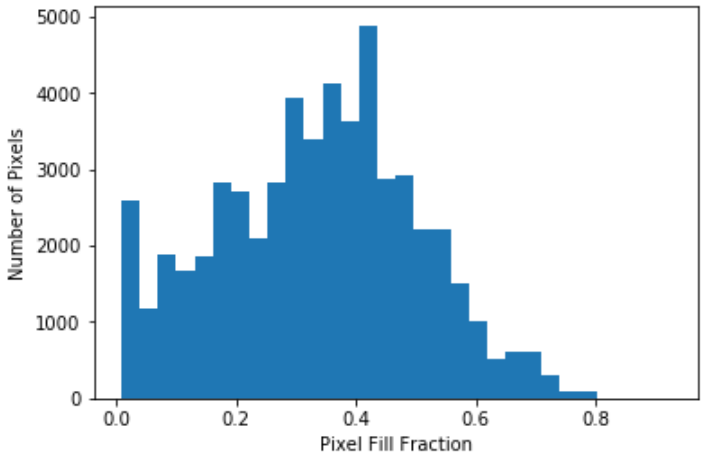

Figure 8.9: Histogram of the spectral images of the ocean for the sets with the highest number of black lifeboats placed in the scene. Median TA was 40%, with maximum TA of 80%.

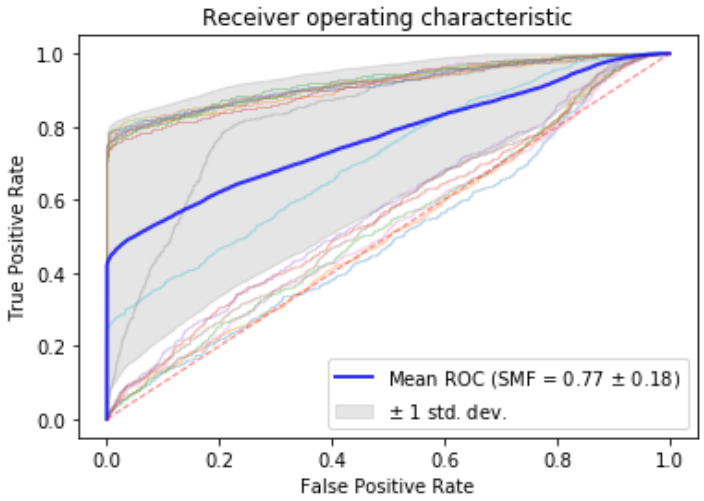

Figure 8.10: ROC curve generated for set of DIRSIG images with TA = 80% for open ocean scene. ROC curves of folds containing positive pixels with low TA have ROC curves with low AUCs. ROC curve of folds containing positive pixels with high TA values have ROC curves with high AUCs.

images with the highest number of lifeboats placed in the scene. While a similar comparison between the predicted results to the assessment could not be made with the black target as was done with the orange target, we can ascertain the congruence between the prediction and assessment. The ROC curves of the different folds indicate utility behavior congruent to the FASSP results where the folds either produce utility ≈ 0.1, or utility ≈ 0.8 as Figure 8.6 shows. There is a jump in the trade curve generated using FASSP, from TA = 40-60% where the utility changes from 0.1 to 0.8. This is consistent with the ROC curves generated using the DIRSIG images where the folds either produce ROC curves with low utility or high utility, with few in-between.

8.1.3 Summary

The comparison between the prediction and assessment of targets placed in a simple open ocean scene indicated that the two models produced congruent results for both an easily detectable target and a difficult target. This comparison also demonstrated the strengths of each model and suggested their appropriate use for this research. This step for comparing the simple scene using FASSP and DIRSIG was used in conjunction with the band selection method validation process to ensure the simulation

Table 8.1: Spectral Similarity Values

Background/Target	White	Orange	Black	Green
Sand	0.28	0.46	0.07	0.21
Grass	0.42	0.39	0.25	0.14

parameters and modeling techniques we selected were able to capture the real world phenomena needed for our research.

8.2 Complex Scene Analysis

Simulated images of Trona, CA was used to analyze a scene that contained objects with 3-D geometry and various material spectra. In order to predict the utility for such a scene, the TA, number of bands, noise, and background complexity were analyzed to find saturation points. The SSVs were calculated for the 8 detection scenarios to quantify separability of the targets to the two backgrounds.

An average of the four background curves for the sand and grass composite spectra, along with the target curves were used to calculate the SSVs of the different scenarios. Table 8.1 shows the SSVs of each target and background combination. Since the SSV accounts for the magnitude difference between two curves, the SSV for the green and black had lower values overall as their reflectance magnitude was lower. Relatively, however the white and black targets had lower SSVs against the sand background, and the orange and green targets against the grass background.

The SSV that would correspond to the example mission scenario that was presented in Section 1.6, was for the green target which for the purpose of this research will say is the spectrum for the green HMMWVs targets. Since the training area in Ft Knox, KY consists mostly of vegetation, we can say that it corresponds to the grass background. For our example mission, the SSV was 0.14.

Table 8.2: Target Abundance Saturation Points

Background/Target	White	Orange	Black	Green
Sand	26%	18%	100%	58%
Grass	6%	11%	45%	16%

8.3 Prediction

The primary advantage of the FASSP model was that it parameterized components of the image chain that affect utility for subpixel target detection. The TA was first analyzed to find a saturation point, which was used as the input parameter for the number of bands. The SNR and background complexity were analyzed in a similar manner fixing each subsequent parameter at the saturation points. The results from the prediction was then used to select the system design parameters for the simulation.

8.3.1 Target Abundance

To analyze the TA, utility was calculated using all the bands in the VNIR spectrum of the HYDICE sensor. The 8 target and background combinations were analyzed initially for the TA range from 0-100% in 15% increments. The range was narrowed down to finer increments between the points where utility first reached perfect detection. For example, for the orange target, the perfect detection was initially found at 30% TA, and so the range was narrowed to 15-30% at 1% increments and reanalyzed. If a utility value at FPR = 0.001 was higher than 0.98, it was determined to be a saturation point.

Figures 8.11 and 8.12 show the trade curves for the TA. The brighter targets reached a saturation point at relatively low target fill fractions, but the darker targets also reached saturation points. The only exception was the black target against the sand background which did not reach utility above 0.4. Table 8.2 shows the TA saturation points that was used as the input value in analyzing the number of bands.

The TA saturation point for the example mission was 16%, which corresponds to the green target in grass background. Given this information, if the green vehicle size was 2m x 2m, then the required GSD

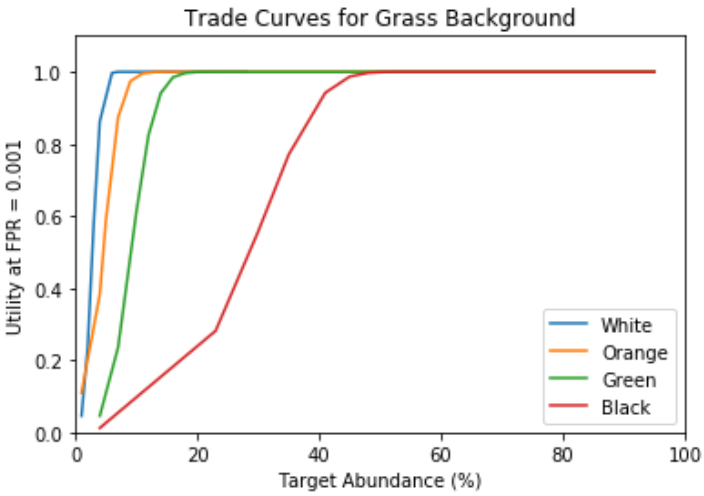

Figure 8.11: Utility vs Target Abundance for grass background.

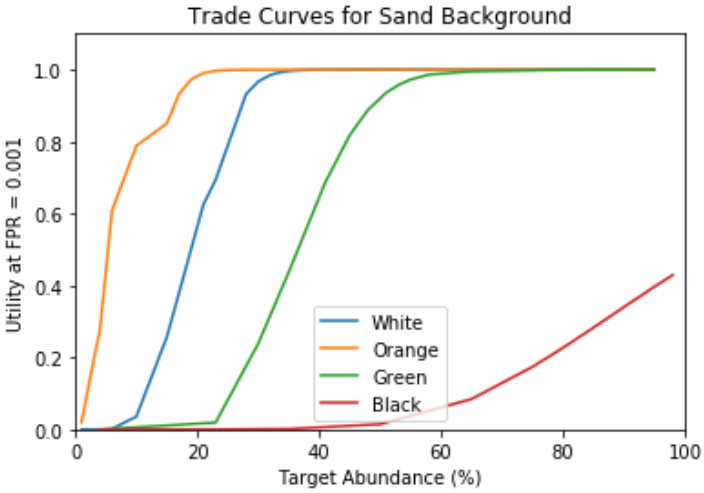

Figure 8.12: Utility vs Target Abundance for sand background.

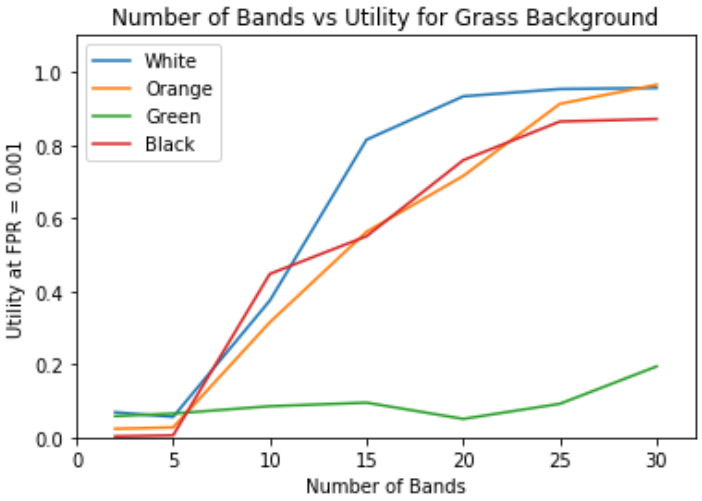

Figure 8.13: Utility vs Number of Bands for grass background.

would be less than 25m to produce a target size to GSD ratio of at least 16%.

8.3.2 Number of Bands

For the number of bands, the saturation point was determined as the number when utility error margin (ϵ) was above 0.1 or achieved a utility of 0.88 or higher for FPR = 0.001. Utility was calculated for a range of 2-30 bands at 5 band increments. Figures 8.13 and 8.14 show the performance curves for the grass and sand backgrounds for the number of bands.

For the white and orange targets, there was a saturation point below 30 bands, but for the black and green targets there was no point where the utility reached 0.88 even with 30 bands. Table 8.3 shows the saturation points for the number of bands, and the input value for the number of bands used in the noise analysis. With the green target against the grass background, there was a saturation point found when all the bands were used, but with less bands, the utility at FPR = 0.001 remained below 0.2 even with 30 bands. The utility for the black target against the grass background increased up to 0.82 with 30 bands.

A similar results is seen for the black target against the sand background, where the utility value was 0.1 for 30 bands. For the green target against the sand background, utility reached 0.92 with 30 bands.

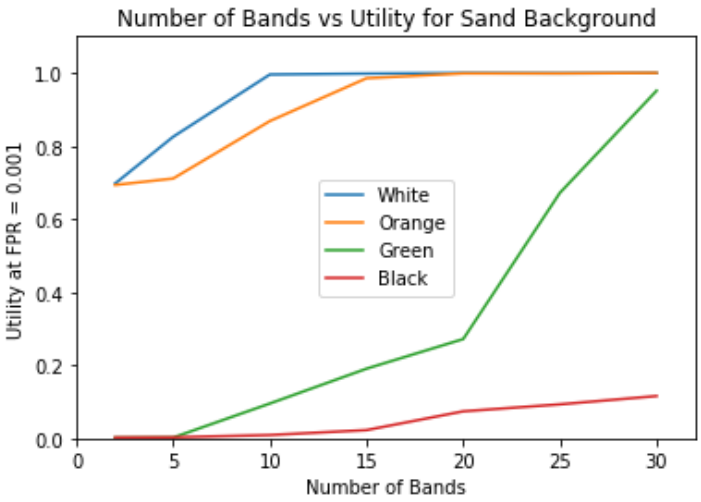

Figure 8.14: Utility vs Number of Bands for sand background.

Table 8.3: Number of Bands Saturation Points

Background/Target	**White**	**Orange**	**Black**	**Green**
Sand	10	15	30	30
Grass	20	25	30	30

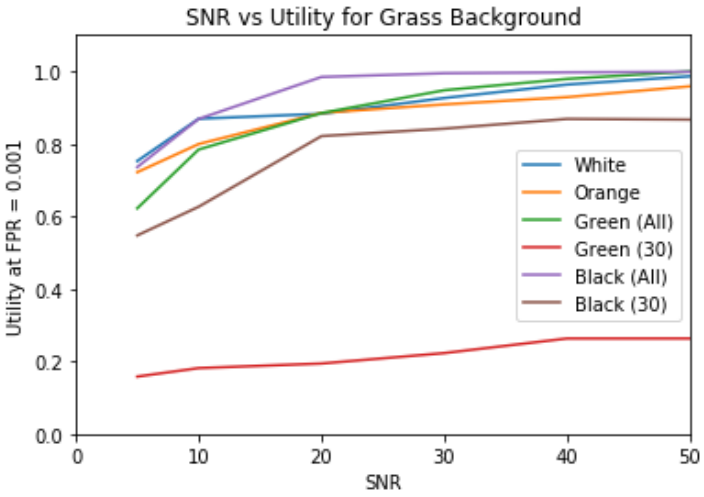

Figure 8.15: Utility vs SNR for grass background.

The SSV of the target and background combinations served as a possible explanation for these results. For our example mission, this showed that we need more than 30 bands. However, since the presence of the vehicles can be easily verified, we determined that the required utility was low. For the purpose of this dissertation, we set the minimum utility at 0.1. What this curve showed, was that utility above 0.1 was achieved using 15 bands, which was also the maximum number of bands that was set for the example mission.

8.3.3 Noise

The utility results for a range of noise levels that produced maximum values of SNR = 5, 10, 20, 30, 40, 50 were analyzed. The range of SNR values for the green and black targets were analyzed using 30 bands as well as all the bands. Figures 8.15 and 8.16 show the performance curves for the range of SNR values. Increasing the SNR had varying effects on performance for each mission scenario. In general, there was no distinct saturation point for any experiment set. However, for most of the targets, there was a slight turning point in utility at SNR = 20, and no discernible increase in utility for a higher SNRs in any of the scenarios. Therefore the SNR of 20 was set as the input value for analyzing background complexity using FASSP.

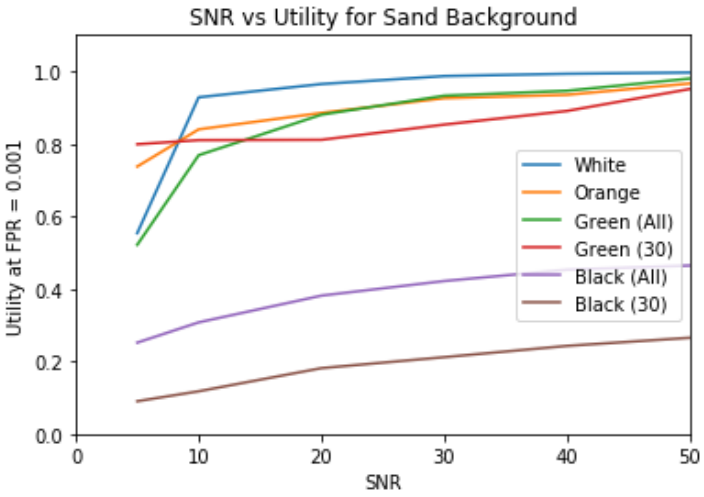

Figure 8.16: Utility vs SNR for sand background.

8.3.4 Background Complexity

The effects of background complexity was analyzed by changing the composition of the spectral reflectance curves used as described in Section 7.5.1. Figures 8.18 and 8.17 show the utility values predicted for a range of Γ values. There was a clear trend in which utility decreased as Γ increased for all the target and background combinations. An increase in background complexity had a greater effect on the darker targets than the brighter targets, especially for the grass background.

The utility value for the green target in grass background mostly remained above 0.1, even for the highest Γ values. This meant that the feasibility recommendation based on the prediction for the example mission was feasible even if the complexity value was high. However, the Γ value assumes a homogeneous background. The area of Ft Knox, KY while mostly vegetation, also had an adjoining urban area. Therefore it was a heterogeneous scene where the background composition would change from pixel to pixel, something that was not captured by the prediction.

Overall the relationship between the 8 scenario based on background complexity indicated the chaotic nature of this analysis. The initial setup and input would change the final results, and so any a priori information in real operations is key. However instead of having specific quantified information, this analysis allows for estimations. This information could be used to redesign the initial setup of the analysis, and

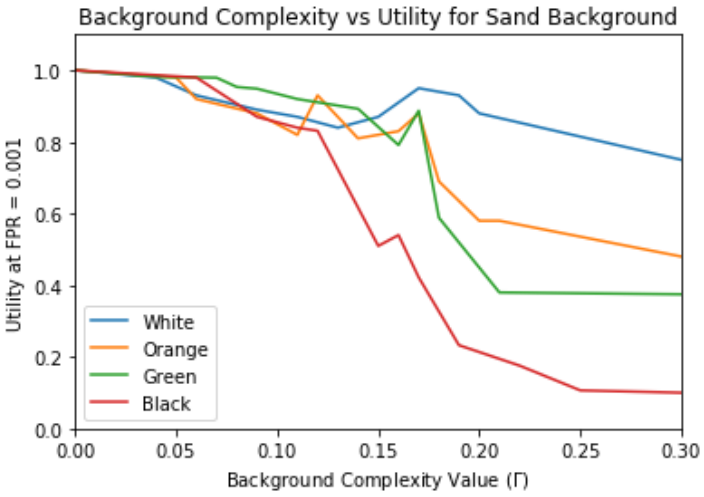

Figure 8.17: Utility vs Γ for sand background.

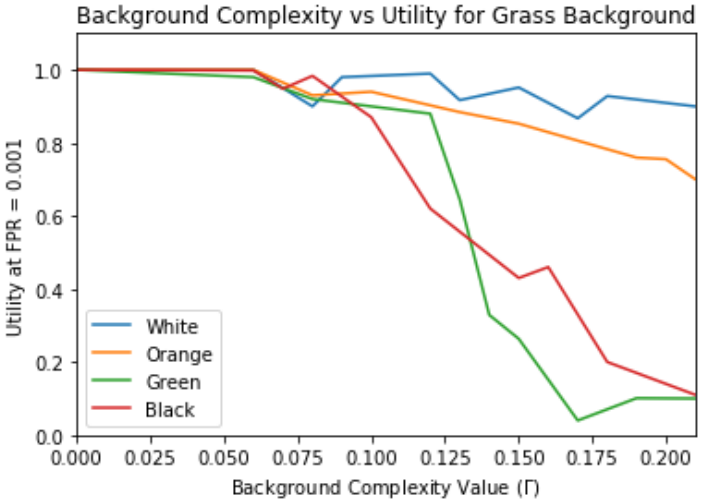

Figure 8.18: Utility vs Γ for grass background.

sensitivity of the final recommendations to the initial values of the design parameters is a potential study for the future.

8.3.5 Prediction Summary

The predictions indicated system parameter requirements for a GSD of 15m for the white and orange targets, and a GSD of 5m for the green and black targets based on the sizes of the target we selected for the simulation. This was determined by a combination of the TA saturation points and the expected background complexity of the Trona, CA scene. Therefore a spectral imaging systems that would produce images with GSDs of 5m, 10m and 15m were simulated for the assessment. In the post-processing step, the bands were selected according to the number of band saturation points with noise added to produce a maximum SNR of 20 at each band.

8.4 Assessment

Using simulation, we generated spectral images collected by a system that produced the GSDs that encompassed the TA saturation points for each of the mission scenarios. Noise was added to produce a maximum SNR of 20. This part of the process introduced some of the real world complexities that might exist in the operational phase, and allowed us to test the predicted system parameters within that context. The simulated images were divided into 54 sets, and each set was analyzed separately to generate its own histogram and ROC curves for the four targets. As such, two variables are introduced that summarize the qualities of each set. The mean target abundance (TA_{mean}) found for each set, was used to calculate detectability. However, this measure did not always fully capture the distribution of the TAs that made up the mean in each set. For example, if a set had a $TA_{mean} = 20\%$, this may be from 200 pixels with less than 1% TA, and 10 pixel with 100% TA. The resulting utility for this data set would be more in line with that of pixels with 1% TA rather than 20%. While the TA_{mean} metric was an oversimplification of a more complex phenomenon, it allowed the analysis to be more tractable.

Table 8.4: Scene Volumes for Suburb Background Simulation Sets

Set/Scene	5m GSD	10m GSD	15m GSD
1	0.47	0.70	0.41
2	0.64	0.31	0.40
3	0.46	0.40	0.30
4	0.30	0.47	0.39
5	0.44	0.41	0.41
6	0.40	0.37	0.42
7	0.32	0.43	0.43
8	0.38	0.49	0.45
9	0.49	0.87	0.44

Table 8.5: Scene Volumes for Desert Background Simulation Sets

Set/Scene	5m GSD	10m GSD	15m GSD
1	0.50	0.48	0.41
2	0.61	0.45	0.40
3	0.62	0.40	0.30
4	0.47	0.59	0.38
5	0.58	0.56	0.39
6	0.44	0.41	0.40
7	0.82	0.50	0.42
8	0.61	0.46	0.45
9	0.63	0.55	0.44

8.4.1 Scene Complexity

Each set was first examined by their histograms along with the TA_{mean} values. Then the scene volumes were calculated for each set, shown in Tables 8.4 and 8.5. The tables show that for both scene types (desert and suburb), when the GSD increases, the volumes decrease. This result is congruent with the assertion that as spatial resolution decreases, the scene complexity also decreases where the material compositions in each pixel approach the scene average. This demonstrates the trade between decreasing GSD to increase TA as opposed to increasing it to reduce scene complexity.

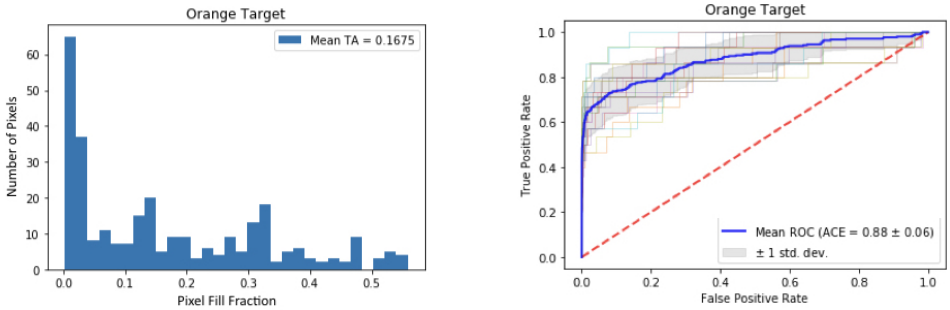

(a) Histogram of target fill fractions.

(b) ROC curves.

Figure 8.19: Histogram and ROC curve for Set 5 of Orange target placed in Trona Desert scene, rendered at 15m GSD.

8.4.2 ROC Curves

ROC curves and histograms of the positive pixels were generated for the targets in each of the 54 sets. There were 180 images per set and this data was divided into 15 folds for analysis. Figure 8.19 shows the ROC curve and histogram of set 5 of the desert scene, rendered at 15m GSD. Figure 8.19a shows a histogram of the TAs for the orange target. The largest bins in the histogram were of the pixels below 1% TA. Figure 8.19b shows the ROC curves generated from this set, and the bold blue line shows the mean ROC curve generated from each of the folds.

The TA_{mean} for this set was 16.75%, but this distribution was an example of a scene where most of the positive pixels were below 2% TA, which results in a lower average utility than what was predicted for an orange target with a TA of 16.75%. This ROC curve and histogram was an example of a TA_{mean} that was not directly correlated to a parameterized target fill fraction to predict utility. However these performance values were consistent with the predicted utility for an orange target in sand background which was an easy detection scenario. Even with a large percentage of pixels with low TA values, the false positives were limited, and the calculated utility at FPR = 0.001 was 0.36 ($Util = 0.36$).

Figure 8.20a shows the histogram of the black targets in set 5 of the suburban scene rendered at 15m GSD, which had a TA_{mean} of 10.74%, much lower than the orange target, and well below the predicted detectability rate. Figure 8.20b shows the ROC curves which had a low standard deviation and AUC of 0.80. While the AUC is relatively high, the utility value calculated at FPR = 0.001 was close to 0. In fact, for most of

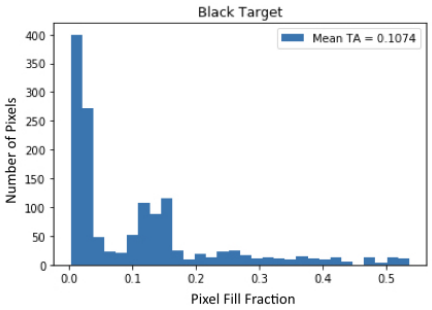

(a) Histogram of target fill fractions.

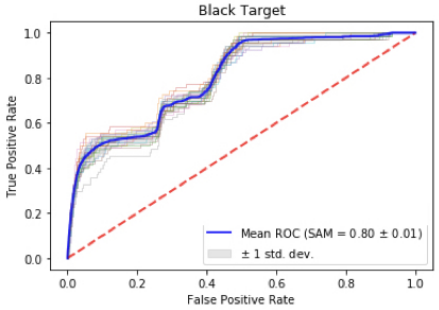

(b) ROC curves.

Figure 8.20: Histogram and ROC curve for Set 5 of Black target placed in Trona Suburban scene, rendered at 15m GSD.

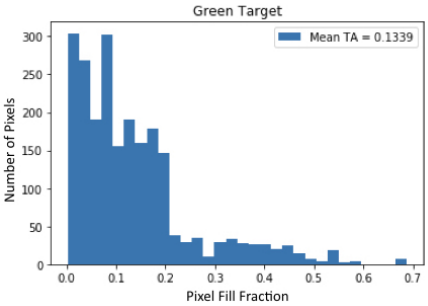

(a) Histogram of target fill fractions.

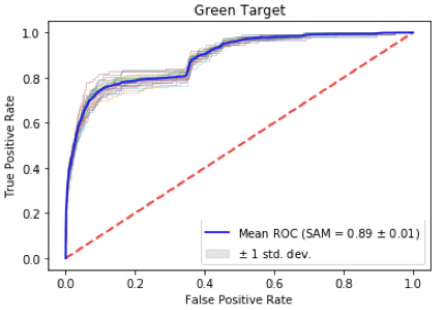

(b) ROC curves.

Figure 8.21: Histogram and ROC curve for Set 5 of Green target placed in Trona Suburban scene, rendered at 15m GSD.

the sets, even when there were full target pixels and the TA_{mean} was higher, the utility values for the black target was always close to 0.

There were complexities that existed in the analysis for spectral image analysis where the AUC did not capture performance. An example where there was a difference in performance depending on the figure of merit used, was between the green target and white target. Figure 8.21 shows the histogram and ROC curves for set 5 of the green target in the suburban scene, rendered at 15m GSD. Figure 8.21a shows the ROC curves that were generated for the histogram shown in Figure 8.21b. The AUC for this set which had a TA_{mean} of 13.39% was 0.89, and $Util = 0.18$. This was a difficult detection scenario, and the results were consistent with the utility prediction.

Figure 8.22 shows the histogram and ROC curves for set 5 of the

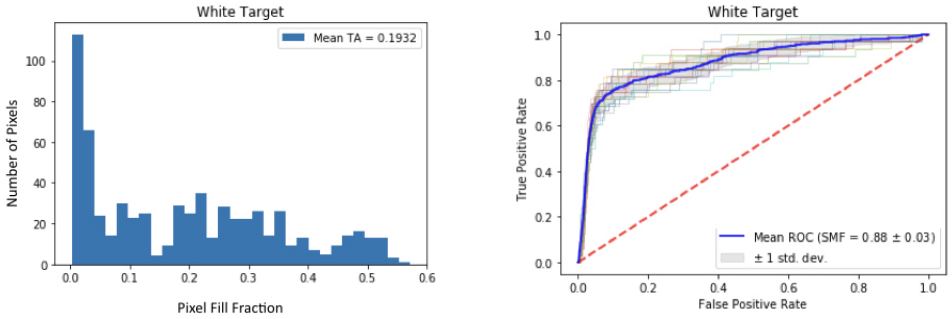

(a) Histogram of target fill fractions.

(b) ROC curves.

Figure 8.22: Histogram and ROC curve for set 5 of white target placed in Trona Suburban scene, rendered at 15m GSD.

white target in the suburban scene, rendered at 15m GSD, same as the green target shown in Figure 8.21. Figure 8.22a shows the histogram of the positive targets in this scene where TA_{mean} was 19.32%. Figure 8.22b shows the ROC curves that were generated for this set. The AUCs for the green target was 0.89, and 0.88 for the white target. Given their standard deviation, these were equivalent AUCs. The utility on the other hand, for the green target was 0.18, but 0.01 for the white target.

This was not consistent with the prediction where the white target in grass background was the easier detection scenario than the green target in grass background. These results indicated not just the complications inherent in spectral utility analysis based on the metrics that were used, but the background and scene effects that were not captured in the predictions. A possible explanation for this phenomenon was that the white target did not have many spectral features, and there were many materials in this scene that were similar to the white target which caused a high number of false alarms. It also signals the importance of spectral features in a target's reflectance signature that would have allowed the detection algorithms to differentiate the white target from the bright surrounding objects.

Figure 8.23 shows the histogram and ROC curves for set 5 of the white target, rendered at 15m GSD. This was the same subset scene as Figure 8.22, but rendered as a desert scene. Figure 8.23a shows the histogram of the positive pixels in this set with a TA_{mean} of 20.1%. Figure 8.23b shows the ROC curves where the AUC is 0.83, which is lower than the AUC for the same subset scene rendered as a suburban scene. We can compare these results those shown in Figure 8.22b which has a similar

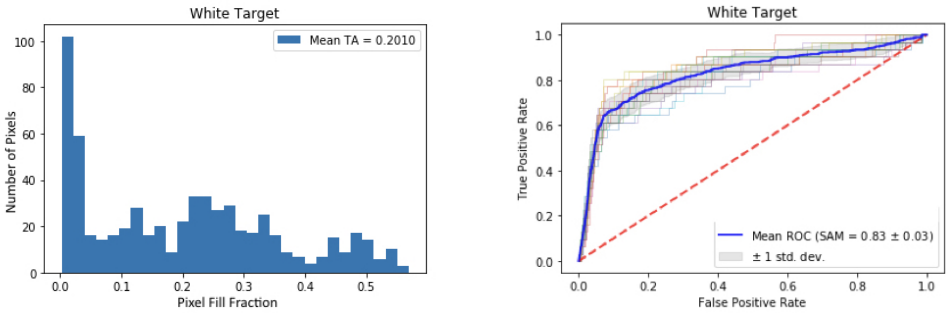

(a) Histogram of target fill fractions.

(b) ROC curves.

Figure 8.23: Histogram and ROC curve for set 5 of white target placed in Trona Desert scene, rendered at 15m GSD.

TA_{mean}, but with a background that has a lower SSV compared to the target. While the utility for both sets are low due to the high number of false alarms, the AUCs are consistent with the predictions where detection performance of the white target was lower against the sand background than the grass background.

Figure 8.24 shows the histogram and ROC curves for the white target, but for set 7, a different subset scene, rendered at 5m GSD as a suburban scene. The TA_{mean} is 17.85%, lower than what was shown in Figure 8.22a, but with more pixels that had higher target fill fractions. The AUC for this set is the same as was with set 5 shown in Figure 8.22 but the utility results are higher with a value of 0.05 as opposed to 0.01, 5 times higher. However, these utility values are still very low indicating that while the target fill fraction increased for many of the pixels due to a smaller GSD, the final utility value was driven primarily by the scene complexity.

All 54 sets were examined by their histograms, ROC curves, and the utility values were calculated for FPR = 0.001. The utility for the black target for all the sets were close to 0, never exceeding 0.05 even when the AUCs were equivalent to the other targets. The white target had low utility for many of sets, especially when the target fill fraction distribution had many pixels below 1% TA. However for some subset scenes, regardless of the target fill fraction distribution or TA_{mean} value, the utility increased. This showed that for the white target, while higher target fill fractions contributed slightly to utility for the white target, the scene complexity and the materials that were present in the scene had a greater effect. On the other hand, utility for the green target increased significantly for sets with higher fill fractions and the scene complexity had a less significant

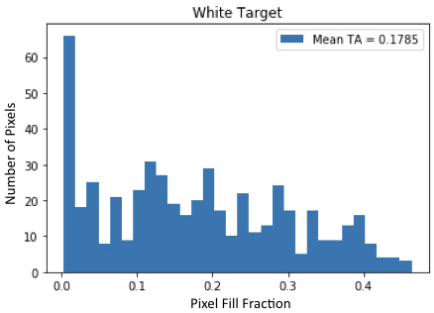

(a) Histogram of target fill fractions.

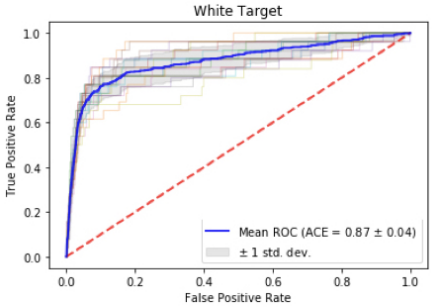

(b) ROC curves.

Figure 8.24: Histogram and ROC curve for set 7 of white target placed in Trona Suburban scene, rendered at 5m GSD.

effect. For the orange target, both increasing the TA and decreasing scene complexity had a significant effect, but only up to a certain point for the TA. Utility for the black target was independent of the scene or the TA and remained low for any combination of TA and scene volume.

The comparison of the overall results for the green and white target were surprising. In almost all the sets, the green target had higher or equivalent utility for the equivalent detectability values of the white target. A potential reason for this may be that other materials present in the scene such as buildings had similar spectral signatures as the white target. Another reason may be the lack of spectral features in the white target, and so the reduced number of bands had a significant effect when analyzed in a complex scene. Compared to the green target that used 30 bands to generate the ROC curves, the white target used 10 bands for the desert scene and 20 bands for the suburban scene, since these were the predicted saturation points for number of bands. This may be an example of a complex scene phenomena that was not captured in the prediction that had a significant effect on the utility.

The results for the orange target was as predicted. It also used less bands than the green target, but the utility of the orange target was higher as predicted, and remained detectable as long as the TA values were above the saturation point, and in many cases, the utility remained high even at lower TA value with limited false alarms. What this demonstrated was that the anomalous results between the prediction and assessment only affected the white and green targets.

Table 8.6: Tally of the best target detection algorithm results for each target of the 54 simulation sets, if the set contained the target.

Algorithm	Orange	White	Green	Black
SAM	0	0	51	54
SMF	4	32	0	0
ACE	46	19	2	0
Total	50	51	53	54

8.4.3 Target Detection Algorithms

The histograms and ROC curves shown in Section 8.4.2 are the best results out of the three target detection algorithms. When comparing the figures between the four targets, each target had a different algorithm that produced the best results. Table 8.6 shows a summary of the target detection algorithms and the number of sets that had the highest utility for each algorithm for each target. There were a total of 54 simulation sets, however some sets did not contain the target, and so they were not included in the tally of which algorithm produced the highest utility.

For the black target, SAM was always the algorithm that produced the best results. The other algorithms rarely produced utility above 0 for this target. Similarly, SAM was also the best algorithm for the green target in almost all the cases except for two. What distinguished these cases from the others was unclear. In many cases however, SAM and ACE produced similar results with SAM producing only a slightly higher utility value.

For the orange target, the best algorithm was usually ACE, but sometimes SMF. The best algorithm seemed to change based on the TA distribution. When the median was below 5%, ACE always had the highest utility. When there was a significant number of pixels with TA values above 10%, SMF was always the best algorithm for the orange target. The best algorithm switched in a similar manner for the white target, but with SMF as the best algorithm for sets with lower TAs. Since the only algorithm that was compared between the prediction and assessment was SMF, examining the comparative results using other detection algorithms for the prediction is a direction for future studies.

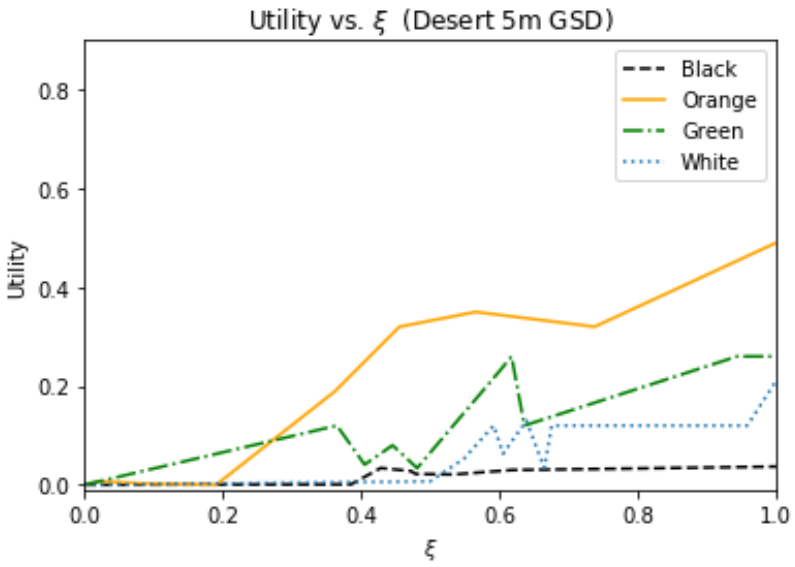

Figure 8.25: Utility at FPR = 0.001 for the scene values calculated for the Trona Desert scene, rendered at 5m GSD.

8.4.4 Detectability

Each GSD of the scene rendered as a desert or suburban scene was grouped to generate 9 detectability values (ξ) for each rendering. The detectability was calculated using the scene volume (V_{scene}) and TA_{mean} for the 9 subset scenes, and the utility was plotted for the ordered range of ξ values. Figures 8.27 to 8.30 shows the utility vs. ξ curves for each rendering.

For our example mission which required utility greater than 0.1, the detectability value was 0.3 for the 5m and 15m GSD images. For the 10m GSD images, only a detectability of 0.8 or higher achieved utility above the required value. This showed, that for this mission, we needed to either decrease the GSD to 5m to increase TA_{mean}, or increase the GSD to 15m and lower the scene volume. Both results were similar, but the utility was slightly higher for the 5m GSD images.

The detectability of the black target, as predicted and expected, remained low whether the subset scene had high or low scene volume and regardless of the TA_{mean} values. However, the prediction was that pixels with high target fill fraction could be detected, and a saturation point was found for the grass background. This discrepancy between the prediction and assessment indicates the potential for use of this target in error

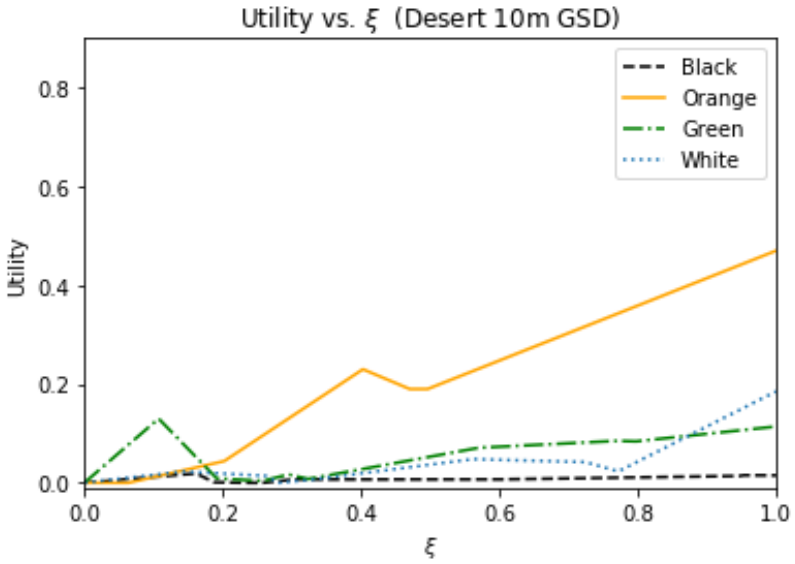

Figure 8.26: Utility at FPR = 0.001 for each scene values calculated for the Trona Desert scene, rendered at 10m GSD.

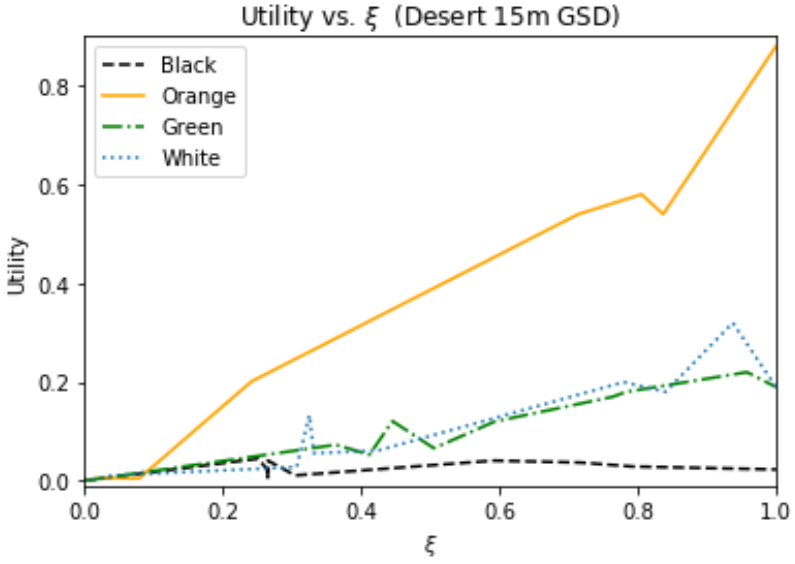

Figure 8.27: Utility at FPR = 0.001 for each scene values calculated for the Trona Desert scene, rendered at 15m GSD.

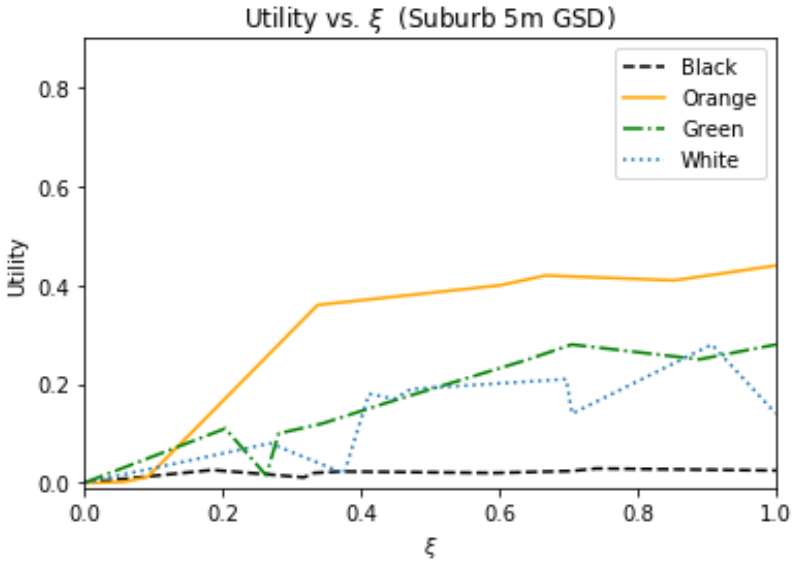

Figure 8.28: Utility at FPR = 0.001 for each scene values calculated for the Trona Suburban scene, rendered at 5m GSD.

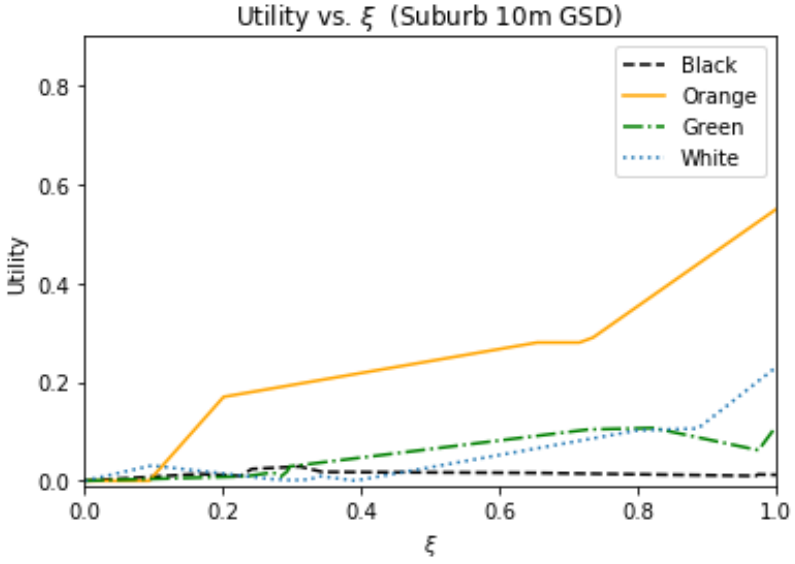

Figure 8.29: Utility at FPR = 0.001 for each scene values, calculated for the Trona Suburban scene, rendered at 10m GSD.

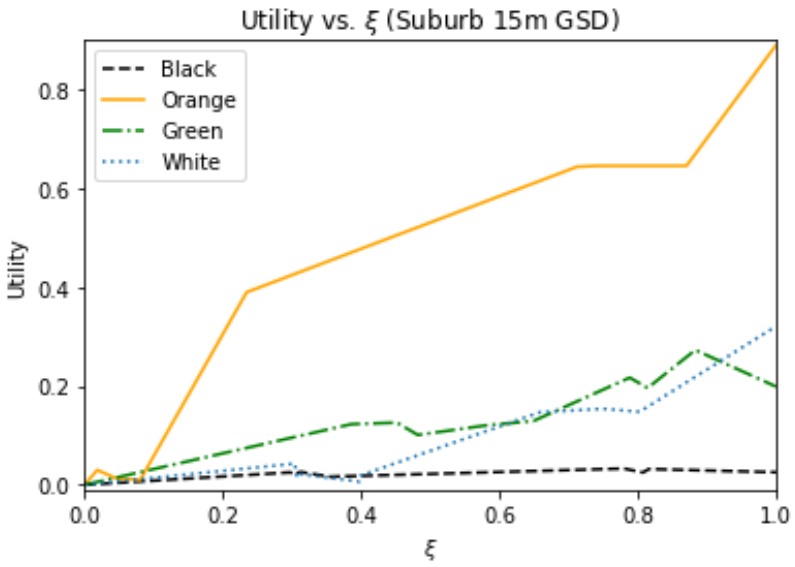

Figure 8.30: Utility at FPR = 0.001 for each scene values, calculated for the Trona Suburban scene, rendered at 15m GSD.

propagation analysis of this process.

The orange target benefited most from a decrease in V_{scene} compared to an increase TA_{mean}. This is likely due to the orange target's TA saturation point. Decreasing the GSD may have resulted in a higher TA, but past this target's saturation point, it benefited more from a decrease in scene complexity. The green and white targets on the other hand, had similar results in the 5m GSD sets and 15m GSD sets. This indicated that for these targets, the benefits of increasing TA had similar effects to decreasing scene complexity.

Overall, for the Trona, CA scene and the targets that were selected, decreasing scene complexity had more impact on utility than higher TA_{mean} values that resulted from lower GSDs. For both sets, the detectability curves were the worst in the 10m GSD images. This indicated that at this GSD which could be seen as a "middle ground" solution, the improved target fill fraction from a lower GSD, was less significant than the high scene complexity which had a more significant effect on detectability. This relationship between the three GSDs indicated that the two metrics were not directly nor linearly related. The nature of their relationship is a possible subject for analysis in the future.

The spectral characteristics of the scene had limited effect on detectability, in that there was some congruence between the predicted results based on the SSV between the target and background, but the overall heterogeneity of the scene was a dominant factor affecting utility in the complex scene analysis. The utility values were similar for the scenes rendered both as a desert scene and a suburban scene for the orange and green targets. There was only a small decrease in utility in the suburban scene compared to the desert scene compared to what was predicted using the FASSP grass and sand background composition comparisons. The green target was not significantly less detectable in the suburban scene as opposed to the desert scene. The white target was less detectable for the 5m GSD desert scene, compared to the 5m GSD suburban scene, but not as significantly as predicted. Given the contrasting results, this relationship between the complexity of scene and detectability is an subject requiring further study. The results indicated that the complexity of a scene that is defined by its homogeneity, effects of the 3-D geometry, and other materials present, had a greater effect on utility compared to the spectral similarity between target and background. For two missions with the same SSVs, the results from a uniform scene was different for a heterogeneous scene.

8.4.5 Summary

The results of the assessment validated many of the predictions on utility, but also highlighted some complexities that would be introduced in a real world situation. The presence of materials in the scene that was not used to characterize the background seemed to have a significant effect on utility, especially for the white target. The trade for increasing target fill fraction came at the cost of increasing scene complexity. For the green and white target, the effects of higher TA values from a smaller GSD was balanced out by the higher scene volume that resulted with limited effect on utility. For the orange target, the gains from improving TA was outweighed by the increased scene volume, which decreased utility. TA_{mean} and scene volume were inversely correlated measures that affected utility differently for each target, and the trade of improving one parameter at the cost of the other, depended on the combined characteristics of the target and scene.

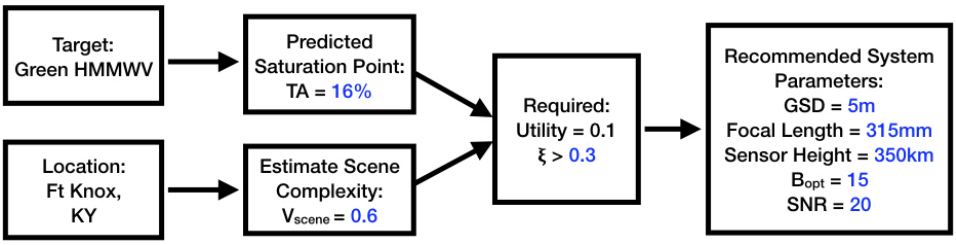

Figure 8.31: Example use of process leading to imaging system parameter recommendation for a green target using the scene volume metric.

8.5 Example Requirement Recommendation Flow Diagram

The results applied to the example mission described in Section 1.6, took only the target and location into consideration, but the operational aspects of how often the images needed to be collected, coupled with the the computational resources available, determined the maximum number of bands. The difficulty of confirming or denying the presence of a target based on the detection probabilities determined the minimum utility requirement, since this value was coupled with the FPR. Given these considerations, detectability values were estimated for mission feasibility and system parameter recommendations.

We summarized the process to reach the example mission introduced at the beginning to reach the final system design recommendations. Figure 8.31 shows the set of recommendations and the process flow for the green vehicle in a mostly uniform scene composed of vegetation. Assuming the target and background were similar to the green target and grass background that we analyzed, the predicted saturation point for this target and background was TA = 16%. Assuming the complexity of this location was similar to set 3 and 5 of the suburban scene rendered at 5m GSD, the V_{scene} estimate was 0.45. This led to a ξ value of 0.36, and for the 10m and 15m GSD images the maximum ξ values were 0.4 and 0.53 respectively.

If our desired utility was at least 0.1, then both the 5m and 15 GSD curves at their corresponding ξ values achieved this. However, the utility at the same ξ value for the scenes rendered at higher GSDs as seen in 8.26 and 8.27, was lower. This led to the recommendation that a smaller GSD was desirable since increasing TA had more impact for this type of scene and target. Therefore, for a GSD of 5m, if the platform height was

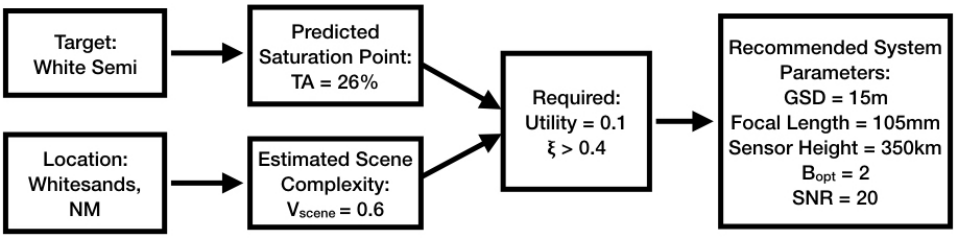

Figure 8.32: Example use of process leading to imaging system parameter recommendation for a white target with using the scene volume metric.

350km, the effective focal length was 315mm. The minimum number of bands that could achieve utility higher than 0.1 was 15.

This recommendation was for a GSD that could produce a TA_{mean} of 16% for the target size we simulated. A higher GSD for this target was unnecessary, but it was a situation where the TA_{mean} as opposed to the V_{scene} value was the primary driver for the parameter recommendations. Even though the predicted utility for reducing the number of bands for this target and background was low, since the required utility was also low, this target was found to be feasible. If the required utility was higher than 0.3, the operational feasibility recommendation would have been that the compact system was unsuitable for the mission. A more detailed, step by step explanation to the final recommendations are presented in Appendix C.

We demonstrate this process for another mission scenario. Figure 8.32 shows a flow diagram for a white semi in a complex desert scene. Assuming the white semi had a similar spectral reflectance signature as the white target we used in our analysis, the predicted TA saturation point was 26%, and we estimated the V_{scene} to be similar to sets 2 of the desert scene rendered at 5m GSD, which was 0.6 (the same as Ft Knox, KY).

The first decision point in the operational phase was the required utility for this target and location. Assuming the required utility value for this mission was 0.1, a feasibility decision was made from this requirement. The estimated ξ value for the saturation point and scene volume was 0.43 (Eq. 8.1).

$$\xi = \frac{TA_{mean}}{V_{scene}} = \frac{0.26}{0.6} = 0.43 \tag{8.1}$$

Examining the assessment results of the desert scene, utility = 0.1 was achieved at $\xi = 0.6$ for the 5m GSD rendering, $\xi = 0.9$ for the 10m GSD,

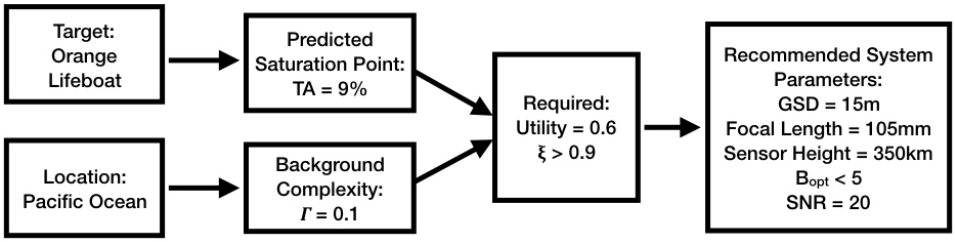

Figure 8.33: Example use of process leading to imaging system parameter recommendation for orange target using background complexity metric.

and $\xi = 0.4$ with the 15m GSD. Only the 15m GSD images produced the required utility at a ξ value that was approximate to the estimated value based on the saturation point.

Therefore the recommended system parameters when the required utility was 0.1 for a mission to determine the presence of a white semi in Whitesands, NM was a focal length of 105mm and sensor height of 350km to produce a GSD of 15m. The number of bands that achieved utility above 0.1 was 2 bands, and so B_{opt} for this mission was 2. The SNR that was predicted and simulated for these results was SNR = 20. This mission was feasible for the utility and number of bands requirements.

Figure 8.33 shows an example of a target detection mission that can use the background complexity value instead of the scene volume. The benefits of using Γ as opposed to V_{scene} was its simplicity. We calculated Γ from a combination of the material spectra in the background. For a scene such as the open ocean, this could be a sufficient estimate of the background complexity even for the real scene. In fact, any scene that is homogeneous enough to be characterized by a finite number of material spectra, could use Γ to estimate scene complexity.

This figure was the same target and scene used in simple scene analysis of the orange lifeboats in open ocean. The saturation point for this target and background was found at 9% and the estimated Γ value was 0.1. At the saturation point, the ξ value was 0.9, and in this case, Γ was fixed, as opposed to TA. With this type of scene using the TA_{mean} vs utility curve, we could adjust the GSD based on requirements. In our simple scene study, $TA_{mean} \approx 2.5\%$ was able to achieve utility ≥ 0.6 for this scenario, which for a lifeboat that was 2.0m x 1.5m in size, was achievable at 15m GSD. Increasing or decreasing GSD was unlikely to change Γ. This was in contrast to the previous scenario where changing the GSD could change the ξ value, and the TA value at the saturation

point was the immovable parameter. With this scenario, depending on the operational requirement, we could increase the GSD, because this type of target could be found even at low TA values. The advantage of doing this would be that the imaging system would have a wider field of view, and so a single image would be able to cover a larger area, saving computational costs. On the other hand, if the GSD was fixed, we could decrease the number of bands to do the same.

If the required utility was 0.6, the recommended system parameters were to increase the GSD and decrease the number of bands. If we fixed the GSD at the maximum of 15m that we analyzed, then we can analyze the trade curve for the number of bands. For the orange target, even for the sand background, using 5 bands could achieve a utility greater than 0.6, and so we determined less than 5 as the recommended number of bands. With further analysis of the detection scenario we could fine B_{opt} for the required utility. These types of decisions can be made from the trade curves generated form this analysis to optimize the system design based on the mission, operational requirements, situation, and computational resources available. For this particular mission, wide area search for the orange target in the open ocean was a highly appropriate mission for compact imaging systems that could achieve a high level of utility.

8.6 Summary

In this research we presented the analysis of a few mission scenarios, and some theoretical examples of the use of this process towards optimization of spectral imaging system designs. We found relationships in the trade space and gained insight into the trade between the system parameters. We presented some example missions to demonstrate the decisions that drove the optimization of the system design using the information gained through this process. In the future this process can be used for other targets, locations, and missions to design a compact imaging system for wide area search.

"See the line where the sky meets the sea?
It calls me.
And no one knows how far it goes.
If the wind in my sail on the sea stays behind me, one day I know, there's just no telling how far I'll go."

- Disney/Pixar Animation, *Moana*, 2017

9 Summary

In this chapter, we present the novel contributions, conclusions, and potential future work. This project combined the use of an analytic prediction model and a simulation model in a novel manner to predict then assess spectral image utility within the design and operational context. The process of analyzing spectral image utility involved multiple components that affected the results, and there were many factors that affected system design recommendations for wide area search missions. For the operational context in which spectral utility was analyzed in this research, the primary contribution to utility was the input mission. What we were looking for and where we were looking were the primary drivers of the requirements in designing a compact spectral imaging system with adaptive band selection capabilities.

9.1 Contributions

The primary contribution of this work was the comprehensive system analysis methodology that used existing tools such as FASSP and DIRSIG in a novel way. We demonstrated this methodology for a few mission scenarios, and in doing so provided insight into the spectral image utility trade space. The novelty of the process compared to previous work and

current state of the art, was that it started with the mission (target and background) to determine the requirements and feasibility of targets for wide area search missions. In order to provide recommendations for a system design, based on the mission, some novel metrics were developed to aid analysis.

The first metric we developed was the optimal number of bands (B_{opt}), making it a function of what was required operationally with data that was generated during the design phase. This metric accounted for the acceptable error and the cost of increasing the number of bands, even if it improved detection. This concept was demonstrated by using the number of band saturation points for the targets and setting a maximum number for all targets. For the green target, although the maximum number of bands in the prediction showed limited utility, the assessment showed that the target was still detectable with less bands. On the other hand, for the white target, the predicted optimal number of bands produced a much lower utility than the assessment. Using the B_{opt} metric, we were able to use the information from the design analysis to account for the operational considerations including data processing costs. In the design phase, we calculated the number of bands vs utility curve, then in the operational phase we used this curve to determine B_{opt} and drive collection decisions. By developing this metric, we were able to bridge the gap between the current state of the art band selection methods with the requirement for optimizing design and operation of systems with adaptive band selection capability.

The next metric we developed was the background complexity value Γ, which could be computed using a finite number of material spectra. While it did not fully characterize a real world scene, when estimating background effects for a location with uniform composition of materials, it was a metric that was simple to calculate. This metric was used in the prediction portion for the complex scene analysis in order to calculate the utility vs background complexity curve. This allowed us to quantify the effects of background complexity for large uniform areas which was prevalent for missions tasked to compact spectral imaging systems to quickly determine the mission feasibility of a selected target. It was a metric that facilitated analysis of wide area missions using compact systems.

The final metric that we developed was the detectability value ξ, which related TA_{mean} to the scene complexity (V_{scene} or Γ). To analyze the mission, this value was used with the required utility value to determine the best GSD from the assessment and verify the predictions.

This value characterized the trade between improving TA or decreasing scene complexity for a specific mission, folded a complex real world situation into a more tractable space for that allowed us to analyze imaging system trades and gain insight into the relationship between parameters. To analyze a spectral imaging system, quantifying the operational aspects in the design and the resulting utility was challenging. While this metric did not absorb all the complexities of designing a spectral imaging system, it allowed us to systematically justify mission feasibility decisions and potential design parameters.

Another requirement of the process that brought about a novel contribution is the band selection method using only the target signature. This was developed in order to account for the envisioned operation of the compact imaging system capable of adaptive band selection. This band selected method was tested against other state of the art methods, and while the bands did not have higher performance, it was a method that could be implemented on a CubeSat. It bridged the gap between the state of the art methods that were not feasible for use on-board a compact system due to their computational complexity, and the the advanced capabilities of a system with adaptive band selection.

In conclusion, this research provided a practical process to optimize the design of a compact spectral imaging system with adaptive band selection capabilities. We also gained novel insight into the trade space for system parameters by developing metrics that could characterize the complex relationships. We developed a process that could quantify and simplify the relationships between parameters to make the decision between the design and operational space more tractable.

9.2 Conclusions

The results presented in this research shows the potential use of this process as a decision tool to optimize the design of spectral imaging systems. The utility trade space was explored from a mission perspective, systematically accounting for the operational aspect of subpixel target detection. This was accomplished by focusing primarily on the targets where the trade space was examined as it related to the material's spectral reflectance signature. This process was developed to work within an operational context where there was a mission, and the imaging system had a specific application.

The key findings from this research was that scene complexity and GSD are inversely related, and the trade between the two components depend on the scene, target, and the requirements. If the mission was determined as feasible for the required utility value, then the decision on whether or not to increase the GSD depended on the predicted TA saturation point and the inherent complexity of the scene. On one hand, there was no need to design a system with a smaller GSD to achieve a TA past the saturation point. On the other hand, a target size to GSD ratio did not guarantee that an image would produce this TA, since the TA could be distributed between more than one pixel. Furthermore, if a scene was inherently simple such as an open ocean, then increasing the GSD to lower the scene complexity had limited effects. Therefore the best GSD to simultaneously maximize TA and minimize scene complexity depended on the requirements, the target, and the scene.

Another finding was that the SSV between the target and background had some effects on detectability, but its effect depends on the other materials present in the scene as well as the target itself. As for the targets, spectral features of a material changed its resulting detectability that was not always captured by the prediction. This was demonstrated by the white target that was thought to be the ceiling due to its high reflectance within the VNIR spectrum, but was found to have lower detectability than the orange target. This could either be from the scene complexity and the materials that contributed to it, or the target material itself which has limited features. The examination of the spectral features of a material and its effect on detectability is a potential subject of future research.

Another finding about the relationships within the trade space was that SSV and scene complexity contributed to the number of bands required to achieve a desired utility value. In a simple scene such as the open ocean, the number of bands required for an orange target could be 5 bands or even lower. On the other hand, the same target in a suburban background required 25 bands to achieve a saturation point. The primary conclusion of this research was that the background scene, target, and what is determined to be acceptable error drives the decisions for designing a compact system. For wide area search missions, all of these effects in the trade space needed to be considered. A key novel contribution of this research was that we found that there was a distinct trend between utility and background complexity as well as utility and detectability. While these observations were from limited data points, it yields itself to future research.

9.3 Future Research

Some areas of study for the future is the use of the simulated images to explore the temporal resolution component of an imaging system with tracking capabilities. While we assumed a fixed satellite orbit in this study, with some modifications this process can be used to account for a system's ability to change its focal plane. If an imaging system can be designed to automatically begin "tracking" the location of a potential target because the pixel was above a detection threshold, this can improve performance by improving TA without increasing scene complexity. The spatial distribution of the target was an effect that was observed in this research that caused target fill fractions to be consistently lower than the maximum achievable abundance, and tracking capabilities can mitigate this effect.

Another area of study if to form a look up table with the detectability index of targets. This information can be used to facilitate decisions of whether or not to even consider a target for wide area search missions without going through the entire process. It can also provide a confidence level in detection results using existing compact imaging systems. In this research, the black tire was found to be a target that was not feasible for any situation, and with a look up table comprehensive trade space analysis for this type of target can be avoided in the future. For other feasible target and background combinations, this process can be used to find more data points in the spectral image utility trade space. The finding that spectral features of a material had affects on the detectability is based on the results of the four target materials examined in this research. Similar analysis of other target materials can be used to confirm or counter these findings in the future.

Examining the comparative results using other target detection algorithms for the prediction is a natural follow on study. The only algorithm implemented in the FASSP analysis tool was CEM. Given the differences in performance for the three target detection algorithms used depending on target that was found using the simulated images, implementing more target detection algorithms may produce better predictions.

Another potential follow-on research project is the development of a reverse process for an existing compact imaging system to determine the confidence level of detection results. For example, this process revealed the black target as one with low utility value more or less independent of the metrics that were used to determine detectability. Therefore, the

confidence value of any detection result for this type of target would be low. On the other hand, for the orange target, especially if the scene was uniform, the high detectability value of this combination would also raise the confidence level of the detection results of this target and background combination. Also, coupled with the detectability of each target and background combination, if an imaging system collects a finite set of bands, targets with tops bands that correspond to the ones collected by the imaging system would yield a higher confidence value in the detection results.

The results of this process and the final set of recommendations were composite optimizations in each dimension of the trade space determined empirically. The relationship between on figure of merit to another are not linear and would be challenging to express as an algebraic equation. Therefore a quantitative examination of uncertainty in the results would require more than the traditional error propagation analysis for each metric since their relationship is more complex. Further examination of the effects due to uncertainty and error on the final decision recommendation provides another potential avenue for future work.

A

Coefficient Analysis for BOTS

A.1 Bank Rankings

Figures A.1 - A.20 show **z** values for range of coefficient values calculated with BOTS. Note: Y-axis values are different from image to image to show changes in low values.

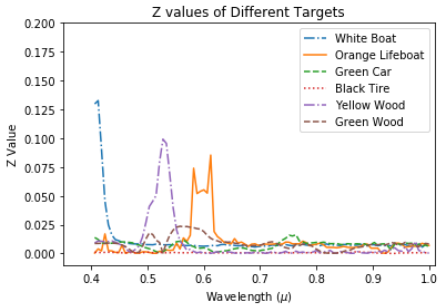

Figure A.1: a = 0.99

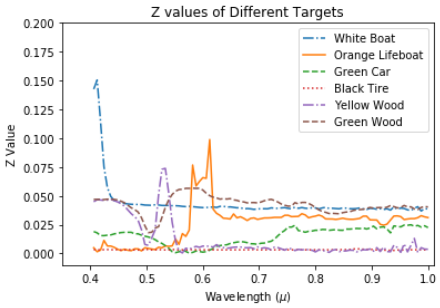

Figure A.2: a = 0.95

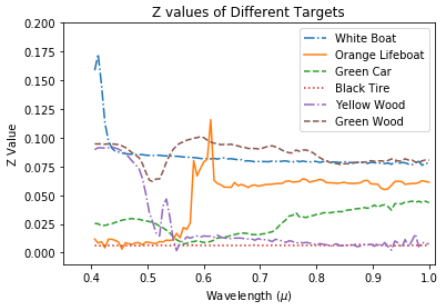

Figure A.3: a = 0.90

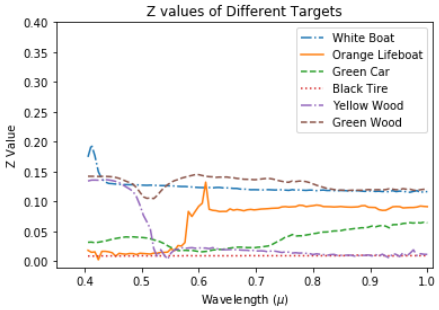

Figure A.4: a = 0.85

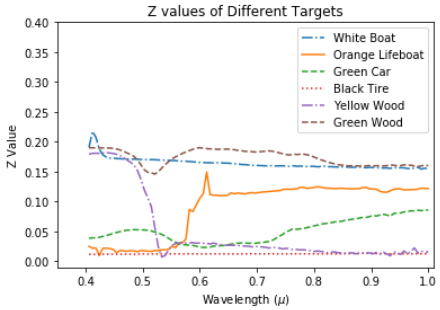

Figure A.5: a = 0.80

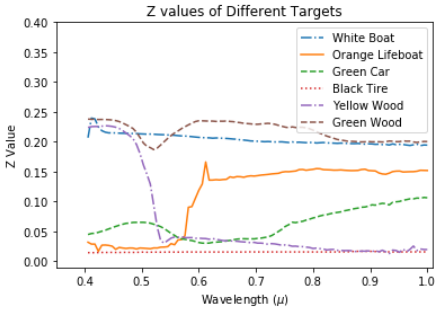

Figure A.6: a = 0.75

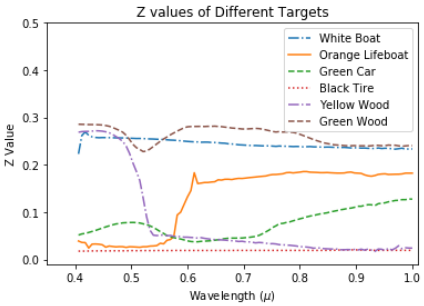

Figure A.7: a = 0.70

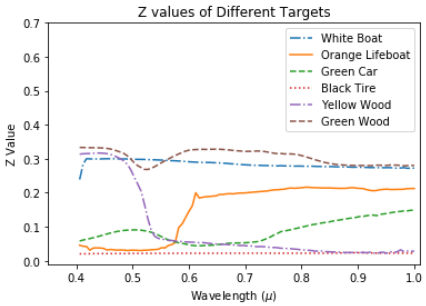

Figure A.8: a = 0.65

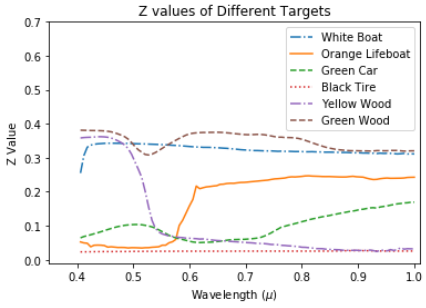

Figure A.9: a = 0.60

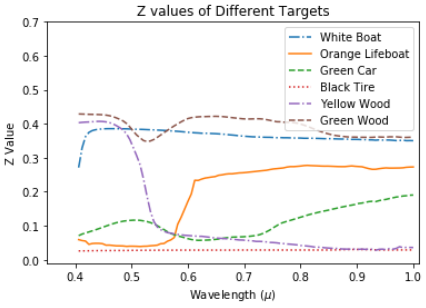

Figure A.10: a = 0.55

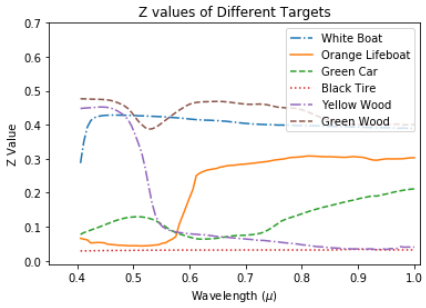

Figure A.11: a = 0.50

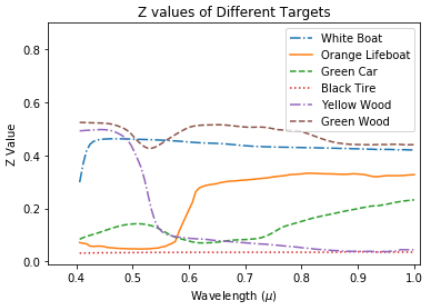

Figure A.12: a = 0.45

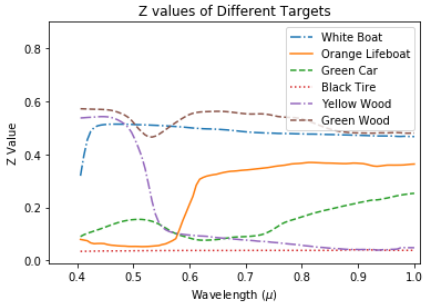

Figure A.13: a = 0.40

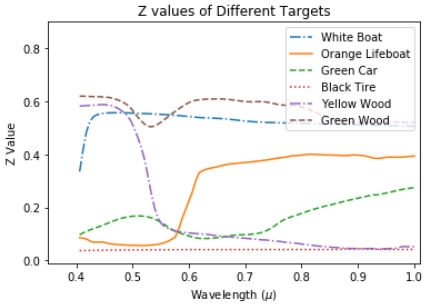

Figure A.14: a = 0.35

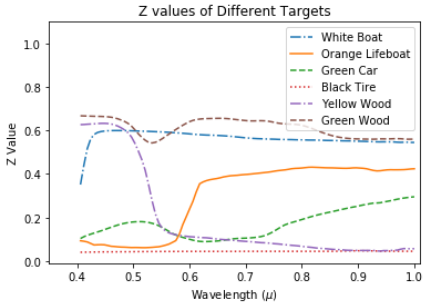

Figure A.15: a = 0.30

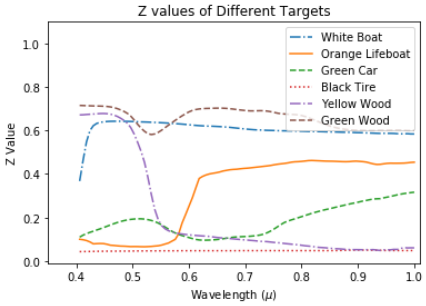

Figure A.16: a = 0.25

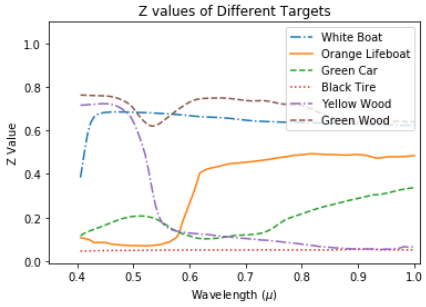

Figure A.17: a = 0.20

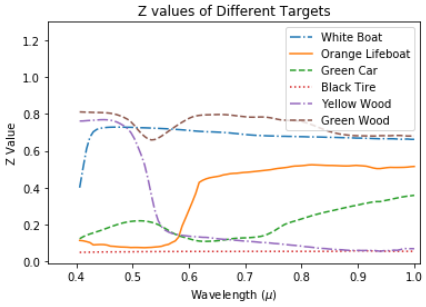

Figure A.18: a = 0.15

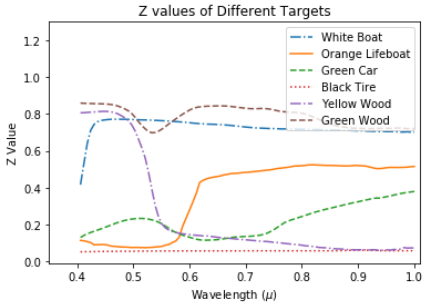

Figure A.19: a = 0.10

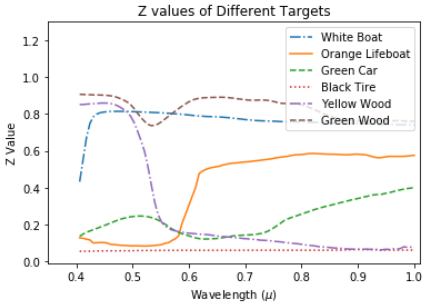

Figure A.20: a = 0.05

A.2 Table of top 30 band wavelengths

Tables A.1 - A.6 show list of band rankings for the top 30 bands for range of coefficients calculated with BOTS.

Table A.1: Best bands for orange lifeboat material.

a values	**Band wavelengths** (μm)
a = 0.99	0.606 0.576 0.594 0.588 0.6 0.582 0.612 0.57 0.618 0.558 0.648 0.624 0.77 0.564 0.739 0.661 0.745 0.63 0.776 0.636 0.545 0.655 0.8 0.939 0.933 0.982 0.642 0.764 0.685 0.758
a = 0.95	0.606 0.576 0.594 0.6 0.588 0.582 0.612 0.618 0.77 0.648 0.776 0.8 0.745 0.739 0.624 0.982 0.939 0.933 0.794 0.885 0.879 0.806 0.764 0.758 0.945 0.752 0.661 0.788 0.988 0.721
a = 0.90	0.606 0.6 0.576 0.594 0.588 0.582 0.77 0.8 0.776 0.806 0.612 0.885 0.794 0.879 0.982 0.745 0.939 0.788 0.739 0.764 0.988 0.933 0.945 0.758 0.752 0.994 0.782 0.842 0.648 0.976
a = 0.85	0.606 0.6 0.8 0.77 0.806 0.776 0.885 0.794 0.879 0.982 0.788 0.594 0.988 0.842 0.939 0.812 0.782 0.764 0.745 0.818 0.994 0.945 0.824 0.758 0.873 0.933 0.836 0.848 0.739 0.83
a = 0.80	0.606 0.8 0.806 0.77 0.885 0.776 0.794 0.879 0.788 0.812 0.982 0.818 0.842 0.824 0.988 0.782 0.836 0.848 0.994 0.83 0.873 0.855 0.764 0.867 0.939 0.945 0.891 0.861 0.897 0.758

Continued on next page

Table A.1 – *Continued from previous page*

a values	**Band wavelengths** (μm)
a = 0.75	0.606 0.8 0.806 0.885 0.794 0.776 0.879 0.77 0.812 0.788 0.818 0.824 0.842 0.836 0.83 0.848 0.782 0.982 0.988 0.873 0.855 0.994 0.891 0.867 0.861 0.897 0.903 0.764 0.945 0.939
a = 0.70	0.8 0.806 0.885 0.794 0.812 0.818 0.879 0.824 0.776 0.788 0.842 0.83 0.836 0.77 0.606 0.848 0.782 0.891 0.855 0.873 0.867 0.861 0.988 0.982 0.897 0.994 0.903 0.764 0.945 0.976
a = 0.65	0.806 0.8 0.812 0.885 0.818 0.794 0.824 0.879 0.842 0.83 0.836 0.788 0.776 0.848 0.891 0.855 0.782 0.873 0.77 0.861 0.867 0.897 0.994 0.988 0.903 0.982 0.764 0.976 0.945 0.939
a = 0.60	0.806 0.8 0.812 0.818 0.885 0.824 0.794 0.83 0.842 0.879 0.836 0.848 0.788 0.891 0.855 0.776 0.782 0.897 0.861 0.873 0.867 0.903 0.77 0.994 0.988 0.982 0.976 0.764 0.945 0.909
a = 0.55	0.806 0.8 0.812 0.818 0.824 0.885 0.794 0.83 0.842 0.836 0.879 0.848 0.891 0.788 0.855 0.897 0.861 0.873 0.776 0.782 0.867 0.903 0.994 0.988 0.77 0.982 0.909 0.976 0.764 0.945
a = 0.50	0.806 0.812 0.8 0.818 0.824 0.885 0.83 0.794 0.842 0.836 0.848 0.891 0.879 0.855 0.788 0.897 0.861 0.873 0.867 0.782 0.903 0.776 0.994 0.988 0.77 0.982 0.909 0.976 0.764 0.945
a = 0.45	0.806 0.812 0.818 0.8 0.824 0.83 0.885 0.836 0.842 0.794 0.891 0.848 0.879 0.855 0.897 0.788 0.861 0.867 0.873 0.782 0.903 0.776 0.994 0.988 0.77 0.909 0.982 0.976 0.97 0.945
a = 0.40	0.806 0.812 0.818 0.824 0.8 0.83 0.836 0.885 0.842 0.891 0.848 0.794 0.855 0.897 0.879 0.861 0.788 0.867 0.873 0.903 0.782 0.776 0.994 0.988 0.909 0.77 0.982 0.976 0.97 0.952
a = 0.35	0.812 0.806 0.818 0.824 0.8 0.83 0.836 0.842 0.891 0.885 0.848 0.794 0.855 0.897 0.879 0.861 0.788 0.867 0.903 0.873 0.782 0.776 0.994 0.909 0.988 0.982 0.77 0.976 0.97 0.952
a = 0.30	0.812 0.806 0.818 0.824 0.83 0.8 0.836 0.891 0.842 0.848 0.885 0.794 0.855 0.897 0.861 0.879 0.788 0.867 0.903 0.873 0.782 0.776 0.994 0.909 0.988 0.982 0.77 0.976 0.915 0.97

Continued on next page

Table A.1 – *Continued from previous page*

a values	**Band wavelengths** (μm)
a = 0.25	0.812 0.806 0.818 0.824 0.83 0.8 0.836 0.891 0.842 0.848 0.885 0.855 0.794 0.897 0.861 0.879 0.867 0.903 0.788 0.873 0.782 0.909 0.994 0.776 0.988 0.982 0.77 0.915 0.976 0.952
a = 0.20	0.812 0.818 0.806 0.824 0.83 0.8 0.836 0.891 0.842 0.848 0.885 0.855 0.897 0.794 0.861 0.879 0.903 0.867 0.788 0.873 0.782 0.909 0.994 0.776 0.988 0.982 0.915 0.77 0.976 0.952
a = 0.15	0.812 0.818 0.806 0.824 0.83 0.8 0.836 0.891 0.842 0.848 0.885 0.855 0.897 0.794 0.861 0.903 0.867 0.879 0.788 0.873 0.782 0.909 0.994 0.776 0.988 0.915 0.982 0.77 0.976 0.952
a = 0.10	0.812 0.818 0.806 0.824 0.83 0.836 0.891 0.8 0.842 0.848 0.855 0.897 0.885 0.794 0.861 0.903 0.867 0.879 0.873 0.788 0.782 0.909 0.994 0.776 0.988 0.915 0.982 0.77 0.976 0.952
a = 0.05	0.812 0.818 0.806 0.824 0.83 0.891 0.836 0.8 0.842 0.848 0.855 0.897 0.885 0.861 0.794 0.903 0.867 0.879 0.873 0.788 0.782 0.909 0.994 0.776 0.988 0.915 0.982 0.77 0.976 0.952

Table A.2: Best band for white boat material.

a values	**Band wavelengths**(μm)
a = 0.99	0.406 0.4 0.412 0.418 0.424 0.43 0.436 0.442 0.448 0.976 0.933 0.455 0.461 0.467 0.758 0.812 0.479 0.473 0.485 0.945 0.509 0.97 0.515 0.873 0.77 0.63 0.842 0.788 0.988 0.891
a = 0.95	0.406 0.4 0.412 0.418 0.424 0.43 0.436 0.442 0.448 0.455 0.461 0.467 0.473 0.479 0.485 0.509 0.515 0.491 0.497 0.503 0.521 0.533 0.527 0.539 0.545 0.552 0.63 0.57 0.558 0.624
a = 0.90	0.406 0.4 0.412 0.418 0.424 0.43 0.436 0.442 0.448 0.455 0.461 0.467 0.473 0.479 0.485 0.509 0.491 0.515 0.497 0.503 0.521 0.533 0.527 0.539 0.545 0.552 0.558 0.57 0.564 0.576
a = 0.85	0.406 0.412 0.4 0.418 0.424 0.43 0.436 0.442 0.448 0.455 0.461 0.467 0.473 0.479 0.485 0.491 0.509 0.497 0.515 0.503 0.521 0.527 0.533 0.539 0.545 0.552 0.558 0.57 0.564 0.576

Continued on next page

Table A.2 – *Continued from previous page*

a values	**Band wavelengths** (μm)
a = 0.80	0.406 0.412 0.4 0.418 0.424 0.43 0.436 0.442 0.448 0.455 0.461 0.467 0.473 0.479 0.485 0.491 0.497 0.509 0.515 0.503 0.521 0.527 0.533 0.539 0.545 0.552 0.558 0.564 0.57 0.576
a = 0.75	0.406 0.412 0.418 0.424 0.43 0.442 0.436 0.448 0.455 0.461 0.467 0.473 0.479 0.485 0.491 0.497 0.509 0.503 0.515 0.521 0.527 0.533 0.539 0.545 0.552 0.558 0.564 0.57 0.576 0.582
a = 0.70	0.412 0.418 0.406 0.424 0.43 0.442 0.448 0.455 0.436 0.461 0.467 0.473 0.479 0.485 0.491 0.497 0.509 0.503 0.515 0.521 0.527 0.533 0.539 0.545 0.552 0.558 0.564 0.57 0.576 0.582
a = 0.65	0.412 0.448 0.455 0.442 0.461 0.467 0.418 0.473 0.479 0.485 0.436 0.43 0.424 0.491 0.497 0.509 0.503 0.515 0.521 0.527 0.533 0.539 0.545 0.552 0.558 0.564 0.57 0.576 0.582 0.588
a = 0.60	0.455 0.461 0.448 0.467 0.473 0.442 0.479 0.485 0.491 0.436 0.497 0.43 0.503 0.509 0.515 0.521 0.527 0.424 0.533 0.539 0.545 0.552 0.558 0.418 0.564 0.57 0.576 0.582 0.588 0.594
a = 0.55	0.461 0.455 0.467 0.448 0.473 0.479 0.485 0.442 0.491 0.497 0.436 0.503 0.509 0.515 0.521 0.43 0.527 0.533 0.539 0.545 0.552 0.424 0.558 0.564 0.57 0.576 0.582 0.588 0.594 0.418
a = 0.50	0.461 0.455 0.467 0.473 0.448 0.479 0.485 0.491 0.442 0.497 0.503 0.509 0.436 0.515 0.521 0.527 0.533 0.43 0.539 0.545 0.552 0.558 0.564 0.57 0.424 0.576 0.582 0.588 0.594 0.6
a = 0.45	0.461 0.467 0.455 0.473 0.479 0.448 0.485 0.491 0.442 0.497 0.503 0.509 0.515 0.436 0.521 0.527 0.533 0.539 0.43 0.545 0.552 0.558 0.564 0.57 0.576 0.582 0.424 0.588 0.594 0.6
a = 0.40	0.461 0.467 0.455 0.473 0.479 0.485 0.448 0.491 0.497 0.442 0.503 0.509 0.515 0.521 0.436 0.527 0.533 0.539 0.545 0.552 0.43 0.558 0.564 0.57 0.576 0.582 0.588 0.424 0.594 0.6
a = 0.35	0.461 0.467 0.473 0.455 0.479 0.485 0.448 0.491 0.497 0.442 0.503 0.509 0.515 0.521 0.436 0.527 0.533 0.539 0.545 0.552 0.558 0.43 0.564 0.57 0.576 0.582 0.588 0.594 0.424 0.6

Continued on next page

Table A.2 – *Continued from previous page*

a values	**Band wavelengths** (μm)
a = 0.30	0.461 0.467 0.473 0.455 0.479 0.485 0.448 0.491 0.497 0.503 0.442 0.509 0.515 0.521 0.527 0.436 0.533 0.539 0.545 0.552 0.558 0.43 0.564 0.57 0.576 0.582 0.588 0.594 0.6 0.606
a = 0.25	.467 0.461 0.473 0.455 0.479 0.485 0.491 0.448 0.497 0.503 0.442 0.509 0.515 0.521 0.527 0.436 0.533 0.539 0.545 0.552 0.558 0.564 0.43 0.57 0.576 0.582 0.588 0.594 0.6 0.606
a = 0.20	0.467 0.461 0.473 0.455 0.479 0.485 0.491 0.448 0.497 0.503 0.442 0.509 0.515 0.521 0.527 0.533 0.436 0.539 0.545 0.552 0.558 0.564 0.43 0.57 0.576 0.582 0.588 0.594 0.6 0.606
a = 0.15	0.467 0.461 0.473 0.479 0.455 0.485 0.491 0.448 0.497 0.503 0.509 0.442 0.515 0.521 0.527 0.533 0.436 0.539 0.545 0.552 0.558 0.564 0.57 0.43 0.576 0.582 0.588 0.594 0.6 0.606
a = 0.10	0.467 0.461 0.473 0.479 0.455 0.485 0.491 0.448 0.497 0.503 0.509 0.442 0.515 0.521 0.527 0.533 0.436 0.539 0.545 0.552 0.558 0.564 0.57 0.43 0.576 0.582 0.588 0.594 0.6 0.606
a = 0.05	0.467 0.461 0.473 0.479 0.455 0.485 0.491 0.448 0.497 0.503 0.509 0.515 0.442 0.521 0.527 0.533 0.539 0.436 0.545 0.552 0.558 0.564 0.57 0.576 0.43 0.582 0.588 0.594 0.6 0.606

Table A.3: Best band for black tire material.

a = 0.99	0.873 0.867 0.861 0.576 0.515 0.497 0.491 0.442 0.43 0.424 0.406 0.4 0.879 0.418 0.539 0.891 0.885 0.467 0.685 0.855 0.679 0.848 0.842 0.461 0.545 0.836 0.897 0.994 0.988 0.982
a = 0.95	0.873 0.867 0.861 0.879 0.891 0.885 0.576 0.515 0.497 0.491 0.539 0.442 0.685 0.43 0.855 0.424 0.897 0.406 0.679 0.467 0.848 0.418 0.4 0.842 0.836 0.545 0.994 0.988 0.982 0.976
a = 0.90	0.873 0.867 0.861 0.879 0.891 0.885 0.897 0.576 0.515 0.685 0.855 0.497 0.539 0.848 0.491 0.842 0.679 0.903 0.909 0.836 0.994 0.988 0.982 0.976 0.97 0.964 0.442 0.958 0.43 0.83

Continued on next page

Table A.3 – *Continued from previous page*

a values	**Band wavelengths** (μm)
a = 0.85	0.873 0.867 0.891 0.879 0.885 0.861 0.897 0.903 0.576 0.909 0.855 0.685 0.915 0.848 0.842 0.515 0.539 0.679 0.994 0.988 0.982 0.976 0.97 0.964 0.836 0.497 0.958 0.945 0.83 0.824
a = 0.80	0.873 0.891 0.885 0.879 0.867 0.897 0.861 0.903 0.909 0.915 0.855 0.576 0.685 0.848 0.842 0.994 0.988 0.982 0.976 0.97 0.964 0.921 0.958 0.939 0.679 0.836 0.945 0.952 0.539 0.515
a = 0.75	0.891 0.873 0.885 0.879 0.897 0.867 0.903 0.861 0.909 0.915 0.921 0.855 0.848 0.685 0.842 0.994 0.988 0.982 0.976 0.97 0.964 0.576 0.939 0.927 0.945 0.958 0.952 0.836 0.679 0.83
a = 0.70	.891 0.885 0.873 0.897 0.879 0.903 0.867 0.909 0.915 0.861 0.921 0.855 0.927 0.939 0.848 0.945 0.994 0.988 0.982 0.976 0.97 0.964 0.958 0.842 0.685 0.952 0.933 0.576 0.836 0.83
a = 0.65	0.891 0.897 0.885 0.879 0.873 0.903 0.909 0.867 0.915 0.861 0.921 0.927 0.855 0.939 0.945 0.933 0.994 0.988 0.982 0.976 0.97 0.964 0.848 0.958 0.952 0.842 0.685 0.836 0.83 0.824
a = 0.60	0.891 0.897 0.885 0.879 0.903 0.873 0.909 0.915 0.867 0.921 0.861 0.927 0.939 0.933 0.855 0.945 0.994 0.988 0.982 0.976 0.97 0.964 0.952 0.958 0.848 0.842 0.685 0.836 0.83 0.824
a = 0.55	0.891 0.897 0.885 0.903 0.879 0.909 0.873 0.915 0.867 0.921 0.927 0.861 0.933 0.939 0.945 0.855 0.952 0.994 0.988 0.982 0.976 0.97 0.964 0.958 0.848 0.842 0.836 0.685 0.83 0.824
a = 0.50	0.891 0.897 0.885 0.903 0.879 0.909 0.915 0.873 0.921 0.867 0.927 0.861 0.933 0.939 0.945 0.855 0.952 0.994 0.988 0.982 0.976 0.97 0.964 0.958 0.848 0.842 0.836 0.83 0.824 0.818
a = 0.45	0.897 0.891 0.903 0.885 0.909 0.879 0.915 0.873 0.921 0.867 0.927 0.861 0.933 0.939 0.945 0.952 0.855 0.958 0.994 0.988 0.982 0.976 0.97 0.964 0.848 0.842 0.836 0.83 0.824 0.818
a = 0.40	0.897 0.891 0.903 0.885 0.909 0.879 0.915 0.873 0.921 0.927 0.867 0.933 0.861 0.939 0.945 0.952 0.958 0.855 0.994 0.988 0.982 0.976 0.97 0.964 0.848 0.842 0.836 0.83 0.824 0.818

Continued on next page

Table A.3 – *Continued from previous page*

a values	**Band wavelengths** (μm)
a = 0.35	0.897 0.891 0.903 0.885 0.909 0.879 0.915 0.921 0.873 0.927 0.867 0.933 0.861 0.939 0.945 0.952 0.958 0.994 0.988 0.982 0.976 0.97 0.964 0.855 0.848 0.842 0.836 0.83 0.824 0.818
a = 0.30	0.897 0.903 0.891 0.909 0.885 0.915 0.879 0.921 0.873 0.927 0.867 0.933 0.939 0.861 0.945 0.952 0.958 0.994 0.988 0.982 0.976 0.97 0.964 0.855 0.848 0.842 0.836 0.83 0.824 0.818
a = 0.25	0.897 0.903 0.891 0.909 0.885 0.915 0.879 0.921 0.873 0.927 0.867 0.933 0.939 0.861 0.945 0.952 0.958 0.994 0.988 0.982 0.976 0.97 0.964 0.855 0.848 0.842 0.836 0.83 0.824 0.818
a = 0.20	0.897 0.903 0.891 0.909 0.885 0.915 0.879 0.921 0.873 0.927 0.867 0.933 0.939 0.945 0.861 0.952 0.958 0.994 0.988 0.982 0.976 0.97 0.964 0.855 0.848 0.842 0.836 0.83 0.824 0.818
a = 0.15	0.897 0.903 0.891 0.909 0.885 0.915 0.879 0.921 0.873 0.927 0.933 0.867 0.939 0.945 0.861 0.952 0.958 0.994 0.988 0.982 0.976 0.97 0.964 0.855 0.848 0.842 0.836 0.83 0.824 0.818
a = 0.10	0.897 0.903 0.891 0.909 0.885 0.915 0.879 0.921 0.927 0.873 0.933 0.867 0.939 0.945 0.952 0.861 0.958 0.994 0.988 0.982 0.976 0.97 0.964 0.855 0.848 0.842 0.836 0.83 0.824 0.818
a = 0.05	0.897 0.903 0.891 0.909 0.885 0.915 0.879 0.921 0.927 0.873 0.933 0.867 0.939 0.945 0.952 0.861 0.958 0.994 0.988 0.982 0.976 0.97 0.964 0.855 0.848 0.842 0.836 0.83 0.824 0.818

Table A.4: Best band for green car material.

a = 0.99	0.758 0.745 0.752 0.4 0.739 0.406 0.733 0.764 0.448 0.77 0.455 0.442 0.806 0.794 0.461 0.897 0.436 0.812 0.467 0.782 0.8 0.788 0.412 0.727 0.952 0.964 0.424 0.933 0.43 0.418
a = 95	0.964 0.952 0.758 0.958 0.976 0.988 0.933 0.897 0.97 0.939 0.915 0.945 0.745 0.982 0.752 0.909 0.994 0.879 0.891 0.867 0.873 0.903 0.861 0.921 0.885 0.848 0.855 0.806 0.812 0.83

Continued on next page

Table A.4 – *Continued from previous page*

a values	**Band wavelengths** (μm)
a = 90	0.964 0.988 0.976 0.958 0.952 0.97 0.982 0.994 0.933 0.939 0.945 0.915 0.897 0.909 0.921 0.891 0.903 0.879 0.885 0.873 0.867 0.861 0.855 0.848 0.927 0.83 0.842 0.836 0.824 0.812
a = 0.85	0.988 0.976 0.964 0.994 0.982 0.97 0.958 0.952 0.945 0.939 0.933 0.915 0.909 0.897 0.921 0.903 0.891 0.879 0.927 0.885 0.873 0.867 0.861 0.855 0.848 0.842 0.836 0.83 0.824 0.818
a = 0.80	0.988 0.976 0.994 0.982 0.964 0.97 0.958 0.952 0.945 0.939 0.933 0.915 0.921 0.909 0.897 0.903 0.927 0.891 0.885 0.879 0.873 0.867 0.861 0.855 0.848 0.842 0.836 0.83 0.824 0.818
a = 0.75	0.988 0.994 0.976 0.982 0.964 0.97 0.958 0.952 0.945 0.939 0.933 0.915 0.921 0.909 0.897 0.927 0.903 0.891 0.885 0.879 0.873 0.867 0.861 0.855 0.848 0.842 0.836 0.83 0.824 0.818
a = 0.70	0.988 0.994 0.976 0.982 0.97 0.964 0.958 0.952 0.945 0.939 0.933 0.915 0.921 0.909 0.927 0.897 0.903 0.891 0.885 0.879 0.873 0.867 0.861 0.855 0.848 0.842 0.836 0.83 0.824 0.818
a = 0.65	0.988 0.994 0.982 0.976 0.97 0.964 0.958 0.952 0.945 0.939 0.933 0.921 0.915 0.927 0.909 0.903 0.897 0.891 0.885 0.879 0.873 0.867 0.861 0.855 0.848 0.842 0.836 0.83 0.824 0.818
a = 0.60	0.994 0.988 0.982 0.976 0.97 0.964 0.958 0.952 0.945 0.939 0.933 0.921 0.915 0.927 0.909 0.903 0.897 0.891 0.885 0.879 0.873 0.867 0.861 0.855 0.848 0.842 0.836 0.83 0.824 0.818
a = 0.55	0.994 0.988 0.982 0.976 0.97 0.964 0.958 0.952 0.945 0.939 0.933 0.921 0.915 0.927 0.909 0.903 0.897 0.891 0.885 0.879 0.873 0.867 0.861 0.855 0.848 0.842 0.836 0.83 0.824 0.818
a = 0.50	0.994 0.988 0.982 0.976 0.97 0.964 0.958 0.952 0.945 0.939 0.933 0.921 0.927 0.915 0.909 0.903 0.897 0.891 0.885 0.879 0.873 0.867 0.861 0.855 0.848 0.842 0.836 0.83 0.824 0.818
a = 0.45	0.994 0.988 0.982 0.976 0.97 0.964 0.958 0.952 0.945 0.939 0.933 0.921 0.927 0.915 0.909 0.903 0.897 0.891 0.885 0.879 0.873 0.867 0.861 0.855 0.848 0.842 0.836 0.83 0.824 0.818

Continued on next page

Table A.4 – *Continued from previous page*

a values	**Band wavelengths** (μm)
a = 0.40	0.994 0.988 0.982 0.976 0.97 0.964 0.958 0.952 0.945 0.939 0.933 0.921 0.927 0.915 0.909 0.903 0.897 0.891 0.885 0.879 0.873 0.867 0.861 0.855 0.848 0.842 0.836 0.83 0.824 0.818
a = 0.35	0.994 0.988 0.982 0.976 0.97 0.964 0.958 0.952 0.945 0.939 0.933 0.927 0.921 0.915 0.909 0.903 0.897 0.891 0.885 0.879 0.873 0.867 0.861 0.855 0.848 0.842 0.836 0.83 0.824 0.818
a = 0.30	0.994 0.988 0.982 0.976 0.97 0.964 0.958 0.952 0.945 0.939 0.933 0.927 0.921 0.915 0.909 0.903 0.897 0.891 0.885 0.879 0.873 0.867 0.861 0.855 0.848 0.842 0.836 0.83 0.824 0.818
a = 0.25	0.994 0.988 0.982 0.976 0.97 0.964 0.958 0.952 0.945 0.939 0.933 0.927 0.921 0.915 0.909 0.903 0.897 0.891 0.885 0.879 0.873 0.867 0.861 0.855 0.848 0.842 0.836 0.83 0.824 0.818
a = 0.20	0.994 0.988 0.982 0.976 0.97 0.964 0.958 0.952 0.945 0.939 0.933 0.927 0.921 0.915 0.909 0.903 0.897 0.891 0.885 0.879 0.873 0.867 0.861 0.855 0.848 0.842 0.836 0.83 0.824 0.818
a = 0.15	0.994 0.988 0.982 0.976 0.97 0.964 0.958 0.952 0.945 0.939 0.927 0.933 0.921 0.915 0.909 0.903 0.897 0.891 0.885 0.879 0.873 0.867 0.861 0.855 0.848 0.842 0.836 0.83 0.824 0.818
a = 0.10	0.994 0.988 0.982 0.976 0.97 0.964 0.958 0.952 0.945 0.939 0.927 0.933 0.921 0.915 0.909 0.903 0.897 0.891 0.885 0.879 0.873 0.867 0.861 0.855 0.848 0.842 0.836 0.83 0.824 0.818
a = 0.05	0.994 0.988 0.982 0.976 0.97 0.964 0.958 0.952 0.945 0.939 0.927 0.933 0.921 0.915 0.909 0.903 0.897 0.891 0.885 0.879 0.873 0.867 0.861 0.855 0.848 0.842 0.836 0.83 0.824 0.818

Table A.5: Best band for yellow wood.

a = 0.99	0.43 0.406 0.412 0.97 0.424 0.418 0.436 0.4 0.442 0.448 0.952 0.933 0.455 0.964 0.915 0.939 0.903 0.982 0.461 0.618 0.891 0.721 0.691 0.988 0.879 0.994 0.885 0.727 0.606 0.83

Continued on next page

Table A.5 – *Continued from previous page*

a values	**Band wavelengths** (μm)
a = 0.95	0.43 0.406 0.412 0.424 0.418 0.436 0.4 0.442 0.448 0.455 0.461 0.467 0.473 0.479 0.485 0.97 0.952 0.491 0.618 0.933 0.964 0.606 0.594 0.6 0.582 0.691 0.624 0.661 0.655 0.721
a = 90	0.43 0.424 0.406 0.412 0.436 0.418 0.442 0.4 0.448 0.455 0.461 0.467 0.473 0.479 0.485 0.491 0.497 0.503 0.509 0.97 0.618 0.582 0.594 0.606 0.6 0.576 0.564 0.588 0.624 0.612
a = 0.85	0.43 0.424 0.436 0.412 0.406 0.418 0.442 0.4 0.448 0.455 0.461 0.467 0.473 0.479 0.485 0.491 0.497 0.503 0.509 0.618 0.564 0.582 0.594 0.576 0.606 0.6 0.588 0.57 0.515 0.612
a = 0.80	0.43 0.436 0.424 0.412 0.418 0.406 0.442 0.4 0.448 0.455 0.461 0.467 0.473 0.479 0.485 0.491 0.497 0.503 0.509 0.515 0.564 0.582 0.576 0.594 0.57 0.618 0.6 0.588 0.606 0.558
a = 0.75	0.43 0.436 0.424 0.442 0.418 0.412 0.406 0.448 0.4 0.455 0.461 0.467 0.473 0.479 0.485 0.491 0.497 0.503 0.509 0.515 0.521 0.564 0.552 0.558 0.582 0.576 0.57 0.545 0.594 0.588
a = 0.70	0.43 0.436 0.424 0.442 0.418 0.412 0.406 0.448 0.4 0.455 0.461 0.467 0.473 0.479 0.485 0.491 0.497 0.503 0.509 0.515 0.521 0.527 0.552 0.545 0.533 0.564 0.539 0.558 0.57 0.576
a = 0.65	0.43 0.436 0.442 0.424 0.418 0.412 0.448 0.406 0.4 0.455 0.461 0.467 0.473 0.479 0.485 0.491 0.497 0.503 0.509 0.515 0.521 0.527 0.533 0.539 0.545 0.552 0.558 0.564 0.57 0.576
a = 0.60	0.436 0.43 0.442 0.424 0.418 0.448 0.412 0.406 0.4 0.455 0.461 0.467 0.473 0.479 0.485 0.491 0.497 0.503 0.509 0.515 0.521 0.527 0.533 0.539 0.545 0.552 0.558 0.564 0.57 0.576
a = 0.55	0.436 0.43 0.442 0.424 0.448 0.418 0.412 0.406 0.455 0.4 0.461 0.467 0.473 0.479 0.485 0.491 0.497 0.503 0.509 0.515 0.521 0.527 0.533 0.539 0.545 0.552 0.558 0.564 0.57 0.576
a = 0.50	0.436 0.442 0.43 0.448 0.424 0.418 0.412 0.406 0.455 0.4 0.461 0.467 0.473 0.479 0.485 0.491 0.497 0.503 0.509 0.515 0.521 0.527 0.533 0.539 0.545 0.552 0.558 0.564 0.57 0.576

Continued on next page

Table A.5 – *Continued from previous page*

a values	**Band wavelengths** (μm)
a = 0.45	0.436 0.442 0.43 0.448 0.424 0.418 0.412 0.455 0.406 0.4 0.461 0.467 0.473 0.479 0.485 0.491 0.497 0.503 0.509 0.515 0.521 0.527 0.533 0.539 0.545 0.552 0.558 0.564 0.57 0.576
a = 0.40	0.436 0.442 0.43 0.448 0.424 0.418 0.455 0.412 0.406 0.4 0.461 0.467 0.473 0.479 0.485 0.491 0.497 0.503 0.509 0.515 0.521 0.527 0.533 0.539 0.545 0.552 0.558 0.564 0.57 0.576
a = 0.35	0.442 0.436 0.43 0.448 0.424 0.418 0.455 0.412 0.406 0.4 0.461 0.467 0.473 0.479 0.485 0.491 0.497 0.503 0.509 0.515 0.521 0.527 0.533 0.539 0.545 0.552 0.558 0.564 0.57 0.576
a = 0.30	0.442 0.436 0.448 0.43 0.424 0.455 0.418 0.412 0.406 0.4 0.461 0.467 0.473 0.479 0.485 0.491 0.497 0.503 0.509 0.515 0.521 0.527 0.533 0.539 0.545 0.552 0.558 0.564 0.57 0.576
a = 0.25	0.442 0.436 0.448 0.43 0.424 0.455 0.418 0.412 0.406 0.4 0.461 0.467 0.473 0.479 0.485 0.491 0.497 0.503 0.509 0.515 0.521 0.527 0.533 0.539 0.545 0.552 0.558 0.564 0.57 0.576
a = 0.20	0.442 0.436 0.448 0.43 0.455 0.424 0.418 0.412 0.406 0.461 0.4 0.467 0.473 0.479 0.485 0.491 0.497 0.503 0.509 0.515 0.521 0.527 0.533 0.539 0.545 0.552 0.558 0.564 0.57 0.576
a = 0.15	0.442 0.436 0.448 0.43 0.455 0.424 0.418 0.412 0.461 0.406 0.4 0.467 0.473 0.479 0.485 0.491 0.497 0.503 0.509 0.515 0.521 0.527 0.533 0.539 0.545 0.552 0.558 0.564 0.57 0.576
a = 0.10	0.442 0.436 0.448 0.43 0.455 0.424 0.418 0.412 0.461 0.406 0.4 0.467 0.473 0.479 0.485 0.491 0.497 0.503 0.509 0.515 0.521 0.527 0.533 0.539 0.545 0.552 0.558 0.564 0.57 0.576
a = 0.05	0.442 0.448 0.436 0.43 0.455 0.424 0.418 0.412 0.461 0.406 0.4 0.467 0.473 0.479 0.485 0.491 0.497 0.503 0.509 0.515 0.521 0.527 0.533 0.539 0.545 0.552 0.558 0.564 0.57 0.576

Table A.6: Best band for green wood.

a = 0.99	0.552 0.564 0.558 0.545 0.57 0.576 0.582 0.588 0.539 0.594 0.533 0.6 0.606 0.612 0.618 0.715 0.63 0.642 0.636 0.624 0.952 0.927 0.709 0.721 0.43 0.527 0.424 0.648 0.703 0.412
a = 0.95	0.576 0.588 0.564 0.57 0.582 0.558 0.552 0.594 0.545 0.6 0.539 0.606 0.612 0.618 0.642 0.63 0.636 0.624 0.424 0.43 0.412 0.715 0.4 0.406 0.436 0.418 0.533 0.648 0.442 0.709
a = 90	0.588 0.582 0.594 0.576 0.57 0.6 0.564 0.606 0.558 0.552 0.612 0.618 0.412 0.4 0.424 0.43 0.406 0.642 0.418 0.436 0.63 0.636 0.442 0.624 0.648 0.545 0.655 0.715 0.448 0.709
a = 0.85	0.588 0.594 0.582 0.6 0.576 0.606 0.4 0.412 0.406 0.424 0.43 0.418 0.436 0.612 0.442 0.618 0.642 0.63 0.57 0.636 0.624 0.448 0.648 0.655 0.564 0.455 0.715 0.661 0.709 0.667
a = 0.80	0.4 0.594 0.406 0.412 0.424 0.43 0.418 0.588 0.436 0.6 0.442 0.606 0.612 0.618 0.642 0.448 0.63 0.636 0.582 0.624 0.648 0.655 0.455 0.661 0.576 0.667 0.715 0.709 0.721 0.673
a = 0.75	0.4 0.406 0.412 0.424 0.418 0.43 0.436 0.442 0.448 0.594 0.6 0.606 0.642 0.618 0.612 0.63 0.636 0.624 0.648 0.455 0.588 0.655 0.661 0.667 0.461 0.582 0.673 0.715 0.679 0.709
a = 0.70	0.4 0.406 0.412 0.424 0.418 0.43 0.436 0.442 0.448 0.642 0.455 0.63 0.618 0.636 0.612 0.648 0.606 0.624 0.6 0.655 0.594 0.661 0.461 0.667 0.588 0.673 0.679 0.715 0.685 0.721
a = 0.65	0.4 0.406 0.412 0.418 0.424 0.43 0.436 0.442 0.448 0.455 0.642 0.636 0.63 0.648 0.618 0.624 0.612 0.655 0.606 0.6 0.661 0.461 0.667 0.594 0.673 0.679 0.467 0.685 0.715 0.588
a = 0.60	0.4 0.406 0.412 0.418 0.424 0.43 0.436 0.442 0.448 0.455 0.642 0.636 0.648 0.63 0.618 0.655 0.624 0.612 0.461 0.661 0.606 0.667 0.6 0.673 0.594 0.679 0.467 0.685 0.715 0.721
a = 0.55	0.4 0.406 0.412 0.418 0.424 0.43 0.436 0.442 0.448 0.455 0.642 0.648 0.636 0.63 0.655 0.461 0.624 0.618 0.612 0.661 0.606 0.667 0.673 0.6 0.467 0.679 0.685 0.594 0.715 0.691

Continued on next page

Table A.6 – *Continued from previous page*

a values	**Band wavelengths** (μm)
a = 0.50	0.4 0.406 0.412 0.418 0.424 0.43 0.436 0.442 0.448 0.455 0.642 0.648 0.461 0.636 0.63 0.655 0.624 0.618 0.661 0.612 0.667 0.606 0.673 0.467 0.6 0.679 0.685 0.691 0.715 0.721
a = 0.45	0.4 0.406 0.412 0.418 0.424 0.43 0.436 0.442 0.448 0.455 0.461 0.642 0.648 0.636 0.655 0.63 0.624 0.618 0.661 0.612 0.667 0.467 0.606 0.673 0.679 0.6 0.685 0.691 0.473 0.721
a = 0.40	0.4 0.406 0.412 0.418 0.424 0.43 0.436 0.442 0.448 0.455 0.461 0.642 0.648 0.636 0.655 0.63 0.624 0.661 0.618 0.667 0.612 0.467 0.673 0.606 0.679 0.685 0.6 0.473 0.691 0.721
a = 0.35	0.4 0.406 0.412 0.418 0.424 0.43 0.436 0.442 0.448 0.455 0.461 0.648 0.642 0.655 0.636 0.63 0.624 0.661 0.618 0.667 0.467 0.612 0.673 0.606 0.679 0.685 0.473 0.6 0.691 0.721
a = 0.30	0.4 0.406 0.412 0.418 0.424 0.43 0.436 0.442 0.448 0.455 0.461 0.648 0.642 0.655 0.636 0.63 0.661 0.624 0.618 0.467 0.667 0.612 0.673 0.606 0.679 0.685 0.473 0.6 0.691 0.721
a = 0.25	0.4 0.406 0.412 0.418 0.424 0.43 0.436 0.442 0.448 0.455 0.461 0.648 0.642 0.655 0.636 0.63 0.661 0.624 0.467 0.618 0.667 0.612 0.673 0.606 0.679 0.473 0.685 0.691 0.6 0.697
a = 0.20	0.4 0.406 0.412 0.418 0.424 0.43 0.436 0.442 0.448 0.455 0.461 0.648 0.642 0.655 0.636 0.661 0.63 0.624 0.467 0.618 0.667 0.612 0.673 0.679 0.606 0.473 0.685 0.691 0.6 0.697
a = 0.15	0.4 0.406 0.412 0.418 0.424 0.43 0.436 0.442 0.448 0.455 0.461 0.648 0.655 0.642 0.636 0.661 0.63 0.467 0.624 0.667 0.618 0.673 0.612 0.679 0.606 0.473 0.685 0.691 0.6 0.697
a = 0.10	0.4 0.406 0.412 0.418 0.424 0.43 0.436 0.442 0.448 0.455 0.461 0.648 0.655 0.642 0.636 0.467 0.661 0.63 0.624 0.667 0.618 0.673 0.612 0.679 0.473 0.606 0.685 0.691 0.697 0.721
a = 0.05	0.4 0.406 0.412 0.418 0.424 0.43 0.436 0.442 0.448 0.455 0.461 0.648 0.655 0.642 0.467 0.636 0.661 0.63 0.624 0.667 0.618 0.673 0.612 0.679 0.473 0.606 0.685 0.691 0.697 0.721

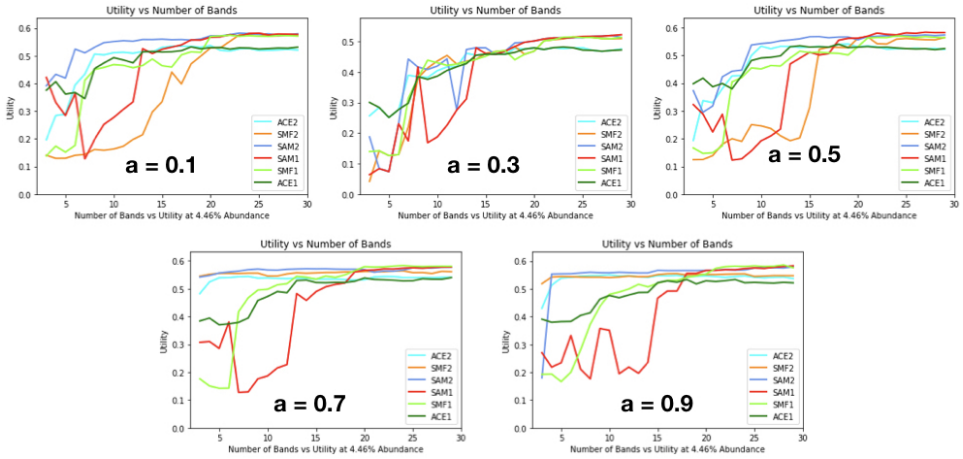

Figure A.21: Results for set with median target abundance of 4.46%.

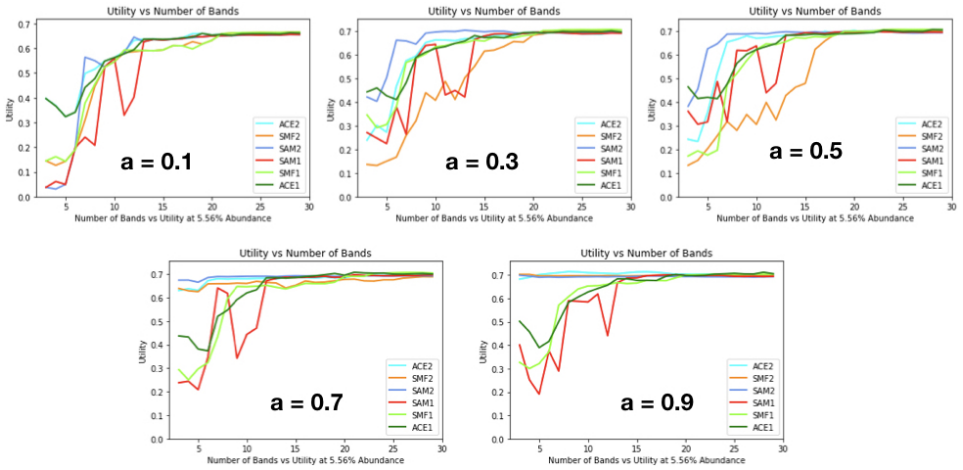

Figure A.22: Results for set with median target abundance of 5.56%.

A.3 Orange Lifeboat Analysis

Figures A.21 - A.27 showing utility vs number of bands for orange lifeboat in ocean. ACE1, SMF1, and SAM1 are results for bands calculated using TBC using the three target detection methods. ACE2, SMF2, and SAM2 are results for bands calculated using BOTS.

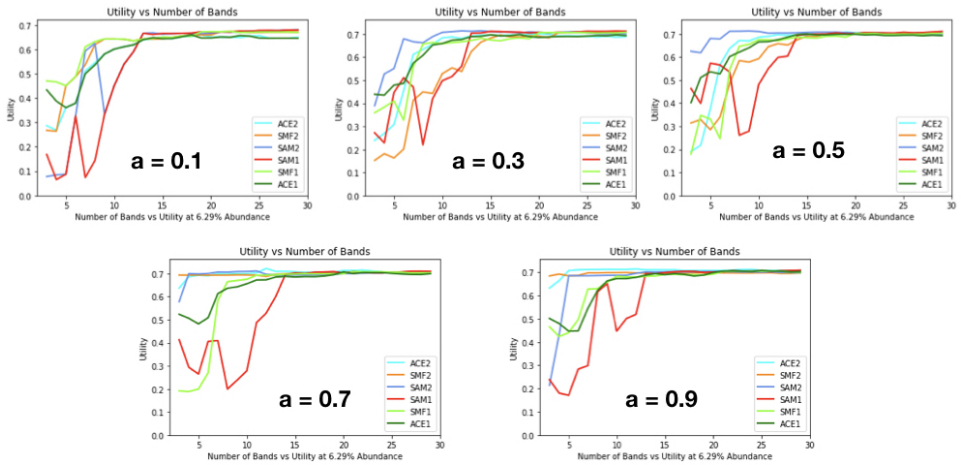

Figure A.23: Results for set with median target abundance of 6.29%.

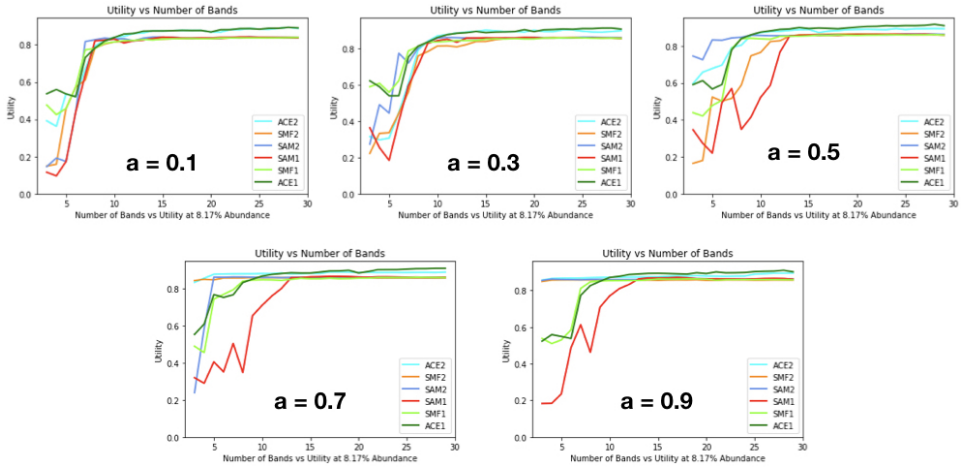

Figure A.24: Results for set with median target abundance of 8.17%.

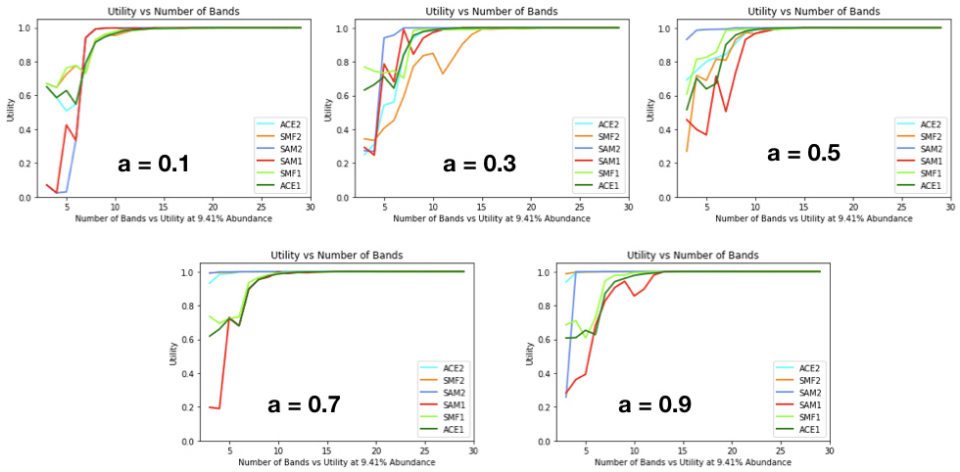

Figure A.25: Results for set with median target abundance of 9.41%.

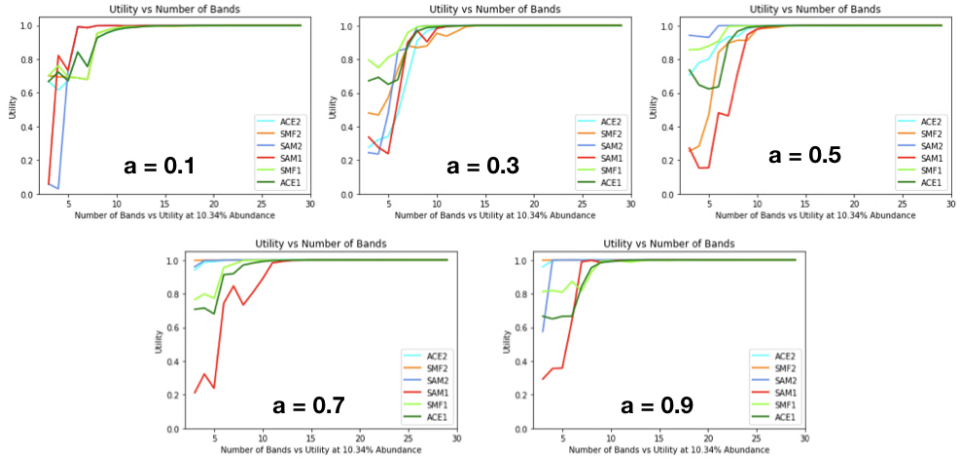

Figure A.26: Results for set with median target abundance of 10.34%.

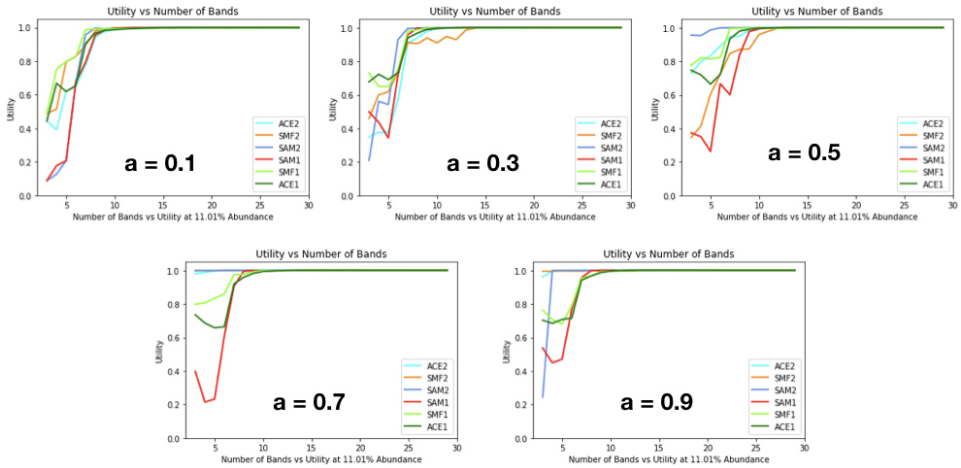

Figure A.27: Results for set with median target abundance of 11.01%.

A.4 Yellow Wood Analysis

Figure A.28 showing utility vs number of bands for yellow wood target. The results show the average of the three target detection methods and four images. Method 1 is the TBC method. Method 2 is the BOTS method.

A.5 Green Wood Analysis

Figures A.29 - A.37 showing utility vs number of bands for green wood target. Max value in each image shows the utiltiy value obtained using all the bands. ACE1, SMF1, and SAM1 are results for bands selected using TBC. ACE2, SMF2, and SAM2 are results for bands selected using BOTS.

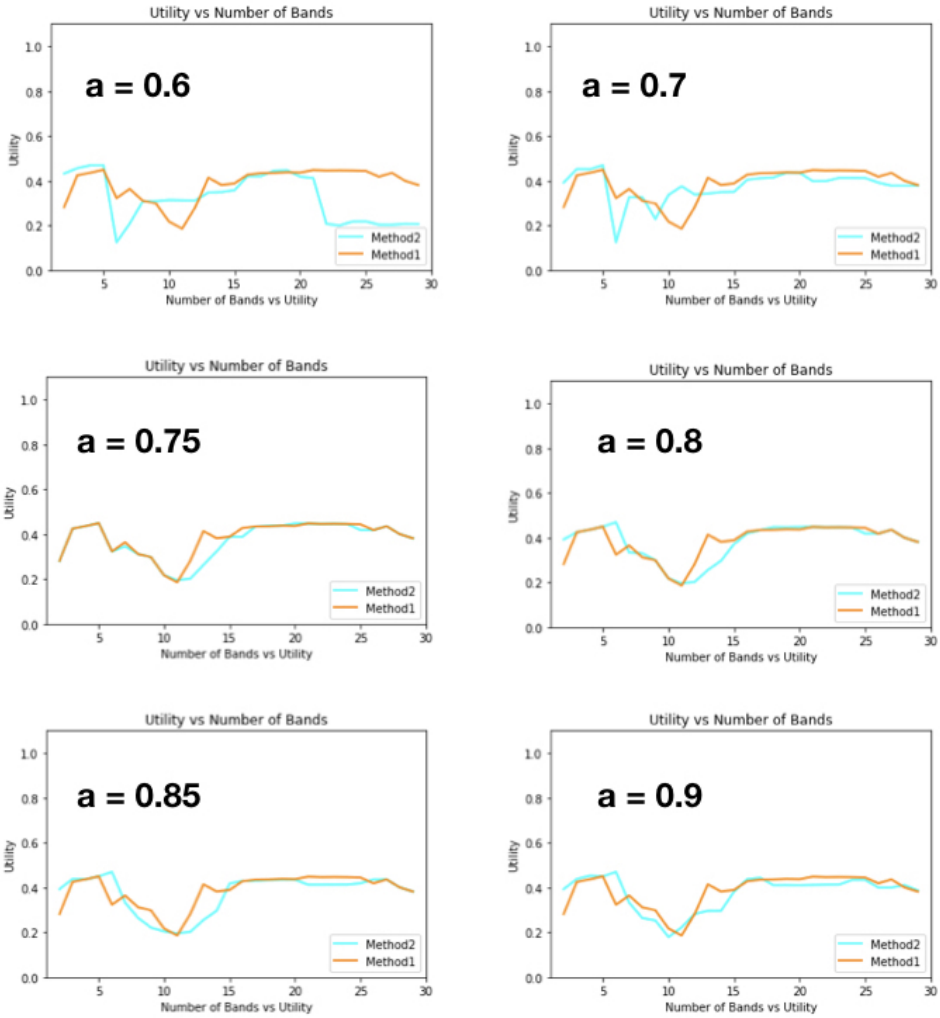

Figure A.28: Utility vs Number of Bands for Yellow Wood target.

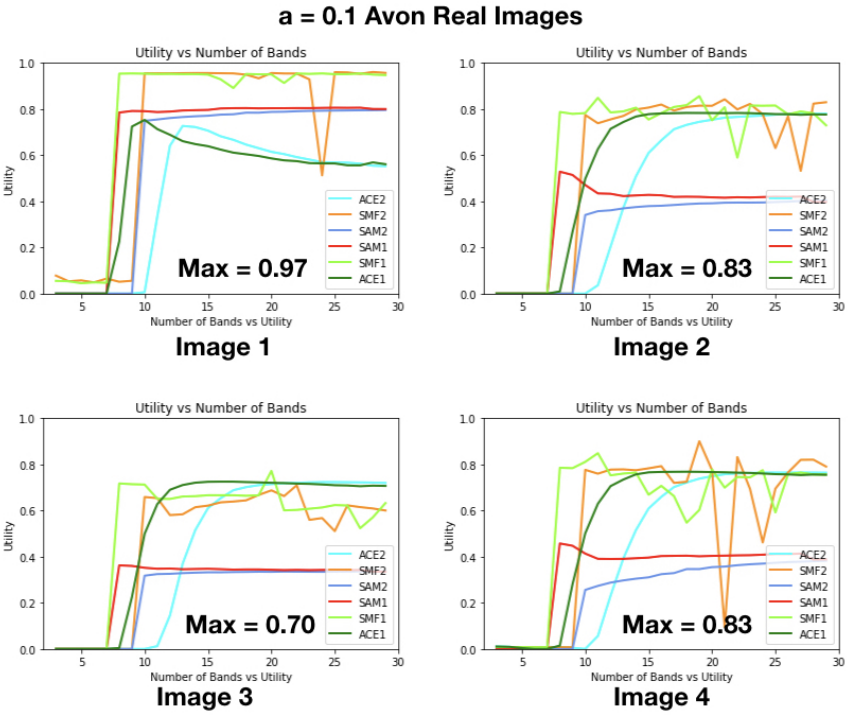

Figure A.29: a=0.1

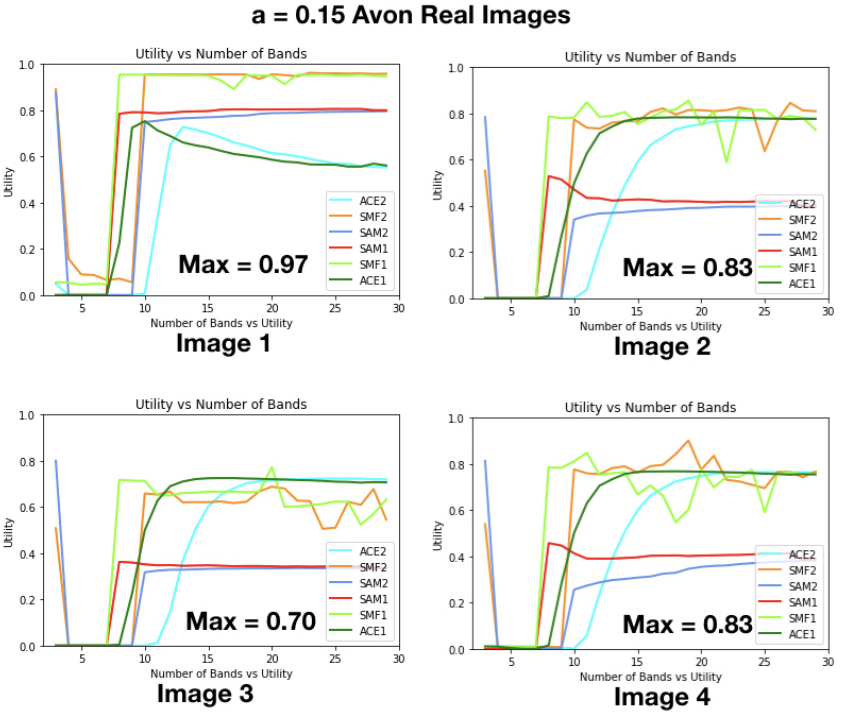

Figure A.30: a=0.15

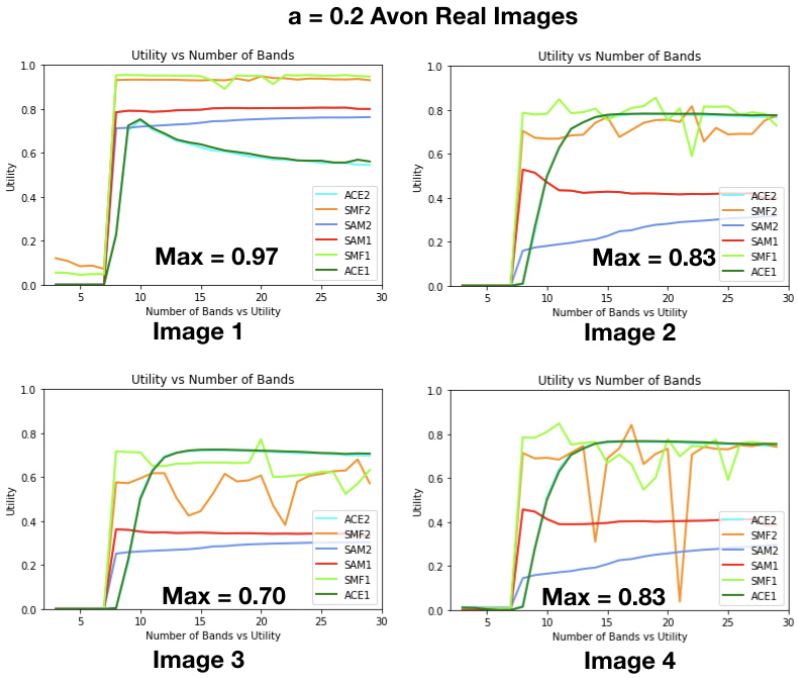

Figure A.31: a=0.2

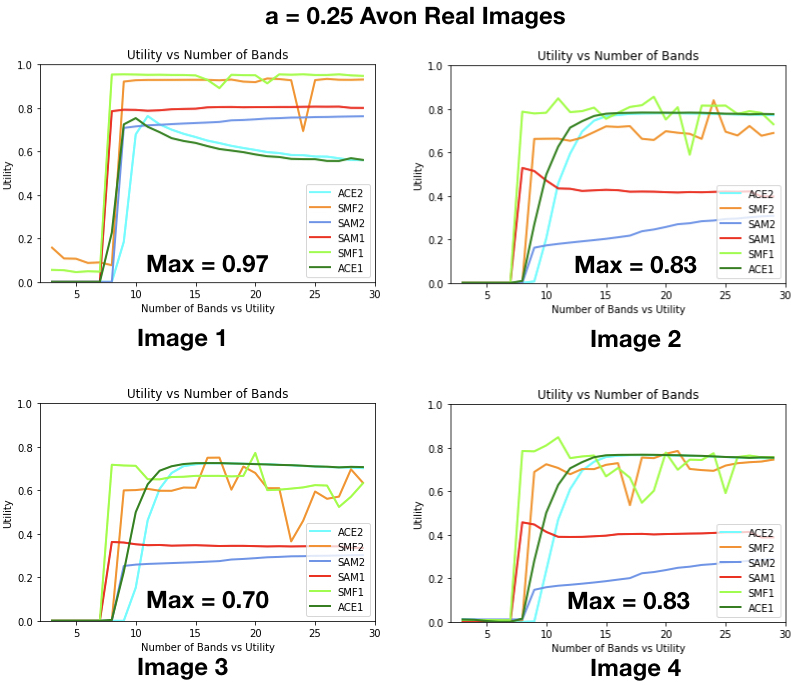

Figure A.32: a=0.25

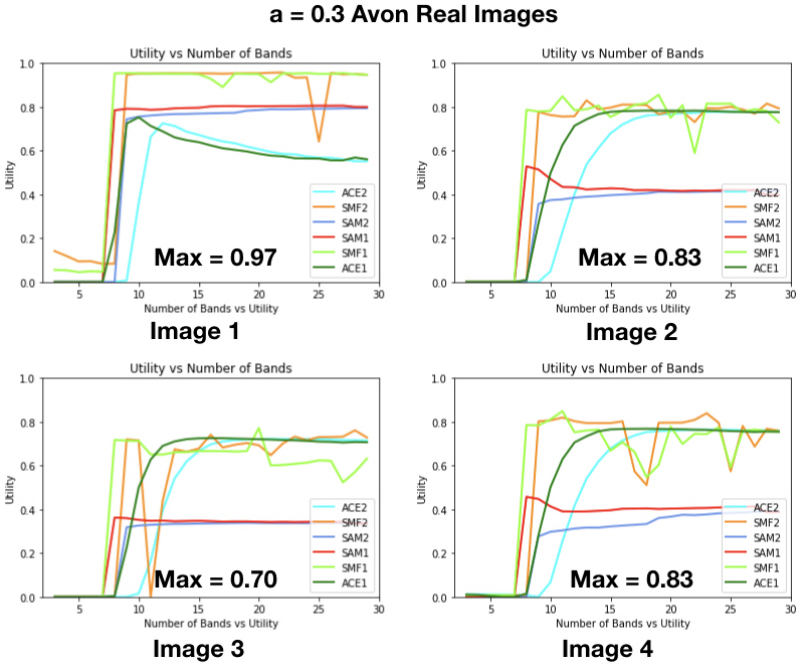

Figure A.33: a=0.3

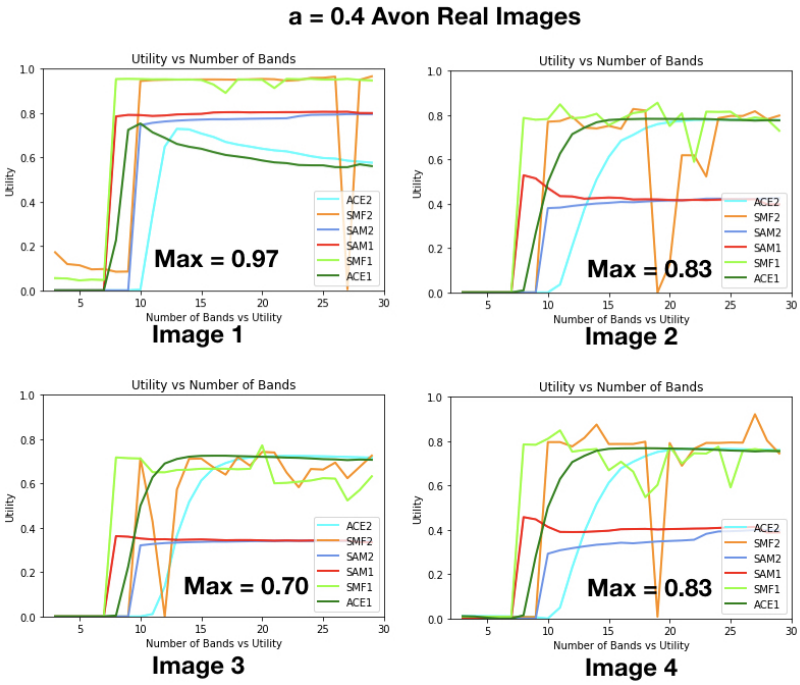

Figure A.34: a=0.4

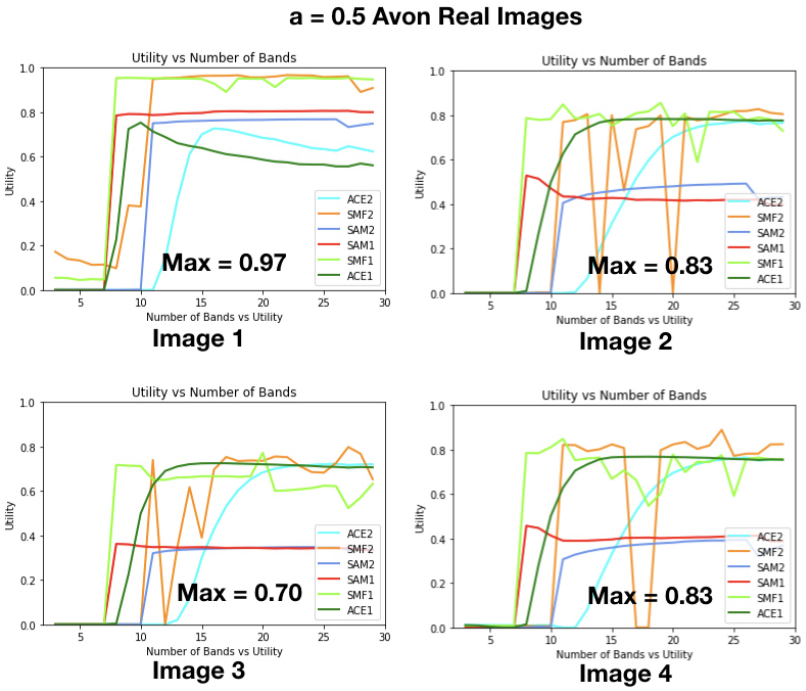

Figure A.35: a=0.5

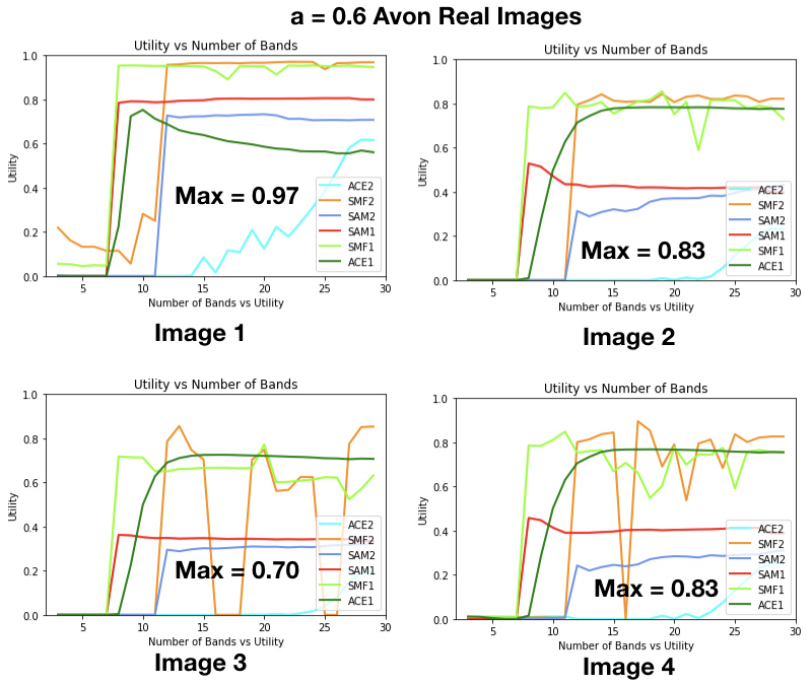

Figure A.36: a=0.6

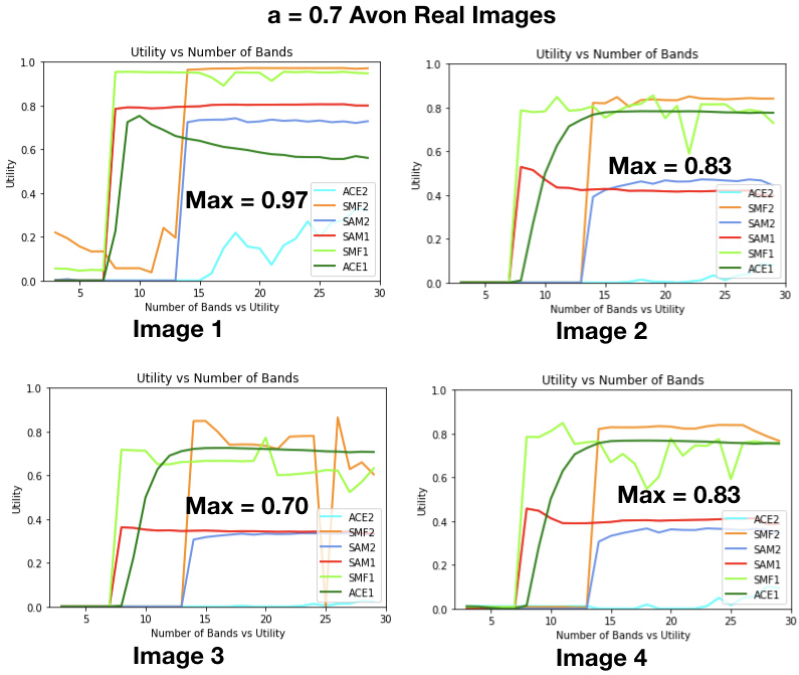

Figure A.37: a=0.7

B

Utility Selection Criteria

These are example situations in during operations that would drive decisions for the minimum utility required that would lead to the feasibility determination. This is only a guideline to illustrate the relationship between required utility, situation, and operational requirements.

Table B.1: Operational Criterion for Minimum Utility Value Selection

Utility	**Target**	**Cross Cue Asset Availability**
0.1	Stationary target	Assets for verification available within 24 hours
0.3	Stationary target	Assets for verification available within 48 hours
0.4	Mobile target	Concurrent target presence verification possible or cross cue available within 1 hour
0.5	Stationary target	Assets for verification available within 72 hours
0.6	Mobile target	Cross cue assets available within 4 hours
0.7	Permanent target	Limited or no assets available for verification
0.8	Mobile targets	Cross cue assets available within 12 hours

C

Recommendation Step by Step

This appendix provides more details along with the step by step instruction to reaching the set of system recommendations for the example mission scenario introduced in Chapter 1 with the assessment presented in Chapter 8. Figure C.1 shows the recap of the example mission.

Mission: Collect weekly images from June to July to detect presence of green vehicles in training areas of Ft Knox, KY.
Target - Green HMMWV
Location - Ft Knox, KY (Mostly vegetation, with urban area)
Situation - The presence of a target is easily verifiable by other intelligence sources. Data processing capabilities for weekly images are a maximum of 15 bands.

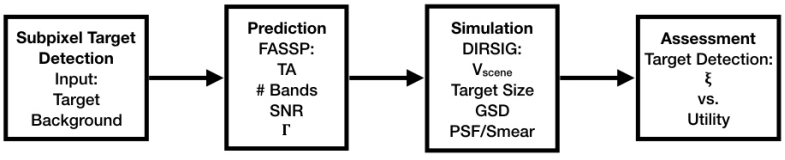

Figure C.1: Example mission scenario with green vehicle target in suburban background.

Step 1: Determine the type of background and the scene complexity metric to use. This is a non-homogenous scene, and so V_{scene} is a more appropriate metric to use than Γ. It is similar to subset scenes 2, 3, and 8 of the Trona, CA Suburban scene. Figure C.2 shows a Google earth image of the location and the similar subset scenes.

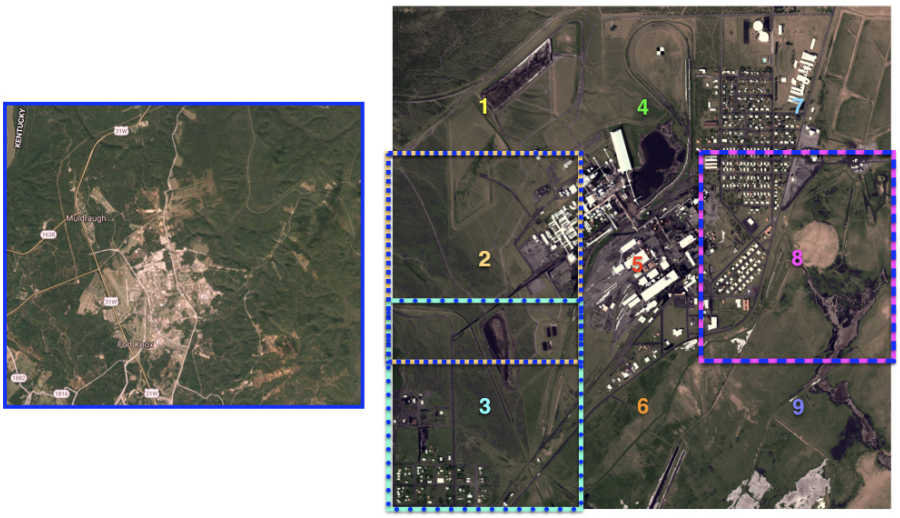

Figure C.2: Google earth image of Ft Knox, KY. with comparable subset scenes from the complex scene analyzed.

Step 2: Estimate the scene complexity. Subset scenes 2, 3, and 8 had $V_{scene} = 0.6$ when rendered at 5m GSD. Figure C.3 shows the scene volumes of the three subset scenes that were determined to be similar to the mission location.

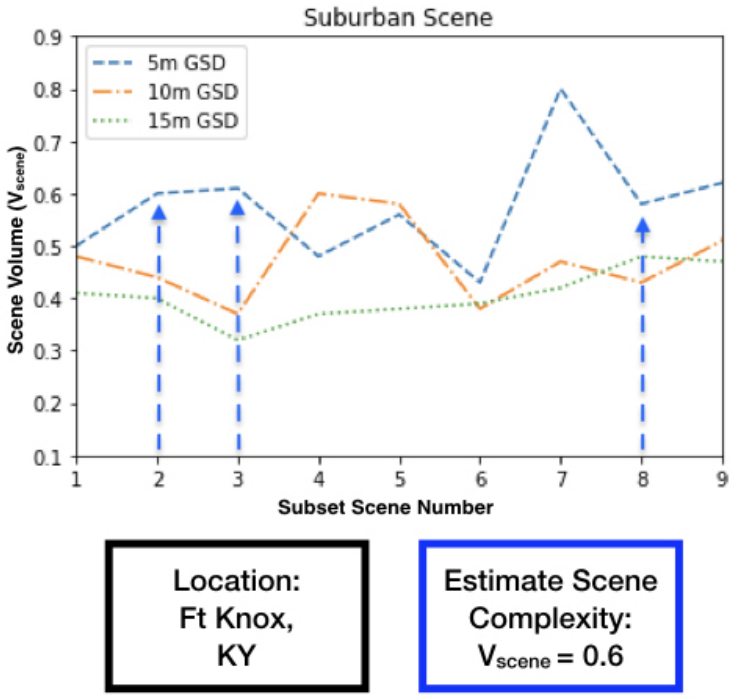

Figure C.3: Scene volume values for the Trona, CA Suburban scene. Subset scene 2, 3, and 8 had a scene volue of 0.6 when rendered at 5m GSD.

Step 3: Estimate TA saturation point and compare it to the target size. The grass background and green target had a saturation point at TA = 16%. Figure C.4 shows the trade curves of the grass background utility prediction for the showing the saturation point of the green target. The HMMWV is usually 4.5x2.0m in size which produces a maximum TA value of 36% at 5m GSD. Therefore, it is capable of generating a target fill fraction distribution above the saturation point.

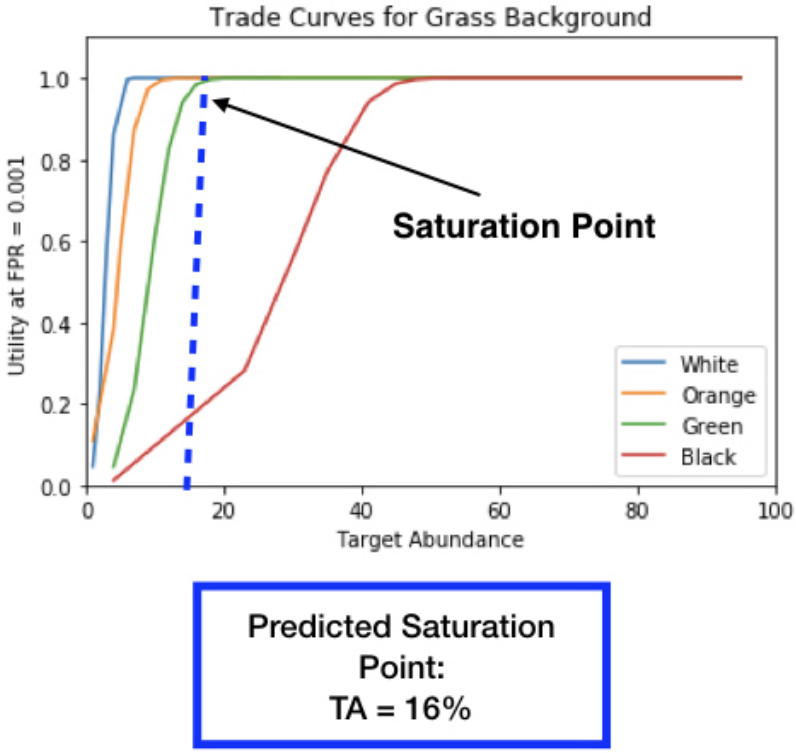

Figure C.4: TA saturation points for the grass background composition. For the green target, the saturation point was at TA = 0.16.

Step 4: Estimate ideal SNR value. For the green target against the grass background, there was a sharp increase in the predicted utility when SNR = 20, and the utility increase slowed for higher SNR values. Therefore the recommended noise parameter for this mission was SNR = 20. Figure C.5 shows the trade curves for the grass background utility prediction for the noise with sharp increase up to SNR = 20.

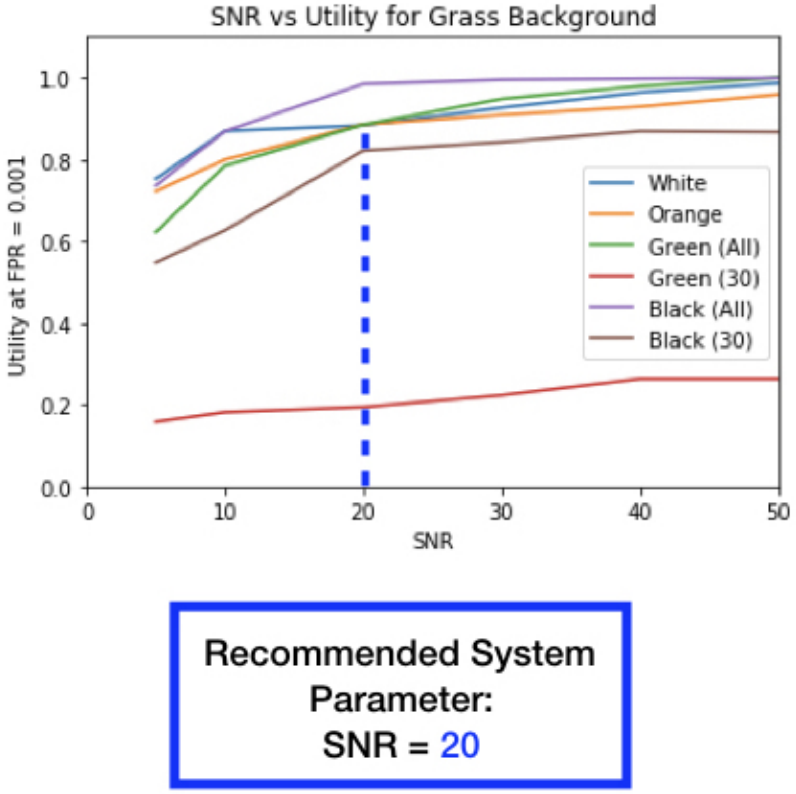

Figure C.5: Utility vs SNR curves. Shows SNR = 20 is best for this mission with limited increase in utility for higher SNR values.

Step 5: Determine the maximum number of bands mission resources would allow based on the required temporal frequency and computational resources available. For this mission that required one image per week, the maximum number of bands was 15. Figure C.6 shows that the predicted utility for the green target using 15 bands was 0.1, which met the minimum utility requirement. Therefore this mission was determined to be feasible.

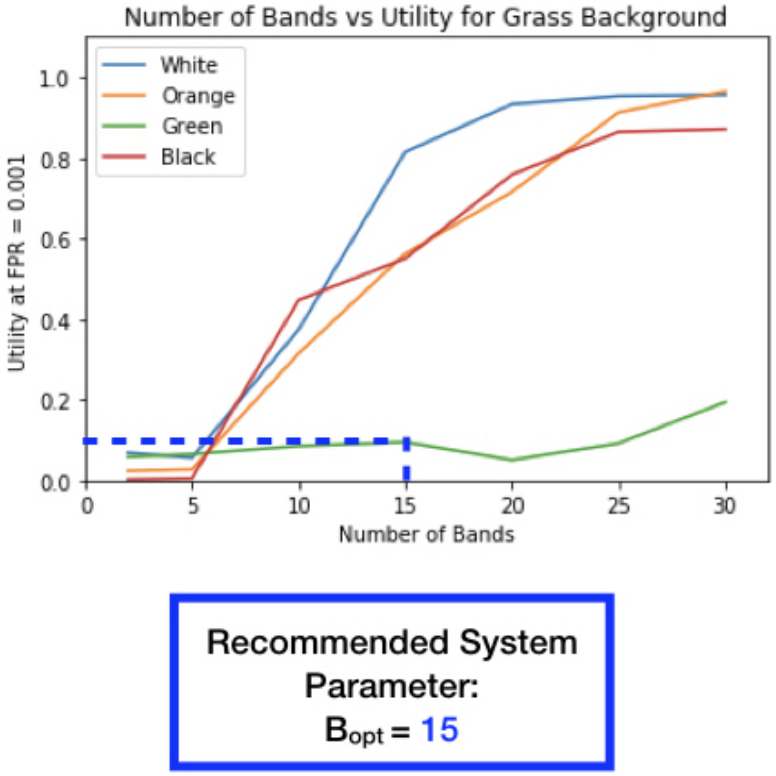

Figure C.6: Utility vs Number of Bands showing that utility of 0.1 is achieved with 15 bands.

Step 6: Determine the estimated ξ value at the predicted saturation point using the V_{scene} at reference GSD. The recommended system parameters should yield the required utility at the estimated ξ value.

$$\xi_{estimated} = \frac{TA}{V_{scene}} = \frac{0.16}{0.6} = 0.27 \tag{C.1}$$

Step 7: Look up the actual ξ value for each GSD for the required utility.

Figure C.7 shows the minimum ξ value that achieves utility ≥ 0.1 is $\xi = 0.7$. Therefore a GSD of 10m did not produce the required utility for a reasonable ξ value which indicates the TA_{mean} and V_{scene} combined value.

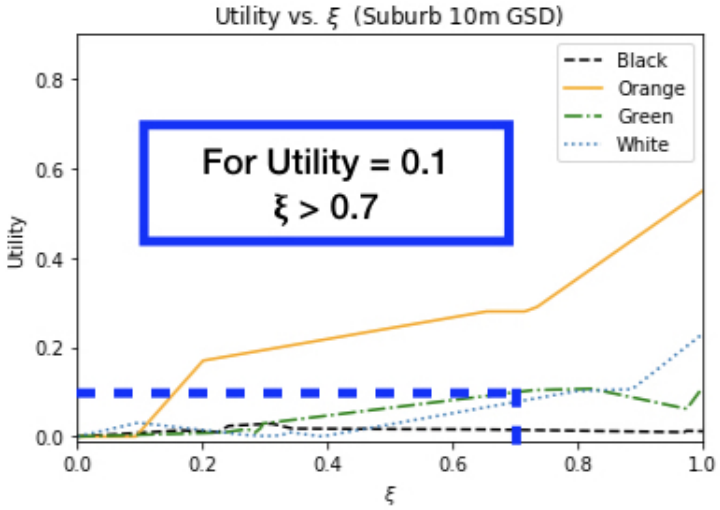

Figure C.7: Utility vs ξ curve from assessment. Showing images with 10m GSD requires $\xi \geq 0.7$ to achieve utility of 0.1.

Figure C.8 shows that the images rendered at 5m and 15m GSD was able to achieve utility = 0.1 when $\xi \geq 0.3$, which is a reasonable TA_{mean} and V_{scene} combination that was close to the estimated ξ value based on the saturation point. There was limited difference between the utility curves between the two GSDs, but the utility of the 5m GSD curves increased faster as ξ increased. Therefore the recommended GSD for this mission was 5m. This mission was determined to be feasible and the

recommended system parameters were SNR = 20, B_{opt} = 15, EFL = 315mm, and Sensor Height = 350km.

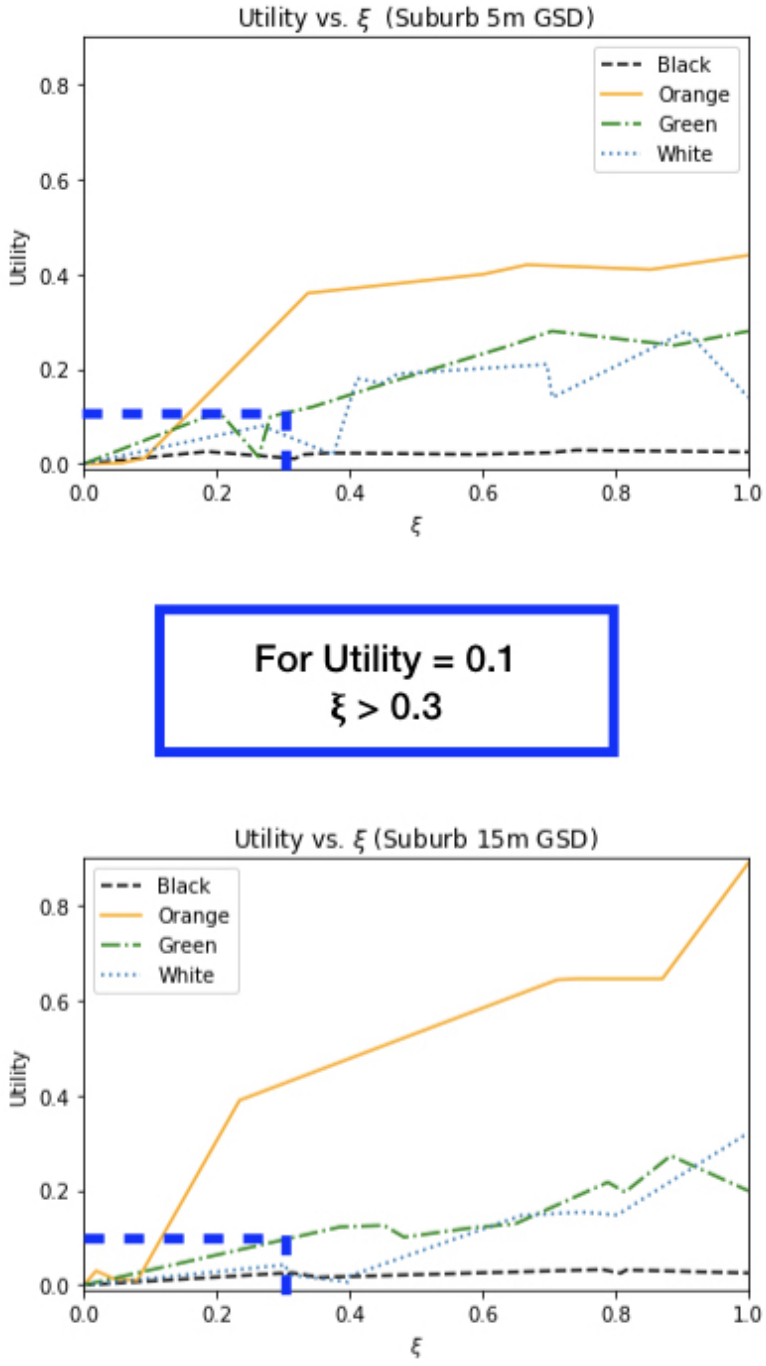

Figure C.8: Utility vs ξ curves from assessment. Shows images with 5m and 15m GSD only requires $\xi \geq 0.3$ to achieve utility of 0.1.

Acronyms

ACE Adaptive Cosine Estimator. 90, 117, 118, 163

AUC Area Under the Curve. 22, 37, 89, 145, 158–161

BOTS Bands from Only the Target Spectrum. 79, 81, 89, 90, 94, 95, 98, 109, 111, 125, 131

BRDF Bi-directional Reflectance Distribution Function. 49, 50

CEM Constrained Energy Minimzer. 74–76, 81, 90, 118, 127, 177

CFPR Constant False Alarm Rate. 22

CPU Central Processing Unit. 71, 77, 110

DIRSIG Digital Imaging and Remote Sensing Image Generation. 48–51, 55, 58, 59, 79, 81, 83, 86, 89, 90, 93, 95, 99, 100, 106, 108, 109, 111, 124, 126–129, 132, 139–141, 147, 173

EFL Effective Focal Length. 14, 52, 54–56, 58, 59

FASSP Forecasting and Analysis of Spectro-radiometric System Performance. 40, 41, 43, 79, 81, 83, 88, 90, 93, 95, 97, 99, 100, 106, 108, 111, 114, 118, 119, 124, 126, 127, 129, 130, 132, 139–141, 143, 147, 149, 153, 168, 173, 177

FPR False Positive Rate. 22, 23, 37, 42, 89, 90, 111, 140, 143, 149, 151, 158, 161, 169

FWHM Full-Width Half-Max. 29, 30, 35

GIQE General Image Quality Equation. 13, 15, 16, 18–20, 23, 36–38, 51, 52, 54, 56, 58

GRD Ground Resolved Distance. 36

GSD Ground Sampled Distance. 13–15, 19, 23–25, 38, 39, 45, 52, 58, 59, 84, 97, 100, 104–106, 111–113, 117, 128–130, 133, 135, 136, 138, 149, 151, 156–161, 164, 167–172, 174, 176

GSUM General Spectral Utility Metric. 39

HSI Hyperspectral Images. vi, 2, 3, 5, 28, 33, 60–63, 65, 66, 69–71, 73, 75, 77, 79, 83, 85, 95, 133

HYDICE Hyperspectral Digital Imagery Collection Experiment. 38, 74, 79, 83, 84, 94, 127, 131, 133, 149

ICA Independent Component Analysis. 70, 71

ID Information Divergence. 79, 90, 94

LCMV Linearly Constrained Minimum Variance. 76, 79, 90, 94

MODTRAN Moderate Resolution Transmission. 41, 51

MSI Multispectral Images. 60–62

MTF Modulation Transfer Function. 18

NDVI Normalized Difference Vegetation Index. 61

NESR Noise Equivalent Spectral Radiance. 34, 35, 45

NIIRS National Image Interpretability Rating Scale. 13–15, 23, 52, 56, 58

NMF Non-negative Matrix Factorization. 69, 70, 74

PCA Principal Component Analysis. 65, 66, 69–71, 74, 75

PDA Perfect Detection Area. 22

PSF Point Spread Function. 24, 55, 100, 109, 128, 129

RER Relative Edge Response. iii, 13, 18, 19, 24, 30, 52, 55, 56, 58, 59

ROC Receiver Operating Characteristic. 22, 40–42, 81, 88–90, 97, 109, 113, 117, 127, 138, 140, 141, 145, 147, 156, 158–163

SAM Spectral Angle Mapper. 90, 117, 163

SCR Signal to Clutter Ratio. 27, 37

SFPR Specified False Positive Rate. 22, 38

SHARE 2012 SpectTIR Hyperspectral Airborne Rochester Experiment 2012. 79, 81, 83, 84, 88, 90

SMF Spectral Matched Filter. 81, 90, 117, 118, 127, 139, 163

SNR Signal-to-Noise Ratio. 13, 16–19, 34, 36–38, 41, 42, 45, 52–54, 58, 88, 97, 100, 109, 110, 131, 132, 149, 153, 156, 171

SQE Spectral Quality Equation. 38

SQRS Spectral Quality Rating Scale. 36–38

SRER Spectral Relative Edge Response. 30, 35

SSV Spectral Similarity Value. 26, 27, 45, 125, 148, 153, 161, 168, 176

SUMO Simulation of Urban Mobility. 134, 136

SUV Sports Utility Vehicle. 135

SVD Singular Value Decomposition. 65

TA Target Abundance or Target Fill Fraction. 24, 25, 40–42, 81, 86, 97, 99, 100, 102–106, 111–114, 127–133, 135, 136, 140, 141, 143, 145, 148, 149, 156–158, 161–163, 167–172, 175–177

TBC Target and Background Comparison. 79, 90, 94, 95

TPR True Positive Rate. 22, 38, 41, 89, 90

VNIR Visible Near Infrared. 32, 38, 79, 121, 122, 131, 149, 176

WASP Wildfire Airborne Sensor Program. 83, 84

Bibliography

[1] Wheelon, A. D., "Corona: The First Reconnaissance Satellites," *Physics Today* **50**, 24–30 (Feb. 1997).

[2] Van Zyl, J. and Kim, Y., [*Synthetic aperture radar polarimetry*], JPL space science and technology series, Wiley, Hoboken, NJ, 1st ed ed. (2011).

[3] Stefanou, M. S., *Spectral image utility for target detection applications*, PhD Thesis, Rochester Institiute of Technology (Aug. 2008).

[4] Oesa A. Weaver, *An analytical framwork for assessing efficacy of small satellites in performing imaging missions*, PhD thesis, Rochester Institiute of Technology, Rochester, NY, USA (July 2015).

[5] Riot, Vincent, "Space Program Innovation, One Small Satellite at a Time," *Science and Technology Review* , 4–11 (Apr. 2019).

[6] Fiete, R. D., "Image quality and λFN/p for remote sensing systems," *Optical Engineering* **38**, 1229 (July 1999).

[7] Shen, S. S., "Spectral quality equation relating collection parameters to material identification performance," in [*SPIE Conference Proceedings Defense and Security*], Shen, S. S. and Lewis, P. E., eds., 448 (June 2005).

[8] Messinger, D. W., Ziemann, Amanda, Baesner, Bill, and Schlamm, Ariel, "Metrics of spectral image complexity with application to large area search," *Optical Engineering* **51**, 036201 (Mar. 2012).

[9] Kerekes, J. and Landgrebe, D., "Simulation of optical remote sensing systems," *IEEE Transactions on Geoscience and Remote Sensing* **27**, 762–771 (Nov. 1989).

[10] Kerekes, John P. and Landgrebe, David A., "An Analytical Model of Earth-Observational Remote Sensing Systems," *IEEE Transactions on Systems, Man, and Cybernetics* **21**, 125–133 (Feb. 1991).

[11] Kerekes, John and Landgrebe, David, "Parameter Trade Offs for Imaging Spectroscopy Systems," *IEEE Transactions on Geoscience and Remote Sensing* **29**, 57–65 (Jan. 1991).

[12] Cao, X., Zhang, F., Lin, X., Sun, Z., and Xu, G., "Optical remote sensing small satellite project," *Acta Astronautica* **54**, 139–143 (Jan. 2004).

[13] Jafarsalehi, A., Fazeley, H., and Mirshams, M., "Conceptual Remote Sensing Satellite Design Optimization under uncertainty," *Aerospace Science and Technology* **55**, 377–391 (Aug. 2016).

[14] Li, N., Huang, P., Zhao, H., and Jia, G., "The quantitative evaluation of application of hyperspectral data based on multi-parameters joint optimization," *Science China Technological Sciences* **57**, 2249–2255 (Nov. 2014).

[15] Jason West, *Matched filter stochastic background characterization for hyperspectral target detection*, Master's thesis, Rochester Instituite of Technology (2005).

[16] Adam Cisz, *Performance comparison of hyperspectral target detection algorithms*, Master's thesis, Rochester Instituite of Technology (2006).

[17] Adam Grimm, *Comparison of hyperspectral imagery target detection algorithm chains*, Master's thesis, Rochester Instituite of Technology (2005).

[18] Leachtenauer, J. C., Malila, W., Irvine, J., Colburn, L., and Salvaggio, N., "General Image-Quality Equation: GIQE," *Applied Optics* **36**, 8322 (Nov. 1997).

[19] Leigh Harrington, David Blanchard, James Salacain, Stephen Smith, and Philip Amanik, "General Image Quality Equation; GIQE version 5," (Sept. 2015).

[20] Tantalo, T., "Comparison of SNR image quality metrics for remote sensing systems," *Optical Engineering* **40**, 574 (Apr. 2001).

[21] Dimitris Manolakis, David Marden, and Gary A. Shaw, "Hyperspectral Image Processing for Automatic Target Detection Applications," *Lincoln Laboratory Journal* **14**(1), 79 – 116 (2003).

[22] Richards, J. A. and Jia, X., [*Remote sensing digital image analysis: an introduction*], Springer, Berlin (2006). OCLC: 225365047.

[23] Sweet, J. N., Sharp, M. H., and Granahan, J. C., "Hyperspectral analysis toolset," in [*SPIE Conference Proceedings Europe Remote Sensing*], Fujisada, H., Lurie, J. B., Ropertz, A., and Weber, K., eds., 396–407 (Feb. 2001).

[24] Kerekes, J. P., Cisz, A. P., and Simmons, R. E., "A comparative evaluation of spectral quality metrics for hyperspectral imagery," in [*SPIE Conference Proceedings Defense and Security*], Shen, S. S. and Lewis, P. E., eds., 469 (June 2005).

[25] Martin, L., Vrabel, J., and Leachtenauer, J., "Metrics for Assessment of Hyperspectral Image Quality and Utility," *Proceedings of International Symposium of Spectral Sensing Research* (1999).

[26] Eismann, M. T., [*Hyperspectral remote sensing*], SPIE Press, Bellingham, Wash (2012).

[27] Stefanou, M. and Kerekes, J., "Image-Derived Prediction of Spectral Image Utility for Target Detection Applications," *IEEE Transactions on Geoscience and Remote Sensing* **48**, 1827–1833 (Apr. 2010).

[28] Kerekes, J. P. and Hsu, S. M., "Spectral quality metrics for VNIR and SWIR hyperspectral imagery," in [*SPIE Conference Proceedings Defense and Security*], Shen, S. S. and Lewis, P. E., eds., 549 (Aug. 2004).

[29] Shen, S. S., "Spectral quality equation relating collection parameters to object/anomaly detection performance," in [*SPIE Conference Proceedings AeroSense*], Shen, S. S. and Lewis, P. E., eds., 29 (Sept. 2003).

[30] Simmons, R. E., Elder, T. D., Stewart, D. J., Cincotta, E. J., Kennedy, C. S., and Van Nostrand, R. C., "General spectral utility metric for spectral imagery," in [*SPIE Conference Proceedings Defense and Security*], Shen, S. S. and Lewis, P. E., eds., 457 (June 2005).

[31] Kerekes, J. and Baum, J., "Spectral imaging system analytical model for subpixel object detection," *IEEE Transactions on Geoscience and Remote Sensing* **40**, 1088–1101 (May 2002).

[32] Berk, A., Bernstein, L., Anderson, G., Acharya, P., Robertson, D., Chetwynd, J., and Adler-Golden, S., "MODTRAN Cloud and Multiple Scattering Upgrades with Application to AVIRIS," *Remote Sensing of Environment* **65**, 367–375 (Sept. 1998).

[33] Kerekes, J., "Model-based Exploration of HSI Spaceborne Sensor Requirements with Application Performance as the Metric," in [*2006 IEEE International Symposium on Geoscience and Remote Sensing*], 1613–1616, IEEE, Denver, CO, USA (July 2006).

[34] Ientilucci, E. J., "Oblique hyperspectral radiometric phenomenology study," in [*SPIE Conference Proceedings Europe Remote Sensing*], Bruzzone, L., Notarnicola, C., and Posa, F., eds., 74770N (Sept. 2009).

[35] Schott, J., Brown, S., Raqueño, R., Gross, H., and Robinson, G., "An Advanced Synthetic Image Generation Model and its Application to Multi/Hyperspectral Algorithm Development," *Canadian Journal of Remote Sensing* **25**, 99–111 (June 1999).

[36] Schott, J. R., [*Remote sensing: the image chain approach*], Oxford University Press, New York, 2nd ed ed. (2007).

[37] Han, S. and Kerekes, J. P., "Overview of Passive Optical Multispectral and Hyperspectral Image Simulation Techniques," *IEEE Journal of Selected Topics in Applied Earth Observations and Remote Sensing* **10**, 4794–4804 (Nov. 2017).

[38] Govaerts, Y. and Verstraete, M., "Raytran: a Monte Carlo ray-tracing model to compute light scattering in three-dimensional heterogeneous media," *IEEE Transactions on Geoscience and Remote Sensing* **36**, 493–505 (Mar. 1998).

[39] Jensen, H. W., [*Realistic image synthesis using photon mapping*], A K Peters, Natick, MA (2001).

[40] Goodenough, A. A. and Brown, S. D., "DIRSIG5: Next-Generation Remote Sensing Data and Image Simulation Framework," *IEEE Journal of Selected Topics in Applied Earth Observations and Remote Sensing* **10**, 4818–4833 (Nov. 2017).

[41] Ientilucci, E. J. and Brown, S. D., "Advances in wide-area hyperspectral image simulation," in [*SPIE Conference Proceedings Targets and Backgrounds IX*], Watkins, W. R., Clement, D., and Reynolds, W. R., eds., **5075**, 110, SPIE, Orlando, FL (Sept. 2003).

[42] Hapke, B., "Bidirectional reflectance spectroscopy," *Icarus* **67**, 264–280 (Aug. 1986).

[43] Hapke, B., "Bidirectional reflectance spectroscopy," *Icarus* **195**, 918–926 (June 2008).

[44] Litvinov, P., Hasekamp, O., Cairns, B., and Mishchenko, M., "Reflection models for soil and vegetation surfaces from multiple-viewing angle photopolarimetric measurements," *Journal of Quantitative Spectroscopy and Radiative Transfer* **111**, 529–539 (Mar. 2010).

[45] Meng, Q., Sun, Y., Xue, X., Gu, X., Vatseva, R., Zhang, J.-h., and Jancso, T., "Study on a bidirectional reflectance distribution function inversion model based on HJ-1 CCD imagery," *Environmental Earth Sciences* **75** (Sept. 2016).

[46] Berk A., Bernstein, L. S., and Robertson, D. C., [*MODTRAN: a moderate resolution model for LOWTRAN7*], Air Force Geopysics Lab, Hanscom AFB, MA (1989).

[47] Berk, A., Conforti, P., Kennett, R., Perkins, T., Hawes, F., and van den Bosch, J., "MODTRAN6: a major upgrade of the MODTRAN radiative transfer code," in [*SPIE Conference Proceedings Defense and Security*], Velez-Reyes, M. and Kruse, F. A., eds., 90880H (June 2014).

[48] Han, S., Higbee, S., Siegel, L., and Kerekes, J. P., "Simulation techniques for image utility analysis," in [*SPIE Conference Proceedings*], 25, SPIE (May 2018).

[49] Gandhi, G. M., Parthiban, S., Thummalu, N., and Christy, A., "Ndvi: Vegetation Change Detection Using Remote Sensing and Gis – A Case Study of Vellore District," *Procedia Computer Science* **57**, 1199–1210 (2015).

[50] An, J., Zhang, X., Zhou, H., and Jiao, L., "Tensor-Based Low-Rank Graph With Multimanifold Regularization for Dimensionality Reduction of Hyperspectral Images," *IEEE Transactions on Geoscience and Remote Sensing* **56**, 4731–4746 (Aug. 2018).

[51] Zhang, M., Du, B., Zhang, L., and Li, X., "A Low-Rank Tensor Decomposition Based Hyperspectral Image Compression Algorithm," in [*Advances in Multimedia Information Processing - PCM 2016*], Chen, E., Gong, Y., and Tie, Y., eds., **9916**, 141–149, Springer International Publishing, Cham (2016).

[52] Qu, J., Lei, J., Li, Y., Dong, W., Zeng, Z., and Chen, D., "Structure Tensor-Based Algorithm for Hyperspectral and Panchromatic Images Fusion," *Remote Sensing* **10**, 373 (Mar. 2018).

[53] Huber-Lerner, M., Hadar, O., Rotman, S. R., and Huber-Shalem, R., "Compression of Hyperspectral Images Containing a Subpixel Target," *IEEE Journal of Selected Topics in Applied Earth Observations and Remote Sensing* **7**, 2246–2255 (June 2014).

[54] Tipping, M. and Bishop, C., "Mixtures of probabilistic principal component analysers," *Neural Computation* , 443 – 482 (1999).

[55] Kerekes, J. P., Ludgate, K., Giannandrea, A., Raqueno, N. G., and Goldberg, D. S., "SHARE 2012: subpixel detection and unmixing experiments," in [*SPIE Conference Proceedings Defense, Security, and Sensing*], Shen, S. S. and Lewis, P. E., eds., 87430H (May 2013).

[56] Jia, S. and Qian, Y., "Constrained Nonnegative Matrix Factorization for Hyperspectral Unmixing," *IEEE Transactions on Geoscience and Remote Sensing* **47**, 161–173 (Jan. 2009).

[57] Sun, W., Li, W., Li, J., and Lai, Y. M., "Band selection using sparse nonnegative matrix factorization with the thresholded Earth's mover distance for hyperspectral imagery classification," *Earth Science Informatics* **8**, 907–918 (Dec. 2015).

[58] Hyvärinen, A. and Oja, E., "Independent component analysis: algorithms and applications," *Neural Networks* **13**, 411–430 (June 2000).

[59] Jing Wang and Chein-I Chang, "Independent component analysis-based dimensionality reduction with applications in hyperspectral image analysis," *IEEE Transactions on Geoscience and Remote Sensing* **44**, 1586–1600 (June 2006).

[60] Wang, L., Li, H.-C., Xue, B., and Chang, C.-I., "Constrained Band Subset Selection for Hyperspectral Imagery," *IEEE Geoscience and Remote Sensing Letters* **14**, 2032–2036 (Nov. 2017).

[61] Rickard, L. J., Basedow, R. W., Zalewski, E. F., Silverglate, P. R., and Landers, M., "HYDICE: an airborne system for hyperspectral imaging," in [*Optical Engineering and Photonics in Aerospace Sensing*], Vane, G., ed., 173 (Sept. 1993).

[62] Karlholm, J. and Renhorn, I., "Wavelength band selection method for multispectral target detection," *Applied Optics* **41**, 6786 (Nov. 2002).

[63] Cover, T. M. and Thomas, J. A., [*Elements of information theory*], Wiley-Interscience, Hoboken, N.J, 2nd ed ed. (2006). OCLC: ocm59879802.

[64] Chein-I Chang, Qian Du, Tzu-Lung Sun, and Althouse, M., "A joint band prioritization and band-decorrelation approach to band selection for hyperspectral image classification," *IEEE Transactions on Geoscience and Remote Sensing* **37**, 2631–2641 (Nov. 1999).

[65] Chein-I Chang and Su Wang, "Constrained band selection for hyperspectral imagery," *IEEE Transactions on Geoscience and Remote Sensing* **44**, 1575–1585 (June 2006).

[66] Han, S., Kerekes, J., Higbee, S., Siegel, L., and Pertica, A., "Band Selection Method for Subpixel Target Detection Using Only the Target Signature," *Applied Optics* , 14 (2019).

[67] Cui, Z., Kerekes, J., DeAngelis, C., Brown, S., and Nance, C. E., "A comparison of real and simulated airborne hyperspectral imagery," in [*2014 IEEE Western New York Image and Signal Processing Workshop (WNYISPW)*], 19–22, IEEE, Rochester, NY, USA (Nov. 2014).

[68] Bloechl, K., De Angelis, C., Gartley, M., Kerekes, J., and Nance, C. E., "A comparison of real and simulated airborne multisensor imagery," in [*SPIE Conference Proceedings Defense and Security*], Velez-Reyes, M. and Kruse, F. A., eds., 90880G (June 2014).

[69] Giannandrea, A., Raqueno, N., Messinger, D. W., Faulring, J., Kerekes, J. P., van Aardt, J., Canham, K., Hagstrom, S., Ontiveros, E., Gerace, A., Kaufman, J., Vongsy, K. M., Griffith, H., Bartlett, B. D., Ientilucci, E., Meola, J., Scarff, L., and Daniel, B., "The SHARE 2012 data campaign," in [*SPIE Conference Proceedings Defense, Security, and Sensing*], Shen, S. S. and Lewis, P. E., eds., 87430F (May 2013).

[70] Canham, K., Goldberg, D., Kerekes, J., Raqueno, N., and Messinger, D., "SHARE 2012: large edge targets for hyperspectral imaging applications," in [*SPIE Conference Proceedings Defense, Security, and Sensing*], Shen, S. S. and Lewis, P. E., eds., 87430G (May 2013).

[71] Sun, Y. and Kerekes, J., "An analysis task comparison of uncorrected vs. geo-registered airborne hyperspectral imagery," in [*SPIE Conference Proceedings Defense and Security*], Velez-Reyes, M. and Kruse, F. A., eds., 94720I (May 2015).

[72] Exelis Visual Information Solutions, Boulder Colorado, "Environment for Visualizing Images."

[73] Kemker, R., Salvaggio, C., and Kanan, C., "Algorithms for semantic segmentation of multispectral remote sensing imagery using deep learning," *ISPRS Journal of Photogrammetry and Remote Sensing* **145**, 60–77 (Nov. 2018).

[74] The Astropy Collaboration, Robitaille, T. P., and Tollerud, E. J., "Astropy: A community Python package for astronomy," *Astronomy & Astrophysics* **558**, A33 (Oct. 2013).

[75] The Astropy Collaboration, Price-Whelan, A. M., and Donath, A., "The Astropy Project: Building an Open-science Project and Status of the v2.0 Core Package," *The Astronomical Journal* **156**, 123 (Aug. 2018).

[76] Lopez, P. A., Behrisch, M., Bieker-Walz, L., Erdmann, J., Flotterod, Y.-P., Hilbrich, R., Lucken, L., Rummel, J., Wagner, P., and WieBner, E., "Microscopic Traffic Simulation using SUMO," in [*2018 21st International Conference on Intelligent Transportation Systems (ITSC)*], 2575–2582, IEEE, Maui, HI (Nov. 2018).

[77] Hilbrich, R., "SUMO - Simulation of Urban MObility DLR - Institute of Transporation."

[78] Presnar, M. D., Raisanen, A. D., Pogorzala, D. R., Kerekes, J. P., and Rice, A. C., "Dynamic scene generation, multimodal sensor design, and target tracking demonstration for hyperspectral/polarimetric performance-driven sensing," in [*SPIE Conference Proceedings Defense, Security, and Sensing*], 76720T (Apr. 2010).

[79] Han, S., Farfard, A., Kerekes, J., Gartley, M., Ientilucci, E., Savakis, A., Law, C., Parhan, J., Turek, M., Fieldhouse, K., and Rovito, T., "Efficient generation of image chips for training deep learning networks," in [*SPIE Conference Proceedings Defense and Security*], **10202**, 1020203 (May 2017).